NUMERICAL MODELLING OF ULTRA LOW FREQUENCY WAVES IN EARTH'S MAGNETOSPHERE

Tom Elsden

A Thesis Submitted for the Degree of PhD
at the
University of St Andrews

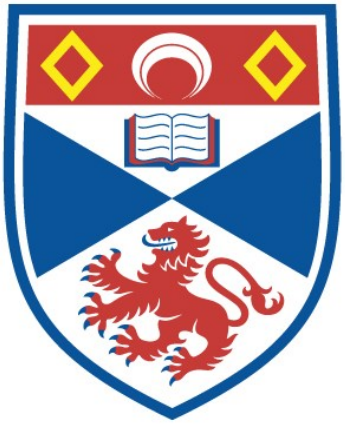

2016

Numerical Modelling of Ultra Low Frequency Waves in Earth's Magnetosphere

Tom Elsden

University of
St Andrews

This thesis is submitted in partial fulfilment for the degree of PhD at the University of St Andrews

May 16, 2016

Candidates Declarations

I, Tom Elsden, hereby certify that this thesis, which is approximately 37,000 words in length, has been written by me, and that it is the record of work carried out by me, or principally by myself in collaboration with others as acknowledged, and that it has not been submitted in any previous application for a higher degree.

I was admitted as a research student in September 2012 and as a candidate for the degree of Ph.D in September 2012; the higher study for which this is a record was carried out in the University of St Andrews between 2012 and 2016.

Date:

Signature of candidate:

Supervisors Declaration

I hereby certify that the candidate has fulfilled the conditions of the Resolution and Regulations appropriate for the degree of Ph.D in the University of St Andrews and that the candidate is qualified to submit this thesis in application for that degree.

Date:

Signature of supervisor:

Permission for Publication

In submitting this thesis to the University of St Andrews I understand that I am giving permission for it to be made available for use in accordance with the regulations of the University Library for the time being in force, subject to any copyright vested in the work not being affected thereby. I also understand that the title and the abstract will be published, and that a copy of the work may be made and supplied to any bona fide library or research worker, that my thesis will be electronically accessible for personal or research use unless exempt by award of an embargo as requested below, and that the library has the right to migrate my thesis into new electronic forms as required to ensure continued access to the thesis. I have obtained any third-party copyright permissions that may be required in order to allow such access and migration, or have requested the appropriate embargo below.

The following is an agreed request by candidate and supervisor regarding the publication of this thesis:

PRINTED COPY

Embargo on all of print copy for a period of 1 year (maximum five) on the following grounds:

Publication would be commercially damaging to the researcher, or to the supervisor, or the University.

Supporting statement for printed embargo request:

Part of this thesis contains unpublished material, which could be used by fellow researchers before publication, which would be damaging for the researcher, supervisor and University.

ELECTRONIC COPY

Embargo on all of electronic copy for a period of 1 year (maximum five) on the following grounds:

Publication would be commercially damaging to the researcher, or to the supervisor, or the University.

Supporting statement for electronic embargo request:

Part of this thesis contains unpublished material, which could be used by fellow researchers before publication, which would be damaging for the researcher, supervisor and University.

Date:

Signature of candidate:

Signature of supervisor:

Acknowledgements

The work in this thesis represents 3 and a half years of my life, which I have been thoroughly grateful to spend in St Andrews. The first acknowledgment goes to the Solar Theory group here, for accepting me as a student. I vividly remember finding out I had funding for a PhD, and ecstatically jumping around not quite believing it. I was unsure as to which career to pursue once I had graduated in 2012, but I found a perfect home staying in St Andrews. Secondly, to my supervisor Andy Wright, who has guided me from beginning to end always with the perfect amount of advice. That is the art of a good supervisor, knowing when to leave the student to work independently and knowing when they need help, and Andy struck that balance perfectly. Enough thanks cannot be given for this.

I've met some incredible people over my time here, some from the very beginning who I am still lucky to call friends. For all who have shared in the journey with me and made this time so memorable, thank you, and long may our friendships continue!

To my family, you have always supported me in everything I do and it is that support which has made me believe I could get to where I have today. For this and so much more, mum, dad and Chris, I love you all so much and thank you.

Finally to Cara, thank you for putting up with me these last few months of hectic late nights writing and coding and for always making me smile even when I was stressed. You have been so supportive and always made me believe anything was possible. This is for you :)

Abstract

Ultra Low Frequency (ULF) waves are a ubiquitous feature of Earth's outer atmosphere, known as the magnetosphere, having been observed on the ground for almost two centuries, and in space over the last 50 years. These waves represent small oscillations in Earth's magnetic field, most often as a response to the external influence of the solar wind. They are important for the transfer of energy throughout the magnetosphere and for coupling different regions together. In this thesis, various features of these oscillations are considered. A detailed background on the history and previous study of ULF waves relevant to our work is given in the introductory chapter. In the following chapters, we predominantly use numerical methods to model ULF waves, which are carefully developed and thoroughly tested. We consider the application of these methods to reports on ground and spaced based observations, which allows a more in depth study of the data. In one case, the simulation results provide evidence for an alternative explanation of the data to the original report, which displays the power of theoretical modelling. An analytical model is also constructed, which is tested on simulation data, to identify the incidence and reflection of a class of ULF wave in the flank magnetosphere. This technique is developed with the aim of future applications to satellite data. Further to this, we develop models both in Cartesian and dipole geometries to investigate some of the theoretical aspects of the coupling between various waves modes. New light is shed on the coupling of compressional (fast) and transverse (Alfvén) magnetohydrodynamic (MHD) wave modes in a 3D dipole geometry. Overall, this thesis aims to develop useful numerical models, which can be used to aid in the interpretation of ULF wave observations, as well as probing new aspects of the existing wave theory.

Collaboration Statement

The work in Chapter 4 of this thesis was completed in collaboration with Dr Michael Hartinger who collaborated on the publication upon which the chapter is based, Elsden et al. [2016].

Related Publications

The work in this thesis has produced two publications, both in the Journal of Geophysical Research, Space Science. The full references for these publications can be found in the bibliography section under Elsden and Wright [2015] and Elsden et al. [2016].

Contents

Chapter 1

Introduction

This thesis concerns itself with low frequency oscillations of the Earth's magnetic field. This introductory chapter will firstly explain many of the core concepts required to appreciate these oscillations, such as the basic structure of the magnetosphere and the theoretical basis for their study, namely the field of magnetohydrodynamics. This will be followed by a brief summary of previous related work to develop a picture of where this thesis positions itself within the existing literature. Finally, the aims of the thesis will be discussed to present a clear outline of the chapters to follow. As a reader, a general background in mathematics or physics would be required to grasp most of the work in this thesis, with a basic knowledge of electromagnetism and Maxwell's equations also being useful.

1.1 Earth's Magnetosphere

The Earth is surrounded by an invisible protective shield known as the magnetosphere. This 'bubble' represents the region where Earth's magnetic field, generated by the motion of liquid iron within Earth's outer core, governs the plasma (ionised gas) behaviour. Outwith this region, the solar wind streams past at average speeds of a few hundred kilometers per second, much like a river diverting its course around a large rock. It is from this wind of charged particles that we are shielded by the Earth's magnetic field. Being comprised of charged particles, the solar wind also carries a magnetic field called the interplanetary magnetic field (IMF). It was originally hypothesised by Chapman and Bartels [1940] that there was no 'interaction' between the IMF in the solar wind and the Earth's magnetic field. However, the works of James Dungey demonstrated that these magnetic fields can interact, through the process of magnetic reconnection [Dungey, 1961]. This process describes how oppositely directed magnetic field lines can change their topology and connections when stressed. Dungey showed how reconnection could occur on the dayside and the nightside of the Earth at magnetic neutral points (points where there is no

magnetic field). When the IMF has a dominantly southward orientation, the field lines can break at the dayside neutral point and be convected in the solar wind across the poles of the Earth into the nightside. This addition of magnetic flux on the nightside compresses the oppositely directed field lines in the tail causing further reconnection events. The occurrence of reconnection either on the day or the nightside can lead to aurora, where particles originating from the solar wind are injected into Earth's upper atmosphere. The energy of the precipitating particles determines the depth into the atmosphere that they will penetrate. The changing chemical composition of the atmosphere with height means that different energy particles will interact with different elements, which is what produces the vast arrays of auroral colours [e.g. Akasofu, 2007; Bone, 1996]. Overall, this passage of energy from the dayside into the nightside and back again, known as the Dungey cycle, describes how the magnetosphere processes the constant disturbances to its equilibrium caused by the inhomogeneous solar wind. Although not discussed directly in this thesis, this fundamental concept of the transfer of energy is central to the understanding of almost all magnetospheric processes. Indeed, it is the Dungey cycle which has shaped the modern understanding of the magnetospheric structure, a schematic of which with the key features highlighted is given in Figure 1.1.1.

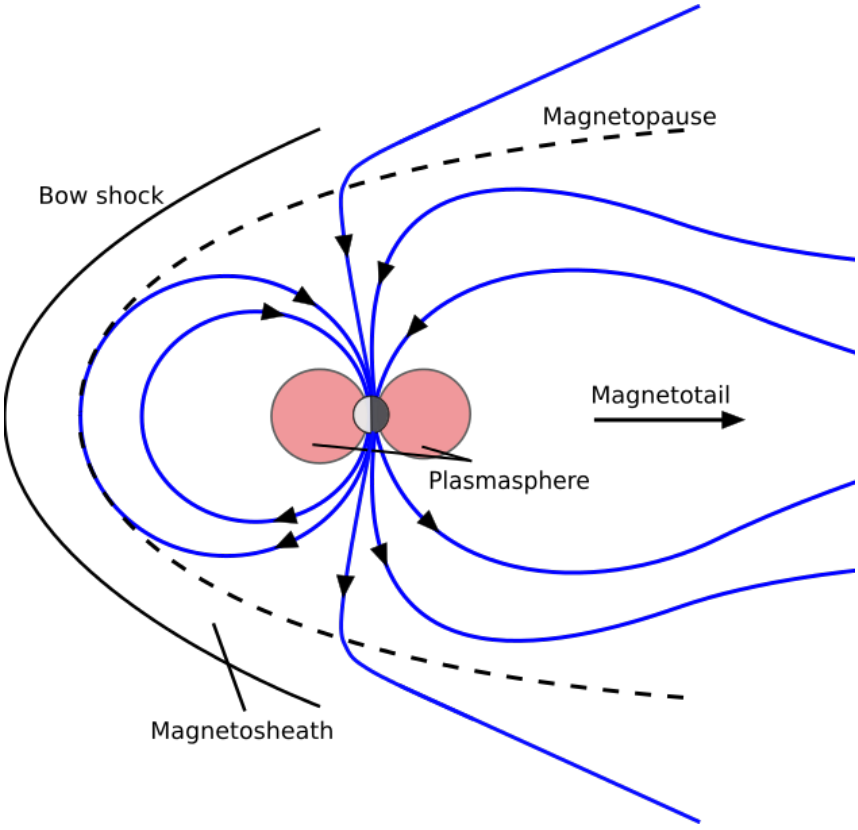

Figure 1.1.1: A schematic of the magnetosphere showing the general structure in a meridional plane, with the sun to the left. Note this is not to scale. The blue lines represent magnetic field lines, with the other areas and boundaries as labelled.

Firstly, a notional position for the magnetopause is denoted by the dashed line. This boundary represents a pressure balance between the solar wind dynamic pressure and the terrestrial magnetic field's pressure, and hence determines the outermost extent of the magnetosphere. The magnetopause has a variable position dependent upon the solar wind conditions, but on average the so called 'standoff' distance is approximately 10 Earth radii (10 R_E). The presence of the magnetopause was only confirmed in 1963 (despite being theorised many years previously), when, in a rather beautifully rudimentary manner, the Explorer 12 satellite was flown straight through it [Cahill and Amazeen, 1963]. The authors comment on the marked change in nature of the oscillations in the magnetic field observed inside and outside the magnetopause boundary. Outside of the magnetopause boundary lies the bow shock, which represents the standing shock wave ahead of the Earth. The Earth can be thought of as a stationary object in the supersonic solar wind flow, and hence the plasma must be slowed (and in the process heated) before reaching the Earth. This shocked plasma forms the magnetosheath, a region of hotter, higher velocity plasma than the magnetospheric interior. The diagram also clearly shows the effects of the solar wind compression on the dayside, with an elongated structure on the nightside. This elongation of the magnetic field on the nightside, forming the magnetotail, is a consequence of the Dungey cycle [Dungey, 1965]. The reconnected field lines from the dayside are dragged over the polar regions, being transported by the solar wind. This leads to a magnetotail of length $\sim 10^3$ R_E. For future reference, when referring to the different sectors of the magnetosphere, it is useful to use magnetic local time (MLT), which in an equatorial plane denotes the Earth-Sun line as 12 noon, and the opposite side as midnight (MLT 24).

The pink shaded areas of Figure 1.1.1 represent the plasmasphere, which extends in an almost toroidal shape around the Earth up to mid latitudes ($\sim< 60°$). This is a region of dense plasma in the inner magnetosphere spanning from the upper ionosphere to a few Earth radii, the specific boundary (the plasmapause) depending heavily upon solar wind conditions. The particle population of the plasmasphere is filled from the ionosphere below and hence largely co-rotates with the planet. Indeed, plasmaspheric field lines never undergo reconnection. This region was first investigated using both ground and space based data in the 1960s. Carpenter [1963] studied the signatures of whistlers, which are radio waves that propagate along magnetic field lines, to identify the so called 'knee' in the equatorial plasma density profile. This represents the steep drop off in the density associated with the location of the plasmapause. Independently, Gringauz [1963] used in situ measurements from the Lunik Moon probes to reveal the existence of the plasmapause. A review of these discoveries and of the plasmasphere in general is given in the book by Lemaire and Gringauz [1998]. Introducing some more useful terminology, to refer to a particular set of field lines we define the L-shell parameter, where L is the radial distance in the equatorial plane (measured in R_E). So for example, we might say the plasmasphere extends to an L value of 5. The study of the plasmasphere is not directly related to the

work of this thesis, however, the plasmapause acts as an important boundary in space for guiding wave modes to be discussed in later sections.

1.2 Ultra Low Frequency (ULF) Waves

To begin to tackle the subject of this thesis, we discuss some of the general properties of what are now termed Ultra Low Frequency (ULF) waves, but were previously in the literature referred to as geomagnetic pulsations or micropulsations. A more specific introduction to the previous work on ULF waves relevant to this thesis is reserved for Section 1.6 of this introduction, after some of the prerequisite fundamental theory has been introduced in the sections to follow. ULF waves are low frequency oscillations of the Earth's magnetic field which are typically small in amplitude compared to the background field strength. Some of the earliest observations of ULF waves date back to the Carrington event of 1859, when a coronal mass ejection collided with the magnetosphere triggering one of the most powerful geomagnetic storms on record. The oscillations of the Earth's magnetic field were recorded by Stewart [1861], noting periods of a few minutes. It was not until 1964 that these oscillations were formally classified dependent on their frequency and wave form [Jacobs et al., 1964]. ULF waves are split into two categories: Pc for continuous pulsations and Pi for more irregular pulsations. In this thesis we discuss Pc pulsations, which are further subdivided into five classes dependent on their frequency, spanning frequencies from 1mHz to 1Hz or periods from 1000 seconds to 1 second.

ULF waves are generated in the magnetosphere in a variety of ways. These generation mechanisms are best separated as either internal or external to the magnetosphere. Two external sources that will receive particular attention here due to their relevance to the work in this thesis are the Kelvin-Helmholtz (KH) instability of the magnetospheric flanks and solar wind dynamic pressure driving. A good summary of some of the other generation mechanisms is given in the review by McPherron [2005]. Beginning with the KH instability, Southwood [1968] first showed that ULF waves could be generated by a shear flow instability of the magnetospheric flanks. Much like the wind causing surface waves on the ocean, the fast magnetosheath flow compared to the slower interior magnetospheric flow could cause magnetopause surface waves to develop. Southwood [1968] considered the mathematical treatment of this, using two perfectly conducting fluids separated by a thin boundary layer. Conditions for stability and the polarization of disturbances were derived, but not until later work (which will be discussed in Section 1.5) was this generation mechanism fully linked to observed ULF modes. Since then, the (KH) instability has received much treatment and has been widely accepted as one of the main generation mechanisms of ULF waves in the magnetosphere.

Secondly, ULF waves can be generated by solar wind dynamic pressure driving, indeed

suggested to be the main source of ULF waves in the magnetosphere [Takahashi and Ukhorskiy, 2007, 2008]. There are two ways in which this can occur. Either a density structure propagating in the solar wind, already carrying ULF waves, is incident upon the magnetosphere, triggering discrete oscillations of the same frequency as those carried by the solar wind [Kepko et al., 2002; Kepko and Spence, 2003]. Or, as has received much attention over the past decades, broadband fluctuations in the solar wind can excite the natural modes of the magnetospheric cavity, the discrete frequencies of which are determined by the size and shape of the cavity in the prevailing solar wind conditions. This train of thought began with the works of Kivelson and Southwood [1985] and Allan et al. [1985] and the ideas presented therein will be treated in more detail in Section 1.6 of this introduction.

1.3 Magnetohydrodynamics (MHD) and the Magnetosphere

Now that some of the general properties of ULF waves have been introduced, we turn to the theoretical aspects. To this end, we begin with the landmark discovery of the Swedish physicist Hannes Alfvén, who in 1942, discovered a type of electromagnetic wave, now famously known as the Alfvén wave [Alfvén, 1942]. Out of this discovery was born the field of magnetohydrodynamics (MHD), a merging of the previously distinct fields of electromagnetism and hydrodynamics. The most important aspect of MHD is that it allows a simplified but accurate description of the overall plasma behaviour in terms of the large scale fields: electric $\mathbf{E}$, magnetic $\mathbf{B}$ and velocity $\mathbf{u}$ without the complicated kinetic (small scale) description involving the particle distribution functions. It turns out that many large scale astrophysical plasmas can be modelled effectively using an MHD approach. For our concerns, the outer magnetosphere can be treated using MHD as realised by Dungey [1954]. This is applicable by considering scale sizes of many times the particle gyroradii, as well as frequencies much less than the particle gyrofrequencies. A good discussion of the applicability of MHD to the magnetosphere is given in the review by Southwood and Hughes [1983].

Before describing the approximations used when applying MHD to the magnetosphere, we introduce the full equations of MHD in order to make the future magnetospheric assumptions clearer. The system of equations can be stated as [e.g. Boyd and Sanderson, 2003]

$$\frac{\partial \mathbf{B}}{\partial t} = \boldsymbol{\nabla} \times (\mathbf{u} \times \mathbf{B}) + \eta \boldsymbol{\nabla}^2 \mathbf{B}, \tag{1.3.1}$$

$$\rho \frac{\partial \mathbf{u}}{\partial t} + \rho (\mathbf{u} \cdot \boldsymbol{\nabla}) \mathbf{u} = -\boldsymbol{\nabla} p + \mathbf{j} \times \mathbf{B} + \rho \mathbf{g}, \tag{1.3.2}$$

$$\frac{\partial \rho}{\partial t} + \boldsymbol{\nabla} \cdot (\rho \mathbf{u}) = 0, \tag{1.3.3}$$

$$\boldsymbol{\nabla} \cdot \mathbf{B} = 0, \tag{1.3.4}$$

$$\frac{\partial p}{\partial t} + \mathbf{u} \cdot \boldsymbol{\nabla} p = -\gamma p \boldsymbol{\nabla} \cdot \mathbf{u} + \frac{\gamma - 1}{\mu_0} \eta (\boldsymbol{\nabla} \times \mathbf{B})^2, \tag{1.3.5}$$

$$p = \rho R T, \tag{1.3.6}$$

$$\mathbf{j} = \frac{1}{\mu_0} \boldsymbol{\nabla} \times \mathbf{B}, \tag{1.3.7}$$

where $\mathbf{B}$ is the magnetic field, $\mathbf{u}$ the velocity field, ρ the plasma density, $\mathbf{j}$ the current density, p the plasma pressure, η the uniform magnetic diffusivity, μ_0 the magnetic permeability in a vacuum, γ the ratio of specific heats, T the plasma temperature and R a gas constant. In order to reach this stage some assumptions have already been made. Firstly, we assume that typical fluid velocities are much less than the speed of light c. This allows us to neglect the displacement current term that appears on the right hand side of Ampère's law, and state it instead as equation (1.3.7). Equation (1.3.5) is an energy equation, where any losses from the system have been neglected. This assumption is called the adiabatic approximation, valid for the plasma populations considered in this thesis. Finally, no viscous forces have been included in the equation of motion (1.3.2).

The system given by equations (1.3.1)-(1.3.7) describes the large scale properties of the plasma, but when applied to the magnetosphere, many terms can be dropped to simplify the problem at hand. As noted by Dungey [1954], in the outer magnetosphere the plasma pressure is far less than the magnetic pressure. This is known as a low β environment, where β is the ratio of the plasma pressure to magnetic pressure. Hence on the right hand side of the equation of motion (1.3.2), the second term called the Lorentz force, dominates the plasma pressure gradient. Together with neglecting gravitational forces, the equation of motion can be restated as

$$\rho \frac{\partial \mathbf{u}}{\partial t} + \rho (\mathbf{u} \cdot \boldsymbol{\nabla}) \mathbf{u} = \mathbf{j} \times \mathbf{B}. \tag{1.3.8}$$

Such an assumption is often termed the cold plasma approximation, where the energy equation is also dropped as we no longer need to solve for the plasma pressure p. Finally, by considering the timescales of the problem we can compare the sizes of the terms on the right hand side of the induction equation (1.3.1). The first term on the right hand side represents the advection of field lines, while the second term represents the diffusive

evolution. On the timescale of the periods of ULF waves, diffusive transport can be neglected and hence the induction equation becomes

$$\frac{\partial \mathbf{B}}{\partial t} = \boldsymbol{\nabla} \times (\mathbf{u} \times \mathbf{B}) \,. \tag{1.3.9}$$

This is known as Alfvén's frozen in flux theorem or generally as ideal MHD, which says that if the plasma elements are connected by a line of $\mathbf{B}$ at one time, then they will remain connected in the subsequent evolution [Alfvén, 1943]. This can be thought of as the magnetic field being frozen in to the plasma. With this assumption, we are ready to introduce the different wave modes supported by the system given by equations (1.3.3), (1.3.4), (1.3.7), (1.3.8) and (1.3.9).

1.4 MHD/ULF Wave Modes

ULF waves can be effectively studied using linear perturbation theory, as they represent small disturbances compared to the background field quantities. In this section we derive some of the general wave modes of MHD, and discuss how these are affected by the above assumptions made for the magnetosphere.

Consider the simple case of a plasma initially at rest such that $\mathbf{u}_0 = 0$, with a uniform background magnetic field $\mathbf{B}_0 = B_0 \hat{\mathbf{z}}$ (in a Cartesian system), with constant pressure p_0 and constant density ρ_0. We further assume that the plasma is ideal ($\eta = 0$) and note that we are not making the cold plasma assumption at this stage. We can then consider perturbations to this equilibrium and linearise the MHD equations, neglecting any second order and higher terms. Denoting first order perturbation quantities with a subscript 1, the system is then expressed as

$$\begin{aligned}
\frac{\partial \mathbf{b}_1}{\partial t} &= \boldsymbol{\nabla} \times (\mathbf{u}_1 \times \mathbf{B}_0), && (1.4.1)\\
\rho_0 \frac{\partial \mathbf{u}_1}{\partial t} &= -\boldsymbol{\nabla} p_1 + \frac{1}{\mu_0} (\boldsymbol{\nabla} \times \mathbf{b}_1) \times \mathbf{B}_0, && (1.4.2)\\
\frac{\partial \rho_1}{\partial t} &= -\rho_0 \boldsymbol{\nabla} \cdot \mathbf{u}_1, && (1.4.3)\\
\boldsymbol{\nabla} \cdot \mathbf{b}_1 &= 0, && (1.4.4)\\
\frac{\partial p_1}{\partial t} &= -\gamma p_0 \boldsymbol{\nabla} \cdot \mathbf{u}_1, && (1.4.5)
\end{aligned}$$

where Ampère's law (1.3.7) has been used to eliminate $\mathbf{j}$ from the equation of motion. Since all coefficients are constants here, we can look for normal (Fourier) modes in each spatial direction and in time of the form $e^{i(\boldsymbol{k}\cdot\boldsymbol{r} - \omega t)}$. This will explicitly define all derivatives.

Eliminating all other dependent variables in favour of the velocity perturbation, after some algebra we can derive [e.g. Roberts, 1985]

$$\left[\omega^4 - \omega^2 k^2 \left(c_s^2 + V_A^2\right) + c_s^2 V_A^2 k^4 \cos^2\theta\right] (\mathbf{k} \cdot \mathbf{u_1}) = 0, \tag{1.4.6}$$

where $c_s^2 = \gamma p_0/\rho_0$ is the square of the sound speed, $V_A^2 = B_0^2/\mu_0\rho_0$ is the square of the Alfvén speed and θ represents the angle between the background field direction $\hat{\mathbf{z}}$ and the wavevector $\mathbf{k}$, such that $k_z = k\cos\theta$. Equation (1.4.6) has two distinct sets of solutions for each bracketed term being zero. Consider firstly $\mathbf{k} \cdot \mathbf{u_1} = 0$. This suggests that the wave is travelling perpendicular to the velocity perturbation and is incompressible. Again with the algebra hidden, this can be described by

$$\begin{aligned} \mu_0\rho_0\omega^2\mathbf{u}_1 &= (\mathbf{k} \cdot \mathbf{B_0})^2 \mathbf{u}_1, & (1.4.7)\\ \Rightarrow \omega^2 &= \frac{B_0^2}{\mu_0\rho_0} k^2 \cos^2\theta, & (1.4.8)\\ \Rightarrow \omega^2 &= k_z^2 V_A^2, & (1.4.9) \end{aligned}$$

which is the dispersion relation for Alfvén waves. These are transverse waves with a group velocity directed along the background magnetic field. The study of Alfvén waves as ULF waves in the magnetosphere forms a significant part of this thesis and will be considered in detail throughout.

The second solution to equation (1.4.6) yields

$$\omega^4 - \omega^2 k^2 \left(c_s^2 + V_A^2\right) + c_s^2 V_A^2 k^4 \cos^2\theta = 0, \tag{1.4.10}$$

which is the magnetoacoustic dispersion relation. Consider dividing equation (1.4.10) by k^4 and treating as a quadratic in ω^2/k^2. This has solutions

$$\frac{\omega^2}{k^2} = \frac{1}{2}\left(c_s^2 + V_A^2\right) \pm \frac{1}{2}\sqrt{\left(c_s^2 + V_A^2\right)^2 - 4c_s^2 V_A^2 \cos^2\theta}.$$

There are two modes described by the solutions here: the positive root yields the fast mode, the negative root the slow mode. These are compressional wave modes ($\mathbf{k} \cdot \mathbf{u_1} \neq 0$) and information about their propagation speeds and directions can be gleaned by considering different values of θ. For $\theta = \pi/2$, there is no slow mode propagation, hence slow modes (like Alfvén modes) do not propagate perpendicular to the magnetic field. The fast mode is given by the relation $\omega^2/k^2 = c_s^2 + V_A^2$. This is the maximal fast mode speed, propagating perpendicular to the background field. For $\theta = 0$ the two modes are given by

$$\begin{aligned} \frac{\omega^2}{k^2} &= V_A^2, \qquad \text{+ve root,} \\ \frac{\omega^2}{k^2} &= c_s^2, \qquad \text{-ve root,} \end{aligned}$$

where the fast mode is the greater of the two speeds and the slow mode the lesser. For more information on the wave characteristics at intermediate values of θ, see, for example, Figure 4 from McPherron [2005].

In the magnetosphere where we have assumed a low β plasma, the pressure terms vanish in the above analysis, which sets the sound speed $c_s = 0$. Hence there is no slow mode and the fast mode travels maximally at the Alfvén speed. The dispersion relations simplify to

$$\begin{aligned} \omega_f^2 &= k^2 V_A^2, \quad \text{Fast,} \\ \omega_A &= k_z V_A, \quad \text{Alfvén.} \end{aligned}$$

The simplifications made above are purely to introduce the different MHD wave modes that exist in the magnetosphere. As mentioned previously, the application of MHD to the magnetosphere began with Dungey [1954], who realised that ground magnetometer observations could be explained in terms of standing Alfvén waves on dipole field lines, whose end points were fixed in a perfectly conducting ionosphere. These transverse oscillations would send energy along the field lines into the ionosphere, to be detected on the ground. This provided the first explanation of the origin of the perturbations seen on the ground. To continue this discussion, we must consider how nonuniformity affects the wave modes.

1.5 Wave Coupling: Waveguide/Cavity modes and Field Line Resonance

The magnetosphere is a nonuniform environment, where the density varies considerably with radius from the Earth. In the uniform density formulation above, the Alfvén and fast modes are decoupled from one another, however in the real magnetosphere, the nonuniformity can couple these modes. The variation of magnetic field strength, density and field line length within the magnetosphere all contribute to varying Alfvén frequencies with position, a spectrum known as the Alfvén continuum. Southwood [1974] and Chen and Hasegawa [1974] proposed a mechanism whereby energy from the fast mode can couple to the Alfvén mode, called field line resonance (FLR). This appears in other fields, particularly solar MHD, under the name of resonant absorption. Such a mechanism explains

the excitation of the perturbations seen on the ground, and justifies the theory of these perturbations being standing Alfvén waves [Dungey, 1954]. The concept of FLR is pivotal to the work in this thesis and so we reproduce some of the working of past authors here to illustrate this mechanism.

Firstly consider rewriting equations (1.4.1) and (1.4.2) in the low β limit (such that the pressure gradient is neglected), as a set of equations for the plasma displacement $\boldsymbol{\xi}$ as

$$\frac{1}{V_A^2}\frac{\partial^2 \xi_x}{\partial t^2} - \frac{\partial^2 \xi_x}{\partial z^2} = -\frac{1}{B_0}\frac{\partial b_z}{\partial x}, \tag{1.5.1}$$

$$\frac{1}{V_A^2}\frac{\partial^2 \xi_y}{\partial t^2} - \frac{\partial^2 \xi_y}{\partial z^2} = -\frac{1}{B_0}\frac{\partial b_z}{\partial y}, \tag{1.5.2}$$

$$b_z = -B_0\left(\frac{\partial \xi_x}{\partial x} + \frac{\partial \xi_y}{\partial y}\right). \tag{1.5.3}$$

where all lower case variables are perturbation quantities. In this form, the coupling of the fast and Alfvénic modes is much easier to see. The left hand sides of equations (1.5.1) and (1.5.2) describe a simple harmonic oscillation, with the right hand sides representing the driving terms. Alfvén waves produce transverse displacements ξ_x and ξ_y, hence it can be seen that these are driven by spatial gradients in b_z. Introducing some terminology, the poloidal Alfvén mode describes radial perturbations to the field line (ξ_x) while the toroidal Alfvén mode represents azimuthal perturbations (ξ_y). It is the toroidal modes that are most readily excited in the magnetosphere. This is because the main variation of the Alfvén speed occurs with radius, and hence along any one L-shell (in azimuth), the natural Alfvén frequencies are similar. This allows a coherent oscillation to develop. Since radially separated field lines have different natural frequencies, poloidal modes are not so easily excited at discrete frequencies. However, outwith an MHD description, poloidal modes with a high azimuthal wavenumber can be driven by wave particle interactions [Mann and Wright, 1995; Mann et al., 1997].

To further highlight the concept of FLR, we consider the model of Southwood [1974] in a Cartesian geometry, with a uniform background magnetic field $\mathbf{B} = B_0\hat{\mathbf{z}}$, and a background density $\rho = \rho_0(x)$, where x represents the radial direction. Fourier analysing by considering modes of the form $b_z(x)e^{i(\omega t \pm k_y y \pm k_z z)}$, equations (1.5.1)-(1.5.3) can be reduced to a single second order ODE for b_z as

$$\frac{\mathrm{d}b_z}{\mathrm{d}x^2} - \frac{\omega^2 dV_A^{-2}/dx}{\omega^2/V_A^2 - k_z^2}\frac{\mathrm{d}b_z}{\mathrm{d}x} + \left(\frac{\omega^2}{V_A^2} - k_y^2 - k_z^2\right)b_z = 0, \tag{1.5.4}$$

(see, for example, Kivelson and Southwood [1985] equation (5) or Wright [1994] equation (19)). b_z represents the compressional fast mode disturbance, which as highlighted by equations (1.5.1) and (1.5.2), drives the Alfvénic modes. What equation (1.5.4) critically reveals is a regular singular point at the location, say x_r, where the fast mode frequency matches the natural Alfvén frequency, i.e. where

$$\omega^2 = k_z^2 V_A(x_r)^2, \tag{1.5.5}$$

the Alfvén dispersion relation, is satisfied. At the field line corresponding to this location, the phase velocity of the Alfvén and fast modes along the field line is the same, or in other words, there is a resonance between these modes. Energy is transferred irreversibly from the fast to the Alfvén mode at this location.

Another important location, that we denote x_t, is determined from setting the coefficient of the final term on the left hand side of equation (1.5.4) to zero, and hence

$$\omega^2 = \left(k_y^2 + k_z^2\right) V_A(x_t)^2. \tag{1.5.6}$$

The meaning of this location can be better understood in terms of a WKB approximation, which to lowest order neglects the second term in equation (1.5.4). This coefficient can then be seen effectively as the square of the wavenumber in the x direction, k_x^2. The point where $k_x^2 = 0$ (i.e. where equation (1.5.6) is satisfied) is called the turning point, and represents the location where the structure of the fast mode (b_z) changes from oscillatory to evanescent in x. This structure can be resolved by thinking of a perturbation of the form $e^{i(k_x x)}$ in x, such that real k_x implies oscillatory and complex k_x implies evanescence. As can be seen from equations (1.5.5) and (1.5.6), the resonant location and the turning point will coincide when the azimuthal wavenumber, k_y, is zero. For $k_y \neq 0$, the resonant location will be in the region where $k_x^2 < 0$ and hence in the evanescent tail of the fast mode.

What Southwood [1974] proposed is that the KH instability could drive FLRs at the location where the fast mode frequency matched the local Alfvén frequency. The KH instability of the magnetopause produces a surface wave, and hence the fast mode that penetrates the magnetosphere has a radially evanescent structure. This fits with the idea that the resonant location exists within the evanescent region of the fast mode.

This mechanism however, is by no means the only way to excite field line resonances in the magnetosphere. The studies of Kivelson and Southwood [1986]; Allan et al. [1986a,b] proposed treating the magnetosphere as a resonating cavity, (or a vibrating bubble) which supported natural modes of oscillation dependent on its shape and internal structure. When driven, for example by solar wind dynamic pressure perturbations, these natural

modes could couple to FLRs of the same harmonic frequencies. Such modes are termed global modes and have since had much success in explaining ULF wave observations. Indeed, Samson et al. [1992] consider the same problem except for an open ended waveguide rather than a closed cavity. This allows a continuum of wavenumbers in azimuth to be supported, rather than k_y being quantized as in the cavity model. The authors show that the set of recurring discrete frequencies observed in ground data (known as the 'magic' frequencies) can be explained by the excitation of FLRs of frequencies corresponding to the natural waveguide harmonics. This will be treated in more detail from an observational stand point in Section 1.6.2

1.6 ULF waves: Previous Studies

1.6.1 Theory

Now that some of the theoretical concepts regarding ULF waves have been introduced, it is possible to consider some of the previous works (aside from those mentioned above) pertinent to our study. As discussed previously, ULF waves have been observed and studied for many decades. Being such a long observed phenomenon, there is a rich body of literature attributed to their study. This section (and introduction) will by no means serve as a comprehensive review of all the works on ULF waves, but it will attempt to cover a few of the most relevant pieces to the work in this thesis. There are many good review papers and books on the subject which should be consulted for further information [e.g. Southwood and Hughes, 1983; Allan and Poulter, 1992; Wright, 1994; Walker, 2004; McPherron, 2005; Wright and Mann, 2006].

As the title of this thesis suggests, we are interested in the numerical modelling of ULF waves. The numerical side developed rapidly in the 1980's and 1990's, with multiple authors investigating ULF waves in various geometries to attempt to support and extend the previous theory, as well as explain the observations. Most of this thesis considers modelling ULF waves in a Cartesian box geometry (more details of which will be given in Chapter 2) and hence previous authors who have adapted similar models will be treated here. In the final chapter, a dipole geometry is considered. As such, the pertinent references for ULF wave modelling in other geometries are reserved for the introduction to Chapter 5 (with a couple of exceptions).

The Cartesian box model [Southwood, 1974] has had much success in explaining many features of ULF waves by various authors. Sharing the most similarity to the work here are the waveguide/cavity models of Rickard and Wright [1994]; Wright and Rickard [1995a]. Both of these papers consider MHD wave coupling in an inhomogeneous waveguide/cavity. As mentioned above, the open ended waveguide model adopted in Rickard and Wright

[1994] has the advantage of not restricting the azimuthal wavenumber. The authors consider an initial perturbation in a domain designed to establish a single Alfvén resonance. It is shown that the resonance is robust to a variety of initial conditions. The second paper, Wright and Rickard [1995a], drives the magnetospheric cavity with a broadband frequency driver, designed to simulate the mixed frequency driving of normal solar wind conditions. It is found that as long as the frequency of the natural cavity modes lies within the spectrum of the driver, Alfvén resonances matching these frequencies can be excited. This further requires that the natural cavity eigenfrequencies are within the Alfvén continuum. These concepts will be used frequently in the simulations presented in later chapters.

Not mentioned thus far is the efficiency of the coupling between the fast and Alfvénic modes. The coupling efficiency to the toroidal Alfvén mode is controlled by the azimuthal wavenumber. In the limit $k_y \to 0$, the gradients in azimuth which drive the resonance disappear. For $k_y \to \infty$, there are large gradients in y but the distance between the turning point of the mode and the resonance has increased (see equations (1.5.5) and (1.5.6) defining x_r and x_t). Hence the resonance exists so far into the evanescent tail of the fast mode that very little power remains to drive it. This is investigated, again in the Cartesian MHD box model, by Inhester [1987] and Zhu and Kivelson [1989], who both find the most efficient coupling for low azimuthal wavenumber modes with $m \sim 3$. It is also suggested by Wright [1994] that it is the near $k_y = 0$ modes that will most realistically drive Alfvén resonances, as the larger k_y modes propagate downtail before being able to transmit much power to the resonance. The lower k_y modes will remain spatially localised long enough to drive the resonance at one location for several cycles.

A couple of notable works, albeit where non Cartesian geometries have been used and are hence also discussed later, need to be mentioned at this stage due to their importance in the development of the field. The works of Allan et al. [1986a,b] present numerical experiments in a hemi-cylindrical geometry where FLRs are shown to be driven by a short lived compressional disturbance at the magnetopause boundary. Similarly, Lee and Lysak [1989] consider a dipole model, studying mode coupling in a meridional plane. They show how the previously defined global modes can exist in the magnetosphere and discuss the effects of the dipole geometry on the global mode frequencies. These studies, together with those mentioned above, laid the foundations for a rich period of ULF wave modelling.

Up to this point, no reference has been made to recent modelling efforts. With the increase in computational resources available, the vast majority of modern modelling work has moved into large 3D global magnetospheric modelling. This is a necessary step to developing a realistic magnetospheric model, combining all of the elements of the system and pushing the boundaries of the numerical landscape. However, this approach is not necessarily best suited for studying the small amplitude ULF waves of interest. For example, Claudepierre et al. [2009, 2010] investigate the solar wind driving of magnetospheric

cavity modes and FLRs, using a global 3D MHD model. These nonlinear simulations provide insight into the global magnetospheric dynamics but perhaps lack the required resolution to fully resolve the waves. A global 3D linear simulation by Degeling et al. [2010] does resolve such waves however. The authors consider a compressed dipole model to study how the coupling efficiency between the fast and Alfvénic modes is affected by the ULF wave power source location. In this way, a ULF wave observation is linked to a Kelvin-Helmholtz source. This model, unlike the global nonlinear models, is more closely linked to our own modelling ethos. In order to study the finer scale wave coupling, we opt for simpler models, but models that we can fully control, resolve and understand. In this way, we hope to cleanly interpret features often overlooked or unresolved by large scale modelling efforts.

1.6.2 Observations

In the excitement of introducing the rich theory that has been developed over decades of study, the observational side has thus far been mostly overlooked. Comparison to observation is critical to keeping the theory relevant and applicable. Indeed, this comparison is one of the main elements of this thesis. Therefore it is important to discuss what observational data, both from the ground and in space, can reveal about ULF waves. A couple of landmark observations which have helped to sculpt and constrain models over the years are also mentioned.

At the beginning of this introduction, the early ground based observations of Stewart [1861] were discussed. Nowadays there are large networks of ground magnetometers spanning an array of latitudes and longitudes to study the full extent of the magnetosphere. Ground based magnetic field signals are the representation of modes that have travelled along magnetic field lines, namely Alfvén waves whose group velocity is directed along the background magnetic field. Hence the ground signatures at a certain latitude map to a corresponding location in the magnetosphere, found by tracing the magnetic field line from Earth at that latitude. Furthermore, to reach the ground the signals have passed through the ionosphere, which was determined to rotate the wave magnetic field by 90°, a concept now known as Hughes rotation [Hughes, 1974].

Early observations (of the modern era) revealed a prevalence of tailward propagating pulsations in the Pc5 band (periods of 150 s to 600 s) [Samson et al., 1971]. Furthermore, observations showed that across a latitudinal extent, an amplitude maximum and a 180° phase change would occur. This feature of ULF waves came to be described as the observational signature of a FLR, discussed in detail above [Walker et al., 1979]. One of the most puzzling and incredible observations was of stable, discrete frequencies, often existing simultaneously [Samson et al., 1992], referred to previously as the 'magic' or 'Samson' frequencies. This came to be explained by cavity/waveguide mode theory discussed in

detail above in Section 1.5. It was considered that these select frequencies were a result of the most natural configuration of the magnetosphere [Mathie et al., 1999], and hence why they were so regularly observed. However, the authors also found evidence to suggest that such frequencies were not as stable as once reported. Ziesolleck and McDiarmid [1994] also discuss the appearance of other frequency modes in the Pc5 range, as well as a variation of the observed signals with local time. It is at least clear, that the natural modes of oscillation are extremely dependent on the solar wind conditions, which affects the size of the magnetospheric cavity as well as influencing the densities. Further study of these magic frequencies is still continuing today [e.g. Archer et al., 2013].

We mostly consider the modelling of space based observations, of which we use reports based on two modern missions, namely Cluster and THEMIS. Both contain arrays of satellites, the orbits of which can be subtly varied to yield a covering of space to reveal desired information. For example, the spacecraft can follow a similar orbit, like beads on a string, to explore the spatial structure along a field line. Each satellite can resolve the components of the electric and magnetic fields, which fits in well with our theoretical approach. Most modern studies utilise both ground and space based data together to validate observations. The ground observations are excellent for yielding the global scale of a pulsation. For example, if magnetometers in Canada and Russia both observe a disturbance (and can correlate it as the same disturbance), then it must span a large spatial extent. Equally, the radial extent can be discerned by latitudinally separated magnetometers. This kind of information is hard to infer from a satellite sitting at a single location. In Chapter 3, satellite observations from Cluster and THEMIS that we model will be discussed in detail.

1.7 Thesis Aims and Layout

The aim of the work in this thesis is to provide numerical models which can shed further light on the propagation of ULF waves in the magnetosphere. The concepts introduced above will be utilised in each of the chapters to follow. A general outline of the work in each chapter is given below.

- Chapter 2: This chapter develops in more detail the theory required to appreciate the modelling efforts of later chapters. The numerical method used is outlined and tested rigorously, considering that all codes used in this work have been developed from scratch in Fortran. We set up the geometry to consider wave propagation in the flank magnetosphere and discuss the modelling of fast waveguide modes, briefly touching upon exciting resonances within the domain. Various driving conditions are investigated involving perturbations to the magnetopause boundary.
- Chapter 3: We model two observations of ULF waves using a Cartesian box waveg-

uide model. By using suitable driving conditions for each observation, we develop theories and explanations for the data, in some cases providing alternative and supplementary descriptions to the original works. Much of the analysis involves the use of the Poynting vector to tease more information from the data.

- Chapter 4: An analytical method is developed to investigate fast waveguide modes which are propagating in azimuth (toward the magnetotail) and have a mixed propagating/standing nature radially. At this stage, the method is not applied to observations but instead is tested on simulated waveguide data, which validates the method. Again we utilise the Cartesian box model in the numerical study.

- Chapter 5: Here we journey into the realm of dipole magnetic field geometries, and consider modelling a 3D Alfvén resonance. Previous work in such geometries is introduced, but we believe we develop entirely new results in terms of understanding how the fast and Alfvén modes couple when there is a 2D variation of the Alfvén eigenfrequencies. The results presented here are at a preliminary stage, however many interesting features are still developed which provide extremely exciting avenues for future investigation.

  As theorists, our job lies in providing well developed and justified theories to help explain observations. Nowadays, the majority of the research in the magnetosphere is observational, which is unsurprising given the plethora of data available from the ground and in space. However, with more detailed observations, our theories and justifications can be refined. It is critical that theorists, whose roots lie in the mathematical physics of the problems at hand, remain to critique the observations, and help the field grow together as it has done for the past 50 years. That is I would say the overall perspective of this thesis, to work with the observations, and to attempt to provide well founded explanations for the observed physical phenomena.

Chapter 2

Model Setup and Numerical Methods

The main purpose of this chapter is to introduce the numerical method and analysis techniques used in the chapters to follow. This involves deriving the appropriate wave equations for the model, stating the finite different scheme employed and testing the numerical method for consistency and stability. Along the way, concepts of magnetospheric modelling such as natural waveguide eigenfrequencies and exciting field line resonances will be discussed.

2.1 Hydromagnetic Box Model

As a means to investigate the properties of ULF waves in Earth's outer magnetosphere, we implement the hydromagnetic box model [Southwood, 1974; Kivelson and Southwood, 1986] as mentioned in the previous chapter. The geometry of the model is shown in Figure 2.1.1. The background field is given simply as the uniform field $\mathbf{B} = B_0\hat{\mathbf{z}}$, which can be pictured as straightening out Earth's dipole field lines. Neglecting the curvature of field lines at high latitudes means the approximation is more suited to the modelling of the near equatorial regions. The radial coordinate is replaced by $\hat{\mathbf{x}}$, positive outward from the Earth, and the right handed system is completed with $\hat{\mathbf{y}}$ as the azimuthal direction (positive tailward on the dusk flank). The box structure shown can be envisaged as looking at the dusk flank of the magnetosphere, where x ranges from the inner magnetosphere (or perhaps the upper ionosphere) to the magnetopause, and y from the Earth-Sun line into the magnetotail.

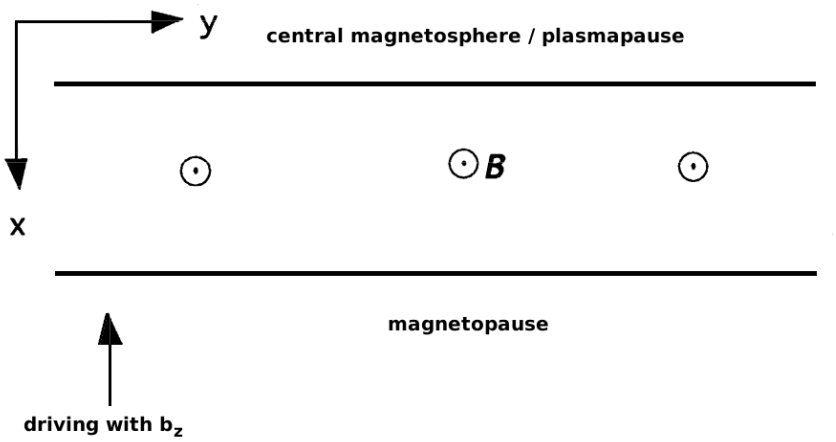

Figure 2.1.1: Hydromagnetic box model for the magnetosphere, adapted from Rickard and Wright [1994]. The highlighted driven region can be varied to model noon local time or flank driving.

2.2 Derivation of Wave Equations

As discussed in the introductory chapter, we treat Earth's outer magnetosphere as a low β environment which implies that the magnetic pressure dominates the plasma pressure. This leads to the validity of the cold plasma equations as a description of the plasma behaviour, an assumption made by many previous authors [e.g. Southwood, 1974; Lee and Lysak, 1989; Samson et al., 1992; Wright, 1994]. Furthermore we consider scale sizes of many times the Larmor radius, as well as a frequency much less than the particle gyrofrequencies, allowing the use of a MHD description [see e.g. Dungey, 1954; Southwood and Hughes, 1983]. Consider an inhomogeneous plasma in the previously described Cartesian geometry with the following background parameters: density $\rho = \rho_0(x)$ (varies only with radius), magnetic field as discussed above, $\mathbf{B} = B_0\hat{\mathbf{z}}$, and a velocity $\mathbf{u}_0 = 0$. We then consider perturbations about this equilibrium given by $\mathbf{b} = \mathbf{b}\,(x, y, z, t)$, $\mathbf{u} = \mathbf{u}\,(x, y, z, t)$ and $\rho_1 = \rho_1\,(x, y, z, t)$. Using ideal MHD as discussed in Section 1.3, the induction equation (1.3.9) becomes

$$\frac{\partial \mathbf{b}}{\partial t} = \boldsymbol{\nabla} \times (\mathbf{u} \times \mathbf{B_0}), \tag{2.2.1}$$

where we have linearised by neglecting any second order and higher perturbations. The equation of motion in the cold plasma limit (1.3.8), is now given by

$$\rho_0 \frac{\partial \mathbf{u}}{\partial t} = \frac{1}{\mu_0}(\boldsymbol{\nabla} \times \mathbf{b}) \times \mathbf{B_0}. \tag{2.2.2}$$

We could further include the equation of mass continuity, but this will only serve to

solve for the perturbation density which is not required for finding the $\mathbf{u}$ and $\mathbf{b}$ fields. Considering the components of the governing equations, we have firstly for induction

$$\begin{aligned}
\frac{\partial \mathbf{b}}{\partial t} &= \boldsymbol{\nabla} \times (\mathbf{u} \times \mathbf{B_0}), \\
\mathbf{u} \times \mathbf{B_0} &= (u_y B_0, -u_x B_0, 0)\,, \\
\boldsymbol{\nabla} \times (\mathbf{u} \times \mathbf{B_0}) &= \left(B_0 \frac{\partial u_x}{\partial z}, B_0 \frac{\partial u_y}{\partial z}, -B_0 \left(\frac{\partial u_x}{\partial x} + \frac{\partial u_y}{\partial y} \right) \right).
\end{aligned}$$

Then using these components we have

$$\frac{\partial b_x}{\partial t} = B_0 \frac{\partial u_x}{\partial z}, \tag{2.2.3}$$

$$\frac{\partial b_y}{\partial t} = B_0 \frac{\partial u_y}{\partial z}, \tag{2.2.4}$$

$$\frac{\partial b_z}{\partial t} = -B_0 \left(\frac{\partial u_x}{\partial x} + \frac{\partial u_y}{\partial y} \right). \tag{2.2.5}$$

Now consider the components of the equation of motion.

$$\begin{aligned}
\rho_0 \frac{\partial \mathbf{u}}{\partial t} &= \frac{1}{\mu_0} (\boldsymbol{\nabla} \times \mathbf{b}) \times \mathbf{B_0}. \\
\boldsymbol{\nabla} \times \mathbf{b} &= \left(\frac{\partial b_z}{\partial y} - \frac{\partial b_y}{\partial z}, \frac{\partial b_x}{\partial z} - \frac{\partial b_z}{\partial x}, \frac{\partial b_y}{\partial x} - \frac{\partial b_x}{\partial y} \right). \\
\Rightarrow (\boldsymbol{\nabla} \times \mathbf{b}) \times \mathbf{B_0} &= \left(\left(\frac{\partial b_x}{\partial z} - \frac{\partial b_z}{\partial x} \right) B_0, - \left(\frac{\partial b_z}{\partial y} - \frac{\partial b_y}{\partial z} \right) B_0, 0 \right).
\end{aligned}$$

The velocity components are then given by

$$\rho_0 \frac{\partial u_x}{\partial t} = \left(\frac{\partial b_x}{\partial z} - \frac{\partial b_z}{\partial x} \right) \frac{B_0}{\mu_0}, \tag{2.2.6}$$

$$\rho_0 \frac{\partial u_y}{\partial t} = \left(\frac{\partial b_y}{\partial z} - \frac{\partial b_z}{\partial y} \right) \frac{B_0}{\mu_0}, \tag{2.2.7}$$

$$\frac{\partial u_z}{\partial t} = 0. \tag{2.2.8}$$

Equation (2.2.8) implies u_z is constant in time and is assumed to be zero from this point. To continue we assume a standing mode structure in the $\hat{\mathbf{z}}$ direction. Choosing $z = 0$ to be the magnetic equator we define

$$u_x = \bar{u_x}\,(x, y, t)\cos\left(k_z z\right), \tag{2.2.9}$$

where the barred quantity refers to the x, y and t dependence in u_x, and k_z is the wavenumber in the $\hat{\mathbf{z}}$ direction. The cosine function is chosen for the radial velocity here such that the maximum displacement occurs at the equator. A choice of $k_z = \pi/2$ creates a fundamental mode in z with the end points of the field lines at $z = \pm 1$, which is a suitable assumption given that many observed pulsations are fundamental along $\mathbf{B}$ [Rickard and Wright, 1994]. Entering this form into the equations yields similar expressions for the other components, given by

$$\begin{aligned}
u_y &= \bar{u_y}\,(x, y, t)\cos(k_z z), && (2.2.10)\\
b_x &= \bar{b_x}\,(x, y, t)\sin(k_z z), && (2.2.11)\\
b_y &= \bar{b_y}\,(x, y, t)\sin\left(k_z z\right), && (2.2.12)\\
b_z &= \bar{b_z}\,(x, y, t)\cos\left(k_z z\right). && (2.2.13)
\end{aligned}$$

Substituting the above components into equations (2.2.3)-(2.2.7) and dropping the bar implying x, y and t dependence, the equations become

$$\begin{aligned}
\frac{\partial b_x}{\partial t} &= -B_0 k_z u_x, && (2.2.14)\\
\frac{\partial b_y}{\partial t} &= -B_0 k_z u_y, && (2.2.15)\\
\frac{\partial b_z}{\partial t} &= -B_0\left(\frac{\partial u_x}{\partial x} + \frac{\partial u_y}{\partial y}\right), && (2.2.16)\\
\frac{\partial u_x}{\partial t} &= \frac{V_A^2}{B_0}\left(k_z b_x - \frac{\partial b_z}{\partial x}\right), && (2.2.17)\\
\frac{\partial u_y}{\partial t} &= \frac{V_A^2}{B_0}\left(k_z b_y - \frac{\partial b_z}{\partial y}\right), && (2.2.18)
\end{aligned}$$

where $V_A = B_0/\sqrt{\mu_0\rho_0}$ is the characteristic Alfvén speed. Finally, we construct dimensionless equations with the magnetic field $\mathbf{B}$ being normalised by the background magnetic field $\mathbf{B}_0$, the density by the background density ρ_0 at $x = 0$ ($\rho_0(0)$), lengthscales by the width of the waveguide L, velocities by the Alfvén speed at $x = 0$ ($V_A(0)$) and time by $L/V_A(0)$. These variables can therefore be written in terms of normalised units as

$$b_x = B_0 \widetilde{b_x}, \tag{2.2.19}$$
$$u_x = \frac{L}{T} \widetilde{u_x}, \tag{2.2.20}$$
$$\rho_0 = \rho_0(0) \widetilde{\rho_0}, \tag{2.2.21}$$
$$k_z = \frac{1}{L} \widetilde{k_z}, \tag{2.2.22}$$

where the tilde represents a normalised variable. In terms of normalised variables (with the tilde removed) the system of equations is

$$\frac{\partial b_x}{\partial t} = -k_z u_x, \tag{2.2.23}$$
$$\frac{\partial b_y}{\partial t} = -k_z u_y, \tag{2.2.24}$$
$$\frac{\partial b_z}{\partial t} = -\left(\frac{\partial u_x}{\partial x} + \frac{\partial u_y}{\partial y} \right), \tag{2.2.25}$$
$$\frac{\partial u_x}{\partial t} = \frac{1}{\rho_0} \left(k_z b_x - \frac{\partial b_z}{\partial x} \right), \tag{2.2.26}$$
$$\frac{\partial u_y}{\partial t} = \frac{1}{\rho_0} \left(k_z b_y - \frac{\partial b_z}{\partial y} \right). \tag{2.2.27}$$

2.3 Boundary Conditions

To solve equations (2.2.23) to (2.2.27) numerically, boundary conditions must be defined. We choose to model the magnetosphere as a waveguide as in Rickard and Wright [1994], rather than the often previously used cavity model [Kivelson and Southwood, 1985; Allan et al., 1986b; Lee and Lysak, 1989]. The cavity model treats the magnetosphere as closed, with the ionosphere being the only sink of energy within the system, allowing only a discrete set of azimuthal wavenumbers [Kivelson and Southwood, 1985]. The waveguide model includes the effects of energy flow into the magnetotail and permits a continuum of azimuthal wavenumbers.

In terms of boundary conditions for the box, we initially assume that the inner and outer boundaries ($x = 0$, $x = x_m$) are perfectly reflecting such that there is no flow through these boundaries i.e. $u_x = 0$. This assumption is used only for the initial testing of the numerical method and will be changed when the outer boundary is driven. By equations (2.2.23) and (2.2.26) the assumption implies that on the x boundaries, b_x and $\frac{\partial b_z}{\partial x}$ are zero. At $y = 0$, we assume a symmetry condition across the subsolar point such that only one flank (say $y > 0$) needs to be considered. This leads to the boundary conditions

that all y components and derivatives in y are 0 on this boundary, such that the only flow here is in x. To deal with the tail end boundary conditions at $y = y_m$, we simply take a perfectly reflecting boundary but ensure that the box is large enough such that no disturbance reaches this boundary over the length of a simulation.

2.4 Numerical Method

We follow the numerical procedure outlined in Rickard and Wright [1994], which uses a leapfrog trapezoidal algorithm developed by Zalesak [1979] to integrate the system forward in time. The method is reproduced here for clarity. Equations (2.2.23) to (2.2.27) can be written in the form

$$\frac{\partial \mathbf{U}}{\partial t} = \mathbf{F} \tag{2.4.1}$$

where

$$\mathbf{U} = \begin{pmatrix} u_x \\ u_y \\ b_x \\ b_y \\ b_z \end{pmatrix}, \qquad \mathbf{F} = \begin{pmatrix} \left(k_z b_x - b_{z,x}\right)/\rho_0 \\ \left(k_z b_y - b_{z,y}\right)/\rho_0 \\ -k_z u_x \\ -k_z u_y \\ -\left(u_{x,x} + u_{y,y}\right). \end{pmatrix} \tag{2.4.2}$$

The notation y, x is a shorthand for $\partial y/\partial x$. Assuming $\mathbf{U}$ is known at times t and $t - \Delta t$, then the scheme is

$$\mathbf{U}^{\dagger} = \mathbf{U}^{t-\Delta t} + 2\Delta t \mathbf{F}^{t} \tag{2.4.3}$$

$$\mathbf{F}^{*} = \frac{1}{2}\left(\mathbf{F}^{t} + \mathbf{F}^{\dagger}\right), \tag{2.4.4}$$

$$\mathbf{U}^{t+\Delta t} = \mathbf{U}^{t} + \Delta t \mathbf{F}^{*}. \tag{2.4.5}$$

Centred differences in space and the dependency on two previous timesteps make this explicit method second order accurate in space and time. To briefly explain the workings of the method, the first step, (2.4.3), is a predictor step, which is an estimate of $\mathbf{U}$ at time $t + \Delta t$, denoted by $\dagger$. Using this estimate in the equation for $\mathbf{F}$ in 2.4.2, the corresponding derivative $\mathbf{F}^{\dagger}$ is calculated. This is then used to calculate an average gradient between timesteps t and $t + \Delta t$, namely $\mathbf{F}^{*}$ in (2.4.4). This average gradient and the known value of $\mathbf{U}$ at t are then used to calculate $\mathbf{U}$ at $t + \Delta t$ in (2.4.5).

2.5 Initial Testing for a Uniform Medium

The 2D code developed here has been written from scratch, and thus required some simple testing to check that it was working as intended. We assume a uniform medium which implies that $\rho_0 = 1$. Rather than driving the system we take an initial profile for the radial velocity component u_x, given as

$$\begin{aligned} u_x &= \cos(\omega t)\sin(\pi x)\cos\left(\frac{\pi}{2}y\right), \\ \Rightarrow u_x(x,y,0) &= \sin(\pi x)\cos\left(\frac{\pi}{2}y\right), \end{aligned} \tag{2.5.1}$$

that will be allowed to relax over the course of the simulation. The wavenumber in x, k_x, is set to π such that there exists half a wavelength over the box domain of $x : 0 \to 1$. The wavenumber in y, k_y is set to $\pi/2$. From our choice of u_x we infer the initial and boundary conditions for the other components. Integrating equation (2.2.23) in time yields

$$\begin{aligned} \Rightarrow b_x &= -\frac{k_z}{\omega}\sin(\omega t)\sin(\pi x)\cos\left(\frac{\pi}{2}y\right), \\ \Rightarrow b_x(x,y,0) &= 0. \end{aligned}$$

The constant of integration is neglected as we are interested in the perturbation wave behaviour, not a constant background shift. The temporal relationship between the perturbations u_x and b_x is realised here, as a maximum of one implies a node (zero) of the other. A nice analogy is a pendulum, which has a maximum velocity when vertical, just as with our oscillating field line. Hence the field line is initially straight and thus has a zero b_x component.

Using (2.2.25) to develop an initial condition for b_z yields

$$\frac{\partial b_z}{\partial t} = -\left(\pi\cos(\omega t)\cos(\pi x)\cos\left(\frac{\pi}{2}y\right) + \frac{\partial u_y}{\partial y}\right).$$

We are left to assume an initial condition in u_y. In order to isolate the Alfvén mode, the above equation is balanced by setting

$$\frac{\partial u_y}{\partial y} = -\pi\cos(\omega t)\cos(\pi x)\cos\left(\frac{\pi}{2}y\right),$$

such that b_z is initially zero and invariant in time. The Alfvén mode is studied merely as a test case for the code. What highlights this case as Alfvénic is $b_z = 0$. For a uniform background field, b_z is the only first order component to the magnetic pressure. Alfvén waves are driven by magnetic tension and hence without a perturbation pressure we lose the fast mode in this set up. Continuing with the algebra, integrating the above equation with respect to y produces

$$\begin{aligned} u_y &= -2\cos(\omega t)\cos(\pi x)\sin\left(\frac{\pi}{2}y\right), \\ \Rightarrow u_y(x,y,0) &= -2\cos(\pi x)\sin\left(\frac{\pi}{2}y\right). \end{aligned}$$

which completes the initial conditions, given that $b_y(x, y, 0) = 0$ by nature of a $\sin(\omega t)$ time dependence. To use the Leapfrog trapezoidal method outlined in Section 2.4, two adjacent time levels must be known. The above initial conditions define the first timestep for $t = 0$; the second is acquired using a forward time central space (FTCS or Euler) method, where 100 steps are taken between the first and second time levels to retain accuracy. To implement the centred differences on the boundaries, ghost cells are used in a manner preserving the boundary conditions.

The final pieces of the puzzle are to decide on the run specifications. We choose a dimensionless box width of 1 in x and length 2 in y, with 101 points in each dimension. The timestep Δt is set to 0.001 and the run covers 5000 timesteps. In choosing the timestep and grid scales in x and y, the Courant-Friedrichs-Lewy (CFL) condition must be satisfied. This condition restricts the temporal and spatial scales such that motions are appropriately sampled. For example, a reduction in the grid scale will often require a reduction in the timestep, so that multiple grid points are not traversed by a disturbance over a single timestep. This condition can be stated generally as

$$\frac{\Delta t V}{\Delta x} < 1,$$

where Δt is the timestep, Δx the grid spacing in x, and V a characteristic speed. In our case, the speed is the Alfvén speed which is unity, $\Delta x = 10^{-2}$ and $\Delta t = 10^{-3}$ and hence we satisfy the CFL condition by a factor of ten.

The wavenumbers are set as $k_x = \pi$, $k_y = \pi/2$ and $k_z = \pi$, which differs from the value of k_z discussed above in Section 2.2. This is just a test case and for most of the future cases, $k_z = \pi/2$.

Figure 2.5.1 shows a time series plot of u_x at the location $x = 0.3$, $y = 0.6$. Evident is a clear wave period of 2. This can be determined using the Alfvén dispersion relation

for a uniform medium, $\omega = k_z V_A$. $V_A = 1$ since the density is uniform and we are using normalised variables. The period is given by $\tau = 2\pi/\omega$ which gives a period of 2 for the chosen k_z equal to π. Reproducing the predicted Alfvén frequency is a simple check that suggests the numerical routines are behaving as expected.

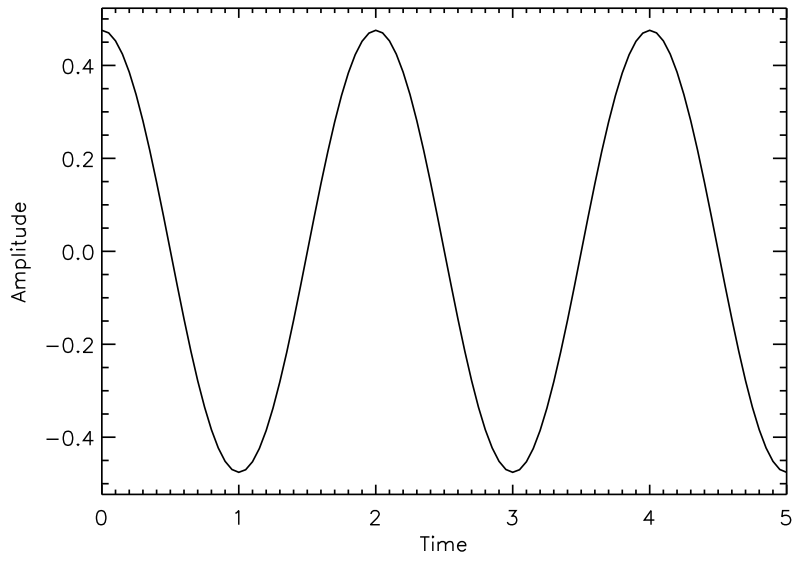

Figure 2.5.1: Time series of u_x for the Alfvén mode at $x = 0.3$, $y = 0.6$.

We can investigate a fast mode wave for this uniform density case in a similar manner, by ensuring b_z is non zero. The same initial form of u_x is considered as given in equation (2.5.1) and the wavenumbers are also kept the same. By equation (2.2.23) b_x is given by

$$b_x = -\frac{\pi}{\omega}\sin(\omega t)\sin(\pi x)\cos\left(\frac{\pi}{2}y\right).$$

Equation (2.2.26) will yield b_z as

$$\begin{aligned} -\omega\sin(\omega t)\cos\left(\frac{\pi}{2}y\right)\sin(\pi x) &= -\frac{\pi^2}{\omega}\sin(\omega t)\sin(\pi x)\cos\left(\frac{\pi}{2}y\right) - \frac{\partial b_z}{\partial x}, \\ \Rightarrow \frac{\partial b_z}{\partial x} &= \left(\omega - \frac{\pi^2}{\omega}\right)\sin(\omega t)\sin(\pi x)\cos\left(\frac{\pi}{2}y\right), \\ \Rightarrow b_z &= \left(\frac{\pi}{\omega} - \frac{\omega}{\pi}\right)\sin(\omega t)\cos(\pi x)\cos\left(\frac{\pi}{2}y\right). \end{aligned}$$

ω is known from the fast mode dispersion relation for a uniform medium as

$$\omega^2 = k_x^2 + k_y^2 + k_z^2 = \pi^2 + \frac{\pi^2}{4} + \pi^2 = \frac{9\pi^2}{4} \Rightarrow \omega = \frac{3\pi}{2}.$$

Hence b_z can be written as

$$b_z = -\frac{5}{6}\sin(\omega t)\cos(\pi x)\cos\left(\frac{\pi}{2}y\right).$$

Equation (2.2.25) can now be used in a similar way to find the appropriate condition for u_y, namely

$$\begin{aligned} \frac{\partial u_y}{\partial y} &= \frac{\pi}{4}\cos(\omega t)\cos(\pi x)\cos\left(\frac{\pi}{2}y\right) \\ u_y &= \frac{1}{2}\cos(\omega t)\cos(\pi x)\sin\left(\frac{\pi}{2}y\right). \end{aligned}$$

So the initial condition for u_y for the fast mode becomes

$$u_y(x, y, 0) = \frac{1}{2}\cos(\pi x)\sin\left(\frac{\pi}{2}y\right).$$

The magnetic field components all have a time dependence of $\sin(\omega t)$ and hence have no initial value. The wave period is given as

$$\tau = \frac{2\pi}{\omega} = \frac{2\pi}{3\pi} \cdot 2 = \frac{4}{3}.$$

Figure 2.5.2 shows the time evolution of u_x at a point in the waveguide for this fast mode frequency. It is clear that the period of the oscillation is indeed $\frac{4}{3}$, which is another check of the reliability of the code.

A final simple test is for the case $k_y = 0$ which will become an important limit in later work in this thesis. The fast mode dispersion relation yields a period of

$$\begin{aligned} \omega^2 = k^2 V_A^2 &= 2\pi^2, \\ \Rightarrow \omega &= \pi\sqrt{2}, \\ \Rightarrow \tau &= \sqrt{2}, \end{aligned}$$

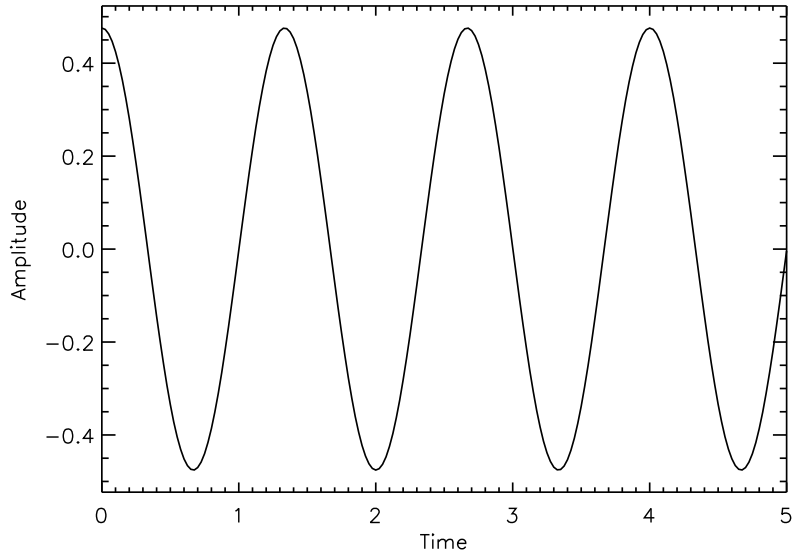

Figure 2.5.2: Time sequence of u_x for the fast mode at $x = 0.3$, $y = 0.6$.

which is again nicely displayed in a time series plot of u_x given in Figure 2.5.3.

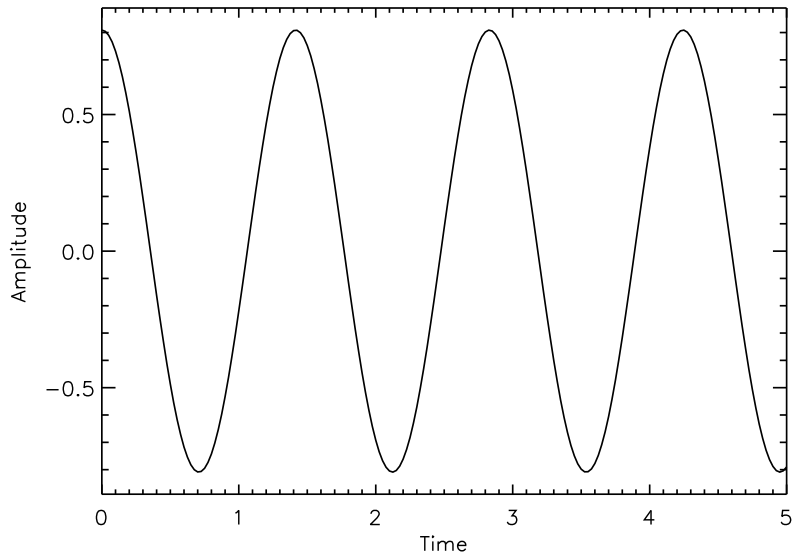

Figure 2.5.3: Time sequence of u_x for the $k_y = 0$ mode at $x = 0.3$, $y = 0.6$.

It is important to demonstrate that the code conserves energy. No energy is being put into the system as there is no flow across any of the boundaries of the simulation domain. There is also no dissipation either and hence we would expect the energy to remain constant over the course of the simulation. We follow the work of Mann et al. [1995] by checking that an energy invariant is conserved by the code. This invariant is formed by considering a wave

energy equation derived from the cold, linearised MHD equations (2.2.1)-(2.2.2) [e.g. Bray and Loughhead, 1974, pg 252]. The magnetic and kinetic energy densities can be formed in the equation

$$\frac{\partial}{\partial t}\left(\frac{\rho_0}{2}\left(\mathbf{u}^*\cdot\mathbf{u}\right)+\frac{\left(\mathbf{b}^*\cdot\mathbf{b}\right)}{2\mu_0}\right)+\boldsymbol{\nabla}\cdot\left(\frac{\mathbf{b}^*}{\mu_0}\times\left(\mathbf{u}\times\mathbf{B}_0\right)\right)=0, \tag{2.5.2}$$

where $\mathbf{b}^*, \mathbf{u}^*$ are the complex conjugates of $\mathbf{b}, \mathbf{u}$ respectively. This is in the form of a conservation equation, namely $\partial W/\partial t + \boldsymbol{\nabla}\cdot\mathbf{S} = 0$, where $\mathbf{S}$ is the Poynting vector. As stated above, there is no flow across any of the domain boundaries, and hence integrating equation (2.5.2) over the volume yields

$$\frac{\partial}{\partial t}\int_V W dV = 0.$$

Therefore W is the invariant that is followed in time. Performing this integration at each timestep yields a constant energy as shown in Figure 2.5.4, conserved to one part in 10^6 or better.

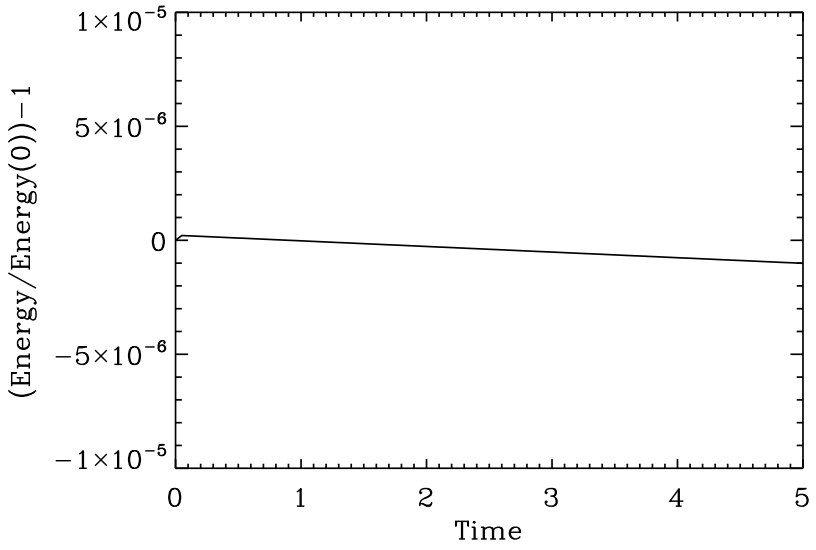

Figure 2.5.4: Energy density (dimensionless) divided by the initial energy density, minus 1, plotted over time for the fast mode simulation.

2.6 Driving the Magnetopause: u_x

We now consider the driving of the outer x boundary, representing the magnetopause, using the x component of the perturbation velocity. This form of driving is intended to model the buffeting of the magnetopause by the solar wind [Wright and Rickard, 1995a,b]. The inner x boundary is maintained as perfectly reflecting and the symmetry condition discussed in Section 2.3 is still present at $y = 0$. Since the system is now being driven, the previous initial condition is replaced by initializing all components to zero throughout the domain for the first two time steps. This is sufficient for starting the leapfrog-trapezoidal scheme without using a first order Euler method to obtain the second time level. The outer x boundary is driven over the full azimuthal extent for the initial test runs. The driving profile for u_x is given by

$$u_x(x=1) = \begin{cases} \cos(k_y y)\left(\sin^2\left(\frac{\pi}{\tau_D}t\right)\right) & \text{if } 0 \le t \le \frac{\tau_D}{2}, \\ \cos(k_y y)\left(\cos\left[2\pi\left(\frac{t}{\tau_D} - \frac{1}{2}\right)\right]\right) & \text{if } \frac{\tau_D}{2} < t \le T, \end{cases} \tag{2.6.1}$$

where τ_D is the period of the driver and T is the end time of the simulation. The profile is split to accommodate a smooth initial time dependence given by the $\sin^2$ function, such that the acceleration is continuous. At the driven boundary, centered differencing can no longer be used for derivatives in x, hence instead we employ 4th order one-sided backward differencing using points in the domain. All other conditions are as mentioned in section 2.3.

For a uniform medium the natural waveguide frequencies can be calculated given the boundary conditions. Driving the outer boundary with perturbations of u_x simulates a node of u_x, which together with a node at $x = 0$ generates a half wavelength fundamental mode. This is not necessarily an obvious deduction, that imposing motion in u_x produces standing modes that have a node of u_x at the driven boundary. An analogy to the given driving is that of a piston driving sound waves in a cylinder. The motion of the piston is prescribed and it does not respond to incident waves that encounter it. These are just reflected off an apparently unresponsive 'brick wall', albeit a moving one that drives the system. The fundamental and some higher harmonics are depicted in Figure 2.6.1. It can be easily noted that the first three harmonics have wavelengths $\lambda_{x1} = 2$, $\lambda_{x2} = 1$ and $\lambda_{x3} = 2/3$. More generally $\lambda_{xn} = 2/n$, where n is the harmonic number of the mode, which implies $k_{xn} = 2\pi/\lambda_{xn} = \pi n$.

Using the fast mode dispersion relation, choosing $k_y = \pi$ and $k_z = \pi/2$ we have

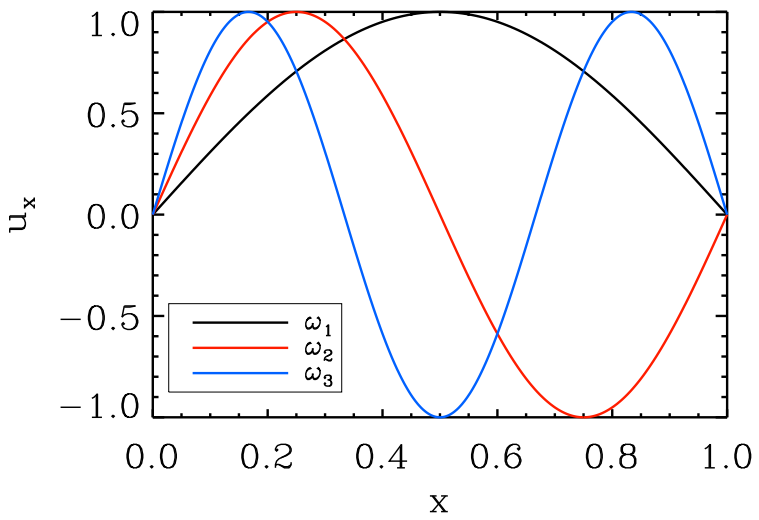

Figure 2.6.1: First 3 harmonics of the waveguide for u_x for the boundary conditions that u_x has a node at $x = 0$ and $x = 1$.

$$\begin{aligned} \omega^2 &= k^2 V_A^2, \\ &= \pi^2 \left(n^2 + 1 + \frac{1}{4} \right), \end{aligned}$$

where $V_A = 1$ for the uniform medium. The expected wave periods are then given by

$$\tau_n = \frac{2\pi}{\omega} = \frac{2\pi}{\pi\sqrt{n^2 + 1 + \frac{1}{4}}}.$$

Substituting $n = 1, 2$ into the above yields periods of $\tau_1 = 1.333$ and $\tau_2 = 0.873$, with frequencies $\omega_1 = 4.712$ and $\omega_2 = 7.198$. It is these frequencies that we expect to see in the simulation. We choose to set the driver period to $\tau_D = 1.10$, approximately in between the first two harmonics to hopefully bring out these frequencies. Figure 2.6.2(a) shows the monochromatic variation of u_x on the driven boundary. A time series of u_x at $x = 0.2$, $y = 0.8$ is given in Figure 2.6.2(b) which shows how the waveguide has responded to the driving, displaying a non monochromatic signal. Figure 2.6.2(c) displays a shaded surface plot of u_x at time $t = 2$, which gives an idea of the structure of the radial velocity in the waveguide. A Fast Fourier Transform (FFT) is given in Figure 2.6.2(d). From this we see clearly the first two harmonics as listed above, and also the driving frequency of $\omega = 2\pi/\tau_D = 5.71$. Correctly predicting these frequencies confirms that driving with u_x

simulates a nodal magnetopause boundary condition.

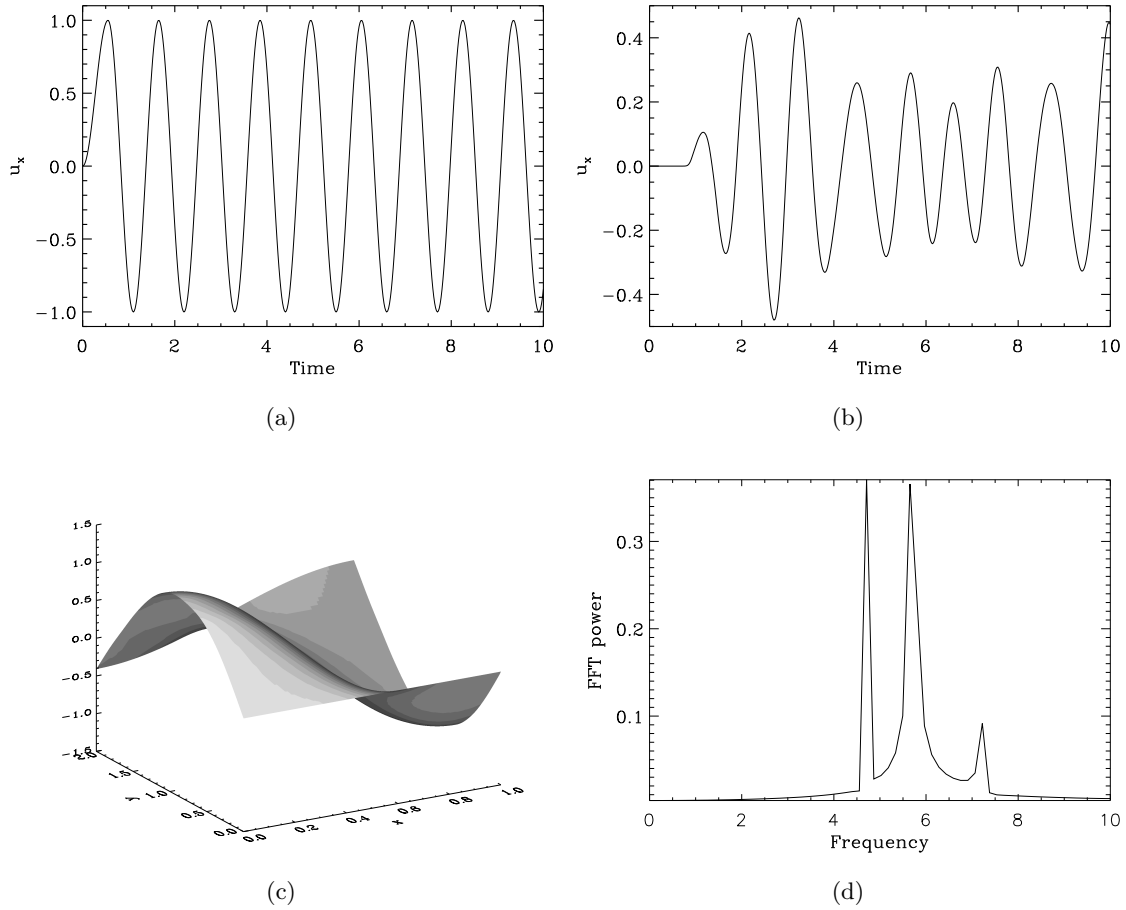

Figure 2.6.2: Uniform waveguide simulation: (a) temporal variation of u_x on the driven boundary $x = 1$; (b) temporal variation of u_x within the waveguide at $x = 0.2$, $y = 0.8$; (c) shaded surface plot of u_x at $t = 2$; (d) FFT power showing dominant frequencies taken at the point $x = 0.4$, $y = 0.1$.

2.7 Non-Uniform Density, u_x Driven

Driving with u_x has been used as a precursor to investigating the effects of driving the boundary with the z component perturbation of the magnetic field, b_z. Before considering this case, we implement a non-uniform density profile with the u_x driver and compare this to previous simulations from Wright and Rickard [1995b].

As discussed in the beginning of this chapter, the background density is allowed to vary in the x (radial) direction for the full hydromagnetic box model. We choose a profile for the Alfvén speed used by Wright and Rickard [1995b] defined as the piecewise function

$$
\begin{aligned}
V_A(x) &= 1 - \frac{x}{x_0}, \quad 0 < x < x_c \\
\frac{1}{V_A^2(x)} &= \frac{(x_0 - 2x_c + 1)(1 - x_c) - (1 - x)^2}{x_0 \left(1 - \frac{x_c}{x_0}\right)^3 (1 - x_c)}, \quad x_c < x < 1.
\end{aligned} \tag{2.7.1}
$$

where x_0 is used to change the gradient of the profile i.e. how quickly the Alfvén speed changes with L-shell and x_c determines the location in x where the profiles switch. This function is displayed in Figure 2.7.1 and is intended to be an approximation to the variation of the Alfvén speed between the plasmapause and the magnetopause.

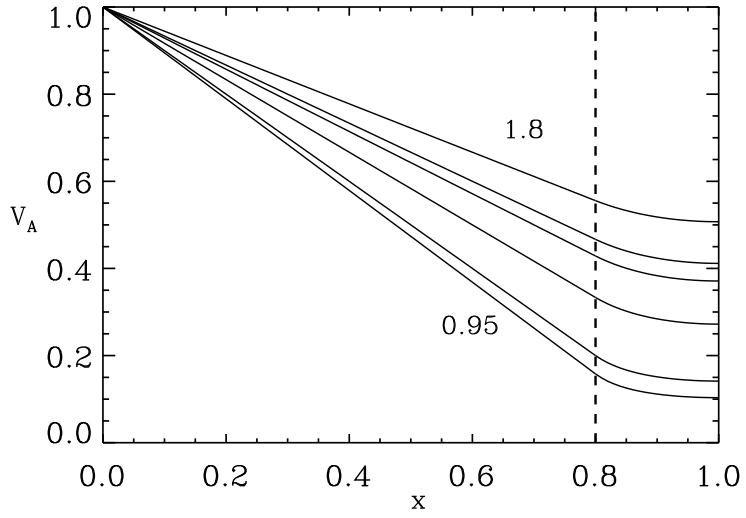

Figure 2.7.1: Alfvén speed profile for various values of the parameter x_0, as depicted by the annotated values for the top and bottom curves. The vertical dashed line represents the value of $x_c = 0.8$, where the profile switches.

With the uniform density case we could predict the waveguide eigenfrequencies, but unfortunately that cannot be done so easily for the non-uniform case. However, we can simplify the problem to looking at $k_y \simeq 0$ modes. The theory developed by Wright [1994] suggests that if waves are introduced over a local source region, the small k_y components will not propagate along the guide, but will instead remain near to the source region. These small k_y components can 'produce a quasi-steady oscillatory fast mode driver for Alfvén resonances near the source'. This will excite field lines where the natural frequency matches that of the driving frequency. The frequency of these resonances can be determined since the guide structure is known, as can the frequency of the natural harmonics. This is done by 'shooting' for the eigenfrequencies, a process by which successive values of ω are tested until the chosen boundary conditions are satisfied.

Let us derive the required equations. Setting $k_y = 0$ implies that all y components vanish as do derivatives in y. The system of equations given by (2.2.23) to (2.2.27) becomes

$$\frac{\partial u_x}{\partial t} = \frac{1}{\rho_0}\left(k_z b_x - \frac{\partial b_z}{\partial x}\right), \tag{2.7.2}$$

$$\frac{\partial b_x}{\partial t} = -k_z u_x, \tag{2.7.3}$$

$$\frac{\partial b_z}{\partial t} = -\frac{\partial u_x}{\partial x}. \tag{2.7.4}$$

Taking the time derivative of equation (2.7.2) yields

$$\frac{\partial^2 u_x}{\partial t^2} = \frac{1}{\rho_0}\left(k_z \frac{\partial b_x}{\partial t} - \frac{\partial}{\partial t}\frac{\partial b_z}{\partial x}\right).$$

Using (2.7.3) and (2.7.4) to replace the magnetic components in (2.7.2), and assuming normal modes in time such that $u_x \sim e^{i\omega t}$ gives

$$\begin{aligned} -\rho_0\omega^2 u_x &= (k_z(-k_z u_x)) + \frac{\mathrm{d}}{\mathrm{d}x}\left(\frac{\mathrm{d}u_x}{\mathrm{d}x}\right), \\ \Rightarrow -\rho_0\omega^2 u_x &= -k_z^2 u_x + \frac{\mathrm{d}}{\mathrm{d}x}\left(\frac{\mathrm{d}u_x}{\mathrm{d}x}\right). \end{aligned}$$

Using $U_x = \mathrm{d}u_x/\mathrm{d}x$ we have two coupled ODEs to solve, given by

$$\frac{\mathrm{d}}{\mathrm{d}x}(U_x) = k_z^2 u_x - \rho_0\omega^2 u_x, \tag{2.7.5}$$

$$\frac{\mathrm{d}u_x}{\mathrm{d}x} = U_x. \tag{2.7.6}$$

The above system can be solved using a Runge-Kutta 4th order method, with the boundary conditions that $u_x = 0$ at $x = 0, 1$ and the gradient, U_x, is equal to 1 at $x = 0$. Values of x_0, the parameter controlling the density profile, are cycled over and the correct frequencies matching the boundary conditions are iterated toward in the shooting algorithm.

This system is also solved by Wright and Rickard [1995b]. They produce plots of the $k_y = 0$ fast waveguide eigenfrequencies against x_0 (their Figure 3) and a prediction of Alfvén resonance location against x_0 (their Figure 4). As a test these plots are reproduced here using the new code as Figure 2.7.2(a) and (b). The importance of the first plot is to allow a prediction of the waveguide frequencies in the non uniform medium case. The

second uses the definition of a resonance as a location where the Alfvén frequency is equal to the fast mode frequency, hence the location x_r where $\omega_r = k_z V_A(x_r)$ is satisfied for the resonant frequency ω_r. The variation of the resonance position with the changing density gradient parameter x_0 is given. Figure 2.7.2 gives an accurate reproduction of the corresponding figures of Wright and Rickard [1995b] which gives confidence for later use of this method with different boundary conditions.

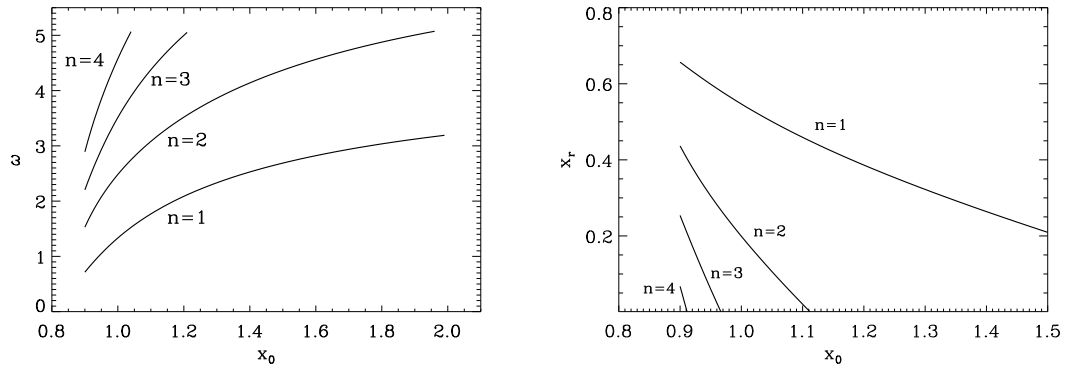

(a) (b)

Figure 2.7.2: Reproduction of Figures 3 and 4 from Wright and Rickard [1995b]. (a) $k_y = 0$ waveguide fast eigenfrequencies dependent on x_0. (b) Predicted location, x_r, of Alfvén resonances as a function of x_0. n is the harmonic number of the mode.

Moving on to consider the simulation run, the density parameters appearing in equation (2.7.1) are set as $x_0 = 1.0$ and $x_c = 0.8$. Reading off the natural waveguide frequencies for this choice of x_0 from Figure 2.7.2(a), gives the first and second harmonics as $\omega_1 \simeq 1.3$, $\omega_2 \simeq 2.5$. Furthermore, from Figure 2.7.2(b) we can estimate the resonance locations for these harmonics as $x_{r1} \simeq 0.55$ and $x_{r2} \simeq 0.2$. We choose a driving frequency between the first and second natural waveguide frequencies of $\omega_d = 2.0$, as a means of producing mixed frequency signals rather than just a clear monochromatic response near to either of the eigenfrequencies. The driven boundary is perturbed as described by (2.6.1), with $k_y = \pi/2$ to give a half wavelength variation over $y : 0 \to 2$. Figures 2.7.3(a) and (b) show the variation of u_x in time and azimuth respectively on the driven boundary. Figure 2.7.3(c) displays the time series of u_x at the point $x = 0.4$, $y = 0.1$ in the waveguide, which despite the inhomogeneity reveals a relatively monochromatic signature. This is due to the consistency of the driver which dominates the natural waveguide frequencies. This nature is confirmed in Figure 2.7.3(d), which shows a small response around the waveguide frequencies ($\omega = 1.3, 2.5$), but is dominated by the driving frequency, $\omega_d = 2$. (e) shows a shaded surface of u_x at time $t = 11.2$, revealing a rather complicated structure.

This complex structure is also shown by a radial dependence of the signals which has been introduced by including a radial density variation, shown in Figures 2.7.4(a) and (b). (a)

displays a time series of u_x at the different location $x = 0.75$, $y = 0.1$ showing the clear presence of a second frequency. This is consolidated by (b), where the FFT power peaks at the first waveguide harmonic as well as the driving frequency. Furthermore, we have some evidence that the $k_y = 0$ waveguide eigenfrequencies are a good approximation to the true eigenfrequencies close to $y = 0$. This is realised by the smaller peaks in the FFT power in Figures 2.7.3(d) and 2.7.4(b), matching the first predicted waveguide harmonic of $\omega_1 \simeq 1.3$. This will only improve once the boundary is not driven over the full extent in azimuth. Overall, the plots from this simulation highlight the rich structure which appears in the waveguide when a radial density variation is included. This case provides an example for the analysis to follow.

2.8 Phase Mixing Length

Now that a density inhomogeneity has been introduced we must ensure that our simulations resolve the phase mixing length. The process of phase mixing describes how neighbouring field lines drift out of phase over time due to the variation of the Alfvén speed in space, with each field line oscillating at the local Alfvén frequency $\omega_A(x)$. This process increases the local wavenumber k_x in time, which can be thought of as a shortening of the radial wavelength. A measure of the change in spatial scale over time is given by the phase mixing length defined as

$$L_{ph} = \frac{2\pi}{k_x(x,t)} = \frac{2\pi}{\omega_A'(x)t}, \tag{2.8.1}$$

where $\omega_A' = d\omega_A(x)/dx$, the local Alfvén frequency gradient [Wright and Mann, 2006; Mann et al., 1995]. To ensure that the structures within the waveguide, particularly close to a FLR, are being properly resolved we impose a minimum of ten grid points over the phase mixing length.

One advantage of the Alfvén speed profile described by (2.7.1) is the constant gradient portion from $0 \leq x \leq x_c$. This implies that the phase mixing length does not vary over this region and hence the same grid resolution can be applied across the whole of the radial extent, improving the efficiency of the code.

2.9 Driving with b_z

We now consider driving with the z component of the magnetic field perturbation, b_z. This has various features of interest. Firstly, driving in this way mimics driving with magnetic pressure, since b_z forms the linear magnetic pressure. As the magnetopause boundary

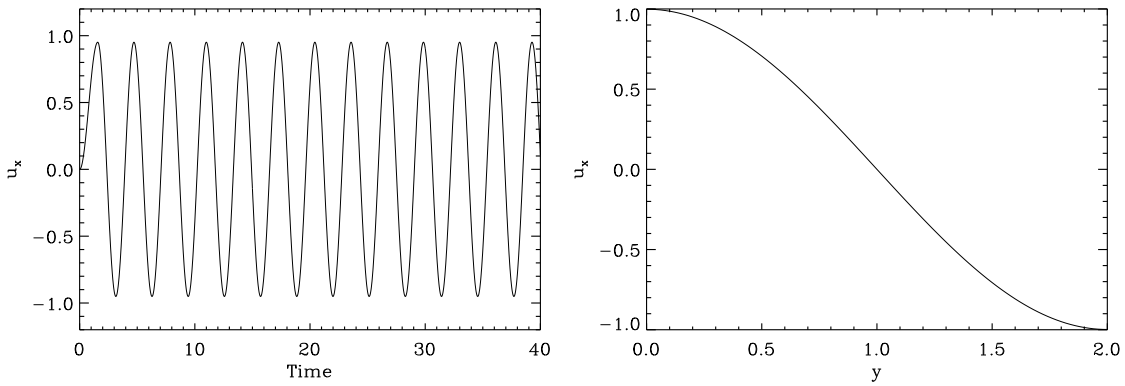

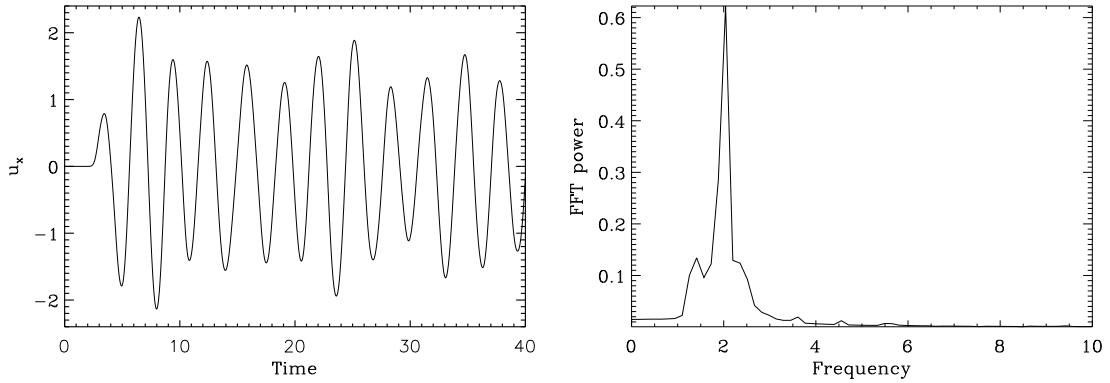

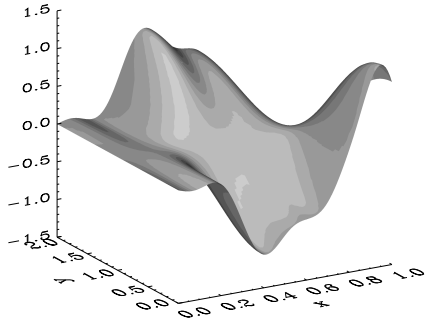

(e)

Figure 2.7.3: Non uniform density, u_x driven waveguide. (a) Time series of u_x on the driven boundary ($x = 1$). (b) Variation of u_x in azimuth (y) on the driven boundary at $t = 2$. (c) Time series of u_x at $x = 0.4$, $y = 0.2$. (d) FFT of u_x taken at point $x = 0.4$, $y = 0.2$, showing angular frequencies. (e) Shaded surface of u_x at time $t = 11.2$

represents the pressure balance between the solar wind dynamic pressure (p_{dyn}) and the Earth's outward magnetic pressure, perturbations in one imply perturbations of the other.

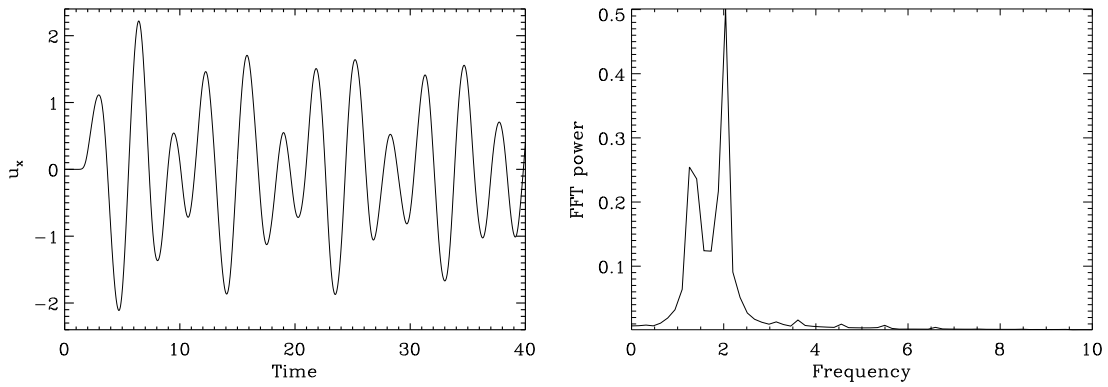

(a) (b)

Figure 2.7.4: Non uniform density, u_x driven waveguide. (a) Time series of u_x at $x = 0.75$, $y = 0.2$. (b) FFT of u_x at $x = 0.75$, $y = 0.2$, showing angular frequencies.

Hence it is instructive to drive with changing b_z to model a magnetopause boundary perturbed by p_{dyn}, which has been shown to be the dominant driver of Pc5 waves at geosynchronous orbit [Takahashi and Ukhorskiy, 2007, 2008]. Secondly, the eigenfrequencies of the waveguide are changed from the u_x driven boundary case. Varying b_z on the driven magnetopause boundary ($x = 1$), simulates a node of b_z there, which results in an antinode of u_x. Together with the assumption of a perfectly reflecting inner boundary, this results in a quarter wavelength fundamental eigenmode. Adopting such a boundary condition is in agreement with Mann et al. [1999], who suggested that overreflected waveguide modes believed to drive discrete FLRs are more accurately modelled by such a boundary condition. They also noted that having a fundamental quarter wavelength mode can help to lower the natural waveguide eigenfrequencies to just a few mHz without changing the magnetospheric plasma density to unrealistic higher values. Claudepierre et al. [2009] also came across this problem in their simulation looking at magnetospheric cavity modes driven by solar wind dynamic pressure fluctuations. They found that adopting a quarter wavelength mode would much better suit the frequencies for the cavity mode. The first three harmonics of the waveguide for u_x, when the boundary is driven with perturbations of b_z, are given in Figure 2.9.1

As an example of why driving the boundary with b_z simulates a node of b_z there, imagine having an organ pipe (or an empty beer bottle) whose natural modes have nodes of pressure at the open end. These modes can be excited by blowing across the open end, driving them with pressure perturbations. To demonstrate that driving in such a way does indeed produce the radial nodal structure depicted in Figure 2.9.1, we consider a uniform medium with $k_y = \pi/2$ and $k_z = \pi$. If the radial fundamental mode is a quarter wavelength mode between $x = 0$ and $x = 1$, this implies a wavelength of $\lambda_{x1} = 4$, with wavenumber $k_{x1} = 2\pi/\lambda_{x1} = \pi/2$. The second and third harmonics have wavelengths $\lambda_{x2} = 4/3$ and

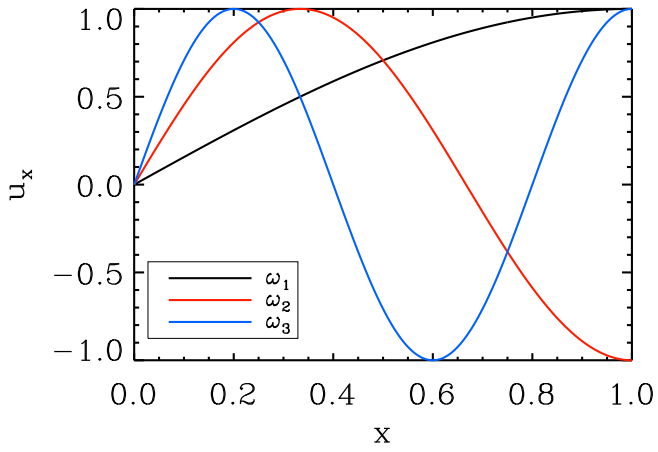

Figure 2.9.1: First three waveguide eigenfrequencies of u_x for a b_z driven magnetopause for a uniform density medium.

$\lambda_{x3} = 4/5$ respectively, with corresponding wavenumbers $k_{x2} = 3\pi/2$ and $k_{x3} = 5\pi/2$. Using the fast mode dispersion relation, given by

$$\omega^2 = V_A^2 \left(k_x^2 + k_y^2 + k_z^2\right), \tag{2.9.1}$$

the eigenfrequencies are predicted as $\omega_1 = 3.85$, $\omega_2 = 5.88$ and $\omega_3 = 8.60$, recalling that $V_A = 1$ for a uniform medium in normalised units. The boundary is driven continuously at a frequency between the first and second harmonics such that neither is preferentially driven. Figure 2.9.2 displays the FFT power spectrum for b_z at a location near to the middle of the waveguide radially, close to the $y = 0$ boundary. There are three peaks clearly visible; at the first and second harmonics, and at the driving frequency. A smaller response is also visible around the third harmonic. This evidently shows that driving with b_z simulates a node of b_z at the outer boundary, producing a quarter wavelength fundamental radial mode. A discussion of this can be found in Appendix A of Elsden and Wright [2015].

In order to implement this driving condition, the value of b_z is prescribed on the boundary at each stage of the Leapfrog-Trapezoidal algorithm given by equations (2.4.3)-(2.4.5). When the boundary value for b_z would be determined through the other components, it is instead overwritten by the prescribed value. Doing this at each time level implements the chosen temporal dependence consistently.

Considering again an inhomogeneous medium as discussed in the previous section, we produce the variation of the eigenfrequencies with the density gradient parameter x_0 for the new boundary conditions, with $x_c = 0.8$. This, together with an estimate of the

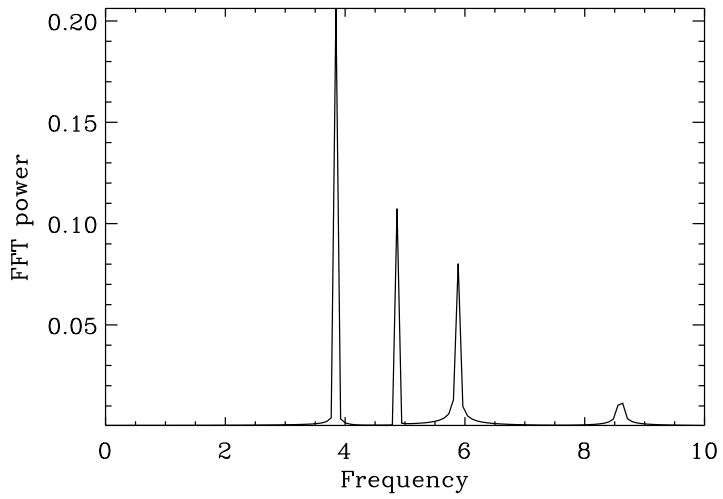

Figure 2.9.2: FFT power spectrum for b_z, at a location in the waveguide, displaying the natural waveguide angular frequencies and the driving frequency.

resonance positions, is shown in Figure 2.9.3. These plots will be used as a reference for many of the simulations in the Chapters to follow.

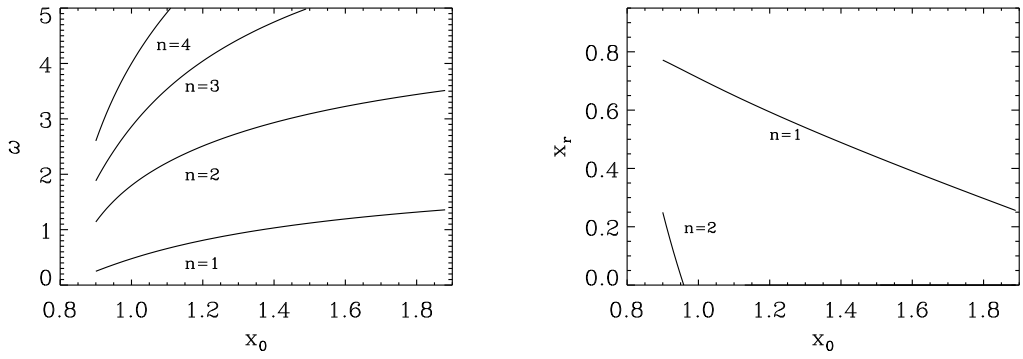

(a) (b)

Figure 2.9.3: For a b_z driven waveguide, with $x_c = 0.8$: (a) $k_y = 0$ fast eigenfrequencies dependent on x_0; (b) predicted location of Alfvén resonances as a function of x_0. n is the harmonic number of the mode.

2.10 Various Drivers

The freedom in the simulation lies firstly with tuning the equilibrium by varying the plasma density and secondly, by changing the type of driving that we impose on the magnetopause boundary. In this section we discuss some of the different forms of driving that can be used, to serve as an introduction to the later sections when different driving mechanisms

are employed when attempting to model observed data.

Thus far, the boundary has been continuously driven at a constant amplitude for the testing of the numerical method. However, we can obviously control how long to drive for i.e. the number of periods in the wave packet as well as the amplitude and the frequency. Furthermore, the spatial structure can be varied in azimuth where the disturbance can either be propagating along the boundary azimuthally, or be stationary, driving the same fixed region in space. This depends on the observation in question. For example, modelling a Kelvin-Helmholtz unstable boundary would require a propagating disturbance along the magnetopause, but a localised disturbance at say the subsolar point, could be modelled with a fixed spatial structure in azimuth.

As an example at the early stages of this thesis, we present two drivers: a half period (temporal) pulse with fixed azimuthal extent and a single period, again fixed azimuthally. The signals produced and waveguide behaviour will not be dissected at great length here, as there is no specific signal or type of behaviour we are trying to produce. These examples are more to demonstrate the flexibility in the choice of driver, and the way in which it is implemented, as a motivation for work in the following chapters.

2.10.1 Half Cycle Pulse

The waveguide has dimensions $x : 0 \rightarrow 1$ and $y : 0 \rightarrow 10$, with density parameters $x_0 = 1.098$ and $x_c = 0.8$ (see equation (2.7.1)). The waveguide has been extended in y such that perturbations do not reach (and hence reflect off) the tailward boundary, providing a more realistic representation of the flank magnetosphere, with energy travelling into the tail. The temporal dependence of the driver (b_z) on the magnetopause boundary is shown in Figure 2.10.1(a), a positive pulse of half period $\tau_d = 2$. The spatial dependence given in Figure 2.10.1(b), shows that only part of the magnetopause is driven, from $y : 0 \rightarrow 0.5$, which corresponds to localised symmetric driving of the subsolar point. To make the form of the driver clear, $b_z(x = 1, y, t) = Y(y)T(t)$, where the functions $Y(y)$ and $T(t)$ are given in Figures 2.10.1(b) and 2.10.1(a) respectively. The simulation is run up until $t = 30$, which allows the natural response of the waveguide to develop post driving. This is demonstrated by looking at the FFT of b_z at the point $x = 0.4$, $y = 0.2$, shown in Figure 2.10.1(c). Four harmonics are clearly shown, which do not correspond to the driven frequency, but instead to the natural $k_y = 0$ waveguide eigenfrequencies. These can be taken from the graph plotting frequency against x_0 (Figure 2.9.3(a)) as $\omega_1 = 0.639$, $\omega_2 = 2.168$, $\omega_3 = 3.470$ and $\omega_1 = 4.827$. This confirms the accuracy of the $k_y = 0$ predictions for the eigenfrequencies when considering a location close to the centre of the driven region for a localised source. Figures 2.10.1(d)-(f) display shaded surface images of b_z at three different times: $t = 1$, $t = 4$ and $t = 20$ respectively. Initially the pulse enters from the $x = 1$ boundary growing to an amplitude of 1 (Figure 2.10.1(d)) . This disturbance propagates radially

and azimuthally, eventually setting up the dynamic structure formed from the combination of the above natural waveguide frequencies (Figure 2.10.1(f)).

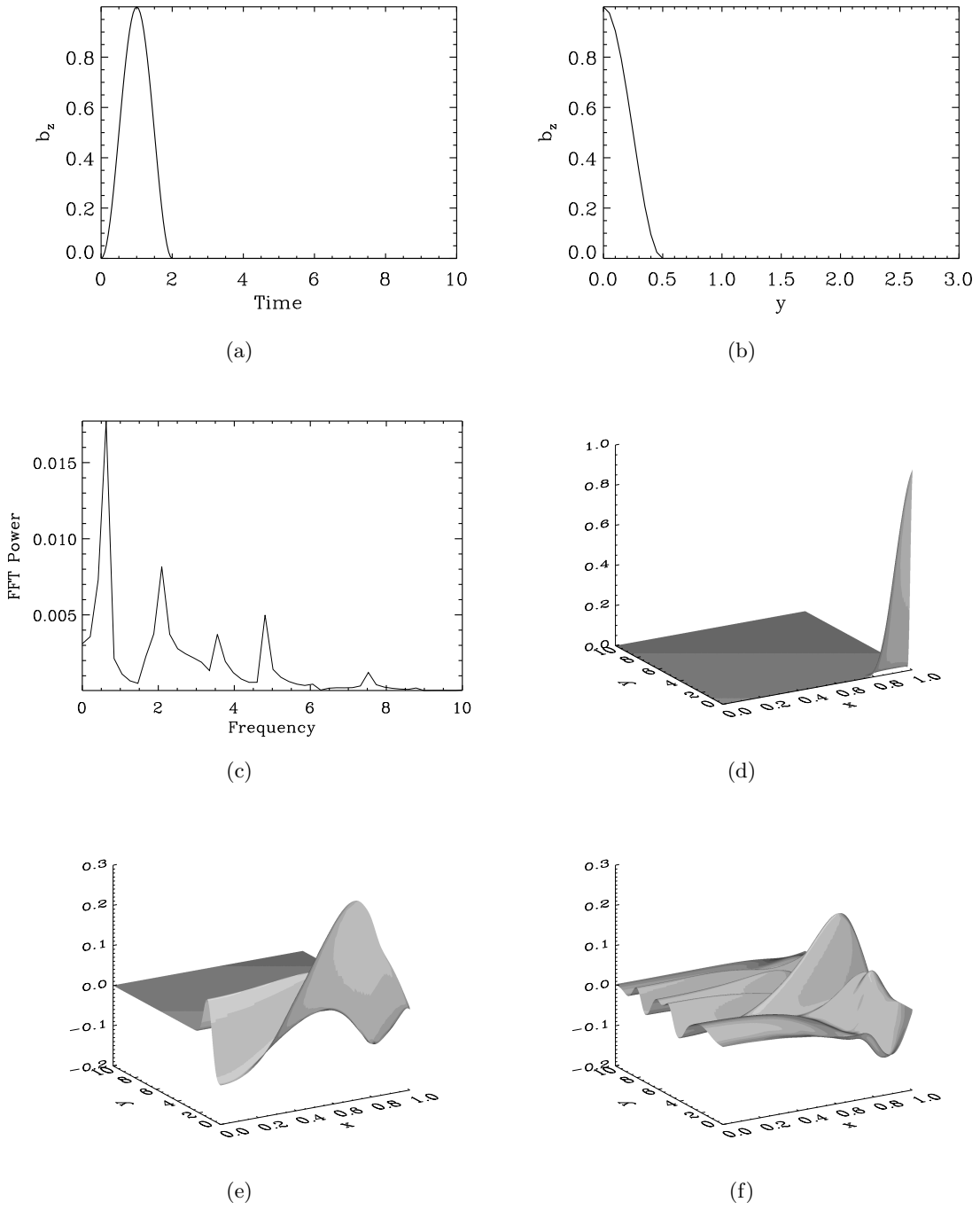

Figure 2.10.1: Pulse driven boundary: (a) temporal variation of b_z at $x = 1$, $y = 0$, the driven boundary; (b) azimuthal variation at $x = 1$, $t = 1$; (c) FFT power spectrum for b_z at $x = 0.4$, $y = 0.2$ showing the angular frequencies; (d)-(f) shaded surfaces of b_z at time $t = 1$, $t = 4$ and $t = 20$ respectively.

2.10.2 Single Cycle

The only change to the above run is to allow the driver to complete a full period, as displayed by the temporal dependence of b_z at $x = 1$, $y = 0$, shown in Figure 2.10.2(a). The spatial dependence of the driver in azimuth is unchanged, shown in Figure 2.10.2(b). The FFT power for b_z at $x = 0.75$, $y = 0.75$ is displayed in Figure 2.10.2(c), which shows how decreasing the period of the driver has preferentially excited the fourth waveguide harmonic. This demonstrates the differences created by changes to the temporal dependence of the driver. To give an idea of the structure within the waveguide, Figures 2.10.2(d) and (e) display shaded surfaces of b_z at times $t = 2.25$ and $t = 5$. Again the presence of several harmonics yields a complex picture. Finally, Figure 2.10.2(f) plots the total energy integrated over the domain against time. While the magnetopause is being driven ($0 < t < 2$), energy enters the domain. Once the driving stops however, energy is clearly conserved over the course of the simulation.

2.11 Exciting Resonances

Absent from the previous sections has been any mention of exciting Alfvén resonances within the waveguide. The reason for this has been to present a simple introduction to the simulations. At this point, we briefly introduce the conceptual ideas behind simulations of resonances, but leave the specific cases to later chapters.

Alfvén resonances can be driven by a compressional fast mode source at the location where the fast and Alfvén frequencies are equal. In our model this location depends upon the frequency of the fast mode driver and the variation of the Alfvén speed with radius. We have to be clear about the terminology. By 'fast mode driver' it is meant that a fast mode source, be that one imposed on the driven boundary, or a natural waveguide response, drives Alfvén resonances. We have already calculated (without saying much about it) the expected resonance position for resonances driven by the natural modes of the waveguide, given in Figure 2.9.3(b). This figure determines whether or not, for the given harmonic frequency, a resonance will exist within the domain. Resonances can be driven at different locations to those suggested in the figure, by imposing a driving frequency different to the natural waveguide harmonics. Simulations doing exactly this will be discussed in Chapters 4 and 5 and hence, we leave further discussion until then.

2.12 Chapter Summary

To summarise the workings thus far:

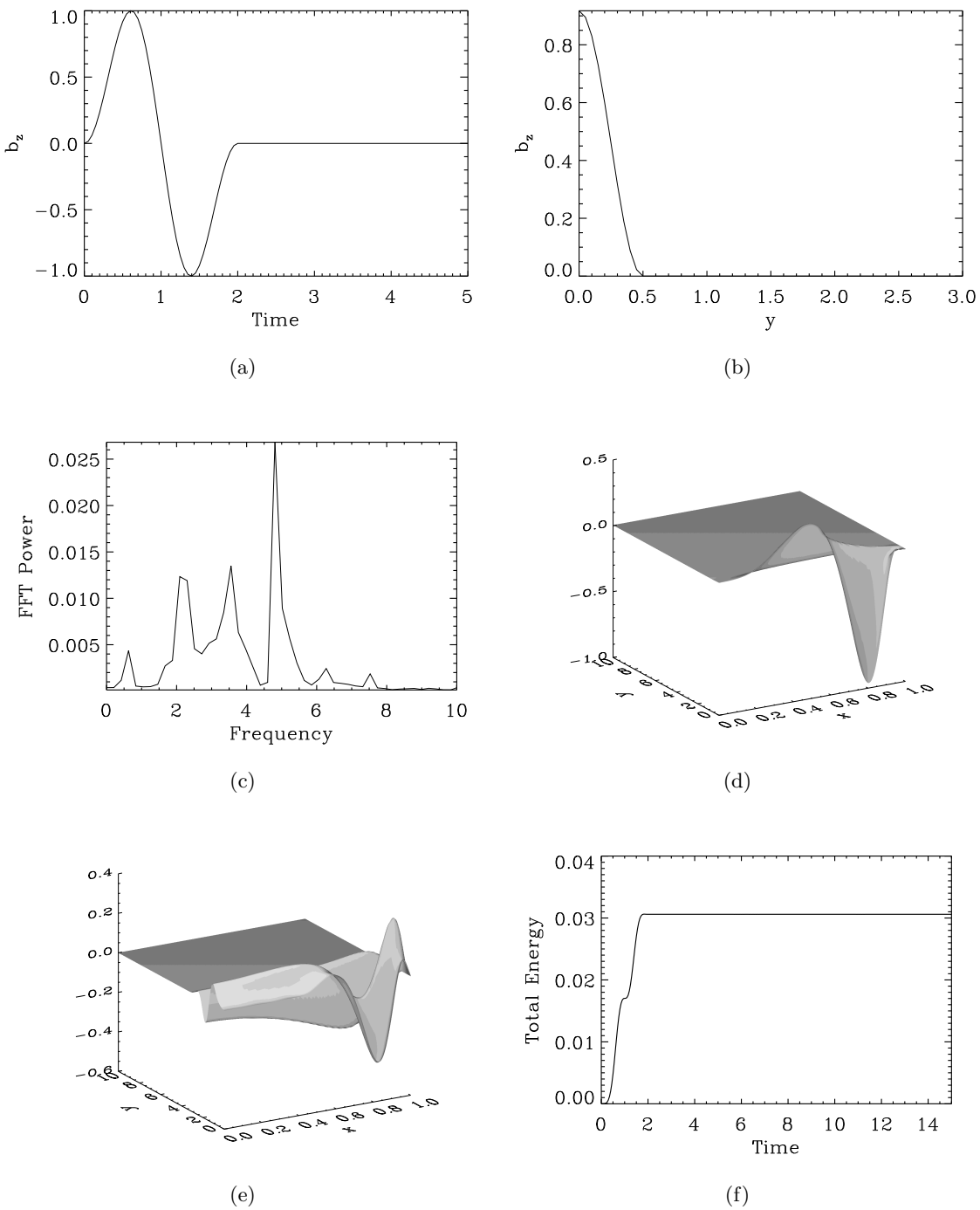

Figure 2.10.2: Single cycle driver: (a) temporal dependence of b_z at $x = 1$, $y = 0$; (b) spatial dependence of b_z at $x = 1$, $t = 0.5$; (c) FFT power of b_z at $x = 0.75$, $y = 0.75$ showing angular frequencies; (d)-(e) shaded surfaces of b_z at times $t = 2.25$, $t = 5$ respectively; (f) total energy against time.

- Pertinent wave equations were derived from the MHD equations.
- Discussed the numerical method that will be employed throughout, and set up the

waveguide box geometry.

- Tested the numerical procedure in various ways, discussing energy conservation, the CFL condition and resolving the phase mixing length.
- Investigated different forms of driving the system for uniform and non-uniform waveguides, most importantly introducing a novel method for driving with the z component of the magnetic field, b_z, to mimic a pressure driven magnetopause.
- Highlighted techniques and concepts to be used later in this thesis such as fast Fourier transforms, exciting Alfvén resonances and using shooting methods to predict waveguide eigenfrequencies.

The following chapter will discuss how we use the techniques developed here to model observational data.

Chapter 3

Application of Simulations to Interpreting Satellite Observations

This chapter discusses the application of the numerical method outlined in Chapter 2 to satellite observations, and is based on work published in the article Elsden and Wright [2015]. Two satellite observations are considered: a large scale Pc4 pulsation observed using Cluster by Clausen et al. [2008] (henceforth *Clausen 08*); a Pc5 waveguide mode observed using THEMIS (Time History of Events and Macroscale Interactions during substorms) by Hartinger et al. [2012] (henceforth *Hartinger 12*). The intention is to demonstrate the important information that can be gleaned by using a relatively simple numerical simulation. We present good matches between the simulations and the observed data and comment on the nature of the wave behaviour, the location of the source region relative to the spacecraft and the length of the driving phase.

Our conclusions throughout this chapter are supported by a careful analysis of the components of the Poynting vector, which has long been used as a diagnostic of the flow of energy for ULF waves. Junginger [1985] provides both an analytical and numerical treatment of the time averaged Poynting vector in a box geometry in the presence of mode coupling. This theory is supported by Proehl et al. [2002], where a 3D MHD simulation shows time averaged radial energy diverted into the resonant surface. Cummings et al. [1978] used the Poynting vector to identify azimuthal propagation of a Pc4 wave. Chi and Russell [1998] found a correlation between the time-averaged Poynting flux and phase skips, a phenomenon where the phase changes suddenly between wave packets with a near constant frequency. The authors also examine the instantaneous Poynting vector to highlight the importance of phase changes between the electric and magnetic fields in determining the direction of energy flow. As in these studies, we demonstrate how the Poynting vector can be used to interpret ULF wave signatures. A significant difference between our work and the first three of these studies is that we use the Poynting vector, rather than its

time-average, and are able to exploit the extra information this retains, building upon the phase analysis of Chi and Russell [1998].

The chapter has the following structure: Section 3.1 discusses in detail the aforementioned observations as a means to motivate our modelling. Sections 3.2 and 3.3 present the results from the modelling of these observations while a comparison between the two and some final thoughts are given in Section 3.4.

3.1 Observations

3.1.1 Cluster Observation

We begin by considering *Clausen 08*, who present an observation of a large scale Pc4 mode by the Cluster satellites which is correlated with ground magnetometer data. Beginning with the ground data, Figure 1 of *Clausen 08* displays multiple wave packets recorded at stations spanning latitudes from $\sim 50°$N to $\sim 75°$. This shows that the event covered a large radial distance in the magnetosphere. The signals are more prominent in the dawn sector at a magnetic local time (MLT) of $\sim$ 7.5 h, but are still present at MLT $\sim$ 14 h, suggesting that the disturbance occurred over a large azimuthal extent. The wave packet of interest occurs over the time interval from 13:30 to 13:42. The right hand panels of Figure 1 from *Clausen 08* display the normalised smoothed Fourier spectra, with a frequency peak around 17.2 mHz.

For the satellite data, the Cluster 3 and 4 satellites are used due to their favourable position, sampling approximately the same set of field lines moving from the southern to northern hemispheres, separated by around $2R_E$. Over the course of the event, the satellites remained relatively close to the magnetic equator, with Cluster 3 between 9.6° and 14.7° magnetic latitude and Cluster 4 between -12.0° and -7.8°. Both satellites remained at a radial distance of $\sim 5R_E$. An estimate of the plasmapause position was determined by *Clausen 08* as $4.1R_E$, close to the satellite locations. This will become a key factor in the placement of the satellites in our model. The data from the two spacecraft are qualitatively similar, so we arbitrarily choose to work with the Cluster 3 data, which is reproduced here as Figure 3.1.1 (taken from Figure 3 of *Clausen 08*). The left hand panels display the components of the magnetic field $\mathbf{b}$ (top), electric field $\mathbf{E}$ (middle) and Poynting vector $\mathbf{S}$ (bottom) which is calculated using the perturbation fields as

$$\mathbf{S} = \frac{1}{\mu_0}\mathbf{E} \times \mathbf{b}. \tag{3.1.1}$$

The coordinates used represent a local coordinate system aligned with the Earth's dipolar magnetic field, where one axis is along the direction of the background magnetic field, the

second is in the azimuthal direction with positive eastward, and the third points radially inward. The data have been bandpass filtered between 12.5 mHz and 50 mHz. Given this broad range the signals are remarkably clear, showing coherent oscillations with a well defined natural frequency. The right hand panels of Figure 3.1.1 show the corresponding fast Fourier transform (FFT) power spectra. These indicate the clearly defined frequency of 17.2 mHz for the electric and magnetic field components, as observed in the ground magnetometer data.

Looking at the components in detail, comparable field-aligned and azimuthal magnetic field perturbations of $\sim$ 1 nT are observed, with a negligible radial contribution. The growth phase of the perturbation is estimated using the b_z data, of approximately four periods, which will be used when modelling as a measure for how long to drive the system. In the electric field a strong radial perturbation is recorded, with a small azimuthal variation and negligible field-aligned component. The Poynting vector derived from these components using equation (3.1.1) has interesting properties. The field-aligned component shows no preferential direction for energy transport between the Northern and Southern hemispheres. The radial signal is small by nature of the diminutive azimuthal electric field. The point of interest comes from the azimuthal Poynting vector signature, showing a unidirectional flow of energy into the tail. This feature suggests this observation is a waveguide mode, and will be examined in depth in the simulations to follow.

3.1.2 THEMIS Observation

We now turn to the observation of a Pc5 mode by *Hartinger 12*, using the THEMIS satellites. The authors describe the observation as a global mode with the definition: 'a standing fast mode wave trapped between different magnetospheric boundaries'. As with the previous observation, ground magnetometer data is presented alongside the satellite data to aid understanding of the nature of the oscillation. The five THEMIS satellites (THA-THE) were in this case able to sample solar wind, magnetosheath, magnetospheric and plasmaspheric plasma. This enables a spatial picture to form of the propagation of the mode from outside the magnetosphere to beyond the plasmapause boundary. The observation was also selected by the authors due to the favourable radial alignment of the spacecraft, in a hope of resolving the spatial structure of the fast mode. The presence of satellites in the solar wind and magnetosheath allowed the identification of the dominant driver of the event as broadband dynamic pressure fluctuations, but with only small changes to the overall dynamic pressure. The plasmapause is estimated to be at a location of $\sim 7\mathrm{R_E}$, while the dawn magnetopause is at a distance of $\sim 17\mathrm{R_E}$.

The main component results that we explain are given in Figure 3.1.2, a reproduction of Figure 7 of *Hartinger 12*. The components are listed in field-aligned coordinates for the THD spacecraft, with z being the field-aligned component, y positive eastward and x

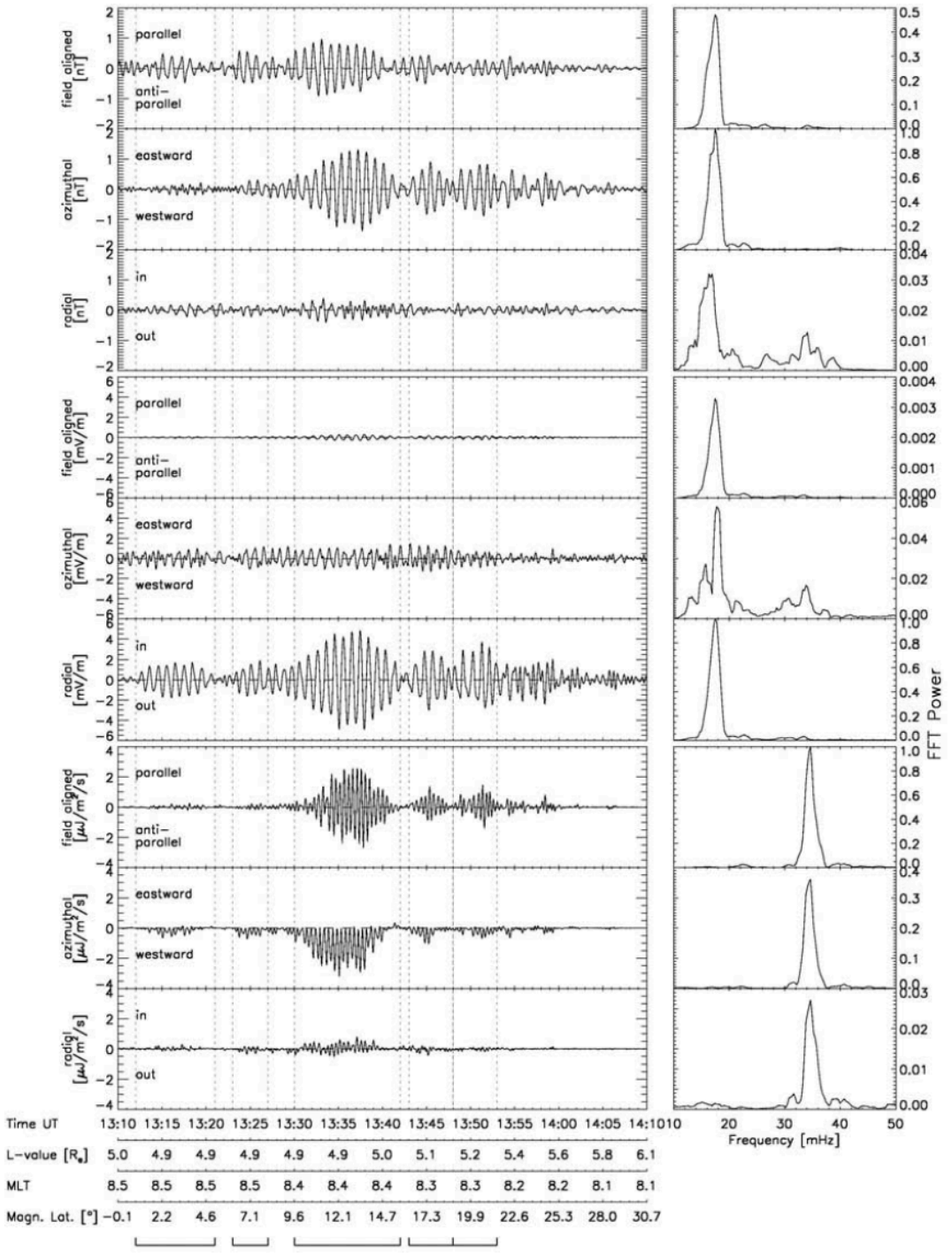

Figure 3.1.1: Reproduction of Figure 3 from Clausen et al. [2008] displaying data from the Cluster 3 satellite. On the left: the 3 components of the magnetic field (top 3 panels), electric field (middle) and the Poynting vector (bottom). On the right are given the corresponding fast Fourier transform powers.

radially outward. THD is situated at an L value of ~ 8.5 and MLT ~ 6 h, and is hence just on the magnetospheric side of the plasmapause on the dawn flank. Over the course

of the event, THD remains within $1R_E$ of the magnetic equator. The data displayed in Figure 3.1.2 is bandpass filtered between 5 and 8 mHz to isolate the global mode frequency of 6.5 mHz. In the top panel showing b_z, the high pass filtered (> 0.5 mHz) signal (black) is shown alongside the bandpass filtered signal (red). It is clear that the filtering process has captured the dominant frequency of the signal. The components b_z (panel 1) and E_y (panel 2) are dominant as expected for a fast mode observation, compared to b_x, b_y and E_x shown in panel 5. Being close to the magnetic equator, we expect to see small transverse magnetic field components since assuming a fundamental magnetic field line structure in $\hat{\mathbf{z}}$, these components have a node at the equator. The components of the Poynting vector are displayed in the bottom three panels of Figure 3.1.2. The radial component is dominant, showing an initial inward flow of energy which returns to a back and forth signal by the end of the event. There is a very slight positive azimuthal Poynting vector signal, with a negligible field-aligned component as expected by the near equatorial position. These Poynting vector signatures are very different from those of the Cluster event, shown in Figure 3.1.1, and will be used to learn about the nature and location of the source of wave energy.

3.1.3 Observation Selection and Modelling Goals

The event outlined in *Clausen 08* was selected for modelling mainly due to the Poynting vector signature showing purely tailward propagation of energy. The second event described by *Hartinger 12* was chosen as a contrast to the Cluster observation in order to compare the two different signatures. The reported global mode shows very little azimuthal Poynting vector with a strong radial Poynting vector, oppositely to the Cluster event. Our goal in modelling the data is to match to the main features of the displayed components and to answer questions such as: What type of driving produces the tailward Poynting vector signal? How is the satellite position related to this signature and to all of the components? Can the differences in the signals be explained purely by satellite position? How can the Poynting vector be used to interpret ULF waves?

In the following two sections we choose simulation parameters appropriate to the Cluster and THEMIS events described in the previous sections. We then experiment with driving conditions and satellite locations in an effort to reproduce notable signatures in the observations. The numerical model employed and pertinent equations have been discussed in detail in the second Chapter, and only specific details relating to the fine tuning of the model in each case will be discussed here.

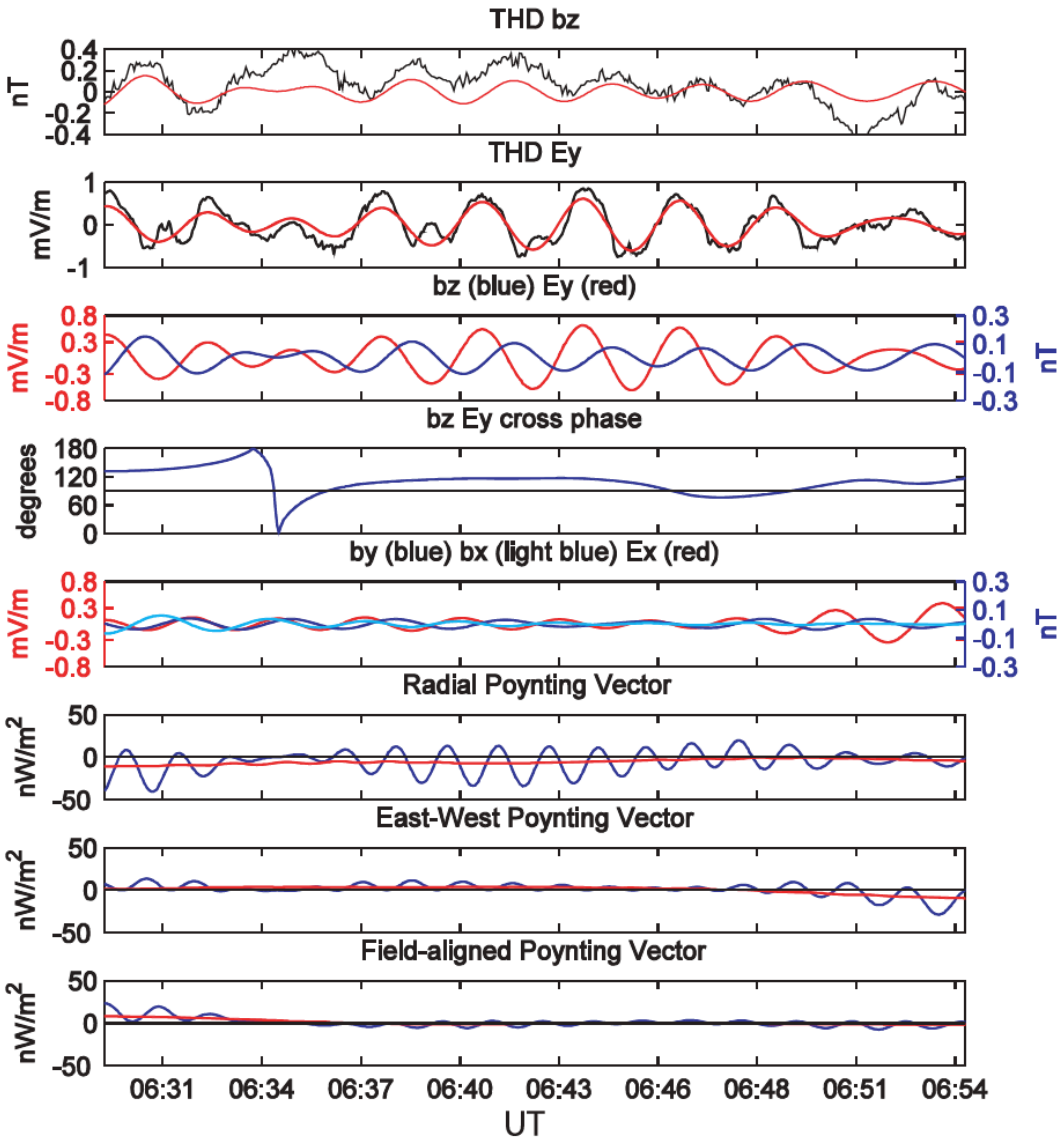

Figure 3.1.2: Reproduction of Figure 7 from Hartinger et al. [2012], showing satellite data from THD. THD is at an L-value of ~ 8.5 and MLT ~ 6 h during the event.

3.2 Cluster Modelling

3.2.1 Tailoring the Model

In order to model the Cluster observations we use specific input parameters given in *Clausen 08*. Figure 10 from their paper displays a model of how the fundamental field line frequency will vary with L-shell. Following the box model structure for the waveguide given in Figure 2.1.1, we take the inner boundary of the waveguide to be the plasmapause at ~ 4 R_E, and allow a radial extent (in x) of 10 R_E to the magnetopause at ~ 14 R_E. Using their Figure 10, we determine that the Alfvén frequency varies from ~ 12 mHz at

the plasmapause to ~ 5 mHz at the magnetopause. Assuming that the Alfvén speed is proportional to the Alfvén frequency, this allows the Alfvén speed profile to be scaled to match this frequency change. We note that these frequencies are a little high for typical fundamental Alfvén modes, probably due to lower plasma densities than normal which have elevated the normal Pc5 frequencies to the Pc4 band. Indeed, *Clausen 08* suggest that it is due to the natural frequencies in this event matching the frequency of waves associated with back-streaming ions at the bow shock that the lowest frequency modes of the magnetosphere can be excited effectively by this method [Le and Russell, 1996].

The system is driven with the b_z perturbation as described in Section 2.9, with a frequency of 17.2 mHz to match the dominant frequency in the Cluster data in Figure 3.1.1. Le and Russell [1996] developed a model to estimate the frequency generated by back-streaming ions at the bow shock, formulating the frequency in terms of the cone angle and the interplanetary magnetic field strength. Figure 8 from *Clausen 08* shows that these parameters were relatively stable over the course of the event from 13:30 to 13:40 UT. Furthermore, even broadband frequency driving can give monochromatic signatures in a cavity or waveguide [Wright and Rickard, 1995a]. Both of these effects justify driving monochromatically. Our equilibrium model is chosen such that the driving frequency of 17.2 mHz is the second radial harmonic of the waveguide. Considering the radial fundamental to be a quarter wavelength mode, with the prescribed boundary conditions the second harmonic has approximately three times the frequency of the fundamental. This implies a fundamental frequency of ~ 6 mHz.

In order to choose the wavenumber in the field-aligned direction k_z, we again refer to the Alfvén frequencies given in Figure 10 of *Clausen 08*. Through the Alfvén dispersion relation $\omega_A = k_z V_A$, k_z can be adjusted with V_A in order to match both the expected fundamental frequency profile and the full dispersion relation of fast waveguide modes. This has been done in the previous Chapter in Section 2.7, where a fourth order Runge-Kutta method is used to solve the simplified system with $k_y = 0$. From this come the finalised values for the $k_y = 0$ fast natural waveguide frequencies, the field-aligned wavenumber k_z and the correctly scaled Alfvén speed profile. (From this analysis we find dimensionless values of $k_z = 2.28$, $x_0 = 1.514$ and $x_c = 0.8$. To get these in terms of $\mathrm{R_E}$, multiply x_0 and x_c by 10, and divide k_z by 10. The normalizing magnetic field and velocity were taken as 90 nT and 2350 km s^{-1} respectively, with an inner boundary Alfvén speed of 2107 km s^{-1}.) The theory of estimating the natural waveguide frequencies by looking at the $k_y = 0$ modes was developed by Wright [1994] and tested in simulations by Rickard and Wright [1994].

The length in the z direction is now fixed by the choice of k_z and the assumption that the modes have a fundamental structure in z. This is consistent with the observed phase shift of 180° in the azimuthal magnetic field component b_y between Cluster 3 and 4.

This infers that the satellites must straddle a node of b_y, one above and one below the magnetic equator. Results from a preliminary simulation using the above input parameters show that assuming a homogeneous medium in the z direction, at a satellite location modelling that of Cluster 3 ($x = 0.05$, $y = 0.6$ and $z = 0.1$ in dimensionless units), the b_y component has too small an amplitude in comparison to b_z. The b_y component is small in the simulation due to the position of both satellites near to a node of b_y at the equator. Including an inhomogeneity in z i.e. a z dependent density profile, would create a z dependent Alfvén speed which could shift the turning point of the mode towards the equator. The low Alfvén speed in this equatorial region tends to cause the mode's phase structure to bunch up there, as seen in Figure 12 of *Clausen 08* showing the Alfvén eigenfunctions. This is important as it would cause more rapid variations closer to the equator and could hence give a better match to the observed amplitudes.

To see the effects of including such an inhomogeneity, we consider resolving the eigenfunctions for the case where $k_y = 0$ (hence $\partial/\partial y = 0$) and $\rho_0 = \rho_0(z)$. In Cartesian coordinates the system is defined by equations (2.2.6), (2.2.3) and (2.2.5) without the y dependence, given by

$$\frac{\mu\rho_0(z)}{B_0}\frac{\partial u_x}{\partial t} = \frac{\partial b_x}{\partial z} - \frac{\partial b_z}{\partial x}, \tag{3.2.1}$$

$$\frac{\partial b_x}{\partial t} = B_0\frac{\partial u_x}{\partial z}, \tag{3.2.2}$$

$$\frac{\partial b_z}{\partial t} = -B_0\frac{\partial u_x}{\partial x}. \tag{3.2.3}$$

Considering a propagating solution in $\hat{\mathbf{x}}$ of the form $b_z = b_z(z)e^{-i(\omega t - k_x x)}$ and rearranging yields

$$\omega\frac{\mu\rho_0(z)}{B_0}u_x = \frac{\mathrm{d}}{\mathrm{d}z}(ib_x) + k_x b_z, \tag{3.2.4}$$

$$-\frac{\omega}{B_0}(ib_x) = \frac{\mathrm{d}u_x}{\mathrm{d}z}, \tag{3.2.5}$$

$$\omega b_z = B_0 k_x u_x. \tag{3.2.6}$$

Equation (3.2.6) can be used to eliminate b_z from the (3.2.4). Normalising the magnetic field and velocity terms as discussed above, yields the system

$$\frac{\mathrm{d}}{\mathrm{d}z}\left(ib_x\right) = \frac{\omega}{V_A^2(z)}u_x - \frac{k_x^2}{\omega}u_x, \tag{3.2.7}$$

$$\frac{\mathrm{d}u_x}{\mathrm{d}z} = -\omega\left(ib_x\right). \tag{3.2.8}$$

where $V_A^2(z) = B_0^2/\mu\rho_0(z)$. We note that k_x appears as k_x^2, so these equations apply equally well to a mode that has a standing structure in x. Also, since $\rho_0 = \rho_0(z)$ there is no preferred direction perpendicular to z, and x may be taken as a general 'perpendicular' direction. To proceed, we transform the system into dipole coordinates, in order to realistically express the variation of the Alfvén speed along a field line. Figure 3.2.1 displays a typical field line in the northern hemisphere of a dipole system. We move from working in z to working with the latitude λ. Derivatives are constructed using the chain rule as

$$\frac{\mathrm{d}}{\mathrm{d}z} = \frac{\mathrm{d}\lambda}{\mathrm{d}z}\frac{\mathrm{d}}{\mathrm{d}\lambda}.$$

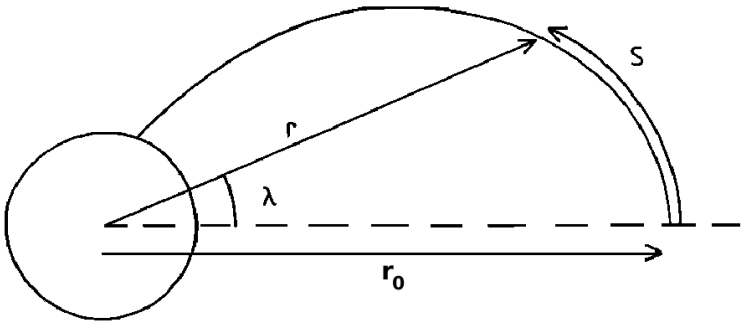

Figure 3.2.1: An example magnetic field line in the northern hemisphere of a dipole coordinate system, adapted from Wright [1987].

Restructuring the system in this way transforms equations (3.2.7) and (3.2.8) to

$$\frac{\mathrm{d}}{\mathrm{d}\lambda}\left(ib_x\right) = \frac{\mathrm{d}z}{\mathrm{d}\lambda}\left[\frac{\omega}{V_A^2(\lambda)} - \frac{k_x^2}{\omega}\right]u_x, \tag{3.2.9}$$

$$\frac{\mathrm{d}u_x}{\mathrm{d}\lambda} = -i\omega b_x\frac{\mathrm{d}z}{\mathrm{d}\lambda}. \tag{3.2.10}$$

To specify the variation of the Alfvén speed with λ, we consider the density profile provided by *Clausen 08*, which once normalised gives

$$\rho_0 = \left(\frac{r_0}{r}\right)^n,$$

where n is a density index set to 1 here, r is the geocentric distance to a point on the field line and r_0 is the geocentric distance along the magnetic equator to the field line. The normalisation by the Alfvén speed at the equator yields a density of 1 at $\lambda = 0$, $r = r_0$.

The magnetic field variation is taken to be a standard dipole variation of

$$B_0(r, \lambda) = \left(\frac{r_0}{r}\right)^3 \left[1 + 3\sin^2\lambda\right]^{\frac{1}{2}},$$

where the magnetic field strength has been normalised by the value at $r = r_0$, $\lambda = 0$. r can be eliminated from the equations using $r = r_0 \cos^2\lambda$ to give

$$\begin{aligned} B_0(r, \lambda) &= \frac{1}{\cos^6\lambda}\left[1 + 3\sin^2\lambda\right]^{\frac{1}{2}}, \\ \rho_0 &= \frac{1}{\cos^2\lambda}. \end{aligned}$$

Hence the normalised Alfvén speed can be expressed as

$$V_A^2(\lambda) = \frac{B_0^2(\lambda)}{\mu\rho_0(\lambda)} = \frac{1}{\cos^{10}\lambda}\left(1 + 3\sin^2\lambda\right).$$

The final step is to evaluate the derivative $\mathrm{d}z/\mathrm{d}\lambda$. z here is essentially the path length S, which can be expressed as

$$S(\lambda) = \frac{r_0}{2\sqrt{3}}\left[p\sqrt{p^2+1} + \ln\left(p + \sqrt{p^2+1}\right)\right],$$

where $p = \sqrt{3}\sin\lambda$, and hence we require $\mathrm{d}S/\mathrm{d}\lambda$, which can be easily evaluated.

To solve the system defined by (3.2.9) and (3.2.10), k_x must be specified. The value is assumed based on a second radial harmonic as chosen for the modelling of this observation. With the boundary condition that u_x has a node at the inner boundary and an antinode at the outer boundary, this gives $\lambda_x = 4/3 \Rightarrow k_x = 4.712$. When solving over the full field line length, the range of λ varies from the point where the field line reaches the Earth in the southern hemisphere, to the equivalent point in the northern hemisphere. This is calculated by considering where the radius is equal to 1. Assuming $r_0 = 5$ consistent with the L-shell of the Cluster satellites, with $r = 1$, using $r = r_0\cos^2\lambda$ gives the maximum value of λ to be 1.107, which implies λ varies over $-1.107 < \lambda < 1.107$.

For the boundary conditions, u_x has a node at each end of the field line, while b_x has

antinodes. Using a fourth order Runge-Kutta method, the value of the frequency is incremented until these boundary conditions are met. In this scenario, the x direction can be thought of as a general perpendicular direction (we could have equally set $\partial/\partial x = 0$ rather than $\partial/\partial y = 0$), and hence we change subscripts from $_x$ to $_\perp$. Figure 3.2.2 plots the fundamental eigenfunctions against distance along the field line, in a similar manner to Figure 12 from *Clausen 08*. The approximate locations of the Cluster satellites are denoted by the vertical dashed lines, and it is first of all evident that we see a 180° phase change in $b_\perp$ (solid blue) between them, which is a feature of the observation. Secondly, the amplitude of $b_\perp$ changes more quickly closer to the equator than for the homogeneous case (blue dashed line). Indeed at the satellite locations the amplitudes of b_z and $b_\perp$ are comparable, when V_A varies with z in accordance with the observations. The fundamental mode in z provides the desired phase shift, while including a density structure along the field produces the more rapidly changing amplitude profile close to the equator, which was the goal from the outset.

Including a z dependence in the density in the full time-dependent simulation increases the computing time, so we opt for a simpler approach of moving our simulation satellites in z to an equivalent phase and amplitude location, whilst retaining a density independent of z for computational convenience. Figure 3.2.2 shows that it is justified to move further away from the equator along the field line closer to the amplitude peak of $b_\perp$ in our simple model. Thinking in terms of nodal structure rather than height or distance from the equator, Figure 3.2.2 demonstrates that the Cluster satellites would lie close to the antinodes of $b_\perp$. Hence moving closer to the antinodes in our original homogeneous z structure, should simulate the amplitudes that would be found closer to the equator when there is inhomogeneity in z.

3.2.2 Results

Figure 3.2.3 shows the time dependence of b_z on the outer driven boundary at $x = 10$ $\mathrm{R_E}$. The system is driven for 4 periods of 17.2 mHz to match the observed growth phase of the b_z perturbation in the Cluster 3 data and after four cycles the driver is switched off. The spatial dependence of b_z along the outer boundary at $x = 10$ $\mathrm{R_E}$ in the y direction is given in Figure 3.2.4. The extent of the disturbance on the magnetopause boundary i.e. the size of the driven region corresponds to a physical length of 5 $\mathrm{R_E}$ (and a full width of 10 $\mathrm{R_E}$).

The satellite position for Cluster 3 is taken to be at 4.5 $\mathrm{R_E}$ in x and 6 $\mathrm{R_E}$ in y. These are taken as approximations to the real location of the satellite and considering the geometric simplifications of our model. This corresponds to dimensionless coordinates $x = 0.05$ and $y = 0.6$, recalling that the inner boundary of the waveguide at $x = 0$ corresponds to a radial position of 4 $\mathrm{R_E}$. The length of a field line in z is determined by the choice of k_z. For the

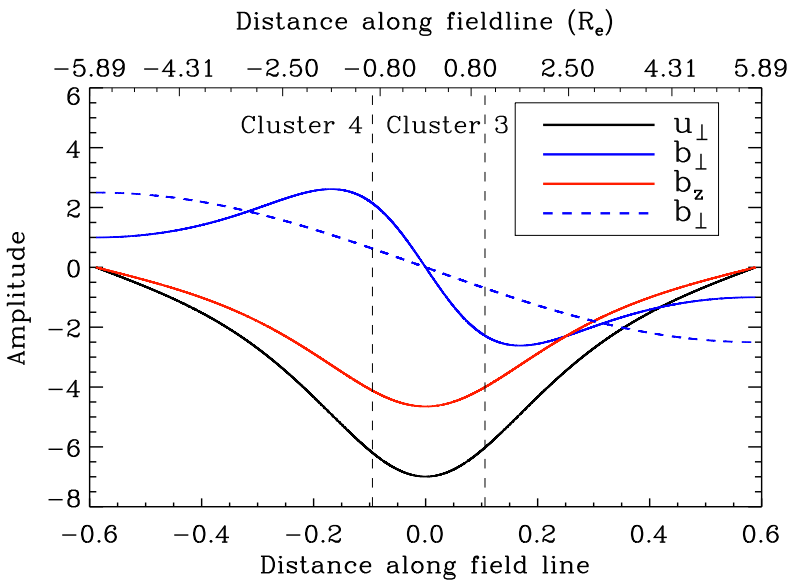

Figure 3.2.2: $u_\perp$, $b_\perp$ and b_z (solid lines) plotted against distance along the field line for a 'dipole' inhomogeneity in z, with the dashed line $b_\perp$ for a homogeneous medium in z. The vertical lines show the approximate location of the Cluster satellites, approximately 2 R_E apart.

given input parameters the length in z is 1.378 and hence extends from $-0.689 \rightarrow 0.689$, corresponding to a dimensional length of almost 14 R_E. The perpendicular components of the magnetic field have antinodes at the ends of the field lines. As discussed above, moving towards the antinodes of $b_\perp$ should simulate the amplitudes that would be observed if an inhomegeneity in z was considered. Hence the position in z is chosen as 0.45 approximately two thirds along the length of the field line.

Figure 3.2.5 displays the magnetic field, velocity field and Poynting vector components from the simulation for the satellite position $x = 0.05$, $y = 0.6$ and $z = 0.45$ as discussed above. The first vertical dashed line represents the time when the driver is switched off at $t = 3.88$ minutes. The heightened amplitudes during driving extend past the driver switch off time by approximately the radial travel time ($t \sim 1.04$ minutes, shown by the second vertical dashed line), since the satellite is located close to the inner boundary. As in the observations, the field-aligned and azimuthal magnetic field components have similar amplitudes, shown in panels (a) and (b) respectively. Notice also how b_y falls off as soon as the driving stops (plus radial travel time) at around $t = 5$ minutes. The field-aligned component is persistent post driving, which is a result of driving on resonance: as we drive with the natural frequency of the second radial waveguide harmonic, no other modes are excited to the same extent, and hence we see a clear monochromatic response after the driving has stopped. The radial component b_x given in panel (c) is small due to the position of the satellite close to the inner boundary (plasmapause), where b_x has a node.

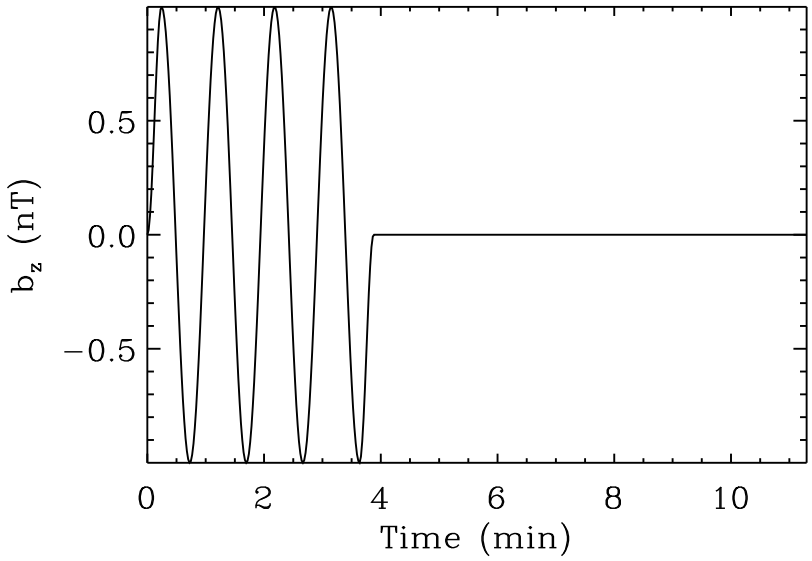

Figure 3.2.3: Temporal variation of the b_z driver on the driven boundary $x = 10$ R_E at $y = 0$.

Through the equations and the simplifications made, only the perpendicular components to the velocity remain and are shown in panels (d) and (e). Recall that the electric field has been eliminated in favour of the velocity field in our model. For the purpose of comparison the components may be indentified as $u_x \sim E_y$ and $u_y \sim -E_x$. The position of the satellite close to the perfectly reflecting inner boundary where $u_x = 0$ causes the radial component of the velocity (and E_y) to be small. The azimuthal component of the velocity (and E_x) has an increased amplitude during the driven phase, but then decays in the same manner as b_y. Note the comparison to the real data here, with a strong E_x and weak E_y matching the simulation with strong u_y and weak u_x.

A diagnostic of energy flow within the system is the Poynting vector, the components of which are given in panels (f)-(h). The field-aligned and azimuthal signatures dominate, with the radial component being weaker, as in the case of b_x and u_x, due to the near inner boundary position. The field-aligned component of $\mathbf{S}$ shows equal parallel to antiparallel transport of energy, as is expected for modes that stand in z in the absence of ionospheric dissipation. The azimuthal component matches well to the striking result from Figure 3.1.1, where we clearly see the purely tailward (positive azimuthally in our model) propagation of energy. Since the perpendicular magnetic and velocity field components have a decreased amplitude signal post driving, this feature is seen in the Poynting vector signal as well.

Clausen 08 report certain phase shifts in the electric and magnetic field components at each Cluster satellite and between the satellites. Firstly, as previously mentioned, the

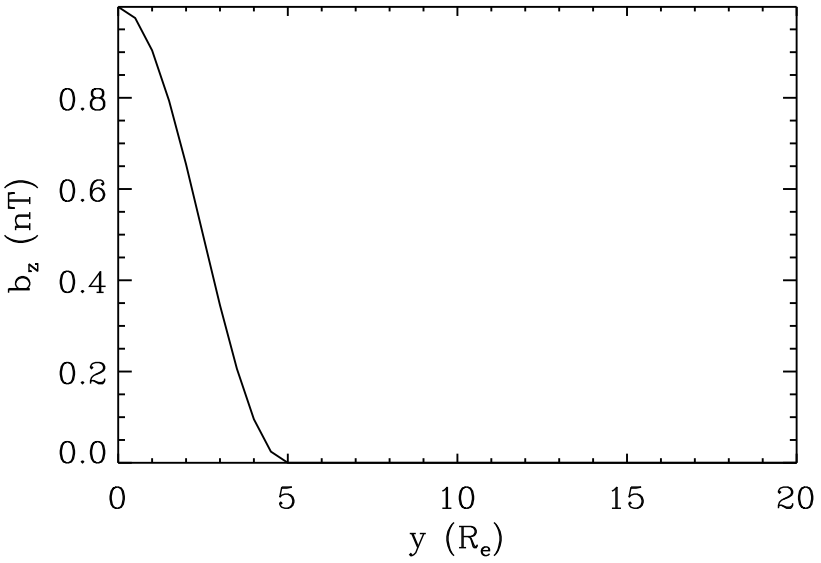

Figure 3.2.4: Spatial variation in y of b_z on the driven boundary $x = 10$ R_E.

observations display a 180° phase shift in b_y between Cluster 3 and Cluster 4. This phase shift indicates that the modes have a fundamental standing structure in z, with Cluster 3 above the magnetic equator and Cluster 4 below. This property is clearly seen in the top panel of Figure 3.2.6, where the simulation position of Cluster 4 is taken to be $x = 0.05$, $y = 0.6$ and $z = -0.45$ Also present in the observations is a 90° phase shift between the field-aligned and azimuthal magnetic field components at any given satellite. The second panel of Figure 3.2.6 shows the phase shift between these components at Cluster 3 and indeed matches well to the observations. Finally, *Clausen 08* observe a 180° phase shift between E_x and b_z which is reproduced from the simulation in panel 3 of Figure 3.2.6. As we have chosen to eliminate the electric field for the velocity field, the plot gives the negative azimuthal velocity which is associated with the radial electric field.

3.2.3 Discussion

Clausen 08 interpret their data as a waveguide mode coupling to two FLRs. These were identified in ground magnetometer data and correspond to a fundamental mode at $L \sim 2 - 3$, and a second harmonic at $L \sim 8 - 10$ (see *Clausen 08* Figure 10 for variation of fundamental frequency with L shell). Note that Cluster (at $L = 5$) is not expected to observe either of the FLRs. Indeed, we suggest that the Cluster observations provide a rather clean observation of a resonantly excited waveguide mode. There are several respects in which the satellite data does not fit well with an Alfvén wave interpretation. The strong b_z component in the observations, of similar amplitude to the b_y perturbation, is not usually associated with an Alfvén wave. If a fast mode was driving an Alfvén resonance

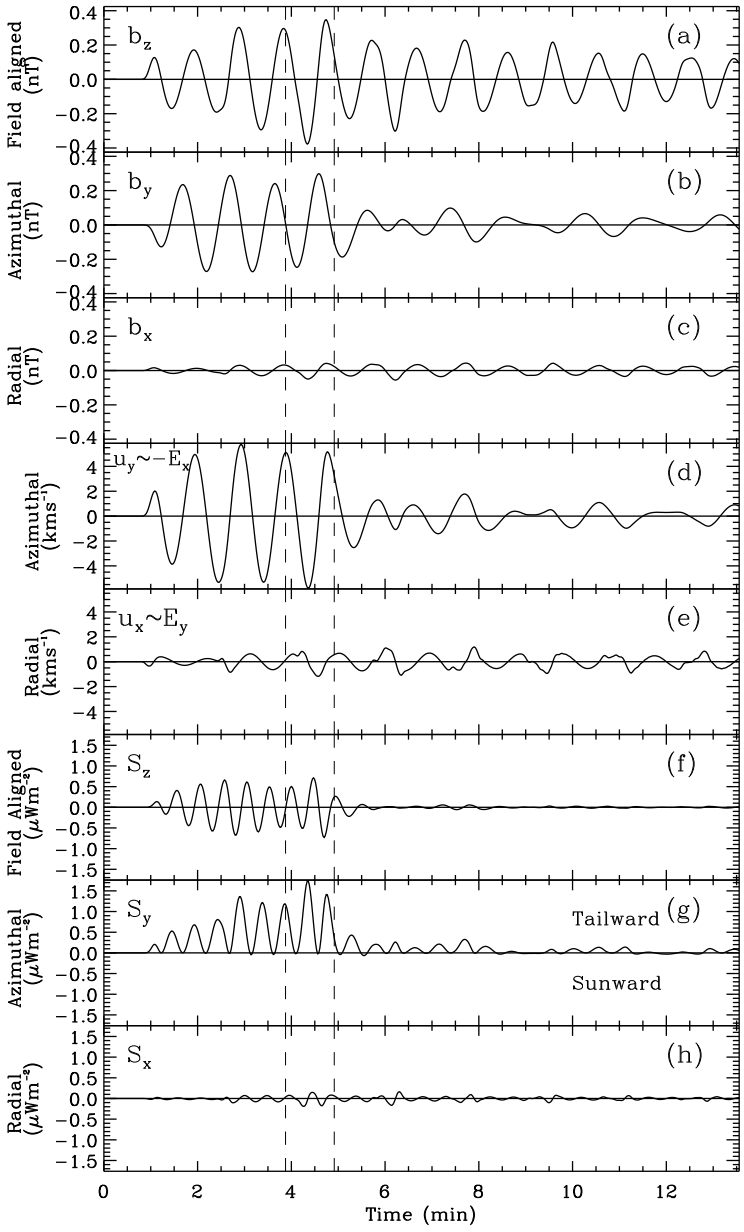

Figure 3.2.5: Components of the magnetic field (panels (a)-(c)), velocity field (panels (d) and (e)) and the Poynting vector (panels (f)-(h)) at $x = 0.05$, $y = 0.6$ and $z = 0.45$, modelling the position of Cluster 3 from *Clausen 08*. The first vertical dashed line at $t = 3.88$ minutes is the time when the driver is switched off and the second at $t = 4.92$ minutes, includes the radial travel time.

one would expect to see persistent signals in b_y and E_x post driving until damped through ionospheric dissipation. Here however, these components are very closely correlated with b_z. Furthermore, the expected resonance position can be estimated in the simulation

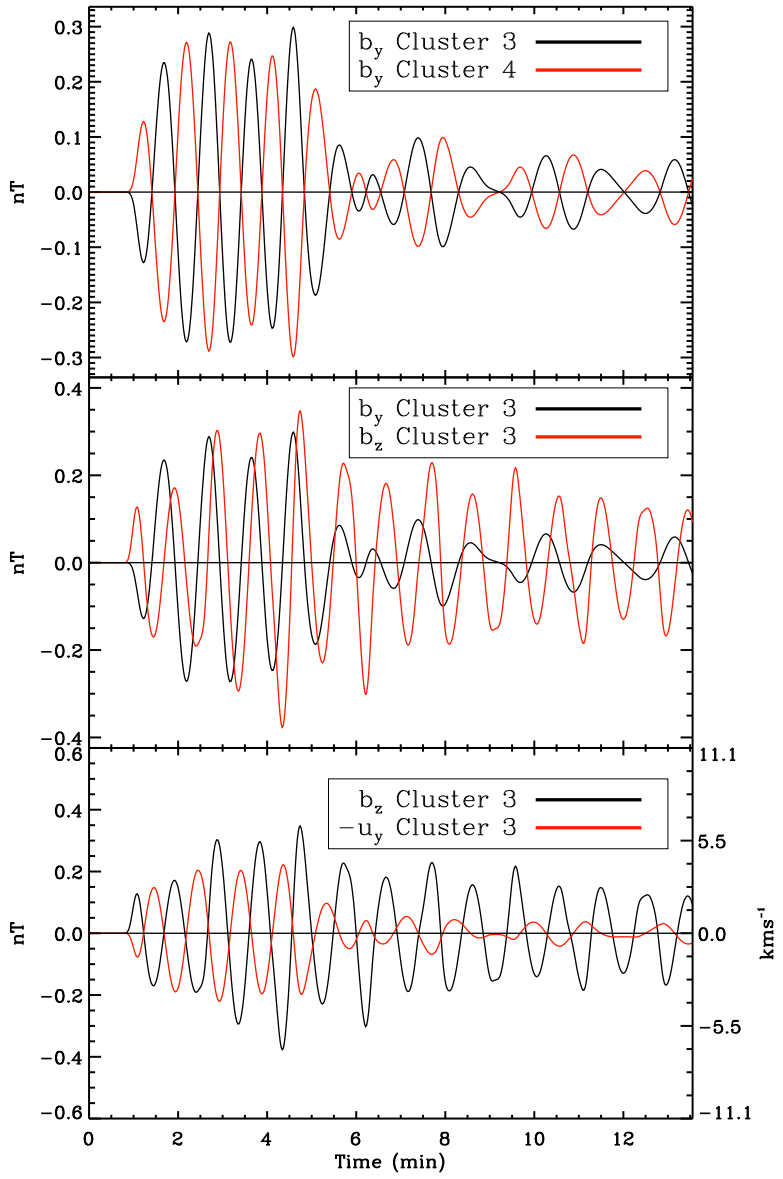

Figure 3.2.6: Simulation results matching observed phase shifts. Top: b_y from Cluster 3 (black) with b_y from Cluster 4 (red); middle: b_y from Cluster 3 (black) with b_z from Cluster 3 (red); bottom: b_z from Cluster 3 (black) with $-u_y$ (E_x) from Cluster 3 (red).

assuming a driving frequency similar to the $k_y \sim 0$ modes is responsible for the driving. As in Figure 4 from *Wright and Rickard* [1995b], we can plot the resonance position as a function of the density parameter x_0. For the given density structure the resonance position does not exist within the domain, suggesting that at no point does the Alfvén frequency at Cluster match the fast mode driving frequency. This conclusion can also

be drawn from Figure 10 of *Clausen 08*, where the fundamental field line frequency is plotted against radial distance. The driving frequency of 17.2 mHz does not lie within the magnetospheric portion of the plot (it is inside the plasmasphere), suggesting that this frequency will not match any field line fundamental frequency within the waveguide domain. (See the earlier comments regarding FLR locations deduced from magnetometer data.)

The simulation provides very similar results to the Cluster observations in terms of a fast waveguide mode. The main factor responsible for the form of the signal is the satellite position relative to the driving region. The purely tailward azimuthal Poynting vector signal can be explained by being tailward of the driving region. Fast mode energy enters the waveguide and the larger k_y modes will propagate downtail, while the small k_y modes will remain close to the $y = 0$ boundary. Other simulations (not shown here) demonstrate that if the satellite sits within the azimuthal extent of the driver, signals travelling sunward (negative S_y) and tailward (positive S_y) can be detected, since a fast mode source element creates a disturbance which propagates in all directions. Being further downtail than the driven region however, only signals travelling downstream can be recorded. We believe this to be the simple explanation of the azimuthal Poynting vector signature: a downstream observation of a fast mode source.

The observed phase shifts can be explained in terms of a simple analytic solution considering a Cartesian geometry with propagation in y and a standing mode in x and z for a uniform density as an illustration. This yields the components

$$u_y \sim \cos(\omega t - k_y y)\cos(k_x x)\cos(k_z z), \tag{3.2.11}$$

$$b_y \sim \sin(\omega t - k_y y)\cos(k_x x)\sin(k_z z), \tag{3.2.12}$$

$$b_z \sim \cos(\omega t - k_y y)\cos(k_x x)\cos(k_z z). \tag{3.2.13}$$

It is clear that the phase shifts depicted in Figure 3.2.6 match those from the above components. The 180° phase shift between E_x and b_z at Cluster 3 or as in our model u_y and b_z being in phase, determines the unidirectionality of the azimuthal Poynting vector. Hence a Poynting vector signature of this type will always coincide with this phase shift. The 90° phase shift between b_z and b_y again at Cluster 3 is also another signature of propagation in the y direction.

3.3 THEMIS Modelling

3.3.1 Tailoring the Model

We now adjust our model to match the situation appropriate to the THEMIS data reported in Figure 3.1.2. We take a waveguide of width 10 R_E spanning from $L \sim 7$ to $L \sim 17$, modelling from the plasmapause to the magnetopause. Using the values quoted for the Alfvén speed at $L \sim 8$ from *Hartinger 12*, we take the Alfvén speed at the plasmapause to be $V_A(0) = 1200$ km s^{-1}. This value together with the normalising length scale of 10 R_E (the width of the waveguide) defines a timescale for the model of $T_0 = 53.1$ s. With these values, the dimensional frequency of 6.5 mHz for the global mode can be converted into a dimensionless angular frequency of $\omega = 2.1683$. As discussed in Section 2.9 of Chapter 2 we drive the system with the b_z perturbation, assuming a quarter wavelength mode as the first harmonic in the radial direction. *Hartinger 12* had difficulty resolving the radial structure in agreement with the observed frequencies. We choose to treat the observed frequency as a second radial harmonic which gives a realistic fundamental natural waveguide frequency value. A fundamental mode structure is assumed in the z direction, taking $k_z = \pi/2$. The values of x_0 and x_c, parameters determining the density profile given in equation (2.7.1), are 1.098 and 0.8 respectively.

We model the THD observations such that a comparison can be made to the component plots of Figure 3.1.2. THD, along with the other satellites within the magnetosphere, is assumed to be in approximate radial alignment with the center of the energy source region on the driven magnetopause. Hence we are assuming that the magnetopause is driven on the flanks in this event, rather than at the subsolar point as in the Cluster event. The reasons for this assumption are apparent from the simulation results and will be discussed in section 3.3.3. Hence the satellite is placed in the simulation domain close to the $y = 0$ boundary, within the azimuthal extent of the driving region, at $y = 1$ R_E. Note that $y = 0$ in this event corresponds to a MLT of 6 hours. The x position is taken to be $x = 2$ R_E, modelling the location of THD approximately 2 R_E outside of the plasmapause. The location in z near to the magnetic equator is chosen as $z = 1$ R_E.

3.3.2 Results

To simulate the observed signal, rather than driving with a broadband signal and filtering the data for the 6.5 mHz signal, the system is driven directly with the global mode frequency. We choose to drive with 5 cycles of b_z, in order to match the observed growth phase of b_z in Figure 3.1.2. The magnetopause boundary is driven over an extent of 5 R_E (0.5 in dimensionless units). The temporal and spatial variation of the driver are shown in Figures 3.3.1 and 3.3.2.

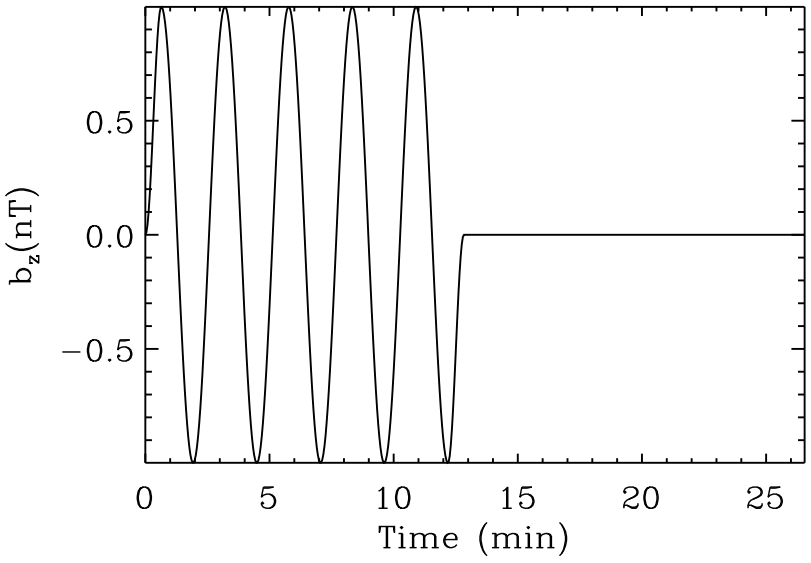

Figure 3.3.1: Temporal variation of b_z on driven boundary at $x = 10$ R_E, $y = 0$ (magnetopause).

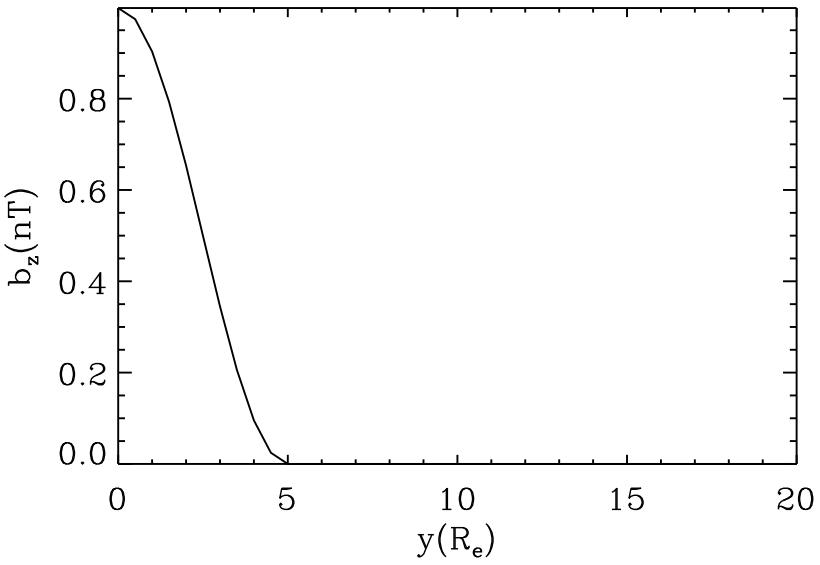

Figure 3.3.2: Spatial variation of b_z on driven boundary at $x = 10$ R_E.

The components of the magnetic field, velocity field and Poynting vector from the simulation at a satellite with position $x = 2$ R_E, $y = 1$ R_E and $z = 1$ R_E modelling the location of THD are displayed in Figure 3.3.3. The first vertical dashed line demarcates the time when the driver is switched off, at $t = 12.82$ minutes, with the second adding on the radial travel time of ~ 2.03 minutes. This second line matches well to the amplitude decrease of the components. The small amplitudes of b_y and b_x in panels (b) and (c) can be attributed

to the close proximity to the magnetic equator, where these components have nodes. The field-aligned magnetic signature in panel (a) dominates with increasing amplitude over the driving period, changing to a decaying amplitude signal post driving. The persistence of a coherent monochromatic signal once the driver has been switched off is due to the system being driven at the second radial harmonic frequency. This precludes the appearance of other frequency modes in the data and therefore post driving, the waveguide reverberates with this natural frequency. Overall, the magnetic field component results from the numerical model compare favourably to the components shown in panels 3 and 5 from Figure 3.1.2. For the velocity field, panel (e) shows a strong radial component corresponding to the negative of the azimuthal electric field (E_y in panel 2 of Figure 3.1.2). The signal is similar in structure to the field-aligned magnetic field, with increasing amplitude during driving leading to a gently decaying oscillation post driving. The azimuthal component in panel (d) is small in good agreement with the radial electric field (E_x) from the real data. Finally for the Poynting vector components, the nodes of b_x and b_y at the magnetic equator translate to a node of S_z, resulting in a negligible field-aligned component shown in panel (f). Panel (g) gives the azimuthal Poynting vector, which is small in amplitude and marginally tailward (positive) during the driving period. Post driving, the signal decays rapidly. The radial Poynting vector given in panel (h) is almost entirely inward until the driver is switched off, at which point the signal recovers to a back and forth flow of energy.

A phase shift of 90° between b_z and E_y is expected for a radially standing global mode [Waters et al., 2002]. Figure 3.3.4 shows the time signals of b_z and u_x (E_y) at the position of THD, with the vertical dashed line marking the radial travel time added to the driver switch off time. Up until this point (during driving), b_z and u_x have a phase difference between 90° and 180°. Post driving, a very clear change in the phase occurs, with the signals being almost exactly 90° out of phase.

3.3.3 Discussion

As with the previous study of *Clausen 08* we show that the observational results of *Hartinger 12* can be reproduced accurately by our numerical simulation. The key to a good match is identifying an appropriate satellite location. The small azimuthal Poynting vector signal, in contrast to the *Clausen 08* study, tells us that THD must have an azimuthal location that is close to the middle of the driven section of the magnetopause. This is a means of inferring the source location in reference to the satellite position i.e. the centre of the energy source lies approximately on the same flank meridian as THD.

The observed signal from *Hartinger 12* is believed to be a global mode, standing in the radial direction. The overall inward S_x shown in panel 6 Figure 3.1.2 suggests that energy is lost either downtail or through the inner boundary at the plasmapause during the

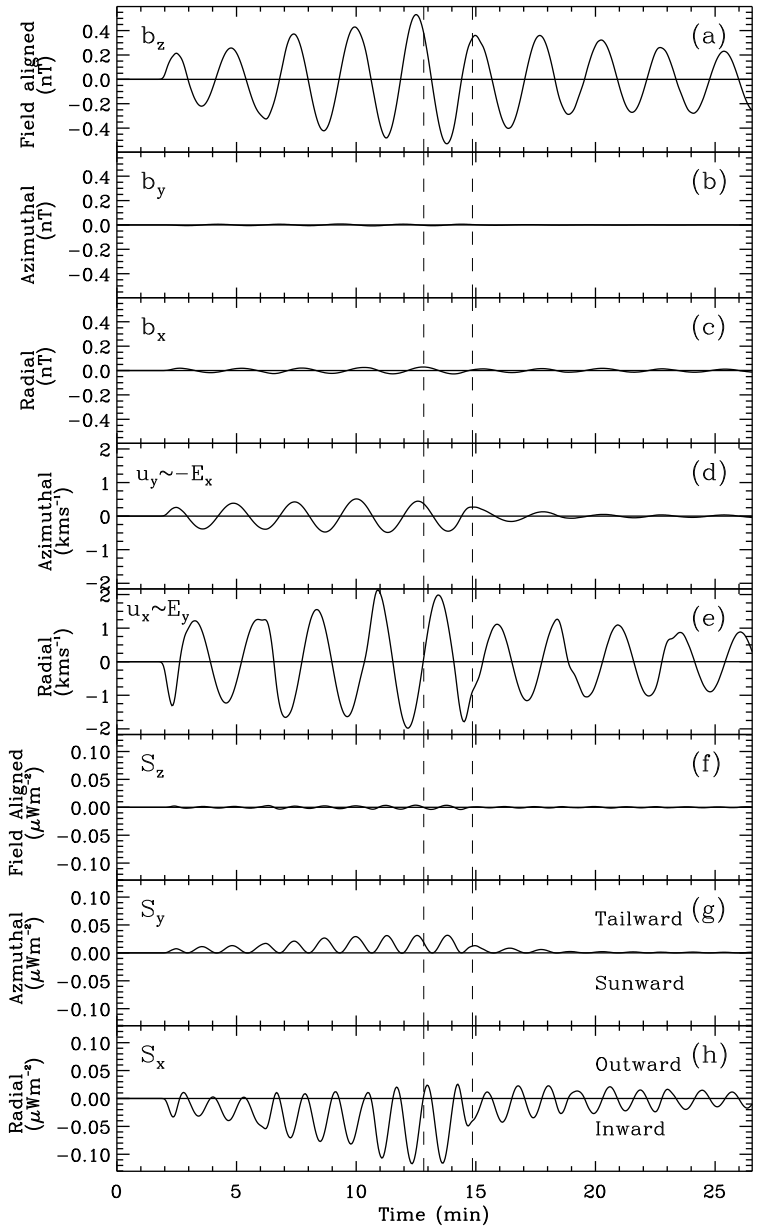

Figure 3.3.3: Components of the magnetic field (panels (a)-(c)), velocity field (panels (d) and (e)) and the Poynting vector (panels (f)-(h)) at $x = 2$ R_E, $y = 1$ R_E and $z = 1$ R_E, modelling the position of THD from *Hartinger 12*. The vertical dashed lines mark firstly the time where the driver is turned off, at $t = 12.82$ minutes and secondly the radial travel time of $t = 2.03$ minutes added to the driver switch off time.

driving phase. The azimuthal Poynting vector signal is small in comparison to the radial component and would at first sight suggest that the energy does not leak out down the tail. The same structure is seen in the simulation however, with a slightly more inward

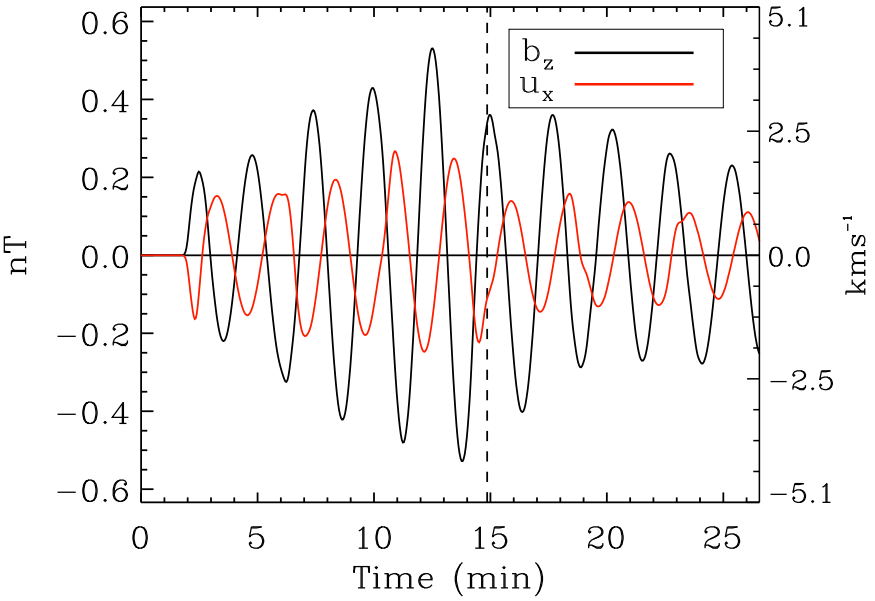

Figure 3.3.4: Phase comparison of b_z and u_x at $x = 2$ R_E, $y = 1$ R_E and $z = 1$ R_E. The dotted line indicates the time when the driver is switched off with the addition of the radial travel time, giving $t = 14.85$ minutes.

radial Poynting vector, yet the simulation allows for no energy to leak out of the inner boundary (which is treated as perfectly reflecting) or to be coupled to a FLR earthward of the spacecraft. This can be confirmed by considering the energy continuity equation

$$\frac{\partial W}{\partial t} + \nabla \cdot \mathbf{S} = 0,$$

where W represents the energy density. Consider a small area in the computational domain, from 0 to a in y and from 0 to b in x. Integrating in space over this area yields

$$\frac{\mathrm{d}}{\mathrm{dt}} \int_0^a \int_0^b W dx dy + \int_0^a S_x dy + \int_0^b S_y dx = 0.$$

Performing the above calculation for the duration of the run for the THEMIS simulation with $a = 0.1$ and $b = 0.2$ (given in dimensionless units matching the y and x locations of THD), we find that the first term accounts for $\sim 1\%$ of the sum. This results in the inward flow of energy being balanced by the flow of energy downtail, despite a cursory inspection of the data suggesting the net inward flow of energy may be balanced by the increasing wave amplitude during driving. This confirms that a net inward S_x can result without the need for a leaky inner boundary or energy loss to a FLR.

The phase comparison between b_z and u_x shown in Figure 3.3.4 highlights the difference

between the driving and post driving phases. During the driving phase, there is an overall inward propagation of energy as evident from the shape of the radial Poynting vector S_x [Chi and Russell, 1998], and hence the phases do not adhere to the radial standing mode phase regime of b_z and u_x being 90° out of phase, but instead are phase shifted by between 90° and 180°. Post driving the phase shift changes to 90° and S_x returns to an equally inward and outward signal. To try to better understand the relation between the inward radial Poynting vector signal S_x and the observed phase shifts, we consider the simplest means of describing the signals in Figure 3.3.4: two sinusoidal curves with a phase shift, expressed as

$$\begin{aligned} \frac{u_x}{u_0} &= \sin(\omega t), \\ \frac{b_z}{b_0} &= \sin(\omega t + \phi), \end{aligned}$$

where ϕ is the phase by which b_z leads u_x. Constructing S_x yields

$$\begin{aligned} S_x &= u_x b_z, \\ \frac{S_x}{u_0 b_0} &= \frac{1}{2}\cos\phi + \frac{1}{2}\left(\sin\phi\sin(2\omega t) - \cos\phi\cos(2\omega t)\right). \end{aligned}$$

The second term on the right hand side can be expressed as a single sinusoid which gives

$$\frac{S_x}{u_0 b_0} = \frac{1}{2}\cos\phi + \frac{1}{2}\cos(2\omega t + \phi_1),$$

where ϕ_1 is the new phase dependent on ϕ. Chi and Russell [1998] give plots of S_x for the two limits $\phi = 0$ (propagating) and $\phi = \pi/2$ (standing). The above equation is valid for intermediate cases too. For a net inward energy flow, $90° < \phi < 270°$. The quantity important for linking the shape of the radial Poynting vector S_x to the phase shift is the ratio of positive to negative S_x signal. This is defined as the absolute value of the maximum outward S_x to the maximum inward S_x:

$$\Delta_s = \left|\frac{\cos\phi + 1}{\cos\phi - 1}\right|.$$

Figure 3.3.5 displays how this ratio Δ_s varies with the phase shift ϕ. It is clear that there is

a unique relationship between these quantities, such that a specific phase shift determines the value of Δ_s. A ratio of 1.0 corresponds to b_z and u_x being 90° (or 270°) out of phase, which is in keeping with the idea of a standing radial mode with equal inward and outward propagation. A ratio of 0 implies a phase shift of 180°, consistent with a purely inward radial Poynting vector . The dashed lines represent the observed phase shifts and ratios from the observation (labelled 'THD') and the simulation (labelled 'Sim'). For the observation, these can be obtained from Figure 3.1.2, with panel 4 showing a phase shift of 120° during driving, with a ratio estimated from panel 6 of $\frac{1}{3}$. This is consistent with the predicted values in Figure 3.3.5. For the simulation, the ratio and phase shift during driving have been estimated at 0.14 and 140° respectively, using Figures 3.3.3 and 3.3.4. As before, the relationship between ϕ and Δ_s approximates the simulation results well.

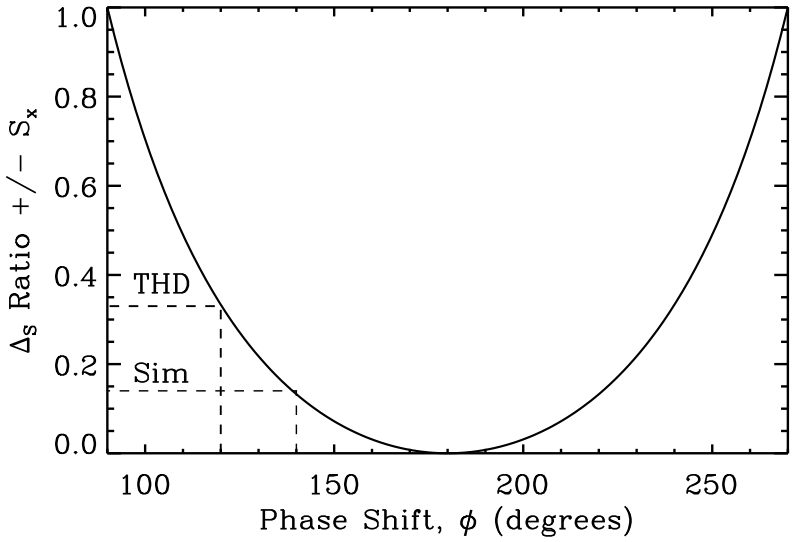

Figure 3.3.5: The absolute value of the ratio of maximum inward to maximum outward radial Poynting vector Δ_s, against the phase ϕ, by which b_z leads u_x. The dashed lines represent the observed phase shifts and ratios from THD and the simulation, labelled 'THD' and 'Sim' respectively.

With an extremely simplified approach, we have determined the relationship between the radial Poynting vector and the phase shift between u_x and b_z. This proves that either can be used as a definitive measure of the end of the driving period: either through a change in the ratio of inward to outward signal of S_x i.e. returning to a standing mode, or through the phase shift returning to 90°. This idea can be extended to considering a more physical model of an inward propagating wave with a smaller amplitude reflected wave, expressed as (in normalized units)

$$\begin{aligned} u_x = &\cos(\omega t + k_x x - k_y y)\cos(k_z z) \\ &+ R\cos(\omega t - k_x x - k_y y)\cos(k_z z), \end{aligned} \tag{3.3.1}$$

for $-1 < R < 1$, where R is the amplitude of the reflected wave, ω the frequency and k_x, k_y and k_z the wavenumbers in the x, y and z directions respectively. Using equations (2.2.23) and (2.2.26) with the z dependence stated explicitly, we can calculate b_z given as

$$\begin{aligned} b_z = &- A\cos(\omega t + k_x x - k_y y)\cos(k_z z) \\ &+ AR\cos(\omega t - k_x x - k_y y)\cos(k_z z), \end{aligned} \tag{3.3.2}$$

where

$$A = \frac{\rho_0 \omega}{k_x} - \frac{k_z^2}{\omega k_x}.$$

and $\omega^2 = V_A^2\left(k_x^2 + k_y^2 + k_z^2\right)$. For the location of THD, we assume $k_y \approx 0$ by the close proximity to the symmetry line of the driver, and $z = 0$ by the small magnetic latitude ($\sim 3°$). With this equations (3.3.1) and (3.3.2) become

$$u_x = \cos(\omega t + k_x x) + R\cos(\omega t - k_x x), \tag{3.3.3}$$

$$b_z = -A'\cos(\omega t + k_x x) + A'R\cos(\omega t - k_x x), \tag{3.3.4}$$

where $A' = k_x/\omega$. To determine the phase shift between these components, we express them as

$$\begin{aligned} u_x &= G\cos(\omega t + \psi), \\ b_z &= G'\cos(\omega t + \psi'), \end{aligned}$$

with

$$
\begin{aligned}
G &= \sqrt{1 + R^2 + 2R\cos(2k_x x)}, \\
G' &= -A'\sqrt{1 + R^2 - 2R\cos(2k_x x)}, \\
\psi &= \tan^{-1}\left(\frac{1-R}{1+R}\tan(k_x x)\right), \\
\psi' &= \tan^{-1}\left(\frac{1+R}{1-R}\tan(k_x x)\right).
\end{aligned}
$$

Hence u_x and b_z can be written as

$$
\begin{aligned}
u_x &= G\cos\left(\omega t + \tan^{-1}(\alpha\tan(k_x x))\right), \\
b_z &= -G'\cos\left(\omega t + \pi + \tan^{-1}\left(\frac{1}{\alpha}\tan(k_x x)\right)\right),
\end{aligned}
$$

where $\alpha = (1-R)/(1+R)$ and $-G'$ is positive. The phase is dependent on R, k_x and the position in x. In order to calculate the phase difference ϕ between the components, we consider b_z to be leading, such that the difference is given by

$$
\begin{aligned}
\phi &= \pi + \tan^{-1}\left(\frac{1}{\alpha}\tan(k_x x)\right) - \tan^{-1}(\alpha\tan(k_x x)) \\
&= \pi + \tan^{-1}\left(\frac{2R}{1-R^2}\sin(2k_x x)\right). \qquad (3.3.5)
\end{aligned}
$$

As in the simplified approach above, we calculate the ratio of inward to outward S_x. We firstly calculate S_x using equations (3.3.3) and (3.3.4) as

$$
\begin{aligned}
S_x &= u_x b_z, \\
&= -A'\cos^2(\omega t + k_x x) + R^2 A'\cos^2(\omega t - k_x x).
\end{aligned}
$$

As previously, we seek to express S_x as a single sinusoidal function, which yields

$$
S_x = \gamma + C\sin(2\omega t + \delta),
$$

where

$$\begin{aligned}\gamma &= R^2 - 1, \\ C &= \sqrt{R^4 + 1 - 2R^2\cos(4k_x x)}, \\ \delta &= \tan^{-1}\left(\frac{R^2 - 1}{\tan(2k_x x)(R^2+1)}\right),\end{aligned} \tag{3.3.6}$$

and a constant factor of $A'/2$ has been removed which will not affect further analysis. Hence the ratio of positive to negative signal Δ_s can be expressed as the maximum outward to the maximum inward Poynting vector as

$$\Delta_s = \left|\frac{R^2 - 1 + \sqrt{R^4 + 1 - 2R^2\cos(4k_x x)}}{R^2 - 1 - \sqrt{R^4 + 1 - 2R^2\cos(4k_x x)}}\right|, \tag{3.3.7}$$

given that the maximum and minimum of S_x will occur where $\sin(2\omega t + \delta) = \pm 1$.

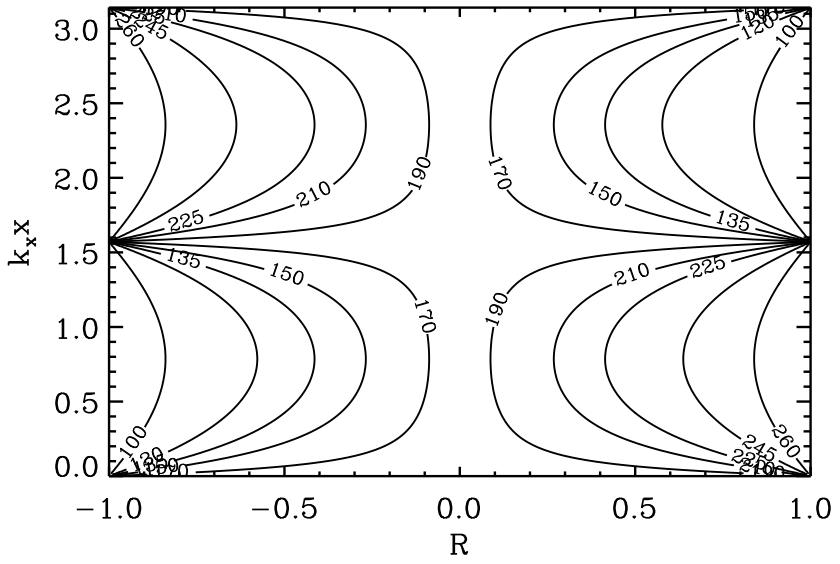

Figure 3.3.6: Contour plot of $\phi(k_x x, R)$, the phase by which b_z leads u_x, with labelled contours in degrees.

The functions ϕ and Δ_s contain the necessary information to link the phase by which b_z leads u_x and the radial Poynting vector ratio. Figure 3.3.6 shows a contour plot of ϕ in R-$k_x x$ space, where the value of the reflection coefficient R is defined over $[-1, 1]$, while $k_x x$ is defined over $[0, \pi]$. This ensures that all possible solutions are considered since ϕ is periodic over π by virtue of the $\sin(2k_x x)$ term appearing in (3.3.5). The contours are labelled in degrees which highlights the symmetry for phase shifts between $90° \rightarrow 180°$

and $180^\circ \rightarrow 270^\circ$. These contours allow the values of $k_x x$ and the reflection coefficient to be constrained. For example, considering a phase shift of 120° implies $0.6 < |R| < 1$ which reveals information about the strength of the reflection of the mode. The contours of Δ_s have been omitted since $\phi(k_x x, R)$ and $\Delta_s(k_x x, R)$ actually have the same contours in R-$k_x x$ space, despite being on first appearance two completely separate functions (see (3.3.5) and (3.3.7)). It can be proven whether these contours are in fact the same by considering the gradients of each function. If the gradients are parallel, this implies that the functions share the same contours and hence one can be expressed as a function of the other. In order to show that the gradients are parallel we require

$$\begin{aligned} \nabla\phi \times \nabla\Delta_s &= 0, \\ \Rightarrow \frac{\partial\phi}{\partial R}\frac{\partial\Delta_s}{\partial(k_x x)} - \frac{\partial\phi}{\partial(k_x x)}\frac{\partial\Delta_s}{\partial R} &= 0. \end{aligned} \tag{3.3.8}$$

After some algebra, equation (3.3.8) can indeed be shown to be satisfied and hence $\phi = \phi(\Delta_s)$. This implies that each phase shift ϕ corresponds to a precise ratio of outward to inward radial Poynting vector Δ_s. This is the same conclusion that was determined by the simple analysis of two phase shifted sine waves. In plotting Δ_s as a function of ϕ for a fixed $k_x x$ we produce exactly the same plot as in Figure 3.3.5. It is, perhaps, surprising that such a plot does not depend upon the choice of $k_x x$. This implies that the relationship between ϕ and Δ_s is independent of nodal structure and position. The more rigorous analysis provided here with the addition of a reflected component, provides a better comparison to a more physical situation, but yields the same relationship between the phase shift and the radial Poynting vector as the simple case.

We have shown that the phase shift between u_x (E_y) and b_z is inextricably linked with the overall shape of the radial Poynting vector. The ratio between the positive and negative S_x signal determines on a continuous scale the phase by which b_z leads u_x, which ranges from 90° (or 270°) for equally inward and outward, to 180° for purely inward propagation. Figure 3.3.5 can be used to determine the validity of an observation as a global mode i.e. if the observed phase shift and ratio of positive to negative radial Poynting vector are a valid pairing. The above analysis also confirms that the change in S_x from the driven to post driven phases correlates directly with the change in the phase shift. Hence, both the S_x signal and the phase shift can be used to clearly infer the end of the driving phase. For example in the THD data in Figure 3.1.2, we can estimate that the driving stops at $\sim$06:46 UT, where the phase changes to $\sim 90^\circ$ (panel 4) and the radial Poynting vector recovers to an equally inward and outward signal (panel 6).

3.4 Summary of Modelling and Further Discussion

The two simulations performed are very similar. In both cases, fast mode waves enter the domain through a disturbance in the compressional magnetic field component b_z. Most of the energy propagates firstly within the azimuthal extent of the driven region shown through S_x, with some energy leaking tailward through S_y. There is no resonance within the domain for either equilibrium as these points would exist beyond the inner boundary. Driving at the second radial harmonic eigenfrequency in each case precludes the appearance of other frequency modes allowing the clear detection of the natural waveguide mode post driving in the compressional components. As mentioned separately in each of the discussion sections, the main influence on signal structure is the satellite location. Here we have investigated two very different signals, that can be explained almost fully by the same simulation just by the positioning of the satellites.

To demonstrate this further, Figure 3.4.1 displays the radial and azimuthal Poynting vector components (S_x and S_y respectively) plotted against time for four satellite locations in our model waveguide using the parameters from the Cluster simulation. The locations are shown as points A-D in the top panel of the figure, the coordinates of which are: A($x = 2$, $y = 1$), B($x = 6$, $y = 2$), C($x = 3$, $y = 8$) and D($x = 6$, $y = 12$), with $z = 4.5$ for all points (all lengths in R_E). The driver is the same as in the Cluster simulation given in Figures 3.2.3 and 3.2.4. In each of the plots, S_x is represented by the black line and S_y by the red line. The driven portion of the $x = 10$ R_E boundary extends to $y = 5$ R_E, as shown by the vertical dashed line in the top panel. The vertical dashed line in the bottom four panels demarcates the time when the driver is switched off at $t = 3.88$ minutes. Position A corresponds to the location of the THEMIS satellite THD, and despite using the parameters for the Cluster simulation, the predominant features are the same: an inward radial Poynting vector during driving levelling out to an equally inward and outward signal post driving with a small positive azimuthal Poynting vector during the driven period. The fact that the signals match purely by positioning the satellite at the same point in the guide, shows the importance of the satellite location. Positions B-D show an interesting trend with satellite location. Consider first the radial Poynting vector S_x. During driving the signal changes from dominantly inward (negative) at B, to equally back and forth at C, to mostly outward (positive) at D. We believe this progression can be best explained by ray trajectories, as shown in Figure 3.4.2. The trajectory depends upon the wavenumbers in the $\hat{\mathbf{x}}$ and $\hat{\mathbf{y}}$ directions, namely k_x and k_y. The driven extent in y suggests a broad range of k_y modes will be excited, with amplitudes peaked at $k_y = 0$, and falling off at $k_y = 10$ (see Rickard and Wright [1994]). Most of the energy is confined around the $k_y = 0$ modes and does not propagate to the locations C and D in Figure 3.4.1 during the simulation time. For the larger k_y modes however, some energy propagates tailward and can have a turning point within the domain depending on k_y. We believe this to be

responsible for the differing S_x signals. It is interesting to note that an outward radial Poynting vector signal can result at a location reasonably far down the magnetospheric flank purely from an upstream source during the driving phase e.g. satellite D. The box outlined in the upper left corner of Figure 3.4.2 is purely to illustrate the directional flow of energy within the driving region close to the inner boundary as discussed in section 3.3.3. We see there is energy flow radially inward and outward, with more rays entering radially. This is balanced by one ray exiting the azimuthal boundary.

The azimuthal Poynting vector also changes markedly with the movement of the satellites further tailward. At B, within the driven region, S_y is small compared to S_x, and is at times sunward (negative). This occurs due to the position within the driving region, where waves can emanate from the furthest azimuthal extent of this region ($y = 5$ R_E) and travel sunward. At location C, S_y is more pronounced and purely tailward. This is a feature of the Cluster data caused by the movement of the satellite further downtail. Finally at D, the signal is again purely tailward by nature of the further downtail position. Considering post driving, there is a clear tendency for S_x to indicate a radial standing structure. Outside the driving region there is tailward propagation, whilst inside dispersion leaves only small k_y modes.

3.5 Chapter Summary

In this chapter, we have modelled two ULF wave observations from the Cluster (*Clausen 08*) and THEMIS (*Hartinger 12*) satellites using a simple numerical waveguide model. We have implemented the new boundary condition at the driven magnetopause outlined in Chapter 1, that acts as a pressure driver. The simulation results match favourably to the aforementioned observations and many interesting features may be discerned from the results.

1. The satellite position is of paramount importance in determining the structure of the signal observed. A location tailward of the disturbed region of the magnetopause will result in a purely tailward azimuthal Poynting vector, which explains the stand out feature of the Cluster data. The location of the source region relative to the spacecraft can also be inferred from the Poynting vector components.

2. An overall inward radial Poynting vector signal does not necessarily require coupling to a FLR or a leaky inner boundary to explain the energy loss. For a satellite within the azimuthal extent of the driven region, the inward energy flow may be entirely balanced by tailward propagation, not immediately apparent from a perhaps small azimuthal Poynting vector signal. When a net inward energy flow does occur, the point where the S_x signal returns to an essentially back and forth oscillation is a

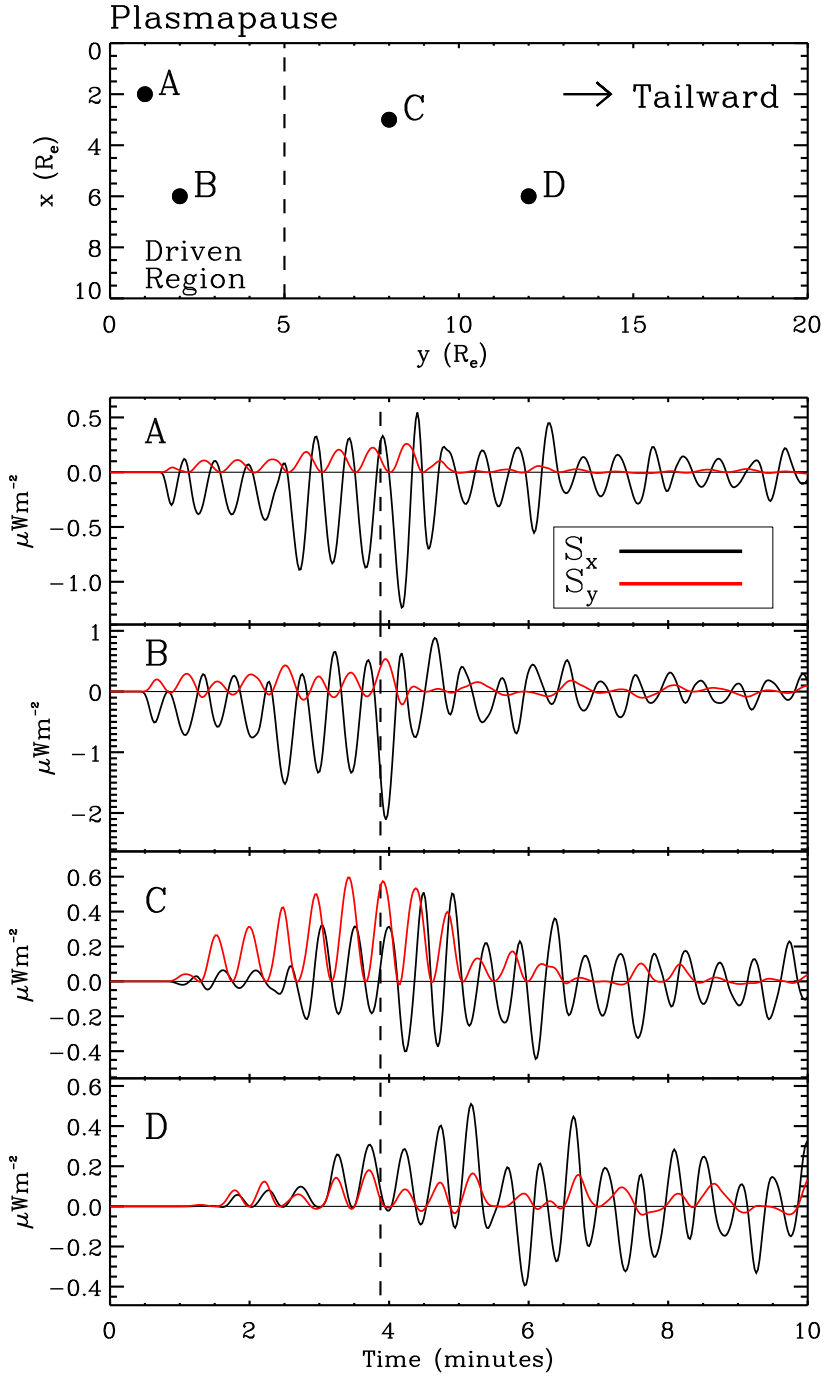

Figure 3.4.1: Top panel shows the positions of 4 satellites placed in the model waveguide with the vertical dashed line indicating the driven region. Bottom four panels display S_x (black) and S_y (red) plotted against time at the 4 satellite positions corresponding to those depicted in the top panel. The vertical dashed line represents when the driver is switched off.

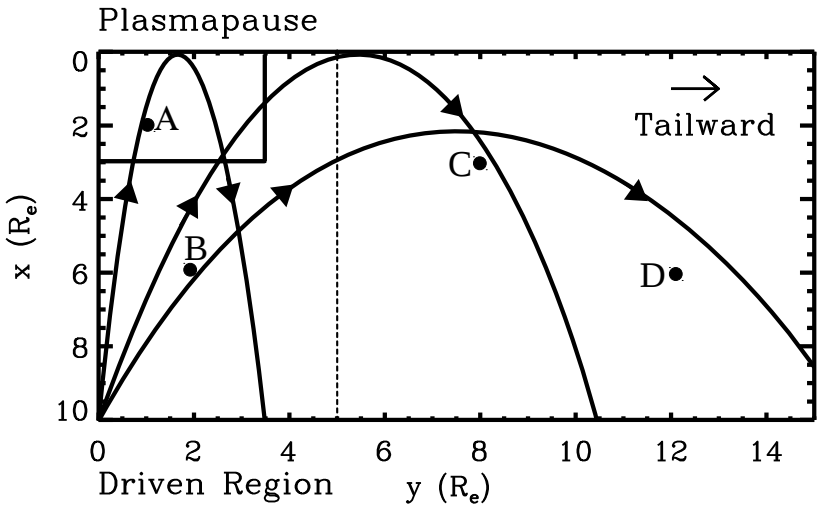

Figure 3.4.2: Waveguide schematic displaying possible ray trajectories. The vertical dashed line marks the extent of the driven region in y.

reasonable indicator of the time when the driving stops (allowing for appropriate travel time).

3. The phase difference between the radial velocity (azimuthal electric field) and the field-aligned magnetic field can be used to infer whether the mode is propagating or standing radially and hence is another indicator of the transition bewteen the driven and post driven phases.

4. We have been able to provide more plausible interpretations of the Cluster event than the original, by interpreting the signatures as fast waveguide modes rather than driven FLRs.

5. The main goal has been achieved: use simulated waveguide data to help interpret observational signatures.

Chapter 4

Deciphering ULF Waveguide Signatures in Satellite Data

In the last chapter we applied our numerical method to two satellite observations of ULF waveguide modes, which resulted in new interpretations of the data. In this chapter, we again look to extend our understanding of ULF waveguide signatures in satellite data, but through different means. It is noted that a large proportion of this work is based on the article Elsden et al. [2016], in collaboration with Dr Michael Hartinger.

We present analytical and numerical models to study ULF waveguide modes in the flank magnetosphere. Our aim is to demonstrate a procedure that can subsequently be used in conjunction with observations. Compressional waveguide modes propagate azimuthally on the flanks but have a mixed standing/propagating nature in the radial direction. We decompose these fluctuations into radially propagating inward (incident) and outward (reflected) waves, which can provide information on energy transport and absorption in the flank magnetosphere. The analysis requires signals whose amplitudes do not vary drastically over one or two periods, and that have a well defined frequency. Space based observations of such ULF waves have been reported by Rae et al. [2005], Eriksson et al. [2006], Clausen et al. [2008], Hartinger et al. [2011], Hartinger et al. [2012]. We apply our method of deriving these coefficients to simulated data, as a means of validating the procedure, with the aim of applications to real data in the future.

While methods exist for the routine identification and characterization of cavity modes in satellite observations [e.g. Waters et al., 2002], there are no comparable techniques for waveguide modes. This adds uncertainty to waveguide/global mode observational studies. For example, in a statistical study estimating global mode occurrence rates outside the plasmasphere, Hartinger et al. [2013] identified potential global modes using cavity mode selection criteria: globally coherent, monochromatic fast mode waves with electric/magnetic perturbations consistent with radially standing waves. As discussed by Hartinger

et al. [2013], these criteria excluded tailward propagating waveguide modes, likely biasing noon occurrence rates higher than flank rates and leading to an unrealistically low overall global mode occurrence rate.

The chapter is laid out as follows: Section 4.1 outlines the equations for the problem, then discusses the steps to follow to perform the analytic method used for deriving the incident and reflection coefficients. In Section 4.2 we apply the method to synthetic data from two waveguide simulations as a means of testing. Section 4.3 discusses the use of hodograms as a tool for interpreting satellite data and outlines how they can be used when applying our analytical model to data. A chapter summary is given in Section 4.4.

4.1 Analytic Model

4.1.1 Tailward Travelling Wave Model

The hydromagnetic box model is employed here as outlined in Chapter 2, with the governing equations given by (2.2.23)-(2.2.27). To make progress analytically, we assume the lowest order WKB estimate to equations (2.2.23)-(2.2.27). This assumption is common to many analytical models of the magnetosphere and is discussed in detail in, for example, Inhester [1987] and Wright [1994]. This gives the radial wavenumber k_x as

$$k_x^2(x) = \frac{\omega^2}{V_A^2(x)} - k_y^2 - k_z^2, \tag{4.1.1}$$

with the phase in x defined as

$$\Phi_x(x) = \int^x k_x(x')dx'. \tag{4.1.2}$$

As mentioned previously, the goal is to understand the dynamics of tailward travelling waves that exhibit a mixed propagating and standing nature radially. In this regard consider a wave of the form

$$\begin{aligned} b_x &= A_i \cos\left(k_y y - \Phi_x - \omega t\right) \sin(k_z z) + \\ &\quad A_r \cos\left(k_y y + \Phi_x - \omega t\right) \sin(k_z z). \end{aligned} \tag{4.1.3}$$

A_i denotes the incident coefficient, A_r the reflected, both with units of Tesla. This stems

from inward propagation being in the negative $\hat{\mathbf{x}}$ direction. k_x, k_y and k_z are the wavenumbers; x, y and z the positions in the $\hat{\mathbf{x}}$, $\hat{\mathbf{y}}$ and $\hat{\mathbf{z}}$ directions respectively. We choose to define the b_x component purely as a start point from which to derive the other component forms. Using equations (2.2.23)-(2.2.27) yields

$$\begin{aligned}
b_y &= -A_i \frac{k_y}{k_x} \cos\left(k_y y - \Phi_x - \omega t\right) \sin(k_z z) \\
&\quad + A_r \frac{k_y}{k_x} \cos\left(k_y y + \Phi_x - \omega t\right) \sin(k_z z). \qquad (4.1.4) \\
b_z &= -\frac{A_i k_z}{k_x} \left\{1 - \frac{\omega^2}{V_A^2 k_z^2}\right\} \sin\left(k_y y - \Phi_x - \omega t\right) \cos(k_z z) \\
&\quad + \frac{A_r k_z}{k_x} \left\{1 - \frac{\omega^2}{V_A^2 k_z^2}\right\} \sin\left(k_y y + \Phi_x - \omega t\right) \cos(k_z z). \qquad (4.1.5) \\
u_x &= -\frac{A_i}{B_0} \frac{\omega}{k_z} \sin\left(k_y y - \Phi_x - \omega t\right) \cos(k_z z) \\
&\quad - \frac{A_r}{B_0} \frac{\omega}{k_z} \sin\left(k_y y + \Phi_x - \omega t\right) \cos(k_z z). \qquad (4.1.6) \\
u_y &= \frac{A_i}{B_0} \frac{\omega k_y}{k_x k_z} \sin\left(k_y y - \Phi_x - \omega t\right) \cos(k_z z) \\
&\quad - \frac{A_r}{B_0} \frac{\omega k_y}{k_x k_z} \sin\left(k_y y + \Phi_x - \omega t\right) \cos(k_z z). \qquad (4.1.7)
\end{aligned}$$

What is the problem we are trying to solve? The question is this: can we take the quantities given in satellite data and use them to determine the unknowns in the above system (4.1.3)-(4.1.7)? These unknowns are A_i, A_r, k_x, k_y, k_z, Φ_x and $k_z z$. The position in y is not required since the model assumes the wave is propagating in the $\hat{\mathbf{y}}$ direction. Hence changing y merely shifts the phase of the entire solution and is similar to moving the time origin, but does not affect any of the quantities listed above. Not all of the quantities provided from satellite data are independent, which reduces the number of 'knowns' (this will be shown in the forthcoming derivation). These independent quantities are the amplitudes of b_x, b_y, b_z and u_x, the frequency ω, the local Alfvén speed V_A and the phase shift between b_x and b_y, denoted by ϕ. Stipulating $-\pi < \phi \leq \pi$, ϕ is positive if b_y leads b_x by less than π, and negative if b_y trails b_x by less than π. u_y is not an independent quantity as it can be expressed in terms of the amplitudes of u_x, b_x and b_y. Equally, any of these quantities could have been removed instead, in favour of u_y.

To proceed with determining the unknowns, it is useful to express the components in terms of a single amplitude and phase for the purpose of comparison to data. For example, we express b_x as

$$b_x = \bar{b_x}\cos(\psi_1 - \omega t), \tag{4.1.8}$$

where $\bar{b_x}$ is the amplitude and ψ_1 a phase shift. For ease of notation, let $\alpha = k_y y - \Phi_x$ and $\beta = k_y y + \Phi_x$. Equating both forms for b_x, namely equations (4.1.3) and (4.1.8), gives

$$\begin{aligned} b_x &= \bar{b_x}\cos(\psi_1 - \omega t) && (4.1.9)\\ &= A_i \cos(\alpha - \omega t)\sin(k_z z) + A_r \cos(\beta - \omega t)\sin(k_z z). && (4.1.10) \end{aligned}$$

Considering when $\omega t = 0, \pi/2$ yields

$$\begin{aligned} \bar{b_x}\cos\psi_1 &= (A_i \cos\alpha + A_r \cos\beta)\sin(k_z z), && (4.1.11)\\ \bar{b_x}\sin\psi_1 &= (A_i \sin\alpha + A_r \sin\beta)\sin(k_z z). && (4.1.12) \end{aligned}$$

Adding the squares of (4.1.11) and (4.1.12) and simplifying results in an expression for $\bar{b_x}$ as

$$\bar{b_x} = \pm\sqrt{A_i^2 + A_r^2 + 2A_i A_r \cos(2\Phi_x)}\sin(k_z z).$$

ψ_1 can be found by dividing (4.1.12) by (4.1.11) which gives

$$\begin{aligned} \tan\psi_1 &= \frac{A_i \sin\alpha + A_r \sin\beta}{A_i \cos\alpha + A_r \cos\beta}, && (4.1.13)\\ \Rightarrow \psi_1 &= \tan^{-1}\left\{\frac{A_i \sin\alpha + A_r \sin\beta}{A_i \cos\alpha + A_r \cos\beta}\right\}. && (4.1.14) \end{aligned}$$

In a similar manner the amplitude and phase for b_y can be determined as

$$\begin{aligned} \bar{b_y} &= \pm\frac{k_y}{k_x}\sqrt{A_i^2 + A_r^2 - 2A_i A_r \cos(2\Phi_x)}\sin(k_z z), && (4.1.15)\\ \psi_2 &= \tan^{-1}\left\{\frac{-A_i \sin\alpha + A_r \sin\beta}{-A_i \cos\alpha + A_r \cos\beta}\right\}. && (4.1.16) \end{aligned}$$

As mentioned above, the phase shift between b_x and b_y is known from observations. It is

of interest therefore to express b_x and b_y in terms of this phase shift. This can be achieved by shifting the time origin such that $\omega t - \psi_1 = \omega t'$ and hence expressing the components as

$$b_x = \bar{b_x}\cos(\omega t'), \tag{4.1.17}$$
$$b_y = \bar{b_y}\cos(\omega t' - (\psi_2 - \psi_1)). \tag{4.1.18}$$

Writing $\phi = \psi_2 - \psi_1$, ϕ represents the phase by which b_y leads b_x. ϕ can be expressed in terms of the incident and reflection coefficients using the forms for ψ_1 and ψ_2, given by (4.1.14) and (4.1.16) respectively, as

$$\psi_2 - \psi_1 = \tan^{-1}\left\{\frac{-A_i\sin\alpha + A_r\sin\beta}{-A_i\cos\alpha + A_r\cos\beta}\right\} - \tan^{-1}\left\{\frac{A_i\sin\alpha + A_r\sin\beta}{A_i\cos\alpha + A_r\cos\beta}\right\}. \tag{4.1.19}$$

This can be compressed using the inverse tangent subtraction formula given by

$$\tan^{-1}a - \tan^{-1}b = \tan^{-1}\left(\frac{a-b}{1+ab}\right). \tag{4.1.20}$$

Considering first the $a - b$ appearing on the rhs of (4.1.20), i.e. a subtraction of the two arguments in (4.1.19), we have

$$\begin{aligned} a - b &= \frac{(-A_i\sin\alpha + A_r\sin\beta)(A_i\cos\alpha + A_r\cos\beta)}{(-A_i\cos\alpha + A_r\cos\beta)(A_i\cos\alpha + A_r\cos\beta)} - \\ &\quad \frac{(A_i\sin\alpha + A_r\sin\beta)(-A_i\cos\alpha + A_r\cos\beta)}{(-A_i\cos\alpha + A_r\cos\beta)(A_i\cos\alpha + A_r\cos\beta)}, \\ &= \frac{-2A_iA_r\sin\alpha\cos\beta + 2A_iA_r\cos\alpha\sin\beta}{-A_i^2\cos^2\alpha + A_r^2\cos^2\beta}, \\ &= \frac{-2A_iA_r\sin(\alpha-\beta)}{A_r^2\cos^2\beta - A_i^2\cos^2\alpha}. \end{aligned}$$

Now forming $1 + ab$ gives

$$
\begin{aligned}
1+ab &= 1+\frac{-A_i^2\sin^2\alpha+A_r^2\sin^2\beta}{-A_i^2\cos^2\alpha+A_r^2\cos^2\beta},\\
&= \frac{A_r^2\cos^2\beta-A_i^2\cos^2\alpha-A_i^2\sin^2\alpha+A_r^2\sin^2\beta}{A_r^2\cos^2\beta-A_i^2\cos^2\alpha},\\
&= \frac{A_r^2\left(\cos^2\beta+\sin^2\beta\right)-A_i^2\left(\sin^2\alpha+\cos^2\alpha\right)}{A_r^2\cos^2\beta-A_i^2\cos^2\alpha},\\
&= \frac{A_r^2-A_i^2}{A_r^2\cos^2\beta-A_i^2\cos^2\alpha}.
\end{aligned}
$$

Putting the above two calculations together implies

$$
\begin{aligned}
\psi_2-\psi_1 &= \tan^{-1}\left(\frac{a-b}{1+ab}\right),\\
&= \tan^{-1}\left\{\frac{\left(\dfrac{-2A_iA_r\sin(\alpha-\beta)}{A_r^2\cos^2\beta-A_i^2\cos^2\alpha}\right)}{\left(\dfrac{A_r^2-A_i^2}{A_r^2\cos^2\beta-A_i^2\cos^2\alpha}\right)}\right\},\\
&= \tan^{-1}\left(\frac{-2A_iA_r\sin(\alpha-\beta)}{A_r^2-A_i^2}\right).
\end{aligned}
$$

Then using that $\alpha-\beta$ can be expressed as $-2\Phi_x$ gives

$$
\tan(\psi_2-\psi_1)\equiv\tan\phi=\frac{2A_iA_r\sin(2\Phi_x)}{A_r^2-A_i^2}. \tag{4.1.21}
$$

We can perform a similar analysis to that applied to b_x and b_y above, for each of the components, which allows the expression of the amplitudes in terms of the incident and reflection coefficients. Some of the resulting equations however are not independent of one another as previously discussed and hence are discarded. The remaining system, after some algebra, is given by

$$\bar{b_x} = \pm\sqrt{A_i^2 + A_r^2 + 2A_iA_r\cos(2\Phi_x)}\sin(k_z z), \tag{4.1.22}$$

$$\bar{b_y} = \pm\frac{k_y}{k_x}\sqrt{A_i^2 + A_r^2 - 2A_iA_r\cos(2\Phi_x)}\sin(k_z z), \tag{4.1.23}$$

$$\bar{b_z} = \pm\frac{k_z}{k_x}\left\{\frac{\omega^2}{V_A^2 k_z^2} - 1\right\}\sqrt{A_i^2 + A_r^2 - 2A_iA_r\cos(2\Phi_x)}\cos(k_z z), \tag{4.1.24}$$

$$\bar{u_x} = \pm\frac{\omega}{B_0 k_z}\sqrt{A_i^2 + A_r^2 + 2A_iA_r\cos(2\Phi_x)}\cos(k_z z), \tag{4.1.25}$$

$$\tan(\phi) = \frac{2A_iA_r\sin(2\Phi_x)}{A_r^2 - A_i^2}, \tag{4.1.26}$$

$$\frac{\omega^2}{V_A^2} = k_x^2(x) + k_y^2 + k_z^2, \tag{4.1.27}$$

where as mentioned above, $\bar{b_x}$, $\bar{b_y}$, $\bar{b_z}$ and $\bar{u_x}$ are the amplitudes of b_x, b_y, b_z and u_x respectively, and we restate the WKB fast mode dispersion relation in (4.1.27), originally given in (4.1.1). This system contains six equations for the seven unknowns previously listed. It is therefore necessary to infer one more piece of information from the satellite data. Multiple satellite missions and ground-based observations have the capability of estimating one of the wavenumbers. For example, phase differences between signals measured at longitudinally spaced satellites or ground stations can be used to obtain k_y [e.g. Mathie and Mann, 2000; Sarris et al., 2013] and phase differences between signals measured at multiple locations on the same field line can be used to obtain k_z [e.g., Takahashi et al. [1987]. Once a component of the wavevector has been estimated, (4.1.22)-(4.1.27) may then be solved.

4.1.2 Solution Method

In this section we outline the steps to follow to determine the unknown quantities required to construct signals of the form of (4.1.3)-(4.1.7). The algebra for the full solution of equations (4.1.22)-(4.1.27) is not listed here for succinctness, but instead can be found in Appendix A. The rearranging of the equations for the desired quantities differs depending on which of the wavenumbers is given from satellite measurements. Hence, we detail each case in the following sections 4.1.2.1, 4.1.2.2 and 4.1.2.3 in a step by step manner, referencing equations found in Appendix A. These sections discuss how to obtain the three wavenumbers which are then used in determining A_i and A_r, shown in section 4.1.2.4. Sections of the same name can be found in Appendix A detailing the full solution in each case.

4.1.2.1 k_z Measured

1. Use (A.1.3) to find k_y, choosing the positive root for an observation in the dusk flank and the negative root for the dawn flank.
2. Use (A.1.4) to find $k_x(x)$.

4.1.2.2 k_y Measured

1. Use (A.2.1) to find k_z, taking the positive root.
2. Use (A.1.4) to find $k_x(x)$.

4.1.2.3 k_x Measured

1. (A.3.2) and (A.3.3) together determine four values for k_y. Take the two positive values for a dusk flank observation and the two negative values for the dawn flank.
2. Use (A.3.4) to find the corresponding k_z value.

4.1.2.4 Determining A_i and A_r

After completing steps 1 and 2 for one of the cases above, proceed to the steps below to determine A_i and A_r.

3. Use (A.1.2) to find $k_z z$. Choose the positive sign for an observation above the magnetic equator ($z > 0$) and the negative sign for an observation below ($z < 0$).
4. Given $k_z z$, determine the coefficients C and D from the first equalities in (A.4.1) and (A.4.2), and P and Q from (A.4.10) and (A.4.11) respectively.
5. Using P and Q in (A.4.9) defines two values for A_i^2, and hence four solutions for A_i.
6. (A.4.12) yields two values of A_r for each A_i, giving eight solution pairs of A_i and A_r.
7. (A.4.15) and (A.4.16), with (A.4.14), define four values of $\Phi(x)$ for each A_i and A_r combination, which implies a total of 32 solution combinations.

Following the above systematic approach, all possible solutions can be determined. To eliminate the spurious solutions that have been introduced, the component time series are

formed using equations (4.1.3)-(4.1.7) and are then compared to the data to see which ones match. It is this procedure which is followed in the next section.

4.2 Method Testing - Simulation Case Studies

We now demonstrate how to test the above analytical method for determining incident and reflection coefficients on simulated data. This will establish the reliability of the method on numerical data before attempting to apply the method to satellite data. The following subsections outline the details of the two simulations to which we apply the method, how to generate appropriate signals to input to the method through signal analysis and the final results demonstrating the use of the method.

4.2.1 Numerical Model

The basis of the numerical model is as outlined in Chapter 2, using the hydromagnetic box model, solving equations (2.2.23)-(2.2.27). The simulations are performed using the normalised equations referenced above and for the cases considered here, we compare to the normalised values outputted from the code. When looking at real data, dimensional values would be used.

The waveguide has a radial extent of 1 which corresponds to a physical length of 10 R_E. The length in y varies for the different simulations dependent on the wavelength. We choose an appropriate spatial resolution of the grid, timestep and total length of simulation to satisfy the CFL condition and resolve the phase mixing length. Typically, energy is conserved to one part in 10^5 or better.

To model tailward travelling waves we drive the system with a running disturbance on the magnetopause, more details of which are given in the results section 4.2. The magnetopause boundary is driven by perturbations in the z component of the magnetic field, b_z, as discussed in Chapter 2. To efficiently model an open-ended waveguide in y we introduce dissipation regions at either end (beyond the region of interest), which act to absorb any perturbations as if they had run out of the waveguide. This is implemented by adding a linear drag term to the equation of motion in these regions, the amplitude of which can be adjusted as per the strength of dissipation required.

4.2.2 Signal Generation and Analysis

Our procedure is appropriate for signals that are purely propagating in the y direction. The signal has to be relatively monochromatic and cannot display a great variation in amplitude over one period. To produce such a signal from our simulations we drive the

outer boundary with a tailward travelling wave packet, an example of which will be given in section 4.2.3. Our control lies with the amplitude, wavelength, phase speed and number of cycles in the packet.

To model a satellite observation, we pick a location in the waveguide and consider the time series of the components. These signals are bandpass filtered using an IDL filtering routine, in a similar manner to the filtering of observational data. For our procedure we require the amplitudes of the components and the phase shift between b_x and b_y, as discussed in Section 4.1.1. To derive these from the simulation data we use an analytic signal method over the desired time interval, which has been used in observations by, for example, Glassmeier [1980]; Hartinger et al. [2011]. The analytic signal $s_a(t)$ is a complex valued function formed from the real signal $s(t)$ and its Hilbert transform $\hat{s}(t)$ as

$$s_a(t) = s(t) + i\hat{s}(t).$$

This removes any negative frequency contributions to the signal. In this form the instantaneous phase of each signal, ψ, is determined by

$$\psi = \tan^{-1}\left(\frac{\hat{s}(t)}{s(t)}\right),$$

and hence we can calculate the required phase shift between the b_x and b_y components. The amplitude envelope for the signal is determined from

$$|s_a(t)| = \sqrt{s(t)^2 + \hat{s}(t)^2}, \tag{4.2.1}$$

which is averaged over the cycles considered to determine their amplitude. This then yields all the required information to determine the incident and reflection coefficients.

We consider two ways of testing the method, both of which involve absorbing energy in the interior of the waveguide and checking how the reflection coefficient changes dependent on the amount of energy absorbed. Firstly, for a uniform medium, we place a dissipation region extending from the interior radial boundary ($x = 0$) to $x = 0.2$. This region is implemented as described for the dissipative buffer zones at the ends of the waveguide, by adding a linear drag term to the equation of motion over this region. A schematic of the waveguide is shown in Figure 4.2.1(a). The idea is relatively simple: we expect to see a decrease in the reflection coefficient as the strength of the dissipation increases. For this simulation, $k_z = \pi/2$ in dimensionless units.

Secondly, we investigate absorbing some of the energy at a field line resonance at a specific location in x. Evidently the medium is taken to be non uniform such that a resonance

can exist within the waveguide. If we place a satellite on the magnetopause side of the resonance we should see an overall inward flow of energy as energy is converted from the compressional fast mode to Alfvénic oscillations. This should mean that the incident coefficient is considerably larger than the reflection coefficient if the wave coupling is efficient. A diagram (not to scale) of the waveguide is given in Figure 4.2.1(b). The position of the resonance can be controlled by the driving frequency and the Alfvén speed profile. The resonance will be excited at the location where the fast mode frequency matches the local Alfvén frequency. Rather than driving the resonance with a natural waveguide eigenfrequency, we choose to drive the resonance with the boundary driving frequency, tuning the equilibrium such that a waveguide resonance is not excited, allowing for a clearer signal for the first testing of this method.

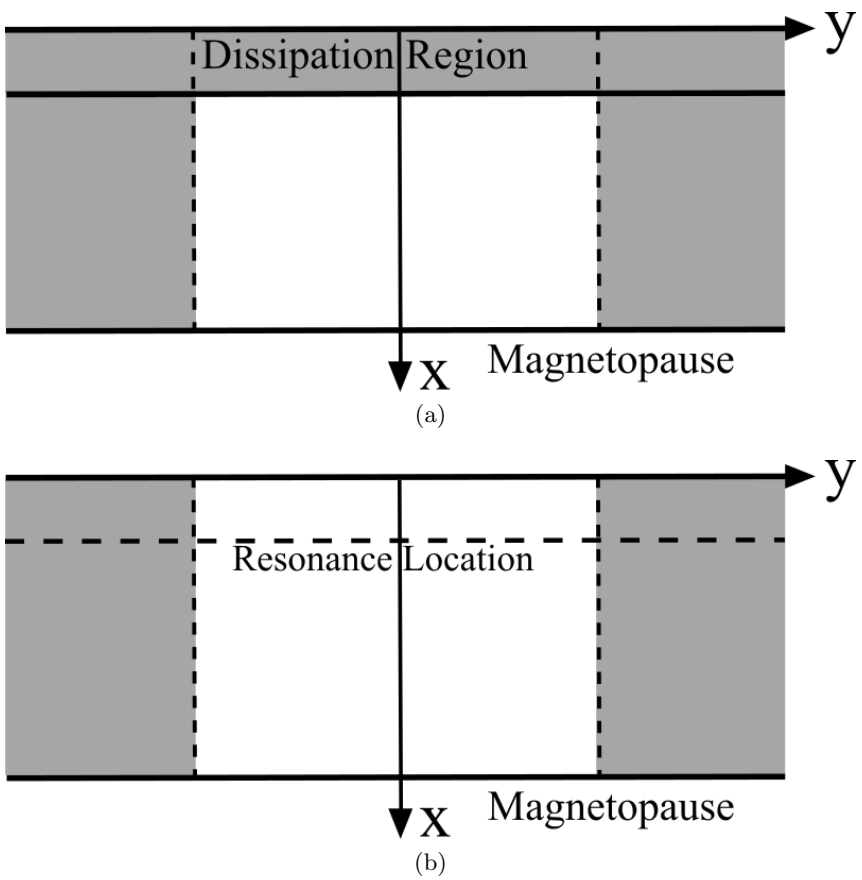

Figure 4.2.1: Schematics (not to scale) of the two model waveguides used in the simulations, where the grey shaded areas represent dissipation regions. (a) Including a dissipation region in x; (b) including a resonance for an inhomogeneous waveguide. Note that the y origin is at an arbitrary location along the waveguide, and would be near dusk for the configuration in the diagram above.

As for the uniform medium simulation, k_z is taken to be $\pi/2$ in dimensionless units (which corresponds to a field line length of $20\mathrm{R_E}$, twice the radial width of the waveguide). The parameter controlling the gradient of the Alfvén speed profile, x_0, (see (2.7.1)) is set

to 2.7, such that the FLR continuum does not overlap any of the $k_y = 0$ waveguide eigenfrequencies as mentioned above. The other parameter in the Alfvén speed definition given in (2.7.1), x_c, is chosen as 0.8. We choose to excite an Alfvén resonance in the guide at $x_r = 0.2$ indicated in the schematic shown in Figure 4.2.1(b), by setting the driving frequency equal to the Alfvén frequency at this location. This yields a dimensionless angular driving frequency of $\omega_r = 1.4544$. k_y varies between each simulation and will control the efficiency of the coupling between the fast and Alfvénic modes. The modes are decoupled in the $k_y \to 0$ and $k_y \to \infty$ limits and hence we expect the strongest coupling for moderate k_y values [Kivelson and Southwood, 1986]. The maximum k_y is determined such that the mode is oscillatory (not evanescent) in x at the satellite location. The driving frequency is held constant between the different simulations by varying the phase speed of the driver accordingly.

Before stating the results, we list a step by step view of the method for clarity.

1. Specify a wavelength and phase speed for the magnetopause driver then run the simulation.
2. Choose the satellite location. Outside the dissipation region for the first simulation and on the magnetopause side of the resonance for the second. Then retrieve the component time series.
3. Bandpass filter the data around the driving frequency.
4. Use the analytic signal method to determine instantaneous phase and amplitude.
5. Derive all possible solution combinations for A_i, A_r values, as per Section 4.1.2.
6. Select correct solutions by reconstructing the signal using A_i and A_r and comparing to the simulation signal.

4.2.3 Results

4.2.3.1 x Dissipation Region Simulation

Figure 4.2.2 displays the temporal dependence (top panel) and the spatial dependence (bottom panel) of b_z on the driven magnetopause boundary, for the uniform medium simulation including a dissipation region in x. The location $y = 0$ corresponds to the centre of the driven magnetopause section, not to the subsolar point as is typical in GSE/GSM coordinates. The boundary is driven for many periods to impose a clear frequency on the interior. The phase speed of the driver is chosen as $v_{ph} = 1.273$ with a dimensionless angular frequency of $\omega = 3.996$ (cyclic frequency $f = 0.636$). The wavelength of the driver is $\lambda_y = 2$, hence $k_y = \pi$. The first and second natural waveguide harmonics can be easily calculated (as discussed in Chapter 1) as $\omega_1 = 3.85$ and $\omega_2 = 5.88$ (for

$k_z = \pi/2$). Therefore the driving frequency is close to the first harmonic. The waveguide is so continuously driven however that this will preclude the appearance of other frequency modes in this case.

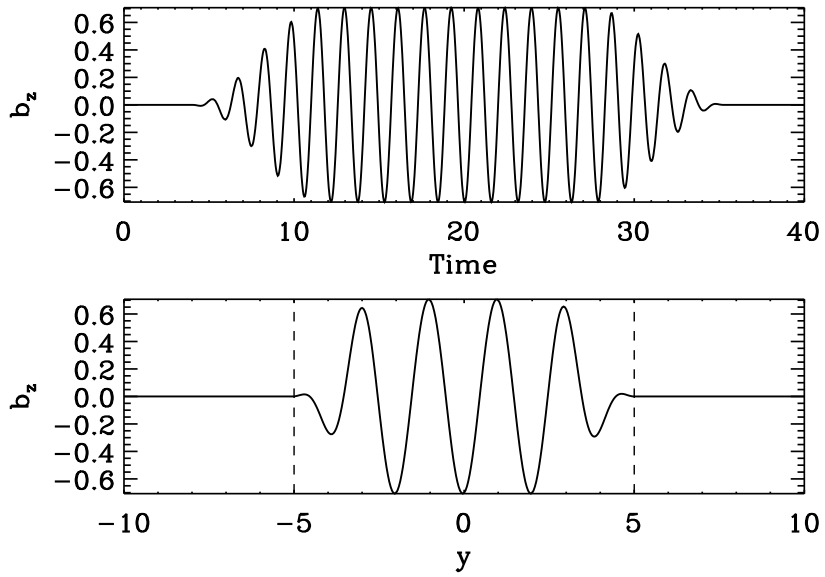

Figure 4.2.2: Top panel: temporal dependence of b_z on the driven magnetopause boundary ($x = 1$), in the centre of the driven region ($y = 0$). Bottom panel: azimuthal dependence of b_z along the magnetopause boundary at time $t = 20$. The vertical dashed lines represent the start of the dissipation regions ($y < -5$, $y > 5$), where the boundary is not driven. The signal on the boundary has a phase motion in the $+y$ direction.

Figure 4.2.3 displays the component time series for a satellite placed at $x = 0.5$, $y = 0$ and $z = 0.5$. The monochromatic nature of the pulsations is immediately evident and confirmed by looking at the FFT power, shown for the b_z component in Figure 4.2.4. This shows the driving frequency of $f = 0.63$ as the dominant frequency. The Poynting vector components displayed in panels 6-8 of Figure 4.2.3 reveal how energy is flowing in the waveguide. The positive S_y signature confirms that we have modelled a tailward travelling wave. The S_x signature is predominantly inward (negative) which is unsurprising given the dissipation region at the inner boundary.

The next step is to bandpass filter the data for the desired frequency. Considering the idealized case that we present here, the effect of filtering is not drastic, but still is a worthwhile procedure to demonstrate how our method would be applied to a real data signal. A small time interval covering 2-3 periods is reconstructed from the signal filtered over cyclic frequencies from 0.57 to 0.71. The top panel of Figure 4.2.5 displays the unfiltered and filtered signals.

Now that the time interval has been selected, the method of the analytic signal is employed to determine the instantaneous phase and average amplitude for each component

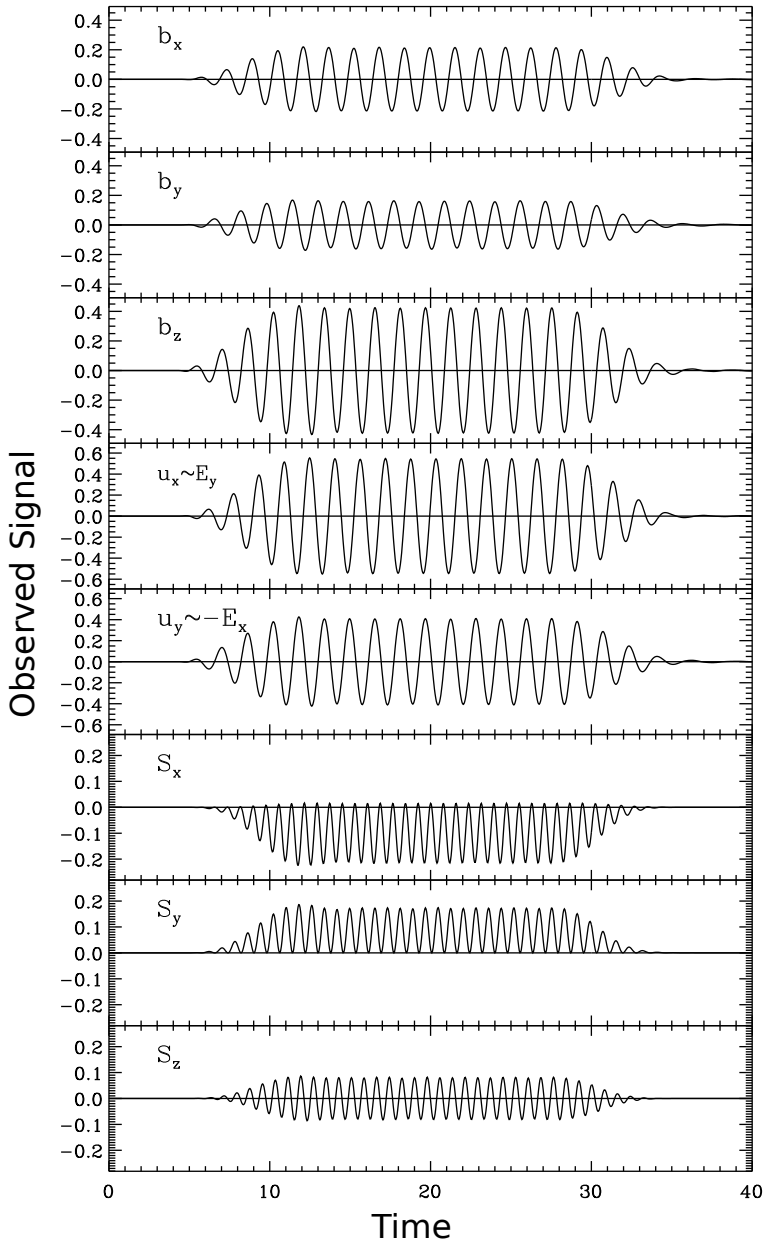

Figure 4.2.3: Component time series for the dissipation region in x simulation, from satellite location $x = 0.5$, $y = 0$ and $z = 0.5$. Top three panels are the magnetic field components, panels four and five are the velocity components, panels six to eight are the Poynting vector components.

time series. These quantities are required for determining the incident and reflection coefficients. We apply the method to the whole signal, then select the desired time interval. Subtracting the instantaneous phase of the b_y signal from the b_x signal, yields their relative phase difference, which is referred to as ϕ in the method outlined in sections 4.1.1

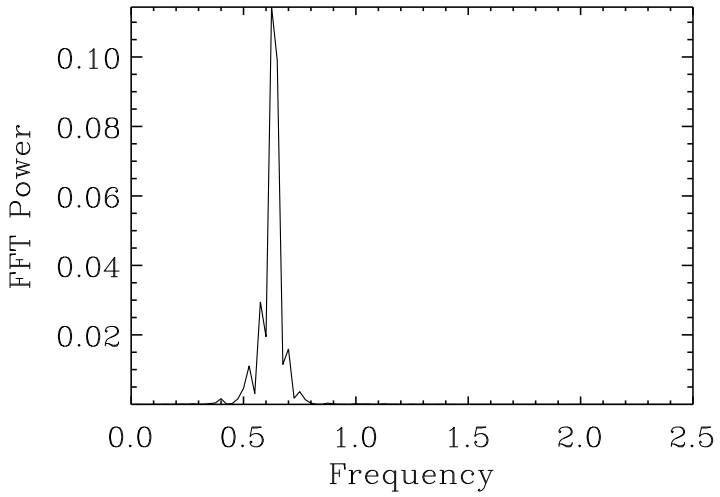

Figure 4.2.4: FFT power spectrum of cyclic frequencies for b_z at the satellite location $x = 0.5$, $y = 0$, $z = 0.5$.

and 4.1.2. The average amplitudes are determined by averaging the signal envelope over the cycles selected. To test the analytic signal method, we fit sinusoids with the derived amplitudes and phases and plot them against the bandpass filtered simulation signals. This is displayed as the middle panel of Figure 4.2.5. Since the filtered signal is already of near constant amplitude and frequency, the dashed line representing the signal constructed from the instantaneous phase and average amplitude lies almost directly on top and is difficult to see.

All of the knowns are now determined and the system can be solved as described in Section 4.1.2. This yields the incident and reflection coefficients A_i and A_r. For the simulation in question, the absolute value of these coefficients was determined as $|A_i| = 0.212$ and $|A_r| = 0.107$. These correct solutions are found by matching the signal components reconstructed from the derived quantities as per (4.1.3)-(4.1.7), with the phase and amplitude averaged signal. The bottom panel of Figure 4.2.11 displays these signals for the b_x (black) and b_y (red) components. The dashed lines are barely visible as they lie directly on top of the original signal, which confirms the values of A_i and A_r used to produce them correspond to the correct roots.

The initial idea was to test how the reflection coefficient would vary when a dissipation region was added. In this regard, we have shown by the predominantly inward Poynting vector signal, and indeed by the fact that $|A_r| < |A_i|$, that the dissipation region has reduced the reflection of the mode. This can be tested further by changing the strength of the dissipation. This is achieved simply by increasing the linear drag term coefficient in the equation of motion, while all other aspects of the simulation are held fixed. Note that

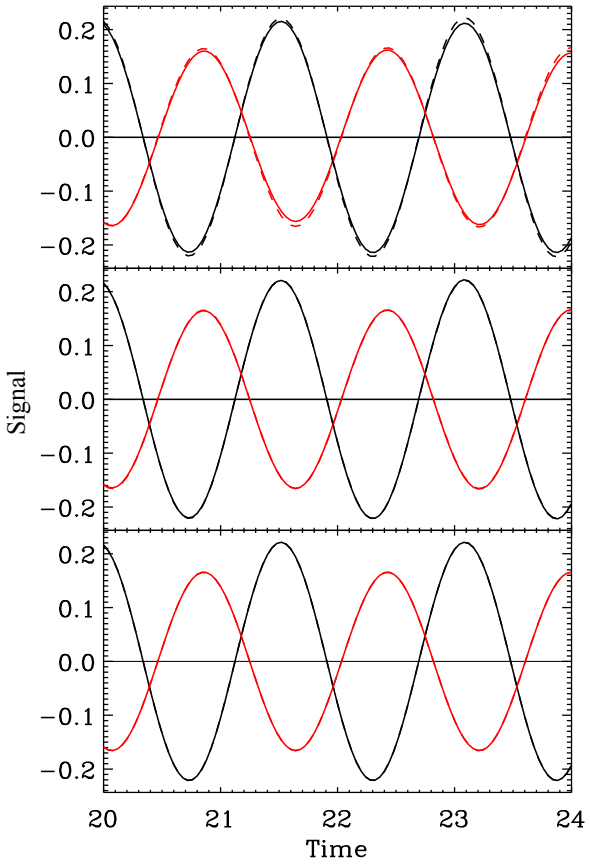

Figure 4.2.5: Time series interval from $t = 20.0$ to $t = 24.0$ of b_x (black) and b_y (red) showing: top panel - the unfiltered data (solid) with the bandpass filtered data (dashed); middle panel - filtered data (solid) with phase and amplitude averaged signal (dashed), vertical dashed lines indicate the phase shift ϕ; bottom panel - phase and amplitude averaged data (solid), reconstructed signal from A_i and A_r values (dashed, which overlies the solid line exactly in this example).

the strength of the dissipation coefficient in the inner dissipation region $0 < x < 0.2$, is set independently of the dissipation used in the buffer zones (the latter being fixed in all simulations). Figure 4.2.6 shows the ratio of A_r/A_i plotted against the dissipation region scaling. It is clear that when there is no dissipation, $A_i = A_r$. Intuitively, increasing the dissipation reduces the size of the reflection coefficient relative to the incident coefficient.

This simplified test case has served as a useful starting point for the validation of the analytical method presented in previous sections. The expected wave behaviour has been produced, and we can now turn to a more involved example involving an inhomogeneous waveguide and the excitation of Alfvén resonances.

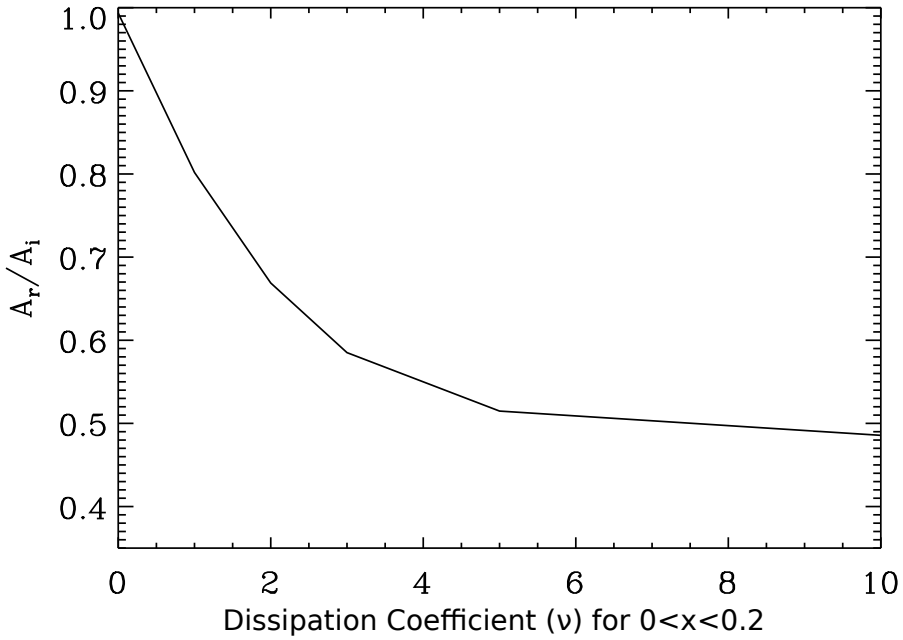

Figure 4.2.6: A_r/A_i plotted against the dissipation coefficient, while the driver phase speed is held constant.

4.2.3.2 FLR Simulation

As mentioned at the end of Section 4.2.2, the value of k_y imposed by the driven boundary can be varied in order to affect the efficiency of the coupling between the fast and Alfvénic modes. Only one of the simulation runs for a specific value of k_y will be discussed here to again demonstrate the method. For the equilibrium parameters described above the value of k_y can vary over $0 \leq k_y \leq 1.503$, the upper bound being determined by maintaining an oscillatory nature in x at the magnetopause. An example of the temporal and spatial dependence of the magnetopause driver is given in Figure 4.2.7, for the case $k_y = 1.4$. Note that the spatial form of the driving condition is a sine wave that travels in the y direction at a speed ω/k_y and is nonzero over the window $-5 < y < 5$ in this example. The frequency ω is chosen to match the Alfvén frequency at $x_r = 0.2$, hence these parameters determine the azimuthal phase speed of the magnetopause driver we impose.

We select a location in the waveguide for the model satellite of $x = 0.9$, $y = 0$, $z = 0.5$. The position is chosen close to the magnetopause boundary such that the mode is oscillatory and not evanescent in x. Recall that the location $y = 0$ corresponds to the centre of the driven region, not the subsolar point. A time series plot over the course of the simulation at this location for each of the components of the magnetic field, velocity and Poynting vector, is displayed in Figure 4.2.8. The driving has produced the intended signals, of relatively

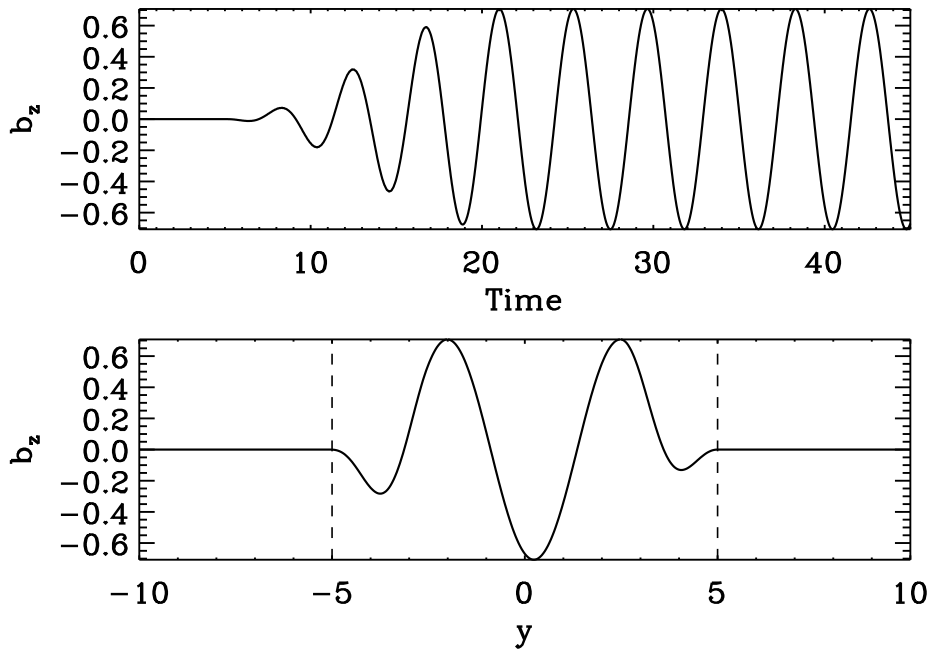

Figure 4.2.7: Top panel: temporal variation of the perturbation b_z on the driven magnetopause boundary ($x = 1$), in the center of the driven section. Bottom panel: spatial variation in azimuth of b_z on the driven magnetopause boundary, at time $t = 45$. The vertical dashed lines represent the start of the dissipation regions ($y < -5$, $y > 5$), where the boundary is not driven.

constant amplitude and monochromatic nature. Panel 7 of the azimuthal Poynting vector S_y shows that the wave is purely tailward travelling as required for our analysis. The sixth panel displays a predominantly inward radial Poynting vector S_x, suggesting energy is being deposited in the waveguide interior. The monochromatic nature of the signal is confirmed by considering the FFT power spectra, displayed in Figure 4.2.9 for b_z at the satellite location. The angular driving frequency of 1.4544 is reproduced as a cyclic frequency of 0.23.

To check that a resonance is being excited at the appropriate location, we check the behaviour of the transverse magnetic field and velocity components. Figure 4.2.10 shows the secular growth in time of these components, which is expected for a steadily driven resonance in the absence of ionospheric dissipation.

The following stages are exactly as discussed for the previous simulation. The data is bandpass filtered over cyclic frequencies between 0.17 and 0.29, with 1-2 cycles displayed in the top panel of Figure 4.2.11 showing the filtered and unfiltered data. The middle panel shows the filtered signal plotted against the phase and amplitude average signal which is the result of applying the method of analytic phase. Similar to the previous case, the averaged signal is a close match to the filtered one. Also indicated here by the vertical

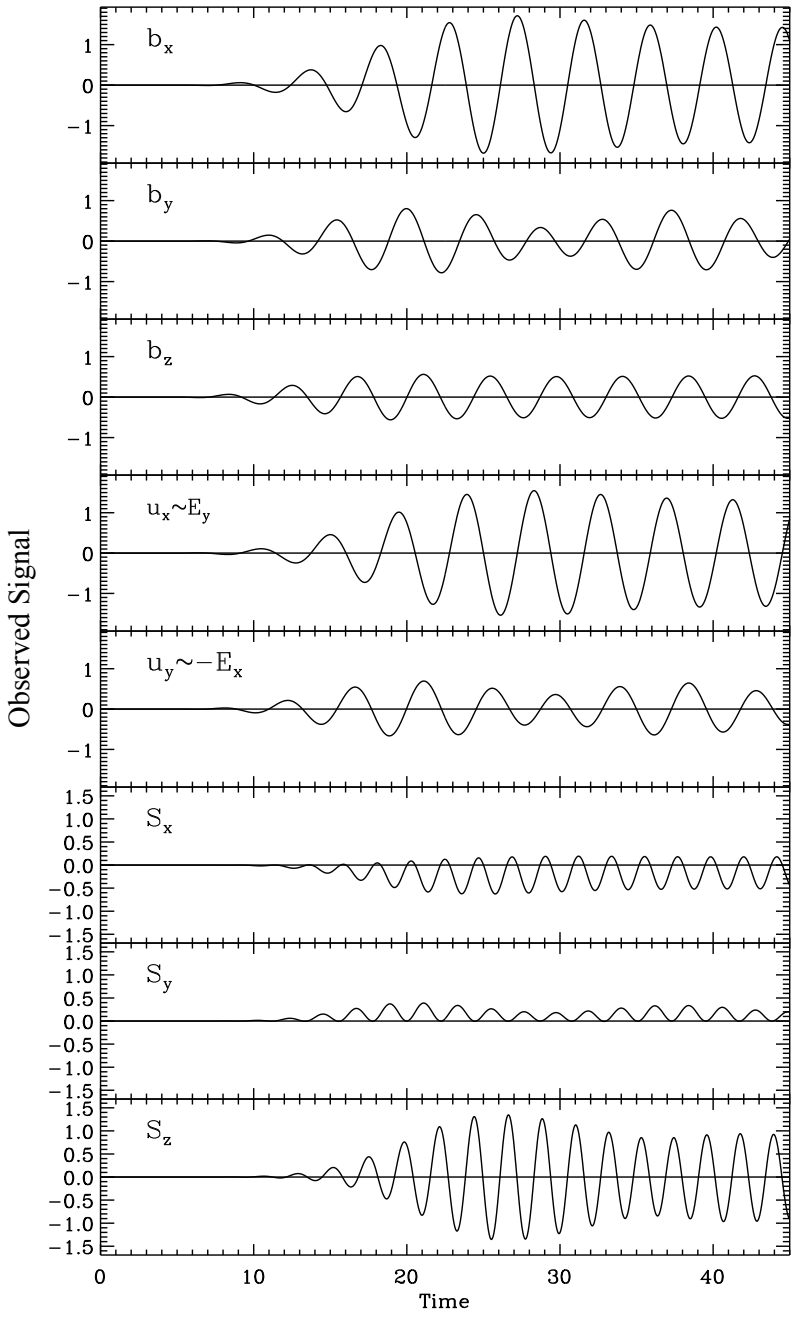

Figure 4.2.8: Component time series from satellite location $x = 0.9$, $y = 0$ and $z = 0.5$. Top three panels are the magnetic field components, panels four and five are the velocity components, panels six to eight are the Poynting vector components.

dashed lines is the value of $\phi = 109.15°$, taken as the phase by which b_y leads b_x as this is less than 180° (see Section 4.1.1 for discussion on choosing ϕ).

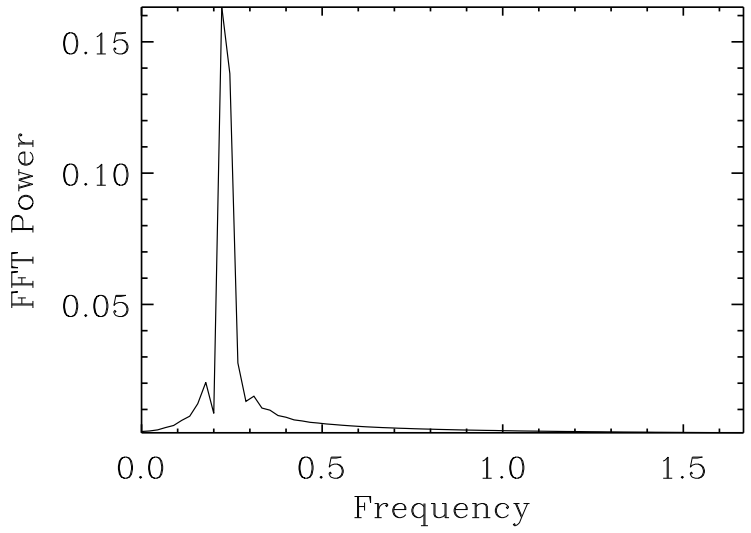

Figure 4.2.9: FFT power spectrum of the unfiltered b_z signal at location $x = 0.9$, $y = 0$ and $z = 0.5$, showing a dimensionless cyclic frequency of 0.23 corresponding to the driving frequency.

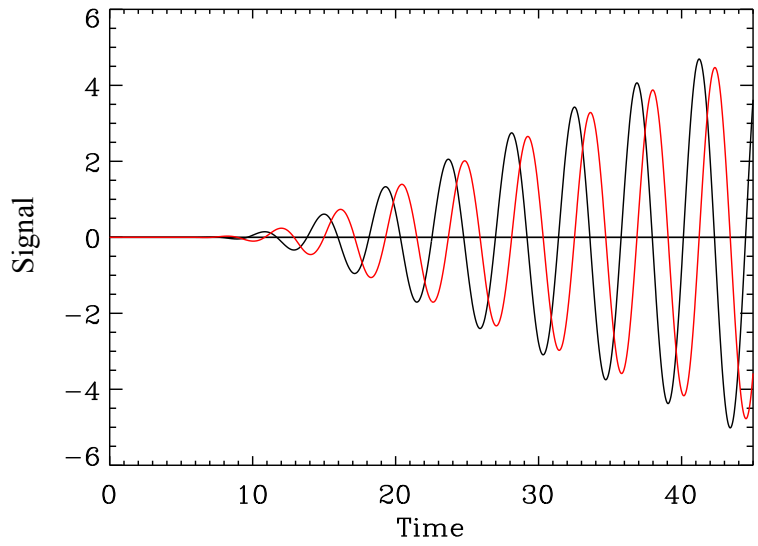

Figure 4.2.10: Time series of b_y (black) and u_y (red) at the Alfvén resonance location $x = 0.2$, with $y = 0$.

Solving the system of equations as outlined in Section 4.1.2 yields the incident and reflection coefficients, which are then used to construct the signals as per equations (4.1.3)-(4.1.7). The coefficients were determined as $|A_i| = 1.202$ and $|A_r = 1.112$ for the chosen value of $k_y = 1.4$. A comparison between the phase and amplitude averaged data and the reconstructed signals using the derived coefficients is given in the bottom panel of

Figure 4.2.11. To illustrate how to identify a spurious solution we give an example of the reconstructed signal in the bottom panel using ultimately incorrect values of A_i and A_r, shown as the dotted lines. Since this solution does not match the original signal shown by solid lines it represents a spurious solution that we shall discard. The dashed lines are barely visible as they lie directly on top of the original signal, which confirms the values of A_i and A_r used to produce them correspond to the correct roots.

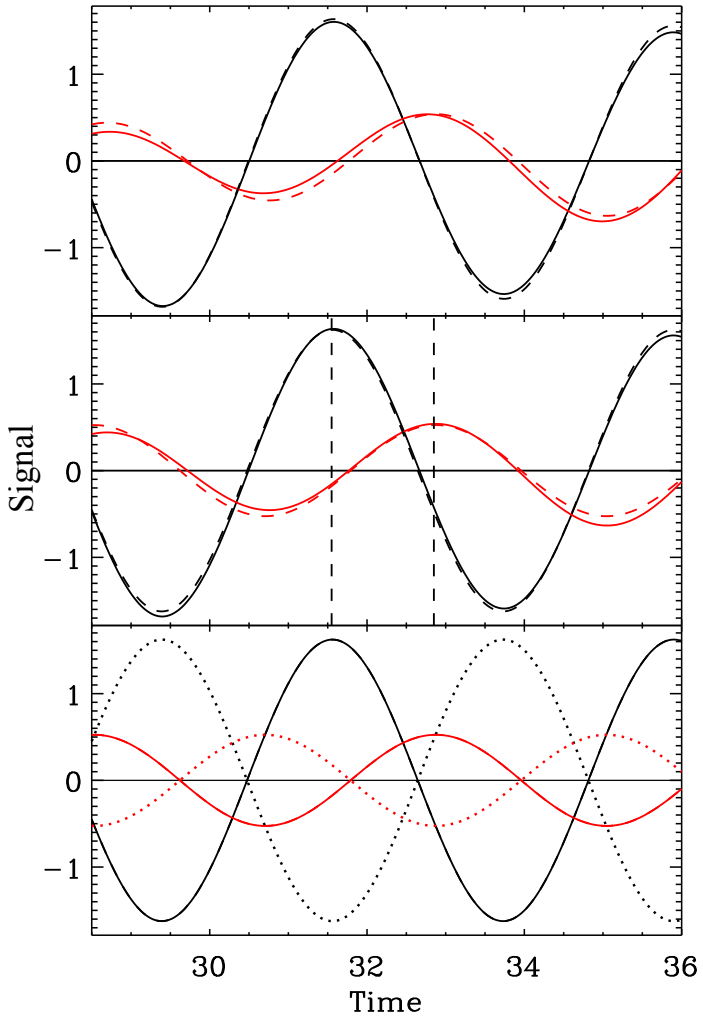

Figure 4.2.11: Time series interval from $t = 28.5$ to $t = 36.0$ of b_x (black) and b_y (red) showing: top panel - the unfiltered data (solid) with the bandpass filtered data (dashed); middle panel - filtered data (solid) with phase and amplitude averaged signal (dashed), vertical dashed lines indicate the phase shift ϕ; bottom panel - phase and amplitude averaged data (solid), reconstructed signal from A_i and A_r values (dashed, which overlies the solid line exactly in this example). The dotted lines represent a spurious solution that does not reproduce the desired (solid line) signals, so is discarded.

Furthermore, the correct values are in line with our original prediction, that the reflection

coefficient will be smaller than the incident due to energy lost from the fast mode at the resonance. The amount of energy deposited and hence the ratio of the reflected to incident coefficients is dependent on the efficiency of the wave coupling, which is controlled by k_y. If k_y is small, the gradients of b_z in the $\hat{\mathbf{y}}$ direction which drive the resonance become small and hence the coupling is weak. For large k_y, the turning point of the mode retreats from the resonance toward the magnetopause boundary, and the amplitude decays evanescently, meaning the fast mode does not penetrate to the resonance location. This behaviour produces a classic curve of absorption against k_y (see Figure 2, Kivelson and Southwood [1986]). As a test of the values produced for A_i and A_r, we ran several simulations for different values of k_y, performed the same analysis as above, and plotted the resulting ratio of A_r to A_i. This is displayed in Figure 4.2.12. A clear trend appears showing the ratio tending to one where little energy is transferred to the resonance (as in the $k_y = 1.4$ case above), while in regions where the coupling is more efficient, the ratio drops considerably. This is further confirmation that the method employed to determine the incident and reflection coefficients is behaving consistently.

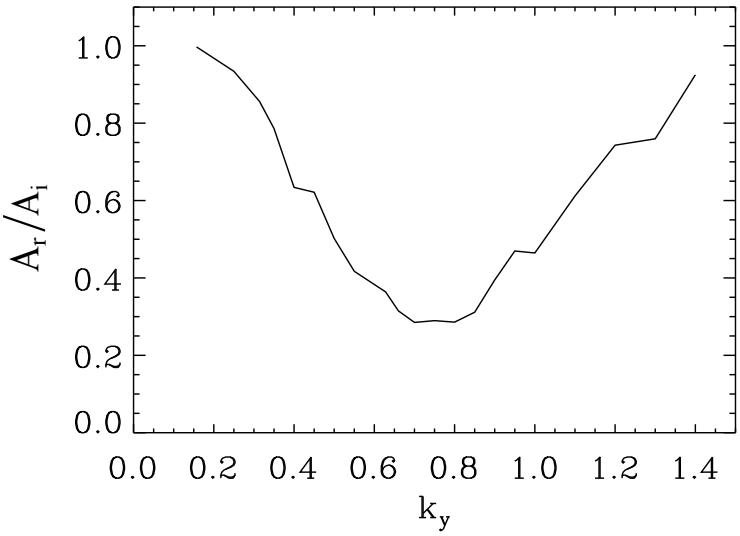

Figure 4.2.12: The ratio A_r/A_i plotted against k_y for twenty one different k_y values.

4.3 Hodograms

Before summarising the above results, we briefly discuss the use of hodograms as a tool to help interpret wave signatures from data, and how they can be used in conjunction with the method described so far in this chapter. When applying the method to observations, hodograms will play a key role in resolving the downtail direction, and hence deserve a mention despite not being used in our simulated case study. A hodogram of, say, the

perpendicular Poynting vector would trace the trajectory of $(S_x(t), S_y(t))$. When done for the full time series a picture forms in the plane, most often an ellipse, which can reveal information about the relationship between the two time series not immediately discernible from a component plot, such as $S_x(t)$ and $S_y(t)$ plotted against time.

Hodograms have long been used in the interpretation of ground based data. Fowler et al. [1967] investigated the polarization properties of quasi-monochromatic magnetic micropulsations (ULF waves), including the angle of polarization (ellipse gradient) and the ellipticity. The authors developed a technique to precisely determine these properties of the magnetic field for such events. This work was extended by Rankin and Kurtz [1970], where a random signal and a monochromatic signal are added, as a means of generating a more realistic time series.

In terms of satellite data, hodograms have been used to determine the orientation of the magnetic field during a crossing of the magnetopause by a satellite [Russell and Elphic, 1978; Berchem and Russell, 1982]. More recently they have been used to analyse polarization properties of Pi2 pulsations in the premidnight sector [Cheng et al., 2009] and as an aid in analysing Alfvén wave phase mixing in ground and space data [Sarris et al., 2009].

For our study, we use hodograms of the transverse components of the Poynting vector in order to determine the propagating direction of a travelling wave packet. Real data does not come with $\hat{\mathbf{y}}$ aligned with the azimuthal direction, which is a requirement for the application of our analytical method. Hence we need to map the data into a suitable coordinate system, so need to resolve the downtail direction. We are unaware of any other such use of Poynting vector hodograms in the literature.

4.3.1 Hodogram Analytics

Before addressing the problem of how to determine the downtail direction, we consider some of the general properties of hodograms and some of the properties specific to a propagating wave solution as discussed previously in this chapter. We begin by looking at the perpendicular components of a magnetic field oscillating in time t, an example of which was given previously by equations (4.1.17) and (4.1.18) but is restated here for convenience as

$$\begin{aligned} b_x &= \bar{b_x}\cos(\omega t), \\ b_y &= \bar{b_y}\cos(\omega t - \phi), \end{aligned}$$

where the barred quantities are the component amplitudes, ω is the frequency and ϕ is

the phase shift between b_x and b_y. The hodogram traced by the above time series will be elliptical (for non-zero ϕ), with the eccentricity and inclination dependent on $\bar{b_x}$, $\bar{b_y}$ and ϕ. These properties can be determined by considering the ratio of the component time series in question, in our case $b_y(t)$ to $b_x(t)$. This will define the gradient of the straight line from the origin to the point $(b_x(t), b_y(t))$. The major/minor axes of the ellipse are defined by such a line, when the distance from the origin is maximised/minimised. To find these points consider the amplitude given by

$$\sqrt{b_x^2 + b_y^2} = \sqrt{\bar{b_x}^2 \cos^2(\omega t) + \bar{b_y}^2 \cos^2(\omega t - \phi)} \tag{4.3.1}$$

Maximising (or minimising) this distance is equivalent to maximising its square. Hence considering $\mathrm{d}/\mathrm{dt} = 0$ yields

$$\begin{aligned}
\frac{\mathrm{d}}{\mathrm{d}t}\left(b_x^2 + b_y^2\right) = -2\omega\bar{b_x}^2 \cos(\omega t)\sin(\omega t) - 2\omega\bar{b_y}^2 \cos(\omega t - \phi)\sin(\omega t - \phi) &= 0, \\
\Rightarrow \bar{b_x^2}\sin(2\omega t) + \bar{b_y^2}\sin(2\omega t - 2\phi) &= 0, \\
\Rightarrow \bar{b_x^2}\sin(2\omega t) + \bar{b_y^2}\left(\sin(2\omega t)\cos(2\phi) - \cos(2\omega t)\sin(2\phi)\right) &= 0, \\
\Rightarrow (\sin(2\omega t))\left(\bar{b_x^2} + \bar{b_y^2}\cos(2\phi)\right) - (\cos(2\omega t))\bar{b_y^2}\sin(2\phi) &= 0, \\
\Rightarrow \tan(2\omega t) = \frac{\bar{b_y^2}\sin(2\phi)}{\bar{b_x^2} + \bar{b_y^2}\cos(2\phi)}&, \\
\Rightarrow t = \frac{1}{2\omega}\tan^{-1}\left(\frac{\sin(2\phi)}{\frac{\bar{b_x^2}}{\bar{b_y^2}} + \cos(2\phi)}\right) + \frac{n\pi}{2\omega}&,
\end{aligned} \tag{4.3.2}$$

for $n = 0, 1$, where t is the time at which the maximum or minimum is reached. Hence, the length of the major/minor ellipse axes is determined by substituting both solutions for the time in equation (4.3.2) into equation (4.3.1). Until this substitution it is unknown which root corresponds to the major/minor axes. No obvious simplification can be made in the resulting expression for the axes lengths in terms of ϕ, and hence such an expression yields no further benefit than the separate equations (4.3.1) and (4.3.2). To find the gradient consider the ratio of b_y to b_x given by

$$\frac{b_y}{b_x} = \frac{\bar{b_y}\cos(\omega t - \phi)}{\bar{b_x}\cos(\omega t)}.$$

Then the time in equation (4.3.2) is again substituted into the above expression to obtain the gradient. As for the axes lengths, the resulting expression for the gradient in terms

of ϕ is no more illuminating than the separate expressions and is thus omitted. With the above forms, the lengths and gradients of the major/minor ellipse axes are determined.

We can also consider the relation between the perpendicular magnetic field hodogram and the hodograms of other components in the previously used tailward travelling wave model of Section 4.1.1. The following results only apply to the form of the wave assumed in that section, namely propagating in y but having an incident and reflected wave in the x direction. In a similar manner to the above general expressions for the perpendicular magnetic field components, we can express the remaining components as

$$u_x = \bar{u_x}\sin(\omega t), \tag{4.3.3}$$

$$u_y = \bar{u_y}\sin(\omega t - \phi), \tag{4.3.4}$$

$$b_z = \bar{b_z}\sin(\omega t - \phi), \tag{4.3.5}$$

with definitions consistent with those given above. We will now show that the perpendicular velocity field components will trace a hodogram of the same inclination and eccentricity as the perpendicular magnetic field components, perhaps a surprising result at first glance. In this model where we have assumed a propagating wave solution, the amplitudes of these components are related (which would not necessarily be the case in a general system). Missing from the system of equations (4.1.22)-(4.1.27) is the definition of the amplitude of u_y. It was disregarded before since it did not provide another independent quantity to aid with the solution of the system. However we state it here as

$$\bar{u_y} = \pm\frac{\omega}{B_0 k_z}\frac{k_y}{k_x}\sqrt{A_i^2 + A_r^2 - 2A_i A_r\cos(2\Phi_x)}\cos(k_z z),$$

to show that the amplitudes are related as

$$\frac{\bar{u_y}}{\bar{u_x}} = \frac{\bar{b_y}}{\bar{b_x}},$$

(see equations (4.1.22), (4.1.23) and (4.1.25)). Hence it can be shown that the expressions derived for the ellipse gradient for the perpendicular magnetic field components will be the same for the perpendicular velocity components, and hence their hodogram direction will coincide.

The relation to the perpendicular Poynting vector hodogram is more subtle because of the dependence of the components of $\boldsymbol{S}_\perp$ on b_z. It can be shown however, that the inclination of the hodogram ellipse for $\boldsymbol{S}_\perp$ will be the same as those of $\boldsymbol{u}_\perp$ and $\boldsymbol{b}_\perp$. Consider the

ratio of the components of $\boldsymbol{S}_\perp$ as

$$\frac{S_y(t)}{S_x(t)} = \frac{u_y(t)b_z(t)}{u_x(t)b_z(t)} = \frac{u_y(t)}{u_x(t)}.$$

This implies that a line drawn to a point on the $\boldsymbol{u}_\perp$ hodogram (and equally for $\boldsymbol{b}_\perp$) at time say t_0, will have the same gradient as the line drawn to a point on the $\boldsymbol{S}_\perp$ hodogram at t_0. This however, does not prove that the hodograms are aligned, because the centre of the $\boldsymbol{S}_\perp$ ellipse is offset from the origin. Figure 4.3.1 shows model hodograms of $\boldsymbol{u}_\perp$ and $\boldsymbol{S}_\perp$ to express this concept. The locations labelled A-H in Figure 4.3.1(a) map to the locations of the same letter in Figure 4.3.1(b), with the same slope to the origin as indicated by the red dashed lines. It can be seen that locations B and F, where $u_x = 0$ correspond to $S_x = 0$, and locations D and H, where $u_y = 0$, map to $S_y = 0$. The latter locations also have $b_z = 0$ (and hence $S_x = S_y = 0$) because u_y and b_z are in phase in this model. Indeed, it is this phase relation that gives S_y as purely positive such that positive $\hat{\mathbf{y}}$ is the downtail direction. Since the Poynting vector components have double the frequency of the velocity/magnetic field components, one orbit of $\boldsymbol{u}_\perp$ traces out two orbits of $\boldsymbol{S}_\perp$. To show that the inclination of the hodograms is the same, we have to show that the gradient of the line through S_0 (the center of the $\boldsymbol{S}_\perp$ hodogram) to the ellipse apex (i.e. the major axis) is the same as the major axis of the $\boldsymbol{u}_\perp$ ellipse. To do this, we use the same method as previously, whereby we attempt to find the time which maximises the distance

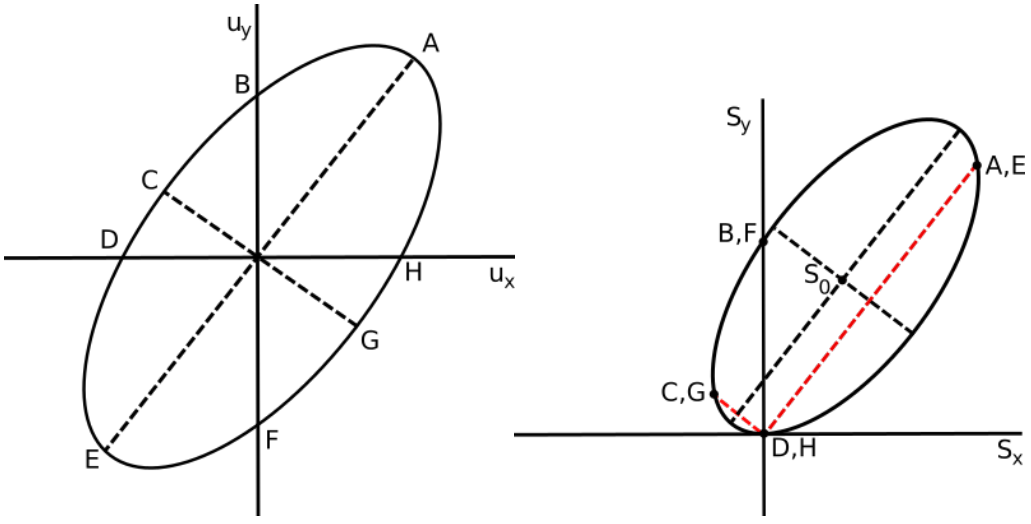

(a) $\boldsymbol{u}_\perp$ (b) $\boldsymbol{S}_\perp$

Figure 4.3.1: Model hodograms for (a) $\boldsymbol{u}_\perp$ and (b) $\boldsymbol{S}_\perp$ for the tailward travelling wave model. The lettered locations A-H map between the hodograms, showing the different locations on each for the same time.

$$\sqrt{(S_x - S_{x0})^2 + (S_y - S_{y0})^2}, \tag{4.3.6}$$

where S_{x0} and S_{y0} are the x and y locations of the $\boldsymbol{S}_\perp$ ellipse center, i.e. $S_0 = (S_{x0}, S_{y0})$. Unfortunately it is not as simple algebraically to extract the time from this formulation, and hence to confirm the orientation of the $\boldsymbol{S}_\perp$ ellipse. However, it is simple to check numerically that in this system, the inclination of the $\boldsymbol{S}_\perp$ hodogram ellipse is the same as that of $\boldsymbol{u}_\perp$ and $\boldsymbol{b}_\perp$. In terms of the ellipticity, the $\boldsymbol{S}_\perp$ hodogram will differ from the others due to the fact that $b_z(t)$ enters the expression (4.3.6). This could be determined as previously from the ratio of S_y to S_x at the maximising/minimising times found numerically.

In this section, we have shown generally how to find the ellipticity and gradient of a hodogram for two harmonic time series. Considering the tailward travelling wave model presented in Section 4.1.1 we have then shown that in such a system, the hodograms for $b_\perp$, $u_\perp$ and $S_\perp$ will always be aligned (have the same ellipse gradient). The next section considers how, in general, we can determine the downtail direction using the $S_\perp$ hodogram.

4.3.2 Determining the Direction of Propagation Using the Poynting Vector Hodogram

The downtail propagating direction is given by considering the tangent to the transverse Poynting vector hodogram at the point where $S_x = S_y = 0$. We infer that the normal to this tangent (on the ellipse side) gives the azimuthal direction of propagation. This may be appreciated from the following perspective. Taking the tangent line to be the 'radial' direction and the normal to it to be the azimuthal direction means the azimuthal Poynting vector will always have one sign, and hence we have identified the 'downtail' direction.

The point where $S_x = S_y = 0$ is given simply by $b_z = 0$, since in linear theory S_x and S_y are proportional to b_z, hence these zeros coincide. In order to find the tangent, we require the time at which $b_z = 0$, which we denote t_0. Then to obtain the gradient of the tangent at $t = t_0$ we differentiate S_x and S_y in time, evaluate at t_0 and take the ratio of S_y to S_x. For S_x in normalised units, this simplifies nicely to

$$\left.\frac{\partial S_x}{\partial t}\right|_{t_0} = u_x \frac{\partial b_z}{\partial t},$$

where the other term from evaluating the derivative of S_x has vanished from the right hand side since we are evaluating for $b_z = 0$. Similarly the derivative of S_y is given by

$$\left.\frac{\partial S_y}{\partial t}\right|_{t_0} = u_y \frac{\partial b_z}{\partial t},$$

and hence the ratio of the derivatives is

$$\left.\frac{\frac{\partial S_y}{\partial t}}{\frac{\partial S_x}{\partial t}}\right|_{t_0} = \left.\frac{u_y}{u_x}\right|_{t_0}.$$

Evaluating this fraction in data would be simple: find the zero of $b_z(t)$ for a particular cycle and calculate u_y/u_x at that time. This gives the gradient of the tangent whose normal yields the direction of propagation. Once the downtail/azimuthal direction has been determined the fields can be mapped to the new rotated coordinate system. This simple evaluation in data will make the method previously discussed for finding incident and reflection coefficients applicable to any quasi monochromatic propagating waveguide events.

To show all of this in practice, Figure 4.3.2(a) displays a hodogram of $\boldsymbol{S}_\perp$ over approximately one cycle, taken from one of the previous simulations in this chapter. In these simulations, we had a downtail direction already aligned with the y axis, hence $S_y > 0$ at all points. Figure 4.3.2(b) shows the same data for $\boldsymbol{S}_\perp$ except rotated by 30° to demonstrate how the method would work for real data. The solid line over-plotted represents the tangent found from the method described above, with the normal given by the dashed line. This would then be used to rotate the data by the appropriate value such that the tangent and tangent normal would align themselves with the x (radial) and y (azimuthal) directions respectively. Clearly the tangent found matches well to the applied 30° rotation.

4.4 Chapter Summary

In this chapter we have introduced a method for determining incident and reflection coefficients for flank ULF waveguide modes. This method is valid for tailward travelling waves of roughly constant amplitude with a clearly defined frequency. Despite seeming like an idealized case, observations of such signals have been recently published [Rae et al., 2005; Eriksson et al., 2006; Clausen et al., 2008; Hartinger et al., 2011, 2012]. The coefficients derived are correlated with the energy absorption of the magnetospheric interior, as demonstrated by the lowering of the reflection coefficient both when a dissipation region is placed in the waveguide and when energy is absorbed at a FLR. The method produces consistent results, reproducing a similar resonant absorption curve to that of Kivelson and

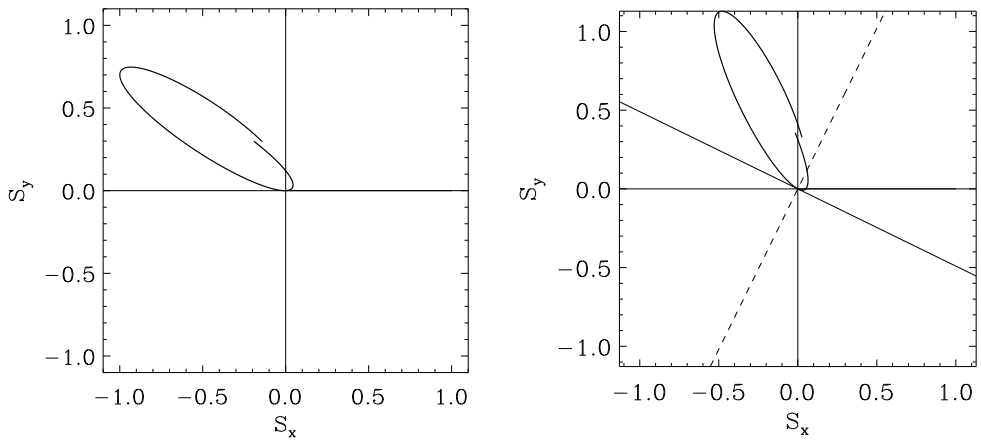

(a) (b)

Figure 4.3.2: Hodograms of $\boldsymbol{S}_\perp$ for a waveguide simulation of a propagating mode from earlier in the chapter. (a) represents the real simulation data and (b) is the same data rotated by 30°. The solid line is the derived tangent line, with the dashed line the tangent normal.

Southwood [1986], showing the change in the efficiency of wave coupling with azimuthal wavenumber. Since the only requirements of the method are a set of time series together with certain amplitudes and phase shifts, this technique could also be applied to results from a global MHD simulation. Evidently, the Cartesian geometry used in our modelling is a simplification. Future studies could employ spatial eigenmodes based upon a realistic magnetospheric equilibrium and so improve the accuracy of our technique when applied to satellite data or results from global magnetospheric simulations. The overall purpose of this work has been to test the method on simulation data in preparation for using it with satellite observations of flank ULF compressional modes in the future. To this end we have demonstrated how the Poynting vector hodogram could be used to rotate data such that the propagating direction is aligned with the chosen azimuthal coordinate, in order for our method to be applicable.

Chapter 5

Modelling Alfvén Resonances in a 3D Waveguide

The previous chapters have considered the modelling of Earth's magnetospheric flanks using a waveguide box geometry. While we have shown this to be a very instructive way of discussing the propagation of fast compressional waves in the magnetosphere, there are evidently many aspects of the true magnetosphere that are neglected in this description. Many subtleties of the wave coupling between fast and Alfvén MHD modes only become apparent when considered in a more realistic geometry, such as the 3D medium considered in this chapter. Here we do not look to create a perfect model of Earth's environment, but instead look to understand the fundamental wave coupling process in 3D. In this regard, we consider a dipole magnetic field model in this chapter.

Modelling Earth's magnetic field as a dipole has been the consideration of many previous authors and requires some introduction as to the progression of the complexity of the models, especially with the development of the large scale numerical simulations now at our disposal. Some of the early work in this area [e.g. Carovillano and McClay, 1965; Radoski, 1966, 1967; Carovillano and Radoski, 1967] discusses the formulation of the MHD wave equations in dipole coordinates and their application to the study of ULF waves (then termed geomagnetic pulsations). At this early stage, wave coupling between compressional and transverse waves is mentioned as an important aspect of the equations and Radoski [1967] notably discusses the differing poloidal and toroidal eigenfrequencies resulting from the dipole geometry, a point which we will cover in more detail in the discussion to follow.

Chen and Hasegawa [1974] used a dipole geometry in considering the notion of field line resonances, although an exact demonstration of the singular nature of the resonant coupling required a Cartesian treatment [Southwood, 1974] with a radial plasma density variation. Chen and Cowley [1989], extended this work to considering also a field aligned variation of the Alfvén speed (in a dipole geometry), and found the field line resonance mechanism

still to be apparent.

At that time, it appears that the field of ULF wave modelling was extremely vibrant, with multiple authors pairing analytical models with new numerical simulations of the coupling of fast compressional disturbances with Alfvén resonances in non uniform magnetic field geometries. Allan et al. [1985, 1986a,b] extended the analytical cylindrical model of the magnetosphere of Radoski [1974] to simulations, showing the excitation of FLRs when driven by a short lived compressional disturbance (of the azimuthal electric field component) at the magnetopause. Lee and Lysak [1989, 1990] studied mode coupling numerically, using a 2D dipole model in a meridional plane, considering the excitation of FLRs under a similar driving condition to that of Allan et al. [1986b].

It should be noted that even in a Cartesian context, with a uniform magnetic field and a density that varies radially and along $\mathbf{B}$, the coupled equations are surprisingly complex. Southwood and Kivelson [1986] demonstrated that (under certain assumptions) resonant coupling would still occur. However, Hansen and Goertz [1992] claimed the effect of field-aligned inhomogeneity was to destroy the resonance completely. Subsequently, Thompson and Wright [1993] demonstrated the general existence of the resonance in this geometry, and identified the error of Hansen and Goertz [1992] (see Thompson and Wright [1994]). Wright and Thompson [1994] further showed the existence of resonances in more general magnetic field geometries, using curvilinear coordinates with one invariant direction.

The importance of the chosen field geometry in terms of the Alfvén eigenfrequencies produced was investigated by Singer et al. [1981]. The authors derive the linearised transverse wave equation for a cold plasma in generalised curvilinear coordinates, such that it can be applied to any field geometry simply by applying the appropriate scale factors. Such an equation can be easily solved along a field line by shooting for the eigenfrequencies matching the imposed boundary conditions. It is found that large discrepancies in the eigenfrequencies can occur between a classical dipole magnetic field model and more realistic magnetic field geometries. This work is closely related to the study by Rankin et al. [2006], who looked to improve upon the model of Singer et al. [1981] by considering a non-orthogonal coordinate system. Typically, when a field aligned orthogonal system is considered, there can be no field aligned currents, since $\boldsymbol{\nabla} \times \mathbf{B}$ has no component along $\mathbf{B}$. In this way, magnetic field configurations which support field aligned currents can be considered in the formalism of Rankin et al. [2006].

More recently, large scale numerical simulations for generalised magnetic field topologies utilising the formalism of [Rankin et al., 2006] have probed some interesting features of ULF waves. For example, using a compressed dipole magnetic field model Kabin et al. [2007] demonstrate how different polarizations of standing Alfvén waves can affect the acceleration of outer radiation belt electrons. Furthermore, Degeling et al. [2010] discuss the importance of day/night asymmetries in the background magnetic field in terms of

the coupling of fast and Alfvén waves. Other global modelling efforts in realistic magnetic geometries have simulated the driving of cavity and Alfvén resonances by solar wind dynamic pressure fluctuations [Claudepierre et al., 2009, 2010].

The above references are included to give a flavour of the progression of the field over the last 50 years, moving from simplified analytical models to large scale 3D numerical experiments. The modelling discussed in this Chapter studies a related problem that was touched upon in the works by Thompson and Wright [1993] and Russell and Wright [2010]. In the former, a Cartesian model with a 2D variation in density along and across the magnetic field is considered and full series solutions describe the resonant excitation of Alfvén waves in response to a fast mode driver. In the latter, the density variation is taken in the two dimensions across a uniform background magnetic field, again in a Cartesian system. The authors discuss how a resonant contour forms at the location where the local Alfvén frequency matches the fast driving frequency, whose form is based upon the imposed density variation. Figure 5.0.1 reproduces Figure 3 from Russell and Wright [2010], which plots two contours of the energy density from a waveguide simulation at four times. Over time, energy is shown to accumulate at the resonant contour given by the black line, where the Alfvén eigenfrequency matches the driving frequency. In this case, the toroidal and poloidal frequencies are the same, as indicated by the Alfvén dispersion relation $\omega_A = k_z V_A(x, y)$. Hence ω_A is independent of the polarization/orientation of the resonant contour.

We consider a dipole version of this system, where the Alfvén speed (or equally the density) is allowed to vary across the background magnetic field. The lengthening of field lines with radius will introduce a natural Alfvén frequency gradient not present in the model of Russell and Wright [2010]. Furthermore, the convergence of field lines with increasing latitude will create different poloidal and toroidal Alfvén eigenfrequencies (as highlighted by Radoski [1967]) compared to a straight background magnetic field model, where they are equal. We aim to fill the gap left by large scale 3D MHD global magnetosphere simulations which cannot resolve the fine scales created by phase mixing during the wave coupling, and to extend the work of Russell and Wright [2010] to a more realistic geometry with the inclusion of the above Alfvén frequency effects. How will fast mode disturbances couple their energy to field line resonances? What will be the shape of the resonant contour? How efficient will the coupling process be? In this scenario, a resonant contour will have an Alfvén frequency somewhere between the poloidal frequency ω_α, and the toroidal ω_β, but it is not obvious what value this will be.

To consider this problem we use a 2D dipole for the background magnetic field, which is invariant in one direction. This more simplified model than the full 3D dipole is used so that we can efficiently investigate the detailed wave coupling with a clean, well resolved numerical experiment. It will also exaggerate the difference between the toroidal and

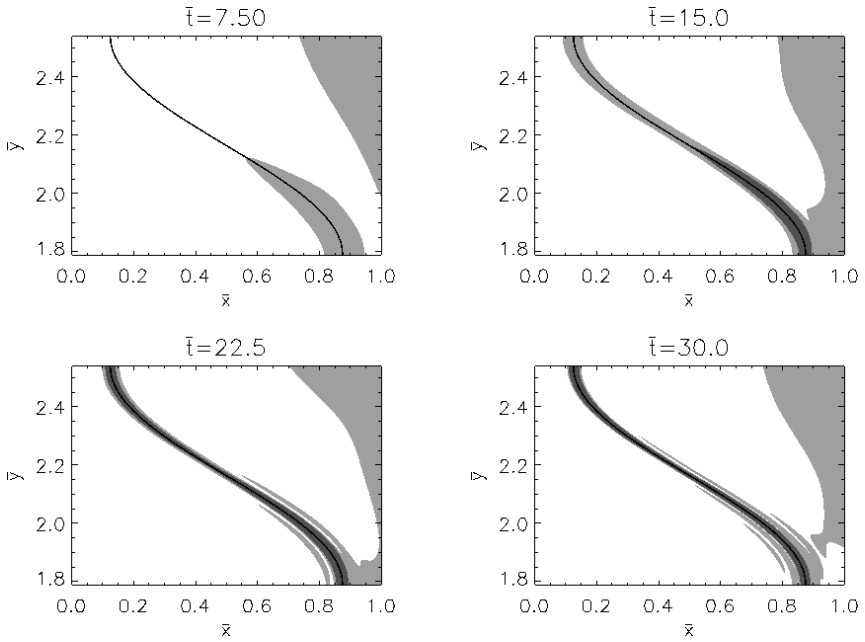

Figure 5.0.1: Reproduction of Figure 3 from Russell and Wright [2010], showing 2 contours of the energy density (grey and dark grey shades) in the $x - y$ plane from a waveguide model at snapshots in time. The resonant contour, where the Alfvén frequency matches the driving frequency, is given by the black line. In this model, $\mathbf{B} = B_0\hat{\mathbf{z}}$, $\rho = \rho(x, y)$ and the fields have a dependence in z of $\sin(k_z z)$ or $\cos(k_z z)$.

poloidal eigenfrequencies further along the field lines compared to the 3D case, which we shall later demonstrate. This enables a better study of how these differing frequencies affect the coupling.

The Chapter is laid out in the following way. Section 5.1 discusses the coordinate system used and the appropriate equations, where the full derivations are reserved for Appendix B. Section 5.2 describes the setup of the numerical method, together with the boundary conditions and waveguide geometry. The preliminary findings from our model are given in Section 5.3, with a discussion of the results in Section 5.4. This is followed by a chapter and thesis conclusion in Sections 5.5 and 5.6 respectively.

5.1 2D Dipole Magnetic Field Model

5.1.1 Coordinate System

For this study, we adopt a field aligned coordinate system which is related to the classical 2D dipole. To begin, we state these classical coordinates (ψ, A_z, z) in terms of cylindrical polar coordinates (R, ϕ, z) given as

$$\psi = B_0 \frac{R_0^2}{R} \sin\phi, \tag{5.1.1}$$

$$A_z = A_0 \frac{R_0}{R} \cos\phi, \tag{5.1.2}$$

$$\mathbf{B} = \boldsymbol{\nabla}\psi = \boldsymbol{\nabla} \times (\hat{\mathbf{z}} A_z), \tag{5.1.3}$$

where B_0 is the background field strength at the point $\phi = 0$, $R = R_0$ and R_0 is the radius to the equatorial crossing point of field line $A_z = A_0$. In this description, field lines are contours of A_z which are circles in the $z = const$ plane, and are intersected by lines of constant ψ (also circles). Such coordinates can be derived from solutions to the 2D Laplace equation in cylindrical coordinates, which hence satisfy the solenoidal magnetic field constraint. ψ is the magnetic scalar potential such that $\mathbf{B} = \boldsymbol{\nabla}\psi = \boldsymbol{\nabla} \times (\hat{\mathbf{z}} A_z)$. A simple schematic of the system is given in Figure 5.1.1.

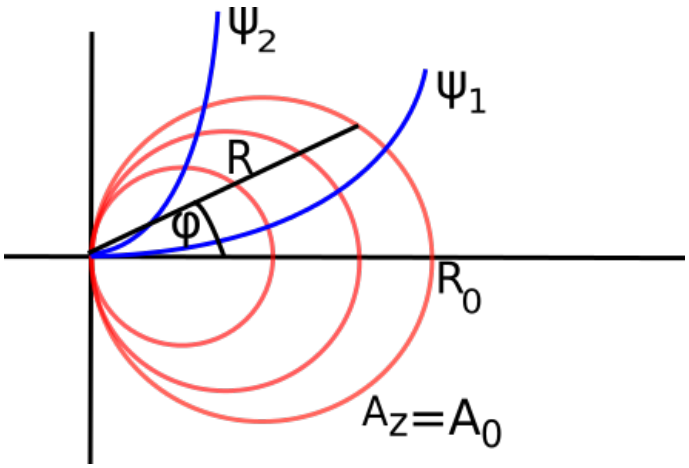

Figure 5.1.1: A schematic of the classical 2D dipole coordinate system. Field lines are contours of A_z, intersected by contours of ψ labelled ψ_1 and ψ_2.

These coordinates present the issue however, that equal increments in $\mathrm{d}\psi$ or $\mathrm{dA_z}$ can produce vastly different increments in path length $\mathbf{dr}$. This point is well demonstrated for 3D dipole coordinates by Kageyama et al. [2006], where the implications for numerical methods using such a coordinate system are discussed. Using equal increments in each of the coordinates leaves the equatorial region massively under resolved, and hundreds of points would be required to appropriately resolve this region. Furthermore, the increasing number of points and reduced grid spacing toward the polar regions produces a hugely restrictive CFL condition. Hence, we can try to work around this resolution issue to some extent by defining a new coordinate system given by (α, β, γ), where $\alpha = g(A_z)$, $\gamma = f(\psi)$ and $\beta = z$. In defining the new coordinates as functions of the old ones, the contours will remain unchanged in the new system.

Before defining these new coordinates, a short mention is made of deriving scale factors in curvilinear coordinate systems for the unfamiliar reader. A scale factor describes the geometric changes in the coordinates. In Cartesian coordinates, these scale factors are just 1, since the coordinate axes are straight lines. Consider the coordinates as stated above, (α, β, γ). A small length element $\mathbf{dr}$ can be expressed as

$$\mathbf{dr} = h_\alpha \mathbf{d}_\alpha + h_\beta \mathbf{d}_\beta + h_\gamma \mathbf{d}_\gamma, \tag{5.1.4}$$

where h_α, h_β and h_γ are the scale factors in the $\hat{\boldsymbol{\alpha}}$, $\hat{\boldsymbol{\beta}}$ and $\hat{\boldsymbol{\gamma}}$ directions respectively. The direction of a coordinate, for example α, is given by the normal to a constant plane/surface of that coordinate. This is conveniently given as $\boldsymbol{\nabla}\alpha$. Hence to find the scale factor for α we can take the dot product of $\mathbf{dr}$ with $\boldsymbol{\nabla}\alpha$ (which is just the length element d_α) which gives

$$\mathbf{dr} \cdot \boldsymbol{\nabla}\alpha = h_\alpha d_\alpha \left(\hat{\boldsymbol{\alpha}} \cdot \boldsymbol{\nabla}\alpha\right) + 0 + 0 = d_\alpha$$

where the other directions evaluate to 0 as they do not contribute in the $\hat{\boldsymbol{\alpha}}$ direction. Cancelling the d_α and seeing that $\hat{\boldsymbol{\alpha}} \cdot \boldsymbol{\nabla}\alpha = |\boldsymbol{\nabla}\alpha|$, yields

$$h_\alpha = \frac{1}{|\boldsymbol{\nabla}\alpha|}.$$

This is the key result in determining the form of the scale factors in terms of the coordinates. At this point, the coordinates and scale factors are merely stated with a little discussion on their properties, with a full derivation given in Appendix B.1, which summarises a private communication with Dr Andrew Wright, January 2016. The coordinates and the corresponding scale factors are

$$\alpha = \frac{R}{\cos\phi}, \tag{5.1.5}$$

$$\beta = z, \tag{5.1.6}$$

$$\gamma = R_g \tan^{-1}\left(\frac{R_g}{R}\sin\phi\right), \tag{5.1.7}$$

$$h_\alpha = \cos^2\phi, \tag{5.1.8}$$

$$h_\beta = 1, \tag{5.1.9}$$

$$h_\gamma = \left(\frac{R}{R_g}\right)^2 + \sin^2\phi, \tag{5.1.10}$$

where R_g is the radial equatorial crossing point of a field line chosen at some point in

the domain, along which $h_\gamma = 1$ and hence γ corresponds to path length along the field line. To see this, consider setting $\alpha = R_g$ and substitute for R using equation (5.1.5) in equations (5.1.7) and (5.1.10). Away from this field line, γ no longer corresponds to path length along the field line and hence to minimise distortion of the grid in γ, it is sensible to choose R_g to correspond to the field line in the middle of the α domain.

With $\beta = z$, the 2D dipole corresponds to a dipole with field lines confined to a plane of constant β. The field is translationally independent of β. This implies that our model will neglect the converging of field lines in β as the poles are approached. This will act to increase the disparity between the toroidal and poloidal eigenfrequencies compared to a model including a variation in β (to be shown in Section 5.1.3), and is the reason we have chosen to use a 2D dipole.

From equation 5.1.5 for α, it can be seen that in the equatorial plane ($\phi = 0$), $\alpha = R$ and $h_\alpha = 1$, which implies that equal increments in α cover a uniform distance in the equatorial plane. This is distorted at higher latitudes, with field lines converging, which is an unavoidable property of a field aligned coordinate system. However, overall we have made a significant improvement to the resolution problems of the original coordinates. This can be easily seen when equally spaced contours of ψ,A_z in the classical 2D dipole are compared with contours of α,γ, from the new coordinates. Figure 5.1.2(a) shows these contours in the x, y plane for the classical 2D dipole coordinates, while (b) displays the new coordinates. It can be clearly seen how the uniformity of α in the equatorial plane makes a huge difference to the grid spacing. Furthermore, the changes to the γ coordinate have drastically improved the spacing along the fieldlines.

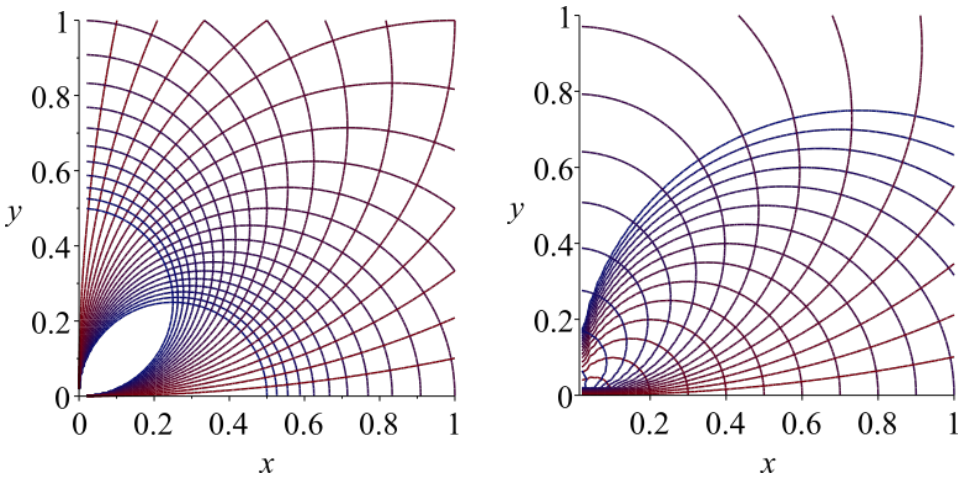

Figure 5.1.2: Comparison of (a) classical 2D dipole coordinates ψ,A_z and (b) the newly derived coordinates α,γ given by equations (5.1.5)-(5.1.10). Plotted are equally spaced contours of (a) ψ,A_z and (b) α,γ.

5.1.2 MHD Equations in Dipole Coordinates

Now that the coordinate system has been determined, we look to the formulation of the MHD equations in this system. Following Wright [1992], the linearized ideal MHD equations in a cold plasma in field aligned curvilinear coordinates can be expressed as

$$\frac{\partial u_\alpha}{\partial t} = \frac{B}{\mu_0 \rho}\frac{1}{h_\alpha h_\gamma}\left[\frac{\partial}{\partial \gamma}\left(b_\alpha h_\alpha\right) - \frac{\partial}{\partial \alpha}\left(b_\gamma h_\gamma\right)\right] - \nu u_\alpha, \tag{5.1.11}$$

$$\frac{\partial u_\beta}{\partial t} = \frac{B}{\mu_0 \rho}\frac{1}{h_\beta h_\gamma}\left[\frac{\partial}{\partial \gamma}\left(b_\beta h_\beta\right) - \frac{\partial}{\partial \beta}\left(b_\gamma h_\gamma\right)\right] - \nu u_\beta, \tag{5.1.12}$$

$$\frac{\partial b_\alpha}{\partial t} = \frac{1}{h_\beta h_\gamma}\frac{\partial}{\partial \gamma}\left(u_\alpha h_\beta B\right), \tag{5.1.13}$$

$$\frac{\partial b_\beta}{\partial t} = \frac{1}{h_\alpha h_\gamma}\frac{\partial}{\partial \gamma}\left(u_\beta h_\alpha B\right), \tag{5.1.14}$$

$$\frac{\partial b_\gamma}{\partial t} = -\frac{1}{h_\alpha h_\beta}\left[\frac{\partial}{\partial \alpha}\left(u_\alpha h_\beta B\right) + \frac{\partial}{\partial \beta}\left(u_\beta h_\alpha B\right)\right]. \tag{5.1.15}$$

B is the background magnetic field strength, ρ the density, μ_0 the magnetic permeability and ν represents the strength of a linear drag term that has been added to the equation of motion. Without this, if we were to continuously drive an Alfvén resonance within the domain, the phase mixing length would decrease over time generating a smaller and smaller resonance width. Adding in this dissipative term will limit this scale length decrease such that a steady state can be reached and a constant resonance width formed. Alternate forms of dissipation could be added, such as viscosity, resistivity or dissipative boundaries. The structure of the resonance is surprisingly insensitive to the exact form of dissipation [Wright and Allan, 1996], and we consider the limit of small dissipation, so the drag is only significant at the resonance.

As can be readily seen from the equations, it is more convenient to work with the terms in the small brackets, and hence we define the new variables:

$$\begin{aligned} U_\alpha &= u_\alpha h_\beta B, \\ U_\beta &= u_\beta h_\alpha B, \\ B_\alpha &= b_\alpha h_\alpha, \\ B_\beta &= b_\beta h_\beta, \\ B_\gamma &= b_\gamma h_\gamma. \end{aligned}$$

This will also make the formulation of the centred differences that will be used in the

numerical method much easier, as only one term needs to be considered. It is also convenient to normalise the equations by characteristic values: lengths by R_0; magnetic field by the background field $B_0 = B(R = R_0, \phi = 0)$, densities by $\rho_0 = \rho(R_0, 0)$, velocities by $V_0 = B_0/\sqrt{\mu_0\rho_0}$ and times by $t_0 = R_0/V_0$.

The final stage for developing the equations for use with the Leapfrog-Trapezoidal method outlined in Section 2.4, is to express the scale factors in terms of the (α, β, γ) coordinates, rather than (R, ϕ). The algebra for this is reserved for Section B.2 of Appendix B. Following this in Section B.3 of Appendix B is a consistency check that the derived coordinates are consistent with a solenoidal, irrotational background magnetic field.

For ease of reference, the scale factors in terms of α and γ are stated here as

$$\begin{aligned} h_\alpha &= \frac{1}{1+\Lambda^2} \\ h_\gamma &= \frac{1}{1+\Lambda^2}\left(\frac{\alpha^2}{R_g^2} + \Lambda^2\right), \end{aligned}$$

where Λ is defined by

$$\Lambda(\alpha, \gamma) = \frac{\alpha}{R_g}\tan\left(\frac{\gamma}{R_g}\right).$$

Considering the above change of variables, normalisation and scale factors, equations (5.1.11)-(5.1.15) become

$$\frac{\partial U_\alpha}{\partial t} = V_A^2 \frac{\left(1+\Lambda^2\right)^2}{\dfrac{\alpha^2}{R_g^2} + \Lambda^2}\left[\frac{\partial B_\alpha}{\partial \gamma} - \frac{\partial B_\gamma}{\partial \alpha}\right] - \nu U_\alpha, \tag{5.1.16}$$

$$\frac{\partial U_\beta}{\partial t} = V_A^2 \frac{1}{\dfrac{\alpha^2}{R_g^2} + \Lambda^2}\left[\frac{\partial B_\beta}{\partial \gamma} - \frac{\partial B_\gamma}{\partial \beta}\right] - \nu U_\beta, \tag{5.1.17}$$

$$\frac{\partial B_\alpha}{\partial t} = \frac{1}{\dfrac{\alpha^2}{R_g^2} + \Lambda^2}\frac{\partial U_\alpha}{\partial \gamma}, \tag{5.1.18}$$

$$\frac{\partial B_\beta}{\partial t} = \frac{\left(1+\Lambda^2\right)^2}{\dfrac{\alpha^2}{R_g^2} + \Lambda^2}\frac{\partial U_\beta}{\partial \gamma}, \tag{5.1.19}$$

$$\frac{\partial B_\gamma}{\partial t} = -\left(\frac{\alpha^2}{R_g^2} + \Lambda^2\right)\left[\frac{\partial U_\alpha}{\partial \alpha} + \frac{\partial U_\beta}{\partial \beta}\right]. \tag{5.1.20}$$

This is the system that will be solved numerically in the following sections.

5.1.3 Estimating the Alfvén Eigenfrequencies for a 2D Dipole

One of the main motivations of this work is to understand how the differing poloidal and toroidal Alfvén eigenfrequencies in a dipole model affects the resonant coupling of fast and Alfvénic modes. Indeed, that is what separates this work from previous studies. To this end, it would be useful to understand how different the poloidal and toroidal frequencies are in the 2D dipole model for differing latitudinal extents. Evidently, the larger the latitude, the greater the convergence of field lines and hence the more marked we would expect the difference in these frequencies to be. In an ideal world, computational resources would not be an issue, and we could readily solve the pertinent equations over the whole latitudinal extent. Realistically however, the field line convergence at high latitudes will drastically increase the resources required, as grid spacings in α will decrease, resulting in a decreased timestep to satisfy the CFL condition. It is therefore of great benefit to understand the latitudinal extent required for our computational domain in order to achieve a significant difference in the Alfvén eigenfrequencies. For example, if we discover that a large latitudinal extent is required to achieve even a minor difference in the frequencies for the 2D dipole, we may re-evaluate the adopted coordinates and the computational approach taken. As it is, we intend to show that the 2D dipole can provide a suitable difference in the frequencies without being too computationally expensive.

In order to investigate the Alfvén eigenfrequencies, we consider the undriven Alfvén wave equations in curvilinear coordinates. The equations here will only be stated, but a nice derivation is given by Wright and Thompson [1994]. Equation (7) from this paper, for the displacement ξ, is restated below:

$$\frac{\partial}{\partial\gamma}\left(H^i_{j\gamma}\frac{\partial\xi_i}{\partial\gamma}\right)+\omega^2 G^{i\gamma}_j\xi_i=0, \tag{5.1.21}$$

where

$$\begin{aligned} H^i_{j\gamma} &= \frac{h_i}{h_j h_\gamma}, \\ G^{i\gamma}_j &= \frac{h_i h_\gamma}{h_j V_A^2}, \end{aligned}$$

with the h terms being the appropriate scale factors and ij has the form $\alpha\beta$ for the poloidal mode and $\beta\alpha$ for the toroidal. Equation (5.1.21) has an evident dependence on γ but also on α and β through the scale factors and the Alfvén speed. To solve this equation, α and β

are specified which designates the particular field line in question, and hence the equation becomes dependent on γ only. We implement a Runge-Kutta fourth order method in a similar manner to Section 3.2, solving over the length of the field line in the northern hemisphere. This works by 'shooting' for a value of ω which gives a displacement matching the given boundary conditions. These are chosen such that the ionospheric end of the field line has a node of displacement, with an antinode at the equator. The resulting eigenmodes for the toroidal and poloidal equations for the case where $V_A = 1$ are shown in Figure 5.1.3. The maximum field line latitude traced to is $\phi = 1.4 \sim 80°$.

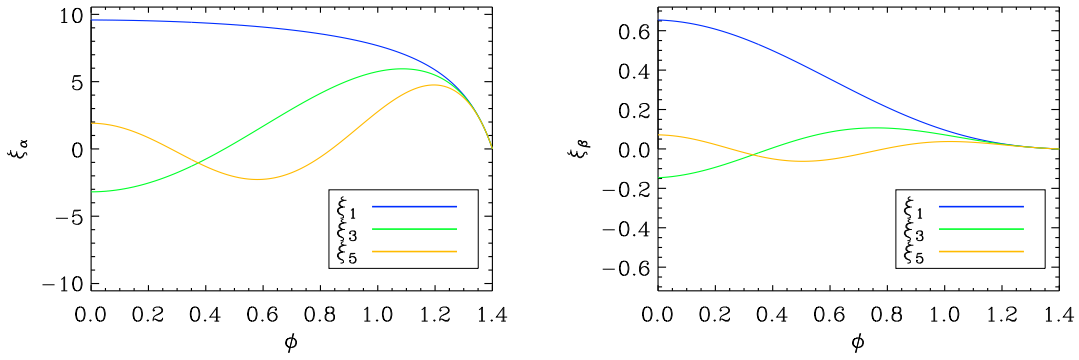

(a) (b)

Figure 5.1.3: Alfvén eigenmodes for the (a) poloidal and (b) toroidal cases, plotted against the latitude ϕ.

Really of interest are the frequencies corresponding to the above solutions. For several different field line lengths (different latitudes) the poloidal and toroidal equations are solved with the boundary conditions and the frequencies are stored. Then the ratio of these frequencies for the various harmonic solutions can be plotted against the latitude of the end of the field line. This is shown in Figure 5.1.4 (a). It is noted that choosing a non uniform V_A evidently changes the frequencies but does not greatly affect the toroidal to poloidal frequency ratios. The ratio of the first harmonics (black line) is the only one that deviates largely from unity. This plot will be instrumental in determining the latitudinal extent of our computational domain. For example we can say that for a field line which extends up to $\phi = 1.0$ radians in latitude, the poloidal and toroidal frequencies differ by a factor of ~ 1.6. This is a significant enough change in the frequencies and deviation from the Cartesian case to suggest that the 2D dipole can provide an interesting framework to study mode coupling. In Figure 5.1.4 (b) the same frequency ratios are shown except for a 3D dipole. As can be seen, the ratio is not as exaggerated as the 2D dipole case, giving a ratio of ~ 1.25 for $\phi = 1.0$. Hence, we use the 2D dipole to better highlight this feature.

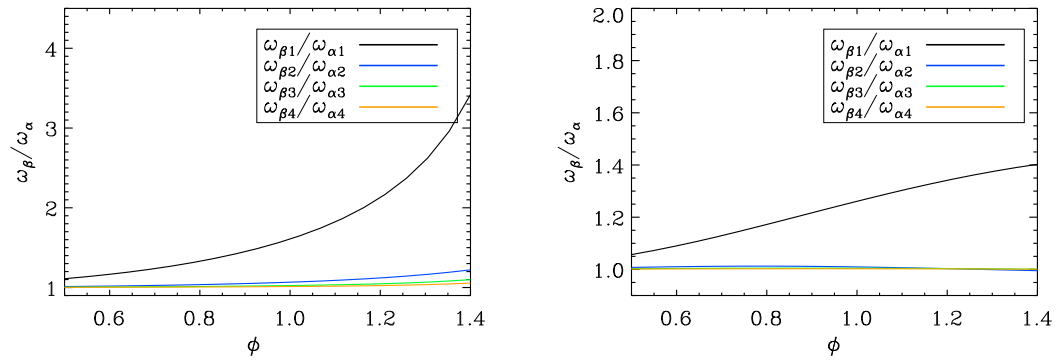

Figure 5.1.4: Ratio of toroidal to poloidal eigenfrequencies plotted against latitude ϕ at the end of the field line for the (a) 2D dipole and (b) 3D dipole. Four harmonics are plotted as indicated by the plot legend.

5.2 Method Setup and Testing

Now that the coordinates and equations ((5.1.16)-(5.1.20)) have been derived and the 2D dipole has been validated as having substantially different toroidal and poloidal frequencies, we look to implementing the same finite difference method used previously, namely the Leapfrog-Trapezoidal method. The equations for this method are given in Section 2.4 as equations (2.4.3)-(2.4.5). We provide less detail here of the rigorous testing of the code, which followed a similar approach to that described in Chapter 2. A modification that we do make is to implement a staggered grid, where different variables are defined on different grids. This aids with the differencing used in defining derivatives and can help to prevent the checkerboard instability, where two consistent decoupled solutions exist simultaneously, separated by a grid cell, resulting in a jagged overall solution. The grid that each component uses depends upon the required boundary conditions, but a full discussion of the grids is omitted here.

We next have to specify the waveguide extent in each of the coordinate directions and enforce the boundary conditions. A general schematic of the waveguide is shown in Figure 5.2.1. The indicated R_g field line, mentioned in detail in the coordinate derivation, is chosen in the middle of the domain in α. As mentioned in Section 5.1.3 discussing the Alfvén eigenfrequencies, increasing the extent in γ considerably increases the run time. We can see this from the scale factor $h_\alpha = \cos^2\phi$. Increasing the latitudinal extent ϕ, (i.e. increasing γ) decreases the grid spacing in α which enforces a much smaller timestep through the CFL condition. Hence, the choice of the maximum value of γ is critical. To save on computational resources, only the northern hemisphere solution is computed. A symmetry condition in the equatorial plane means the full solution corresponds to a

fundamental mode in γ.

For the boundary conditions we impose nodes of velocity at the ionospheric end of the field lines (γ_{max}), with antinodes at the equator ($\gamma = 0$). The inner boundary in α (α_{min}) is assumed to be perfectly reflecting (node of velocity), while the outer boundary (α_{max}) is driven with perturbations of b_γ in a similar way to previous driving with b_z. This will generate a quarter wavelength fundamental radial mode, something discussed at length in previous chapters. In β we implement dissipation regions at either end in a similar manner to the method of Chapter 4 (see Figure 4.2.1). These act to dissipate any perturbations such that they do not return to the solution domain of interest.

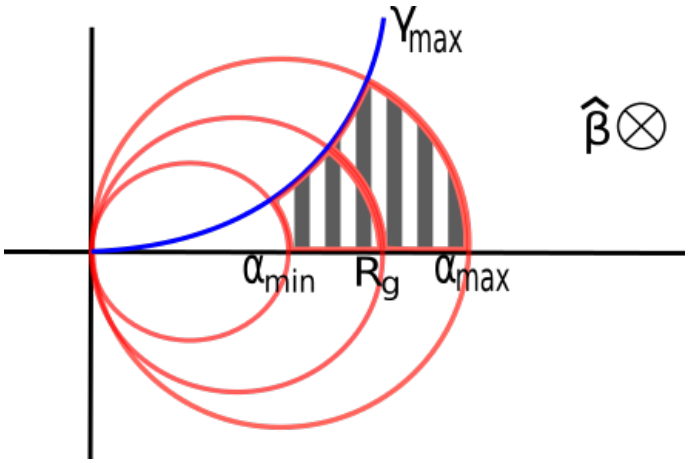

Figure 5.2.1: Schematic of the solution domain (striped shaded area) in the derived (α, β, γ) coordinates. α_{min} and α_{max} are the inner and outer radial boundaries respectively, while R_g represents the field line in the middle of the domain. γ_{max} represents the upper boundary.

Many runs have been performed with this method as a means of testing and furthering our understanding. For example: setting the scale factors to 1 to reproduce Cartesian results; including and not including dissipation; beginning with an initial displacement in the domain and not driving; driving the outer boundary. In this section, we present one of the test runs which shows that the code is correctly solving the equations and conserving energy, whilst also displaying some interesting features to build upon.

Consider a weakly non uniform small (α,β,γ) cube like domain of side length 0.2, ranging from $0.8 \rightarrow 1.0$ in α and $0 \rightarrow 0.2$ in β. The length in γ is dependent on the latitude which is taken to be $\phi = 0.2$. Hence, choosing the R_g field line to be at $\alpha = 0.9$, implies a maximum value in γ of $\gamma_{max} = 0.2018$, with $\gamma_{min} = 0$ at the equator. 40 grid points are taken in each direction and the value of the dissipation is set as $\nu = 0.2$ throughout the whole domain. There are no dissipation regions set up at either end in β in this simulation, so there are simply perfectly reflecting conditions at each end ($\beta = 0$, $\beta = 0.2$). The Alfvén speed is set to be 1 (in normalised units) everywhere, but an Alfvén continuum still exists through

the changing field line length in α. Thus we can specify a boundary driving frequency to match the local Alfvén frequency of a location in the domain to set up a resonance. Using a simple bounce time calculation of the Alfvén frequency of $\omega_A = V_A\pi/2L_\gamma$, where L_γ is half the field line length, we calculate $\omega_A(\alpha = 0.9) = 7.784$. Then choosing a wavelength in β on the driven boundary ($\alpha = 1.0$) of $\lambda_d = 0.15$, together with a phase speed of $v_{ph} = 0.191$, produces a driving frequency matching the Alfvén frequency at $\alpha = 0.9$. Finally, a quarter wavelength mode structure for b_γ in γ is imposed on the driven boundary with a node at γ_{max} and an antinode at γ_{min}. This requires $k_\gamma = 7.78$.

Figure 5.2.2 displays the temporal dependence (upper panel) and the spatial dependence in β (lower panel) of b_γ on the magnetopause boundary. The boundary is driven for a few cycles then closed to become perfectly reflecting. The functional form of this boundary motion is composed of three separate functions of time and space, given below by equations (5.2.1)-(5.2.3).

$$A(\beta,t) = \sin\left(\frac{2\pi}{\lambda_\beta}\left(\beta - V_{ph}t\right)\right), \quad V_{ph}t \le \beta \le L + V_{ph}t, \tag{5.2.1}$$

$$B(\beta,t) = \begin{cases} \sin^2\left(\dfrac{a\pi}{L}\left(\beta - V_{ph}t\right)\right) & V_{ph}t \le \beta \le \dfrac{L}{2a} + V_{ph}t, \\ 1 & \dfrac{L}{2a} + V_{ph}t < \beta \le \dfrac{2a-1}{2a}L + V_{ph}t, \\ \sin^2\left(\dfrac{a\pi}{L}\left(\beta - V_{ph}t\right)\right) & \dfrac{2a-1}{2a}L + V_{ph}t < \beta \le L. \end{cases} \tag{5.2.2}$$

$$C(\beta) = \begin{cases} \sin^2\left(\dfrac{\pi}{2\beta_d}\beta\right) & 0 \le \beta \le \beta_d, \\ 1 & \beta_d < \beta \le \beta_{max} - \beta_d, \\ \sin^2\left(\dfrac{\pi}{2\beta_d}\left(\beta - \beta_{max}\right)\right) & \beta_{max} - \beta_d < \beta \le \beta_{max}. \end{cases} \tag{5.2.3}$$

$$b_\gamma(\beta,t) = A(\beta,t) \times B(\beta,t) \times C(\beta) \tag{5.2.4}$$

To explain the new terms: λ_β is the wavelength on the driven boundary; V_{ph} is the phase speed; L is the total length of the packet found from the number of cycles in β multiplied by the wavelength; a is a parameter used in determining the width of the packet envelope; β_d is where the spatial profile switches to become constant in function C; β_{max} is the end point of the β domain. The function A generates a constant amplitude sinusoidal wave packet which propagates in the positive β direction. B creates a smooth packet envelope, while C is a purely spatial envelope, ensuring that when the disturbance enters the domain

of interest, it does so in a continuous fashion over all times. This driver can be pictured as a propagating wave packet, entering the domain at $\beta = 0$, where the domain of interest extends from $\beta = 0$ to $\beta = \beta_{max}$.

As with the previous box model simulations, we can follow an invariant in the code describing the total energy, as described in Chapter 2, equation (2.5.2). This is plotted over time for the simulation in Figure 5.2.3 (a). This shows that over the initial portion of the driven phase, energy enters the domain, but in the latter phase of driving, the total energy decreases. Once the driver is switched off, there is a decay in the energy due to the dissipation enforced by the non zero linear drag term added to the equation of motion. To consider conservation of energy within the code, we can calculate the expected losses through dissipation. The change in energy over time with the dissipative term added to the equation of motion has the form

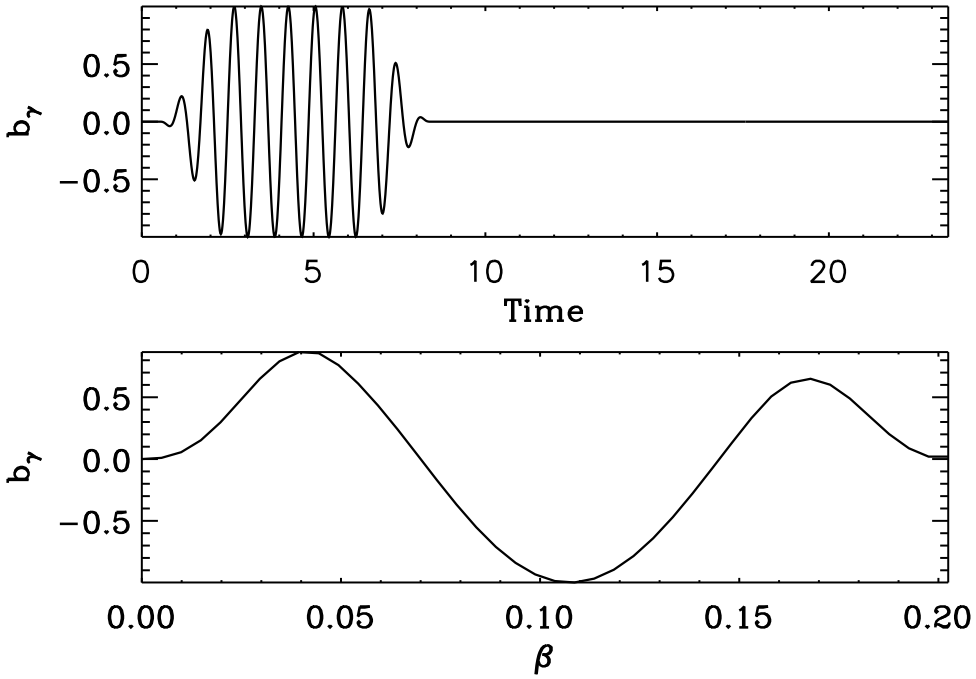

Figure 5.2.2: Upper panel: variation of b_γ in time in the middle of the magnetopause boundary ($\alpha = 1.0$, $\beta = 0.1$). Lower panel: variation of b_γ in space at a time during the driven period.

$$\frac{\mathrm{d}W}{\mathrm{d}t} = -\nu \int \rho u^2 dV = -L,$$

where W is the total energy and L represents the total losses. Integrating in time yields

$$W(t) + \int L dt = c, \tag{5.2.5}$$

for some constant c. Figure 5.2.3(b) plots the left hand side of (5.2.5) over time. Clearly once the driver is switched off (at $t \sim 8.5$), the curve becomes constant, and can be shown to be conserved to 1 part in 10^4 or better. This indicates that the code is consistently solving the equations as desired.

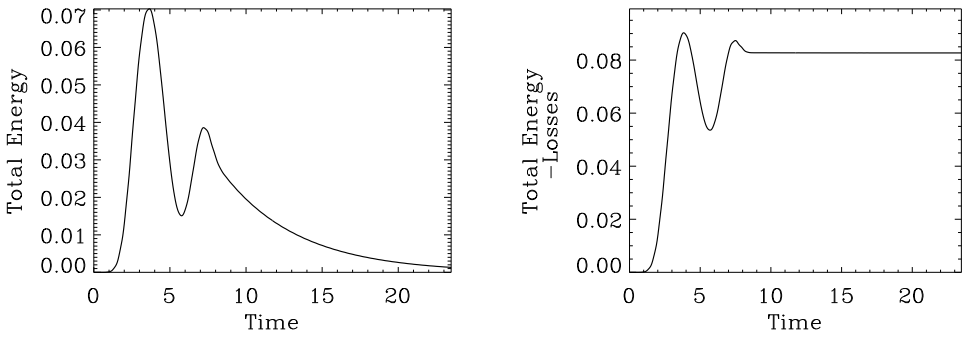

(a) (b)

Figure 5.2.3: (a) Total energy against time. (b) Total energy with the integrated losses accounted for.

Figure 5.2.4 displays time series of each of the components of the magnetic and velocity fields at the predicted resonance location of $\alpha = 0.9$. The toroidal components b_β and u_β in panels two and five respectively are clearly dominant, with growth during driving as expected at the resonance location. The dissipation causes the slow decay of these components post driving. The fast mode component b_γ is essentially zero which is also consistent with the Alfvénic modes being dominant. Further evidence of the excitement of a resonance within the domain is provided in Figure 5.2.5, showing shaded surfaces of u_β at increasing times. Over time, smaller and smaller scales are generated around the resonance location at $\alpha = 0.9$, a characteristic of Alfvén wave phase mixing (see for example, Mann et al. [1995] Figure 2; Russell and Wright [2010] Figure 4.)

Overall, the case presented has validated many aspects of the code. The driven boundary has been effectively implemented, such that in future runs we have confidence in being able to define any wavelength or phase speed of driving to suit the problem. The code is conserving energy and hence is consistently solving the equations. We have been able to excite a resonance at a chosen point within the domain, something that will be done in future runs. Furthermore, the dissipation is behaving as expected, which will become key in later simulations where the system is steadily driven for many periods.

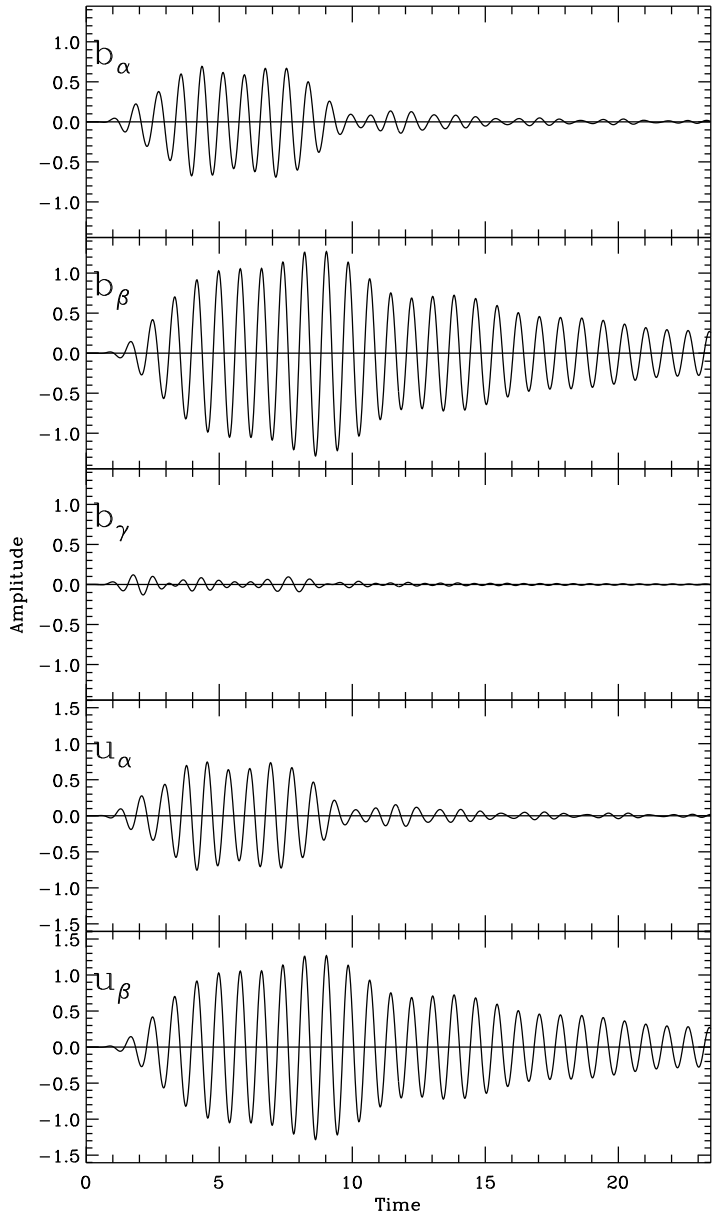

Figure 5.2.4: Magnetic field components (panels one to three) and velocity components (panels four and five) against time at the location ($\alpha = 0.9, \beta = 0.099, \gamma = 0.1$), with the α position being the location of the resonance.

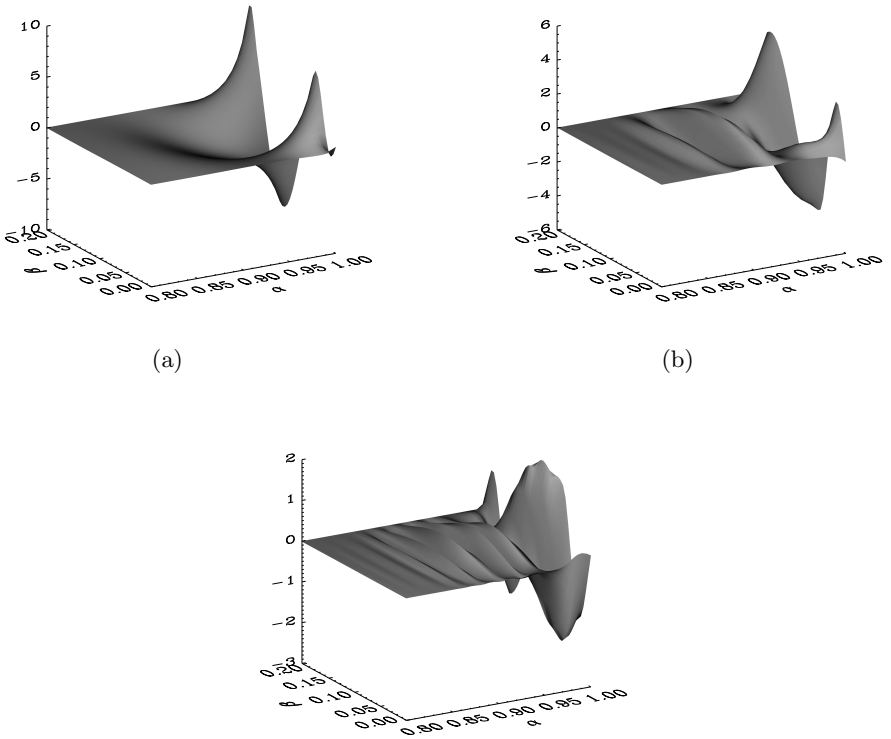

(a) (b)

(c)

Figure 5.2.5: Shaded surfaces in (α, β) of u_β in the equatorial plane, at times (a) 4.69, (b) 12.52 and (c) 21.91.

5.3 Results

We now consider a simulation of a 3D Alfvén resonance, using an extended domain, which will include far greater inhomogeneity than the previous test case. Many intermediate cases have been tried which have furthered our understanding and have more rigorously tested the numerical routines. These are omitted for brevity and we simply include the case which explores the furthest. We choose a domain which extends over $\alpha : 0.6 \to 1.0$ (radially) and $\beta : 0 \to 0.8$ (azimuthally). The upper extent of the domain in γ is determined by first choosing the R_g field line as $\alpha = 0.8$. Recall that on this field line, the γ coordinate represents path length along this background field. We choose $\phi = 0.9$, where ϕ gives the angle in radians from the equator to the R_g field line (see Figure 5.1.1). This determines the domain size in γ as $\gamma : 0 \to 0.72$, which is simply the arc length of the sector of a circular field line at radius 0.8 over an angle of 0.9 radians. Referring to Figure 5.1.4(a) displaying the variation of the ratio of the fundamental toroidal to poloidal Alfvén eigenfrequencies with ϕ, we observe that a ratio of approximately 1.45 is expected for $\phi = 0.9$. This is a significant difference, which should yield interesting variations to the Cartesian case.

Dissipation regions are implemented at each end of the waveguide in β as discussed previously. These span $\beta : 0 \to 0.15$ and $\beta : 0.65 \to 0.8$, leaving the region of interest as $\beta : 0.15 \to 0.65$. These regions can be shown to effectively dissipate any perturbations such that no reflection from the boundaries returns to this interior region.

The Alfvén speed is chosen to vary only with azimuth. This simplification, particularly neglecting the variation along the field line, drastically aids with the CFL constraints. The domain naturally provides a variation in the Alfvén eigenfrequency with α, and the imposed Alfvén speed profile provides a variation with β. To state this simply, the natural frequencies are different at each point in (α, β) and could represent a simple model of a flared flank waveguide. The variation of the Alfvén speed with β is given in Figure 5.3.1, with the mathematical representation given as

$$V_A(\beta) = \begin{cases} 1 & 0 \leq \beta \leq \beta_{V_{A1}}, \\ 1 - \delta_{V_A} \sin^2 \left[\dfrac{\pi}{2} \left(\dfrac{\beta - \beta_{V_{A1}}}{\beta_{V_{A2}} - \beta_{V_{A1}}} \right) \right] & \beta_{V_{A1}} < \beta < \beta_{V_{A2}}, \\ 1 - \delta_{V_A} & \beta \geq \beta_{V_{A2}}, \end{cases} \tag{5.3.1}$$

where $\beta_{V_{A1}} = 0.175$ and $\beta_{V_{A2}} = 0.625$, and δ_{V_A} gives the overall change in the value of V_A and has a value here of $\delta_{V_A} = 0.40234$. Uniform V_A regions exist at either end of the waveguide in β where a 2D purely toroidal resonance will form. A decrease in V_A with β in the interior region will imply the point where the Alfvén frequency matches the driving frequency will move inward toward shorter field lines. The profile of V_A is chosen

specifically such that the uniform regions lead to 2D toroidal resonances at approximately $\alpha = 0.95$ and $\alpha = 0.65$ for the chosen driving frequency. The question is how much of each mode, poloidal and toroidal will be excited between these two uniform regions, which is to say, what path will the resonance take? This is perhaps the most intriguing question we address, and one to which the answer is not known.

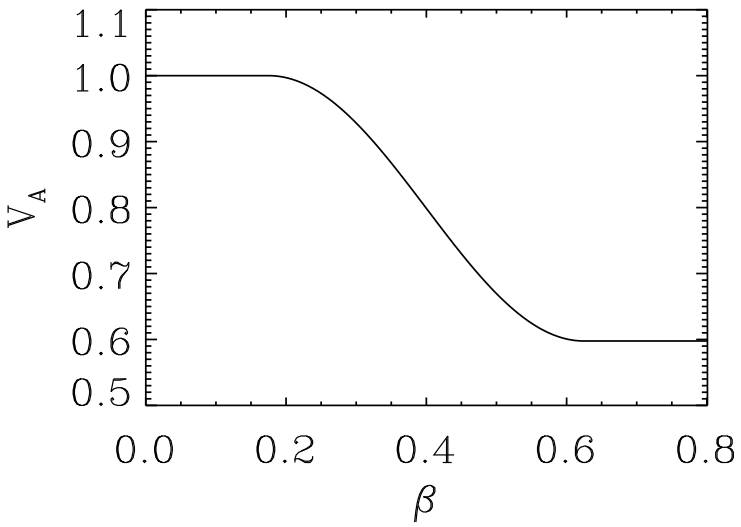

Figure 5.3.1: V_A variation with β. V_A is invariant in α and γ.

The outer boundary at $\alpha = 1.0$ is driven continuously over the course of the simulation. This is intended to set up a steady state in the interior, where the narrowing of length scales caused by phase mixing has been limited by the applied dissipation. The time required to reach such a state and the final resonance width, will be dependent on the dissipation. We opt for a dissipation value of $\nu = 0.04$ and run for many decay times $(1/\nu)$ to reach a steady state. The frequency of the driver is chosen as $\omega = 2.0709$ to excite a toroidal resonance in the left hand uniform V_A region at $\alpha = 0.95$. For these parameters, the fast mode will have an evanescent structure throughout the domain (given $k_\beta \neq 0$ which is always the case here). This can be adjusted to some extent by changing the wavelength of the driver: by decreasing the azimuthal wavenumber k_β, but increasing the driver phase speed to maintain the same driven frequency, we can reduce the evanescence allowing more power to reach the resonance. We take the wavelength of the driver as $\lambda_\beta = 10$, such that only a small portion of a wavelength is present on the boundary at any one time. This still produces a clear driving frequency in the interior.

Figure 5.3.2 displays shaded surfaces of what we have called the 'flux tube energy density (FTED)'. This quantity is obtained by integrating the total energy along a field line in γ, hence finding the energy residing in a flux tube of unit area cross section in the equatorial

plane at any one time. This allows a clean view of the energy in the (α,β) plane to examine the resonance structure through accumulation of energy density. The FTED is a key quantity for interpreting our results. In Figure 5.3.2(a) the resonant surface is evidently distinguishable from the background, forming a clear contour in the plane. A rotated view is shown in Figure 5.3.2(b). These very neatly show the coupling to a 3D resonance. This surface presumably represents the locations where the natural Alfvén eigenfrequency matches the driven frequency. Also clear is how the evanescence of the fast mode controls the amplitude of the resonance, with less power reaching the inner α region resulting in a smaller resonance. The choice by the medium of such a contour will be discussed in detail in the discussion to follow. Figure 5.3.2(c) shows a view above the (α,β) plane, which highlights the resonant path. Also present are 'ripples' away from either side of the main contour, but predominantly toward lower values of α and β. These are well resolved structures that will be investigated in the discussion section.

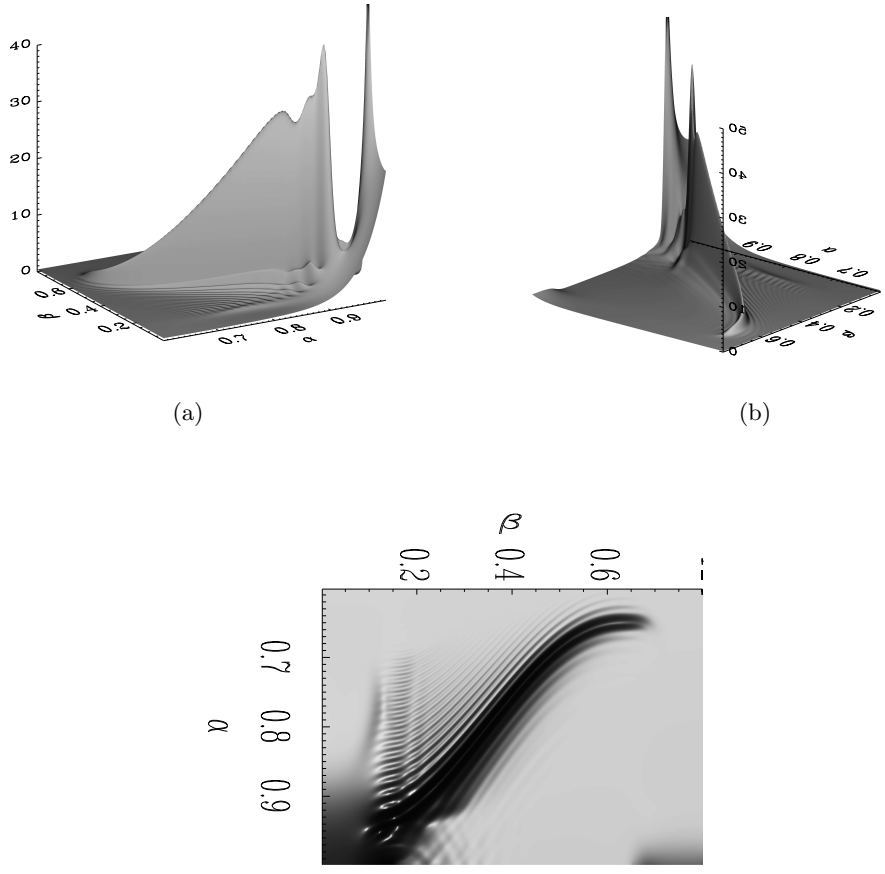

Figure 5.3.2: Shaded surfaces of the flux tube energy density (FTED, explained in the main section) in the (α,β) plane from different angles at the final simulation time.

It can also be confirmed that the position of the resonance in α and β is the same at

different points along the field line i.e. at different values of γ. Figure 5.3.3 plots the energy density at γ values (a) $\gamma = 0.232$ and (b) $\gamma = 0.511$. The resonance position does not change between the two plots, which gives confidence that the resonant contour displayed through shaded surfaces of the FTED shown in Figure 5.3.2 is correctly placed.

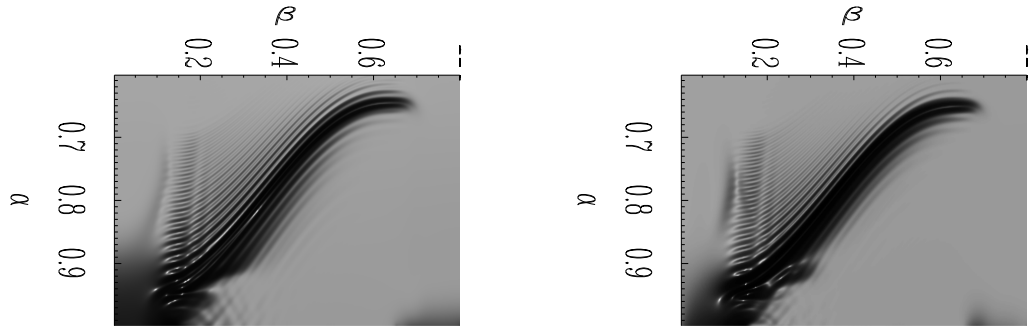

(a) (b)

Figure 5.3.3: Shaded surfaces of the energy density in planes of constant γ at (a) $\gamma = 0.232$ and (b) $\gamma = 0.511$, to demonstrate that the resonance position is fixed in (α,β), for all γ.

Figure 5.3.4 (a) displays a cut of the FTED in the α direction at $\beta = 0.4$, with Figure 5.3.4 (b) giving a cut in β at $\alpha = 0.757$. Therefore these cuts intersect at the point ($\alpha = 0.757$, $\beta = 0.4$) which lies on the resonant contour. These plots display the similar resonance widths, as has been tailored by the gradient of the Alfvén speed profile and the waveguide dimensions. This was done such that a similar resolution was required in each direction, to have at least ten grid points across the phase mixing length (which corresponds to the resonance width). Figures 5.3.4 (c) and (d) show the variation across the resonance in α, of u_α and u_β respectively. The typical 180° phase change associated with resonances is observed. The rippling away from the resonance seen in the previous FTED plots is also clear.

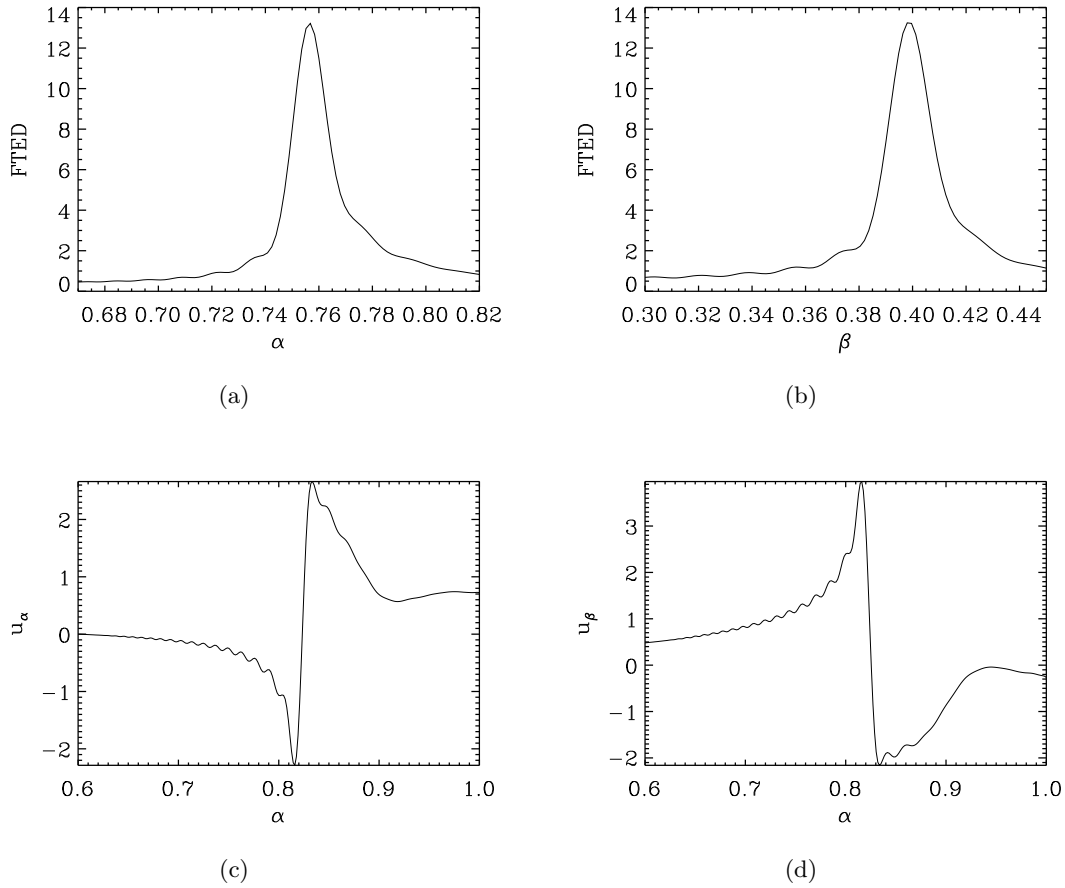

Figure 5.3.4: Cuts in (a) α at $\beta = 0.4$ and (b) β at $\alpha = 0.757$ of the FTED displaying the resonance widths. Variation of (c) u_α and (d) u_β with α, showing the change of polarization across the resonance.

5.4 Discussion

The above results present, as far as we are aware, some of the first insights into three dimensional fast-Alfvén wave coupling, identifying processes that will operate in the Earth's magnetosphere. The resonant contour has a clearly defined shape in the (α, β) plane, but how do the toroidal and poloidal modes combine to produce such a contour? Furthermore, is this contour unique? Or is its position determined by the uniform V_A regions at either end of the waveguide, providing some kind of 'initial condition' for the solution to follow. We are at a preliminary stage of analysing these results, but still have drawn some interesting conclusions.

Russell and Wright [2010] found that in the 2D Cartesian case, the dominant velocity contribution at the resonance is parallel to the resonant contour. Hence we are expecting a similar situation here. Figure 5.4.1(a) shows the perpendicular velocity hodogram taken

at a point on the resonance, namely ($\alpha = 0.757$, $\beta = 0.398$) in the equatorial plane ($\gamma = 0$), where there is an antinode of $u_\perp$. This aligns well with a close up of the resonant contour shown in Figure 5.4.1(b), suggesting that indeed the dominant velocity contribution is parallel to the resonant contour.

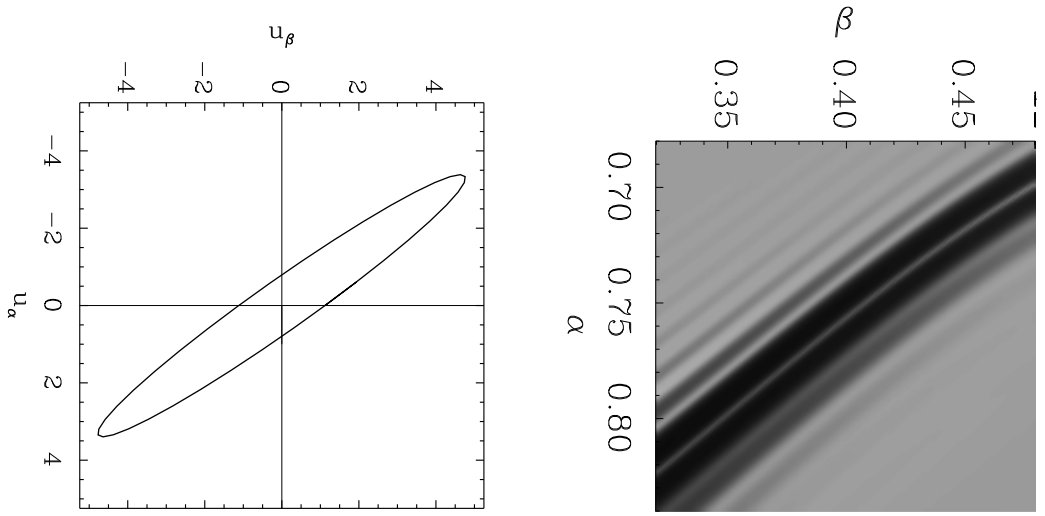

(a) (b)

Figure 5.4.1: (a) Perpendicular velocity hodogram at location ($\alpha = 0.757$, $\beta = 0.398$), $\gamma = 0$), rotated by 90° to match the waveguide plots coordinate axes. (b) FTED from an aerial view, zoomed in on the appropriate section of the resonant contour.

Wright (private communication, March 2016) hereafter Wright [2016], has suggested that the formulation for the Alfvén frequency given by Singer et al. [1981] can be adapted to explain this result by introducing a local coordinate system (α',β') aligned with the resonant contour. Evidently the Alfvén frequency depends upon the location and the polarization of the Alfvén wave, which we denote by the angle θ that the Alfvén perturbations make to the β axis. Hence $\omega_A = \omega_A(\alpha, \beta, \theta)$. With β' along the resonant contour, Wright [2016] has shown the appropriate scale factors on a given field line are

$$h'_\alpha(\gamma) = h_\alpha(\gamma) h_\beta(\gamma) \sqrt{\frac{h_\alpha^2(0)\sin^2\theta + h_\beta^2(0)\cos^2\theta}{h_\alpha^2(\gamma)\sin^2\theta + h_\beta^2(\gamma)\cos^2\theta}}, \tag{5.4.1}$$

$$h'_\beta(\gamma) = h_\beta(0) \sqrt{\frac{h_\alpha^2(\gamma)\sin^2\theta + h_\beta^2(\gamma)\cos^2\theta}{h_\alpha^2(0)\sin^2\theta + h_\beta^2(0)\cos^2\theta}}, \tag{5.4.2}$$

where h_α, h_β are the previously defined scale factors in α and β respectively. We expect ω_A for the β' direction to match the driving frequency, ω_d such that

$$\omega_A(\alpha, \beta, \theta) = \omega_d. \tag{5.4.3}$$

Since the orientation of the contour in the (α,β) plane also has a slope of θ,

$$\frac{\mathrm{d}\alpha}{\mathrm{d}\beta} = \tan\theta. \tag{5.4.4}$$

Wright [2016] also notes that equations (5.4.3) and (5.4.4) supply an ODE for the resonant contour, but shows that this contour is just one of a whole family as follows: combining (5.4.3) and (5.4.4) gives an equation of the form

$$\frac{\mathrm{d}\alpha}{\mathrm{d}\beta} = F(\alpha, \beta, \omega_d) \Rightarrow G(\alpha, \beta, \omega_d) = const, \tag{5.4.5}$$

where G defines the resonant contour. Hence there are several contours along which the Alfvén frequency can match the driving frequency. We shall now explore these speculations and confirm their validity.

We begin with the calculation of the Alfvén frequency $\omega_A(\alpha, \beta, \theta)$. As mentioned above, we choose to rotate our coordinates to align with the resonant contour. This changes the scale factors h_α,h_β from describing the poloidal/toroidal directions to h'_α,h'_β describing the directions perpendicular/parallel to the resonance respectively. We have defined θ as the angle the resonant contour makes with the β axis. Hence for $\theta = 0$, we have a toroidal resonance and for $\theta = \pi/2$, a poloidal resonance. The contributions to the Alfvén frequency from each of the modes can be considered by solving the rotated version of the Alfvén wave equation (5.1.21) for each value of θ over $0 \rightarrow \pi/2$. We simply replace h_α and h_β in these equations with h'_α and h'_β as defined in equations (5.4.1) and (5.4.2). This is done for a chosen field line at $\alpha = 0.8$, with an Alfvén speed of $V_A = 0.8697$, corresponding to the Alfvén speed at the β location of the resonance for this field line in the above simulation. The resulting natural frequencies are plotted against θ in Figure 5.4.2. The gradients are zero for $\theta = 0, \pi/2$ as the resonant contour approaches the purely toroidal or poloidal configurations. This curve (as may be expected from the dependence of h'_α and h'_β on θ) shows the relation between the orientation of the resonant contour and the natural frequency. Indeed we can see that for the above simulation with a driving frequency of $\omega_d = 2.0709$, the expected angle is $\theta \sim 0.67$. The value of $d\alpha/d\beta$ for the contour can be estimated from a close inspection of Figure 5.3.2(c) as 0.8 (at $\alpha = 0.8$). Then calculating θ from equation (5.4.4) gives 0.67, which is in excellent agreement with the estimated value of $\theta = 0.67$ from Figure 5.4.2.

We can extend this idea to solving over the whole domain using equation (5.4.4). Given a start location in the domain (α_0,β_0), the value of θ such that the Alfvén eigenfrequency

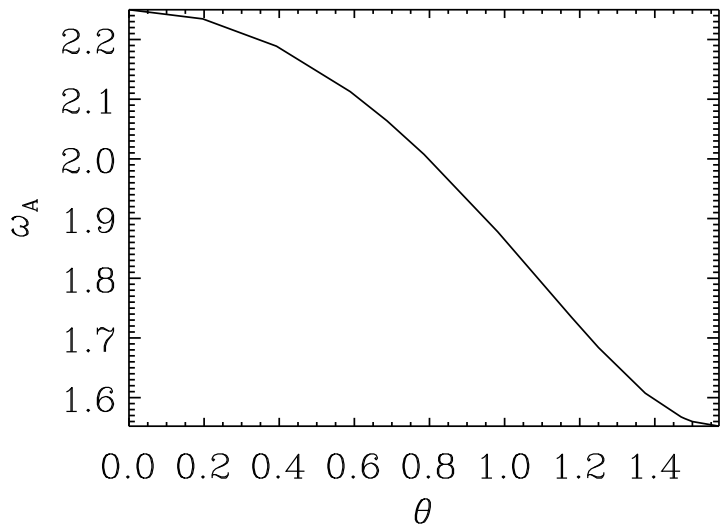

Figure 5.4.2: Alfvén eigenfrequency plotted against the angle of the resonant contour, θ.

matches the driving frequency can be determined, just as implemented above. Together with a chosen step size in β, say d_β, we can use a simple Euler method to determine the step in α, d_α. We then move to the new position $(\alpha_0 + d_\alpha\ ,\ \beta_0 + d_\beta)$ and repeat the process. This is continued until a value of θ such that the Alfvén eigenfrequency matches the driven frequency, cannot be found. In this way, several solution curves can be traced, as shown in Figure 5.4.3, where the Alfvén speed profile is taken as in Figure 5.3.1. A start value of $\beta = 0.15$ has been chosen for each curve, modelling the beginning of the waveguide 3D structure used in the simulations. It is interesting to note that only initial values leading to a resonant contour very close to that of the main contour found in the simulations continue for the full length in β. Solutions that are terminated early clearly enter a region where the driving frequency lies outwith the continuum of Alfvén eigenfrequencies found by varying θ, such as in Figure 5.4.2. It had been thought that the solution curves found would explain the 'ripples' observed around the main resonant contour in Figure 5.3.2. However, it appears that in Figure 5.4.3 the curves are diverging away from the main resonant line, whereas in the simulation, the ripples (Figure 5.4.3) lie parallel. Understanding the meaning of these ripples is an ongoing investigation.

Another aspect of interest brought up by the simulations is how the resonant line is chosen. The uniform Alfvén speed regions at either end of the waveguide could act like initial conditions in some sense, with the resonance being forced to choose a path linking these regions. To investigate this, we consider a similar simulation to that presented above in Section 5.3, except with a linear Alfvén speed profile without any uniform V_A regions. This means there are no sections that are invariant in β, i.e. the 2D case where the

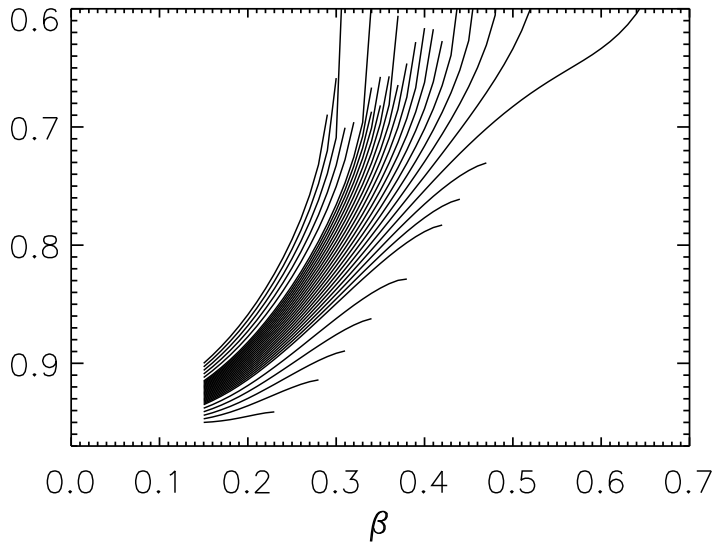

Figure 5.4.3: Solution curves for various initial values of α and β, where along a curve, the Alfvén eigenfrequency matches the driven frequency of $\omega_d = 2.0709$.

resonant location is well defined. Figure 5.4.4(a) shows the Alfvén speed variation with β, with values similar to the previous simulation such that a resonance can exist within the domain. Figure 5.4.4(b) shows an aerial view of the FTED, as plotted for the previous simulation in Figure 5.3.2(c). This reveals that a dominant resonant contour still forms without the uniform Alfvén speed regions guiding the solution. It is encouraging that a 3D FLR can still be excited in a more realistic scenario. For example, it could have been that the energy was dispersed across many resonant curves as shown in Figure 5.4.3. Instead it is clear that there is a preferential contour, however, the choice of this contour remains unresolved.

The efficiency of the coupling between 2D and 3D FLRs can also be investigated. Using two identical simulations, differing only in the Alfvén speed profile, we can investigate this idea. For a 2D resonance, V_A is constant everywhere, the value of which will determine the location in α of the resonance. The resonance amplitude is determined in large part by the distance from the resonance to the turning point of the fast mode. Hence we choose a value of the Alfvén speed in the 2D case such that at this value of α there is a resonance in the 3D case also. Figures 5.4.5(a) and (b) are taken from the 3D resonant case, which are very similar to the simulation run presented in Section 5.3. (a) shows the shaded surface of the FTED, while (b) shows a cut in α at $\beta = 0.16$ to look at the amplitude of the resonance peak. Comparing these to the 2D resonant case in Figures 5.4.5(c) and (d), the amplitudes are of a similar order. This is extremely useful in showing that the 3D FLR can be excited as efficiently as the 2D case. It could have easily been that the 3D FLR

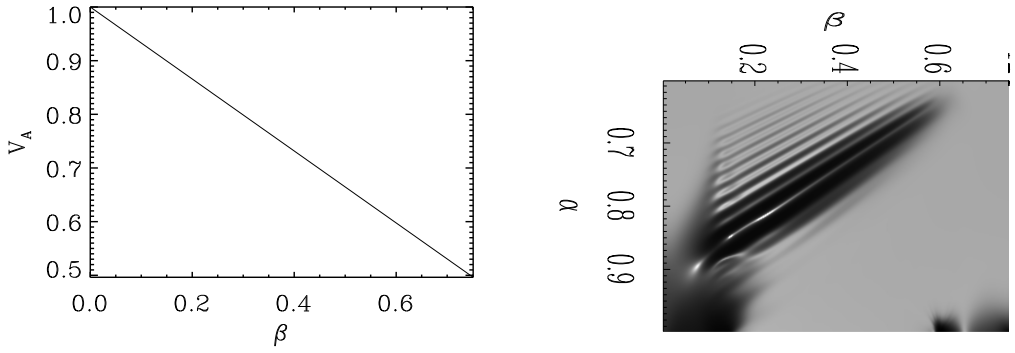

(a) (b)

Figure 5.4.4: (a) Alfvén speed variation with β. (b) Flux tube energy density from above, showing the location of the resonant contour in the (α, β) plane.

was massively more inefficient, however we now seem to have evidence that this is not the case.

5.5 Chapter Summary

In this chapter we have considered modelling Alfvén resonances in a 3D waveguide using a 2D dipole background magnetic field model. The main points are as follows:

- Developed a set of coordinates using functions of the classical 2D dipole coordinates. This radically reduced the grid spacing issues and hence CFL constraints along field lines, which occur when using the scalar potential as the field aligned coordinate. This allowed the modelling of a complex system with a relatively simple computer code (no parallelisation required).
- Developed numerical routines (from scratch) to solve the cold plasma equations in the new dipole coordinates. These were thoroughly tested and were shown to consistently solve the equations, sufficiently conserving energy.
- Explored the shape of the 3D resonant contour. Different Alfvén eigenfrequencies in different directions (unlike in the Cartesian case) imply that the orientation of the contour changes the natural frequency. Before these simulations, many aspects of 3D FLRs remained unrecognised. It was unknown whether a 3D FLR could be formed efficiently or whether the fast mode energy would couple to many resonant regions. We have shown however that there is still a dominant, preferred resonant contour in 3D.

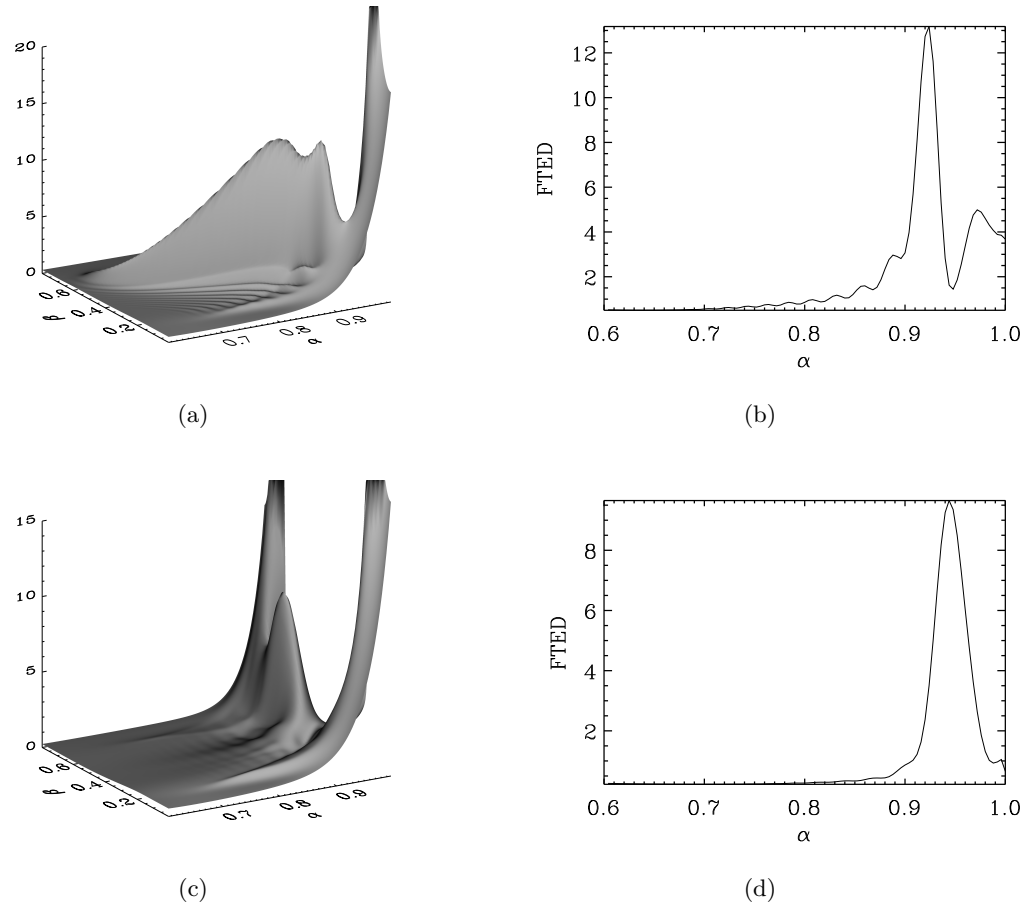

Figure 5.4.5: 3D resonance: (a) shaded surface of the FTED; (b) cut in α at $\beta = 0.16$ of the FTED showing the resonance peak. 2D toroidal resonance: (c) shaded surface of the FTED; (d) cut in α at $\beta = 0.499$ of the FTED.

There is still work to be done here to resolve some of the questions which have arisen from the simulations. Firstly, the ripples which seem to emanate from the main resonant contour need to be explained. They do not seem to represent separate solutions where the Alfvén frequency matches the driven frequency and so a different reasoning is required. Secondly, a further study pushing the latitudinal extent through larger values of ϕ could reveal how significant the difference between the Alfvén frequencies is. It is still unknown how much of an effect the differing frequencies has, considering a main resonant contour is still formed in the simulation presented above as in the Cartesian case. This is for a frequency ratio of $\omega_\beta/\omega_\alpha = 1.45$, so what happens if this ratio is 1.6 or 1.8? Increasing ϕ (the latitude of the fieldline ends) however, would be substantially more computationally expensive. Despite these questions, we feel this has been a very successful preliminary study, providing insight into the nature of driven 3D FLRs.

5.6 Thesis Conclusions and Future Work

This thesis has studied various features of ULF waves in Earth's magnetosphere. We began by developing and testing the required numerical routines, which have been used throughout, to solve the cold plasma equations in a Cartesian box model of the magnetosphere. Using this model, we were able to compare our simulation results with two space based observations of ULF waves. Both observations were of cavity/waveguide modes coupling to FLRs. The simulations provided further insight into these observations, that we managed to neatly describe solely in terms of waveguide modes. This demonstrates the power of modelling and theory in helping to critique the observations. Furthermore, the study describes how the Poynting vector can be used to help identify the source location relative to the spacecraft and to measure the driven period of the oscillation.

The Cartesian box model was also adopted in the study of Chapter 4, where we developed an analytical method to describe propagating waveguide modes. This works on the basis that in the flank magnetosphere, compressional waveguide modes propagate azimuthally but have a mixed standing/propagating nature radially. In this way, we can express these modes in terms of incident and reflection coefficients. Two simulations using the previously described numerical method were used to test this analytical method. The first had a dissipation region at a location in the interior and the second coupled to a FLR. In this way, we showed a reduction in the reflection of the modes in both simulations, which in the second was consistent with the standard coupling efficiency of fast-Alfvén modes.

Finally, we moved from the Cartesian regime into a 2D dipole magnetic field model (with one invariant direction), which we used to study the coupling of fast to Alfvén waves in a 3D geometry. This required the development and testing of new numerical routines and the implementation of a staggered grid. To this end, we derived a new set of field aligned coordinates as functions of the classical 2D dipole coordinates. This helped to massively reduce the resolution issues which occur when using the magnetic scalar potential of the classical 2D dipole as the field aligned coordinate. The main point of interest was to investigate the effect of differing poloidal/toroidal Alfvén eigenfrequencies with increasing latitude. We managed to derive some preliminary results, which showed that a preferred resonant contour can be efficiently formed in a 3D geometry. However, the full effects of the added inhomogeneity of the dipole are still to be investigated.

This leads on to the future work and obvious avenues of study arising from the work in this thesis. Continuing with the 2D dipole model, there are features of the current simulations which need to be resolved and extended, as discussed at the end of Section 5.5. Taking this further, we could consider a steady state solution to the cold plasma equations in the derived dipole system, as after all, that is the situation that we achieve in the simulations by constantly driving. This should provide a good comparison to the current simulation

results. If desired, the numerical routines could be parallelised, such that larger latitudinal extends could be considered. However, this would have to be weighed up against other means of deriving information from the system, since parallelising such lengthy routines is no mean feat.

The second area which could be developed further is the work of Chapter 4. The analytic method derived for determining incident/reflection coefficients of tailward propagating waveguide modes could be applied to real satellite data. We are currently working with collaborators on satellite observations to hopefully provide observations of such events valid for use with our method. This will be an exciting venture, providing the ultimate test for the theory. Overall, this summarises well the outline of the thesis given at the end of the introduction: 'to work with the observations, and to attempt to provide well founded explanations for the observed physical phenomena'. To this end, we believe that the work in this thesis merits this statement.

Appendix A

Solution Method for Finding Incident and Reflection Coefficients

We outline the solution method for solving the system of equations (4.1.22)-(4.1.27). From satellite data it is assumed that the amplitudes of b_x, b_y, b_z and u_x (denoted by $\bar{b_x}$, $\bar{b_y}$, $\bar{b_z}$ and $\bar{u_x}$) are known. Further to this, we require the frequency ω, the Alfvén speed V_A and the phase difference between b_y and b_x, denoted by ϕ (refer to Section 4.1.2 for full details on ϕ). As discussed at the end of Section 4.1.1, one of the wavenumbers is also required to solve the system. In each of the sections below, we discuss the different approaches depending on which wavenumber is estimated most accurately. Firstly however, we must resolve the choices of signs in equations (4.1.22)-(4.1.27). Since it is the amplitudes of the components (denoted by an overscore) that are being used, the expressions for these amplitudes must be positive. Hence the choice of sign is dependent on the signs of $\sin(k_z z)$ and $\cos(k_z z)$. For a fundamental mode in the $\hat{\mathbf{z}}$ direction, $-\pi/2 < k_z z < \pi/2$. $\cos(k_z z)$ is positive over the range of $k_z z$, and hence the signs in equations (4.1.24) and (4.1.25) are taken to be positive. If the observation is taken below the magnetic equator, z is less than zero, which implies $\sin(k_z z) < 0$ and hence we choose negative signs for equations (4.1.22) and (4.1.23) such that the amplitudes remain positive. Equally if the satellite is above the magnetic equator, positive signs are taken in these equations.

There is one exception to this which occurs when k_y is negative, since k_y appears as a coefficient in (4.1.23). If the observation is in the dusk flank, take k_y to be positive, and if in the dawn flank, take k_y to be negative. This stems from the positive $\hat{\mathbf{y}}$ direction being tailward in the dusk flank. Therefore in the situation where k_y is negative, the above sign choices must be reversed for equation (4.1.23) such that the amplitude remains positive.

A.1 k_z Measured

To begin with, consider the case where k_z, the field aligned wavenumber, is known from observations. To find the position z we divide (4.1.22) by (4.1.25) to give

$$\begin{aligned} \tan(k_z z) &= \pm\frac{\omega\bar{b_x}}{k_z\bar{u_x}}\frac{1}{B_0}, & \text{(A.1.1)} \\ \Rightarrow k_z z &= \tan^{-1}\left(\pm\frac{\omega\bar{b_x}}{k_z\bar{u_x}}\frac{1}{B_0}\right), & \text{(A.1.2)} \end{aligned}$$

where the sign choice is determined from the position in z above or below the magnetic equator (positive if $z > 0$). k_y can be determined from the ratio of (4.1.24) to (4.1.23), substituting for $\tan(k_z z)$ using (A.1.1) to give

$$\begin{aligned} \frac{\bar{b_z}}{\bar{b_y}} &= \pm\frac{B_0}{\omega k_y}\left(\frac{\omega^2}{V_A^2} - k_z^2\right)\frac{\bar{u_x}}{\bar{b_x}}, \\ \Rightarrow k_y &= \pm\frac{\bar{u_x}\bar{b_y}}{\bar{b_x}\bar{b_z}}\frac{B_0}{\omega}\left(\frac{\omega^2}{V_A^2} - k_z^2\right), & \text{(A.1.3)} \end{aligned}$$

where the plus/minus root is taken for observations on the dusk/dawn flank. $k_x(x)$ can now be determined from the fast mode dispersion relation (2.9.1) as

$$k_x(x) = \sqrt{\frac{\omega^2}{V_A^2} - k_y^2 - k_z^2}, \qquad \text{(A.1.4)}$$

where $k_x(x)$ is taken to be positive (inward and outward propagation in x is accommodated in the definition of b_x in equation (4.1.3)). At this point, $k_z z$, k_y and $k_x(x)$ are known and we can proceed to section A.4 to calculate A_i and A_r.

A.2 k_y Measured

If instead k_y, the azimuthal wavenumber, is provided by satellite data we proceed in a similar manner to the above for k_z. Rearranging (A.1.3) gives

$$k_z = \sqrt{\frac{\omega^2}{V_A^2} - |k_y|\frac{\omega}{B_0}\frac{\bar{b_x}\bar{b_z}}{\bar{u_x}\bar{b_y}}}. \qquad \text{(A.2.1)}$$

The absolute value sign here covers the cases for $k_y > 0$ and $k_y < 0$, which both result in the same expression for k_z. The positive root is taken for k_z since the sign of $k_z z$ is determined by the choice of z either above or below the magnetic equator. The value of $k_z z$ is then determined from A.1.2. Now given k_y and k_z, $k_x(x)$ is determined from (A.1.4) as previously, and we can again proceed to section A.4 to find A_i and A_r.

A.3 k_x Measured

The case where k_x, the radial wavenumber, is provided from observations is not so straightforward as we lack an expression for one of the other wavenumbers in terms of k_x alone. We proceed by rewriting (A.1.3) using (A.1.4) as

$$k_y = \pm \frac{\bar{u_x}\bar{b_y}}{\bar{b_x}\bar{b_z}} \frac{B_0}{\omega} \left(k_x^2(x) + k_y^2\right). \tag{A.3.1}$$

Again the sign for k_y is determined as being positive on the dusk flank and negative on the dawn flank. Rearranging (A.3.1) as a quadratic for k_y and solving yields

$$k_y = \pm \frac{X}{2} \pm \sqrt{\frac{X^2}{4} - k_x(x)^2}, \tag{A.3.2}$$

where

$$X = \frac{\bar{b_x}\bar{b_z}}{\bar{u_x}\bar{b_y}} \frac{\omega}{B_0}. \tag{A.3.3}$$

For $k_y > 0$ choose the first sign to be positive, while for $k_y < 0$ choose the first sign to be negative. The second sign choice represents two distinct solutions which have to be carried through the procedure until they can be tested for their validity. This doubles the total number of possible solutions, and indeed each of the above k_y values can lead to a correct solution. For this reason, it is preferable for the azimuthal or field aligned wavenumbers to be provided instead of the radial wavenumber, as for these cases a single solution can always be determined. Once the values of k_y have been calculated, the corresponding k_z values are determined from the fast mode dispersion relation as

$$k_z = \sqrt{\frac{\omega^2}{V_A^2} - k_y^2 - k_x^2(x)}, \tag{A.3.4}$$

and then the values of $k_z z$ are found from (A.1.2). Now that the wavenumbers are known, proceed to section A.4.

A.4 Determining A_i and A_r

The above steps outline how to determine the wavenumbers depending on which is provided by the observation. The following working shows how then to calculate the incident and reflection coefficients A_i and A_r given the wavenumbers. We begin by squaring (4.1.22) and (4.1.23), then adding and subtracting to give

$$C = \bar{b_x}^2 + \frac{k_x^2}{k_y^2}\bar{b_y}^2 = 2\left(A_i^2 + A_r^2\right)\sin^2(k_z z), \tag{A.4.1}$$

$$D = \bar{b_x}^2 - \frac{k_x^2}{k_y^2}\bar{b_y}^2 = 4A_i A_r \cos(2\Phi_x)\sin^2(k_z z). \tag{A.4.2}$$

We attempt to form the terms on the right hand side of (4.1.26). The denominator can be written using (A.4.1), as

$$A_r^2 - A_i^2 = A_r^2 + A_i^2 - 2A_i^2 = \frac{C}{2\sin^2(k_z z)} - 2A_i^2. \tag{A.4.3}$$

The numerator can be formed using (A.4.2) as

$$2A_i A_r \sin(2\Phi_x) = \pm\frac{1}{2}\sqrt{16A_i^2 A_r^2 - \frac{D^2}{\sin^4(k_z z)}}. \tag{A.4.4}$$

Using (A.4.3) and (A.4.4) in (4.1.26) gives

$$\tan(\phi) = \frac{\pm\frac{1}{2}\sqrt{16A_i^2A_r^2 - \frac{D^2}{\sin^4(k_z z)}}}{\frac{C}{2\sin^2(k_z z)} - 2A_i^2}, \tag{A.4.5}$$

$$\Rightarrow \tan^2(\phi)\left(\frac{C}{2\sin^2(k_z z)} - 2A_i^2\right)^2 = \frac{1}{4}\left(16A_i^2A_r^2 - \frac{D^2}{\sin^4(k_z z)}\right). \tag{A.4.6}$$

The goal is to eliminate A_r in terms of A_i. Expanding brackets and replacing A_r^2 using a rearrangement of (A.4.3), we arrive at a fourth order equation for A_i as

$$A_i^4 - \frac{C}{2\sin^2(k_z z)}A_i^2 + \frac{C^2\sin^2\phi + D^2\cos^2\phi}{16\sin^4(k_z z)} = 0. \tag{A.4.7}$$

The above equation can be written as

$$A_i^4 - PA_i^2 + Q = 0, \tag{A.4.8}$$

$$\Rightarrow A_i^2 = \frac{P}{2} \pm \frac{1}{2}\sqrt{P^2 - 4Q}, \tag{A.4.9}$$

where

$$P = \frac{C}{2\sin^2(k_z z)}, \tag{A.4.10}$$

$$Q = \frac{C^2\sin^2\phi + D^2\cos^2\phi}{16\sin^4(k_z z)}. \tag{A.4.11}$$

(A.4.9) defines four solutions for A_i given C, D, P and Q. Through squaring, spurious roots will have been introduced that will be discarded at the end. A_r is found from rearranging (A.4.3) as

$$A_r = \pm\sqrt{P - A_i^2}. \tag{A.4.12}$$

This implies that there are eight possible combinations of A_i and A_r values. Each of these combinations can then be used to calculate the WKB phase Φ_x. Rearranging (4.1.22) gives

$$2A_iA_r\cos(2\Phi_x) = \frac{\bar{b_x}^2}{\sin^2(k_z z)} - A_i^2 - A_r^2, \tag{A.4.13}$$

$$\Phi_x = \frac{1}{2}\cos^{-1}\left\{\frac{1}{2A_iA_r}\left(\frac{\bar{b_x}^2}{\sin^2(k_z z)} - A_i^2 - A_r^2\right)\right\}. \tag{A.4.14}$$

Taking the inverse cosine results in four solutions for Φ_x, which can be expressed as

$$\Phi_x = \frac{1}{2}\cos^{-1}(\alpha) + n\pi,\ n = 0, 1, \tag{A.4.15}$$

$$\Phi_x = \frac{1}{2}\left(2\pi - \cos^{-1}(\alpha)\right) + n\pi,\ n = 0, 1, \tag{A.4.16}$$

where α is the curly bracketed term in (A.4.14), and $\cos^{-1}$ lies between 0 and π. Thus with four solutions for $\Phi_x(x)$ and eight combinations of A_i and A_r, there are 32 possible solutions. The correct solutions are determined by constructing the components given in (4.1.3)-(4.1.7) using the derived values of A_i, A_r etc, then checking these signals against the data. The solutions associated with the spurious roots acquired during the calculation may be identified and disregarded as the reconstructed signals will not match the original ones. This procedure will leave four valid combinations, one for each of the arbitrary phase choices in (A.4.15) and (A.4.16). Any one of these solutions may be used unless additional information is available to identify a particular solution as being more appropriate.

Appendix B

Derivation of 2D Field Aligned Dipole Coordinates

In this Appendix, we outline the derivation of the coordinates used in the 2D dipole field model, presented in Chapter 5, together with some of their properties. This summarises a private communication with Dr Andrew Wright, January 2016.

B.1 Dipole Coordinate Derivation

Consider the classical 2D dipole coordinates stated in equations (5.1.1)-(5.1.3). We consider new coordinates (α, β, γ) which are functions of the classical 2D dipole coordinates. In this way, the coordinates will share the same contours. Beginning with α:

$$\begin{aligned} \alpha = g(A_z) &= \frac{A_0 R_0}{A_z}, \\ &= \frac{A_0 R_0 R}{A_0 R_0 \cos\phi}, \\ &= \frac{R}{\cos\phi}. \end{aligned} \tag{B.1.1}$$

As per the discussion in Section 5.1 of Chapter 5, we can find the corresponding scale factor as

$$
\begin{aligned}
h_\alpha &= \frac{1}{|\boldsymbol{\nabla}\alpha|}, \\
\boldsymbol{\nabla}\alpha &= \boldsymbol{e_r}\frac{\partial}{\partial R}\left(\frac{R}{\cos\phi}\right) + \boldsymbol{e_\phi}\frac{1}{R}\frac{\partial}{\partial\phi}\left(R\left(\cos\phi\right)^{-1}\right), \\
&= \frac{\boldsymbol{e_r}}{\cos\phi} + \boldsymbol{e_\phi}\frac{\sin\phi}{\cos^2\phi}, \\
|\boldsymbol{\nabla}\alpha| &= \frac{1}{\cos^2\phi}|\boldsymbol{e_r}\cos\phi + \boldsymbol{e_\phi}\sin\phi| = \sec^2\phi, \\
\Rightarrow h_\alpha &= \cos^2\phi. \qquad \text{(B.1.2)}
\end{aligned}
$$

It is easy to see that in the equatorial plane where $\phi = 0$, $h_\alpha = 1$, and α corresponds to radial distance (normalised by R_0) and is equivalent to the L-shell parameter.

For the field aligned coordinate, consider $\gamma = f(\psi)$, where f is chosen such that on a reference field line passing through $(R, \phi) = (R_g, 0)$, γ corresponds to path length along the field line, and hence on this line, $h_\gamma = 1$. Note that R_0 and R_g are different. R_0 will be chosen to be the outer extent of our domain, and we would then normalise all lengths by R_0. R_g is a point somewhere near to the middle of the domain, chosen to optimize the 'grid' spacing, hence the subscript 'g'.

Since we want to specify γ as path length along the R_g field line, we require a general expression for the path length along any field line. An incremental distance along a field line, dS can be expressed in terms of R and ϕ as

$$dS^2 = dR^2 + R^2 d\phi^2.$$

Hence the path length changes with latitude as

$$\frac{\mathrm{d}S}{\mathrm{d}\phi} = \sqrt{\left(\frac{\mathrm{d}R}{\mathrm{d}\phi}\right)^2 + R^2}. \qquad \text{(B.1.3)}$$

A field line is defined by $A_z = const$, which from equation (5.1.2) gives

$$
\begin{aligned}
R &= \frac{A_0 R_0}{A_z}\cos\phi, \\
&= R_{eq}\cos\phi,
\end{aligned}
$$

where $R_{eq} = A_0 R_0 / A_z$ and represents the radius to the equatorial crossing point. From this we can calculate $\mathrm{dR}/\mathrm{d}\phi$ as

$$\frac{\mathrm{d}R}{\mathrm{d}\phi} = -R_{eq}\sin\phi.$$

Then we can evaluate the expression in equation (B.1.3) as

$$\begin{aligned} \frac{\mathrm{d}S}{\mathrm{d}\phi} &= \sqrt{R_{eq}^2\sin^2\phi + R_{eq}^2\cos^2\phi} = R_{eq}, \\ S &= R_{eq}\phi + const, \end{aligned} \tag{B.1.4}$$

where the constant is 0 given that $S = 0$ at $\phi = 0$. Hence along the R_g field line, $S = R_g\phi$. We require that $\gamma = f(\psi)$ such that on the R_g field line, $\gamma = S$ i.e.

$$\gamma = f(\psi) = R_g\phi.$$

Recall from equation (5.1.1) that $\psi = (B_0R_0^2/R)\sin\phi$, which together with $R = R_g\cos\phi$ gives

$$\begin{aligned} \gamma = f(\psi) &= f\left(\frac{B_0R_0^2}{R_g}\frac{\sin\phi}{\cos\phi}\right), \\ &= f\left(\frac{B_0R_0^2}{R_g}\tan\phi\right) = R_g\phi, \end{aligned}$$

which defines the function f. Consider $f(\nu)$ where $\nu = (B_0R_0^2/R_g)\tan\phi$. Then

$$f(\nu) = R_g\phi = R_g\tan^{-1}\left(\frac{\nu R_g}{B_0R_0^2}\right),$$

which follows from $\phi = \tan^{-1}\left(\nu R_g/B_0R_0^2\right)$. Thus we can express γ as

$$\begin{aligned} \gamma &= f(\psi) = R_g\tan^{-1}\left(\frac{R_g}{B_0R_0^2}\psi\right), \\ &= R_g\tan^{-1}\left(\frac{R_g}{R}\sin\phi\right). \end{aligned} \tag{B.1.5}$$

Checking that on the $R = R_g$ field line, γ corresponds to path length along the field line we have

$$\begin{aligned}\gamma &= R_g \tan^{-1}\left(\frac{R_g \sin\phi}{R_g \cos\phi}\right), \\ &= R_g \tan^{-1}(\tan\phi) = R_g\phi,\end{aligned}$$

in agreement with equation (B.1.4). Then we can calculate the scale factor h_γ as

$$h_\gamma = \frac{1}{|\boldsymbol{\nabla}\gamma|},$$

and after some algebra we derive that

$$h_\gamma = \left(\frac{R}{R_g}\right)^2 + \sin^2\phi. \tag{B.1.6}$$

As a check we can show that when $R = R_g\cos\phi$, $h_\gamma = 1$, confirming that γ corresponds to path length on the R_g field line.

$$h_\gamma(R_g) = \cos^2\phi + \sin^2\phi = 1.$$

Thus, equations (B.1.1), (B.1.2), (B.1.5) and (B.1.6), together with assuming β as the cylindrical polar coordinate z, with $h_\beta = 1$, yields the coordinate system defined by equations (5.1.5)-(5.1.10) in Chapter 5.

B.2 Deriving Scale Factors as Functions of α, γ

For use in the numerical method for solving the system of equations given by (5.1.11)-(5.1.15), we need to express the scale factors h_α and h_γ in terms of α and γ. We begin by expressing ϕ and R in terms of α and γ. Consider rewriting equations (5.1.5) and (5.1.7) as

$$\cos\phi = \frac{R}{\alpha}, \tag{B.2.1}$$

$$\sin\phi = \frac{R}{R_g}\tan\left(\frac{\gamma}{R_g}\right), \tag{B.2.2}$$

respectively. Thus we can express ϕ by dividing equation (B.2.2) by equation (B.2.1) to give

$$\begin{aligned}\tan\phi &= \frac{\alpha}{R_g}\tan\left(\frac{\gamma}{R_g}\right),\\ \Rightarrow \phi &= \tan^{-1}\left[\frac{\alpha}{R_g}\tan\left(\frac{\gamma}{R_g}\right)\right].\end{aligned}$$

R can be found from squaring and adding the terms in equations (B.2.2) and (B.2.1) as

$$\begin{aligned}\sin^2\phi+\cos^2\phi=1 &= \frac{R^2}{R_g^2}\tan^2\left(\frac{\gamma}{R_g}\right)+\frac{R^2}{\alpha^2},\\ \Rightarrow 1 &= R^2\left(\frac{1}{R_g^2}\tan^2\left(\frac{\gamma}{R_g}\right)+\frac{1}{\alpha^2}\right)\\ \Rightarrow R &= \left[\frac{1}{R_g^2}\tan^2\left(\frac{\gamma}{R_g}\right)+\frac{1}{\alpha^2}\right]^{-\frac{1}{2}}.\end{aligned}$$

Defining

$$\Lambda(\alpha,\gamma)=\frac{\alpha}{R_g}\tan\left(\frac{\gamma}{R_g}\right), \tag{B.2.3}$$

we can express ϕ and R as

$$\phi(\alpha,\gamma) = \tan^{-1}(\Lambda), \tag{B.2.4}$$

$$R(\alpha,\gamma) = \left[\frac{\Lambda^2}{\alpha^2}+\frac{1}{\alpha^2}\right]^{-\frac{1}{2}}=\frac{\alpha}{\sqrt{1+\Lambda^2}}. \tag{B.2.5}$$

Now the scale factors h_α and h_γ defined in equations (5.1.8) and (5.1.10) can be reformulated in terms of α and γ. We firstly note that

$$\begin{aligned}\cos\phi &= \cos\tan^{-1}(\Lambda)=\frac{1}{\sqrt{1+\Lambda^2}},\\ \sin\phi &= \sin\tan^{-1}(\Lambda)=\frac{\Lambda}{\sqrt{1+\Lambda^2}},\end{aligned}$$

which follow from using standard trigonometric identities. Hence the scale factors become

$$h_\alpha = \cos^2\phi = \frac{1}{1+\Lambda^2}, \tag{B.2.6}$$

$$h_\gamma = \frac{R^2}{R_g^2} + \sin^2\phi = \frac{\alpha^2}{R_g^2\,(1+\Lambda^2)} + \frac{\Lambda^2}{1+\Lambda^2},$$

$$= \frac{1}{1+\Lambda^2}\left(\frac{\alpha^2}{R_g^2} + \Lambda^2\right). \tag{B.2.7}$$

B.3 Showing B Irrotational and Solenoidal

Following Wright [1992], in (α, β, γ) coordinates we require that

$$Bh_\alpha h_\beta = f(\alpha, \beta), \tag{B.3.1}$$

$$Bh_\gamma = g(\gamma), \tag{B.3.2}$$

in order to obtain a magnetic field that is solenoidal ($\boldsymbol{\nabla}\cdot\mathbf{B} = 0$) and irrotational ($\boldsymbol{\nabla}\times\mathbf{B} = 0$) respectively. f and g are arbitrary functions with no relation to any previously defined functions. Recalling that the magnetic field strength is given by $B = B_0R_0^2/R^2$, together with the definitions of R and h_α given by equations (B.2.5) and (B.2.6) respectively, and recalling that $h_\beta = 1$, we have

$$Bh_\alpha h_\beta = B_0R_0^2\left(\frac{1+\Lambda^2}{\alpha^2}\right)\frac{1}{1+\Lambda^2},$$

$$= \frac{B_0R_0^2}{\alpha^2} \equiv f(\alpha, \beta),$$

and hence equation (B.3.1) is satisfied. Moving to the irrotational condition given in equation (B.3.2), using again the definition of R from equation (B.2.5) and h_γ from equation (B.2.7), gives

$$Bh_\gamma = B_0R_0^2\left(\frac{1+\Lambda^2}{\alpha^2}\right)\frac{1}{1+\Lambda^2}\left[\frac{\alpha^2}{R_g^2} + \Lambda^2\right],$$

$$= B_0R_0^2\left(\frac{1}{R_g^2} + \frac{\Lambda^2}{\alpha^2}\right),$$

$$= \frac{B_0R_0^2}{R_g^2}\left(1 + \tan^2\left(\frac{\gamma}{R_g}\right)\right) \equiv g(\gamma),$$

where the final step follows from the definition of Λ in equation (B.2.3). Hence $\mathbf{B}$ is irrotational in our derived coordinates. These checks help confirm the scale factors and coordinates have been derived correctly.

Bibliography

S.-I. Akasofu, editor. *Exploring the Secrets of the Aurora*, volume 346 of *Astrophysics and Space Science Library*, 2007. 11

H. Alfvén. Existence of Electromagnetic-Hydrodynamic Waves. *Nature*, 150:405–406, October 1942. doi: 10.1038/150405d0. 14

H. Alfvén. On the Existence of Electromagnetic-Hydrodynamic Waves. *Arkiv for Astronomi*, 29:1–7, 1943. 16

W. Allan and E. M. Poulter. ULF waves-their relationship to the structure of the Earth's magnetosphere. *Reports on Progress in Physics*, 55:533–598, May 1992. doi: 10.1088/0034-4885/55/5/001. 21

W. Allan, S. P. White, and E. M. Poulter. Magnetospheric coupling of hydromagnetic waves - Initial results. *Geophysical Research Letters*, 12:287–290, May 1985. doi: 10.1029/GL012i005p00287. 14, 116

W. Allan, E. M. Poulter, and S. P. White. Hydromagnetic wave coupling in the magnetosphere - Plasmapause effects on impulse-excited resonances. *Planetary Space Science*, 34:1189–1200, December 1986a. doi: 10.1016/0032-0633(86)90056-5. 20, 22, 116

W. Allan, S. P. White, and E. M. Poulter. Impulse-excited hydromagnetic cavity and field-line resonances in the magnetosphere. *Planetary Space Science*, 34:371–385, April 1986b. doi: 10.1016/0032-0633(86)90144-3. 20, 22, 30, 116

M. O. Archer, M. D. Hartinger, and T. S. Horbury. Magnetospheric "magic" frequencies as magnetopause surface eigenmodes. *Geophysical Research Letters*, 40:5003–5008, October 2013. doi: 10.1002/grl.50979. 24

J. Berchem and C. T. Russell. Magnetic field rotation through the magnetopause - ISEE 1 and 2 observations. *Journal of Geophysical Research*, 87:8139–8148, October 1982. doi: 10.1029/JA087iA10p08139. 108

N. Bone. *The aurora. Sun-earth interactions*. New York: Wiley, 1996. 11

T. J. M. Boyd and J. J. Sanderson. *The Physics of Plasmas*. Cambridge University Press, January 2003. 14

R. J. Bray and R. E. Loughhead. *The solar chromosphere*. The International Astrophysics Series, London: Chapman and Hall, 1974. 37

L. J. Cahill and P. G. Amazeen. The Boundary of the Geomagnetic Field. *Journal of Geophysical Research*, 68:1835–1843, April 1963. doi: 10.1029/JZ068i007p01835. 12

R. L. Carovillano and J. F. McClay. Hydromagnetic Eigenmodes in Multipole Fields. *Physics of Fluids*, 8:2006–2013, November 1965. doi: 10.1063/1.1761149. 115

R. L. Carovillano and H. R. Radoski. Latitude-Dependent Plasmasphere Oscillations. *Physics of Fluids*, 10:225–229, January 1967. doi: 10.1063/1.1761979. 115

D. L. Carpenter. Whistler Evidence of a 'Knee' in the Magnetospheric Ionization Density Profile. *Journal of Geophysical Research*, 68:1675–1682, March 1963. doi: 10.1029/JZ068i006p01675. 12

S. Chapman and J. Bartels. *Geomagnetism*. Number v. 1 in The International series of monographs on physics. Clarendon Press, 1940. URL `https://books.google.co.uk/books?id=_NQgAAAAMAAJ`. 10

L. Chen and S. C. Cowley. On field line resonances of hydromagnetic Alfven waves in dipole magnetic field. *Geophysical Research Letters*, 16:895–897, August 1989. doi: 10.1029/GL016i008p00895. 115

L. Chen and A. Hasegawa. A theory of long-period magnetic pulsations: 1. Steady state excitation of field line resonance. *Journal of Geophysical Research*, 79:1024–1032, March 1974. doi: 10.1029/JA079i007p01024. 18, 115

C.-C. Cheng, C. T. Russell, V. Angelopoulos, I. Mann, K. H. Glassmeier, U. Auster, and W. Baumjohann. THEMIS observations of consecutive bursts of Pi2 pulsations: The 20 April 2007 event. *Journal of Geophysical Research (Space Physics)*, 114:A00C19, April 2009. doi: 10.1029/2008JA013538. 108

P. J. Chi and C. T. Russell. Phase skipping and Poynting flux of continuous pulsations. *Journal of Geophysical Research*, 103:29479–29492, December 1998. doi: 10.1029/98JA02101. 54, 55, 76

S. G. Claudepierre, M. Wiltberger, S. R. Elkington, W. Lotko, and M. K. Hudson. Magnetospheric cavity modes driven by solar wind dynamic pressure fluctuations. *Geophysical Research Letters*, 36:L13101, July 2009. doi: 10.1029/2009GL039045. 22, 46, 117

S. G. Claudepierre, M. K. Hudson, W. Lotko, J. G. Lyon, and R. E. Denton. Solar wind driving of magnetospheric ULF waves: Field line resonances driven by dynamic pressure fluctuations. *Journal of Geophysical Research (Space Physics)*, 115:A11202, November 2010. doi: 10.1029/2010JA015399. 22, 117

L. B. N. Clausen, T. K. Yeoman, R. Behlke, and E. A. Lucek. Multi-instrument observations of a large scale Pc4 pulsation. *Annales Geophysicae*, 26:185–199, February 2008. doi: 10.5194/angeo-26-185-2008. 54, 57, 86, 113

W. D. Cummings, S. E. Deforest, and R. L. McPherron. Measurements of the Poynting vector of standing hydromagnetic waves at geosynchronous orbit. *Journal of Geophysical Research*, 83:697–706, February 1978. doi: 10.1029/JA083iA02p00697. 54

A. W. Degeling, R. Rankin, K. Kabin, I. J. Rae, and F. R. Fenrich. Modeling ULF waves in a compressed dipole magnetic field. *Journal of Geophysical Research (Space Physics)*, 115:A10212, October 2010. doi: 10.1029/2010JA015410. 23, 116

J. W. Dungey. Interplanetary Magnetic Field and the Auroral Zones. *Physical Review Letters*, 6:47–48, January 1961. doi: 10.1103/PhysRevLett.6.47. 10

J. W. Dungey. The Length of the Magnetospheric Tail. *Journal of Geophysical Research*, 70:1753–1753, April 1965. doi: 10.1029/JZ070i007p01753. 12

J.W. Dungey. *Electrodynamics of the Outer Atmosphere: Report to National Science Foundation on Work Carried on Under Grant NSF-G450.* Scientific report // Ionospheric research, Ionosphere Research Labor, The Pennsylvania State University. Pennsylvania State University, Ionosphere Research Laboratory, 1954. URL `https://books.google.co.uk/books?id=3NrUAAAAMAAJ`. 14, 15, 18, 19, 27

T. Elsden and A. N. Wright. The use of the Poynting vector in interpreting ULF waves in magnetospheric waveguides. *Journal of Geophysical Research (Space Physics)*, 120: 166–186, January 2015. doi: 10.1002/2014JA020748. 6, 47, 54

T. Elsden, A. N. Wright, and M. D. Hartinger. Deciphering satellite observations of compressional ulf waveguide modes. *Journal of Geophysical Research: Space Physics*, pages n/a–n/a, 2016. ISSN 2169-9402. doi: 10.1002/2016JA022351. URL `http://dx.doi.org/10.1002/2016JA022351`. 2016JA022351. 6, 86

P. T. I. Eriksson, L. G. Blomberg, S. Schaefer, and K.-H. Glassmeier. On the excitation of ULF waves by solar wind pressure enhancements. *Annales Geophysicae*, 24:3161–3172, November 2006. doi: 10.5194/angeo-24-3161-2006. 86, 113

R. A. Fowler, B. J. Kotick, and R. D. Elliott. Polarization analysis of natural and artificially induced geomagnetic micropulsations. *Journal of Geophysical Research*, 72: 2871–2883, June 1967. doi: 10.1029/JZ072i011p02871. 108

K.-H. Glassmeier. Magnetometer array observations of a giant pulsation event. *Journal of Geophysics Zeitschrift Geophysik*, 48:127–138, 1980. 95

K. I. Gringauz. The structure of the ionized gas envelope of earth from direct measurements in the U.S.S.R. of local charged particle concentrations. *Planetary and Space Science*, 11:281–296, March 1963. doi: 10.1016/0032-0633(63)90030-8. 12

P. J. Hansen and C. K. Goertz. Validity of the field line resonance expansion. *Physics of Fluids B*, 4:2713–2719, September 1992. doi: 10.1063/1.860141. 116

M. Hartinger, V. Angelopoulos, M. B. Moldwin, K.-H. Glassmeier, and Y. Nishimura. Global energy transfer during a magnetospheric field line resonance. *Geophysical Research Letters*, 38:L12101, June 2011. doi: 10.1029/2011GL047846. 86, 95, 113

M. Hartinger, V. Angelopoulos, M. B. Moldwin, Y. Nishimura, D. L. Turner, K.-H. Glassmeier, M. G. Kivelson, J. Matzka, and C. Stolle. Observations of a Pc5 global (cavity/waveguide) mode outside the plasmasphere by THEMIS. *Journal of Geophysical Research (Space Physics)*, 117:A06202, June 2012. doi: 10.1029/2011JA017266. 54, 59, 86, 113

M. D. Hartinger, V. Angelopoulos, M. B. Moldwin, K. Takahashi, and L. B. N. Clausen. Statistical study of global modes outside the plasmasphere. *Journal of Geophysical Research (Space Physics)*, 118:804–822, February 2013. doi: 10.1002/jgra.50140. 86

W. J. Hughes. The effect of the atmosphere and ionosphere on long period magnetospheric micropulsations. *Planetary and Space Science*, 22:1157–1172, August 1974. doi: 10.1016/0032-0633(74)90001-4. 23

B. Inhester. Numerical modeling of hydromagnetic wave coupling in the magnetosphere. *Journal of Geophysical Research*, 92:4751–4756, May 1987. doi: 10.1029/JA092iA05p04751. 22, 87

J. A. Jacobs, Y. Kato, S. Matsushita, and V. A. Troitskaya. Classification of Geomagnetic Micropulsations. *Journal of Geophysical Research*, 69:180–181, January 1964. doi: 10.1029/JZ069i001p00180. 13

H. Junginger. Poynting vector as a diagnostic of hydromagnetic wave structure. *Journal of Geophysical Research*, 90:4155–4163, May 1985. doi: 10.1029/JA090iA05p04155. 54

K. Kabin, R. Rankin, I. R. Mann, A. W. Degeling, and R. Marchand. Polarization properties of standing shear Alfvén waves in non-axisymmetric background magnetic fields. *Annales Geophysicae*, 25:815–822, March 2007. doi: 10.5194/angeo-25-815-2007. 116

A. Kageyama, T. Sugiyama, K. Watanabe, and T. Sato. A note on the dipole coordinates. *Computers and Geosciences*, 32:265–269, March 2006. doi: 10.1016/j.cageo.2005.06.006. 119

L. Kepko and H. E. Spence. Observations of discrete, global magnetospheric oscillations directly driven by solar wind density variations. *Journal of Geophysical Research (Space Physics)*, 108:1257, June 2003. doi: 10.1029/2002JA009676. 14

L. Kepko, H. E. Spence, and H. J. Singer. ULF waves in the solar wind as direct drivers of magnetospheric pulsations. *Geophysical Research Letters*, 29:1197, April 2002. doi: 10.1029/2001GL014405. 14

M. G. Kivelson and D. J. Southwood. Resonant ULF waves - A new interpretation. *Geophysical Research Letters*, 12:49–52, January 1985. doi: 10.1029/GL012i001p00049. 14, 20, 30

M. G. Kivelson and D. J. Southwood. Coupling of global magnetospheric MHD eigenmodes to field line resonances. *Journal of Geophysical Research*, 91:4345–4351, April 1986. doi: 10.1029/JA091iA04p04345. 20, 26, 97, 107, 113

G. Le and C. T. Russell. Solar wind control of upstream wave frequency. *Journal of Geophysical Research*, 101:2571–2576, February 1996. doi: 10.1029/95JA03151. 60

D.-H. Lee and R. L. Lysak. Magnetospheric ULF wave coupling in the dipole model - The impulsive excitation. *Journal of Geophysical Research*, 94:17097–17103, December 1989. doi: 10.1029/JA094iA12p17097. 22, 27, 30, 116

D.-H. Lee and R. L. Lysak. Effects of azimuthal asymmetry on ULF waves in the dipole magnetosphere. *Geophysical Research Letters*, 17:53–56, January 1990. doi: 10.1029/GL017i001p00053. 116

J. F. Lemaire and K. I. Gringauz. *The Earth's Plasmasphere*. Cambridge University Press, January 1998. 12

I. R. Mann and A. N. Wright. Finite lifetimes of ideal poloidal Alfvén waves. *Journal of Geophysical Research*, 100:23677–23686, December 1995. doi: 10.1029/95JA02689. 19

I. R. Mann, A. N. Wright, and P. S. Cally. Coupling of magnetospheric cavity modes to field line resonances: A study of resonance widths. *Journal of Geophysical Research*, 100:19441–19456, October 1995. doi: 10.1029/95JA00820. 36, 44, 130

I. R. Mann, A. N. Wright, and A. W. Hood. Multiple-timescales analysis of ideal poloidal Alfvén waves. *Journal of Geophysical Research*, 102:2381–2390, February 1997. doi: 10.1029/96JA03034. 19

I. R. Mann, A. N. Wright, K. J. Mills, and V. M. Nakariakov. Excitation of magnetospheric waveguide modes by magnetosheath flows. *Journal of Geophysical Research*, 104:333–354, January 1999. doi: 10.1029/1998JA900026. 46

R. A. Mathie and I. R. Mann. Observations of Pc5 field line resonance azimuthal phase speeds: A diagnostic of their excitation mechanism. *Journal of Geophysical Research*, 105:10713–10728, May 2000. doi: 10.1029/1999JA000174. 92

R. A. Mathie, I. R. Mann, F. W. Menk, and D. Orr. Pc5 ULF pulsations associated with waveguide modes observed with the IMAGE magnetometer array. *Journal of Geophysical Research*, 104:7025–7036, April 1999. doi: 10.1029/1998JA900150. 24

R. L. McPherron. Magnetic Pulsations: Their Sources and Relation to Solar Wind and Geomagnetic Activity. *Surveys in Geophysics*, 26:545–592, September 2005. doi: 10.1007/s10712-005-1758-7. 13, 18, 21

J. A. Proehl, W. Lotko, I. Kouznetsov, and S. D. Geimer. Ultralow-frequency magnetohydrodynamics in boundary-constrained geomagnetic flux coordinates. *Journal of Geophysical Research (Space Physics)*, 107:1225, September 2002. doi: 10.1029/2001JA000135. 54

H. R. Radoski. Magnetic toroidal resonances and vibrating field lines. *Journal of Geophysical Research*, 71:1891–1893, April 1966. doi: 10.1029/JZ071i007p01891. 115

H. R. Radoski. A note on oscillating field lines. *Journal of Geophysical Research*, 72:418–419, 1967. doi: 10.1029/JZ072i001p00418. 115, 117

H. R. Radoski. A theory of latitude dependent geomagnetic micropulsations: The asymptotic fields. *Journal of Geophysical Research*, 79:595–603, February 1974. doi: 10.1029/JA079i004p00595. 116

I. J. Rae, E. F. Donovan, I. R. Mann, F. R. Fenrich, C. E. J. Watt, D. K. Milling, M. Lester, B. Lavraud, J. A. Wild, H. J. Singer, H. RèMe, and A. Balogh. Evolution and characteristics of global Pc5 ULF waves during a high solar wind speed interval. *Journal of Geophysical Research (Space Physics)*, 110:A12211, December 2005. doi: 10.1029/2005JA011007. 86, 113

D. Rankin and R. Kurtz. Statistical study of micropulsation polarizations. *Journal of Geophysical Research*, 75:5444–5458, October 1970. doi: 10.1029/JA075i028p05444. 108

R. Rankin, K. Kabin, and R. Marchand. Alfvénic field line resonances in arbitrary magnetic field topology. *Advances in Space Research*, 38:1720–1729, January 2006. doi: 10.1016/j.asr.2005.09.034. 116

G. J. Rickard and A. N. Wright. Alfven resonance excitation and fast wave propagation in magnetospheric waveguides. *Journal of Geophysical Research*, 99:13455, January 1994. doi: 10.1029/94JA00674. 21, 27, 29, 30, 31, 60, 82

B. Roberts. Magnetohydrodynamic waves. In E. R. Priest, editor, *Solar System Magnetic Fields*, pages 37–79, 1985. 17

A. J. B. Russell and A. N. Wright. Resonant absorption with 2D variation of field line eigenfrequencies. *Astronomy and Astrophysics*, 511:A17, February 2010. doi: 10.1051/0004-6361/200912669. 117, 118, 130, 137

C. T. Russell and R. C. Elphic. Initial ISEE magnetometer results - Magnetopause observations. *Space Science Reviews*, 22:681–715, December 1978. doi: 10.1007/BF00212619. 108

J. C. Samson, J. A. Jacobs, and G. Rostoker. Latitude-dependent characteristics of long-period geomagnetic micropulsations. *Journal of Geophysical Research*, 76:3675–3683, June 1971. doi: 10.1029/JA076i016p03675. 23

J. C. Samson, B. G. Harrold, J. M. Ruohoniemi, R. A. Greenwald, and A. D. M. Walker. Field line resonances associated with MHD waveguides in the magnetosphere. *Geophysical Research Letters*, 19:441–444, March 1992. doi: 10.1029/92GL00116. 21, 23, 27

T. E. Sarris, A. N. Wright, and X. Li. Observations and analysis of Alfvén wave phase mixing in the Earth's magnetosphere. *Journal of Geophysical Research (Space Physics)*, 114:A03218, March 2009. doi: 10.1029/2008JA013606. 108

T. E. Sarris, X. Li, W. Liu, E. Argyriadis, A. Boudouridis, and R. Ergun. Mode number calculations of ULF field-line resonances using ground magnetometers and THEMIS measurements. *Journal of Geophysical Research (Space Physics)*, 118:6986–6997, November 2013. doi: 10.1002/2012JA018307. 92

H. J. Singer, D. J. Southwood, R. J. Walker, and M. G. Kivelson. Alfven wave resonances in a realistic magnetospheric magnetic field geometry. *Journal of Geophysical Research*, 86:4589–4596, June 1981. doi: 10.1029/JA086iA06p04589. 116, 138

D. J. Southwood. The hydromagnetic stability of the magnetospheric boundary. *Planetary and Space Science*, 16:587–605, May 1968. doi: 10.1016/0032-0633(68)90100-1. 13

D. J. Southwood. Some features of field line resonances in the magnetosphere. *Planetary Space Science*, 22:483–491, March 1974. doi: 10.1016/0032-0633(74)90078-6. 18, 19, 20, 21, 26, 27, 115

D. J. Southwood and W. J. Hughes. Theory of hydromagnetic waves in the magnetosphere. *Space Science Reviews*, 35:301–366, 1983. doi: 10.1007/BF00169231. 14, 21, 27

D. J. Southwood and M. G. Kivelson. The effect of parallel inhomogeneity on magnetospheric hydromagnetic wave coupling. *Journal of Geophysical Research*, 91:6871–6876, June 1986. doi: 10.1029/JA091iA06p06871. 116

B. Stewart. On the Great Magnetic Disturbance Which Extended from August 28 to September 7, 1859, as Recorded by Photography at the Kew Observatory. *Philosophical Transactions of the Royal Society of London Series I*, 151:423–430, 1861. 13, 23

K. Takahashi and A. Y. Ukhorskiy. Solar wind control of Pc5 pulsation power at geosynchronous orbit. *Journal of Geophysical Research (Space Physics)*, 112:A11205, November 2007. doi: 10.1029/2007JA012483. 14, 46

K. Takahashi and A. Y. Ukhorskiy. Timing analysis of the relationship between solar wind parameters and geosynchronous Pc5 amplitude. *Journal of Geophysical Research (Space Physics)*, 113:A12204, December 2008. doi: 10.1029/2008JA013327. 14, 46

K. Takahashi, J. F. Fennell, E. Amata, and P. R. Higbie. Field-aligned structure of the storm time Pc 5 wave of November 14-15, 1979. *Journal of Geophysical Research*, 92: 5857–5864, June 1987. doi: 10.1029/JA092iA06p05857. 92

M. J. Thompson and A. N. Wright. Resonant Alfven wave excitation in two-dimensional systems - Singularities in partial differential equations. *Journal of Geophysical Research*, 98:15, September 1993. doi: 10.1029/93JA00791. 116, 117

M. J. Thompson and A. N. Wright. Comment on "Validity of the field line resonance expansion" [Phys. Fluids B 4, 2713 (1992)]. *Physics of Plasmas*, 1:1092–1094, April 1994. doi: 10.1063/1.870789. 116

A. D. M. Walker, R. A. Greenwald, W. F. Stuart, and C. A. Green. STARE auroral radar observations of Pc 5 geomagnetic pulsations. *Journal of Geophysical Research*, 84:3373–3388, July 1979. doi: 10.1029/JA084iA07p03373. 23

A.D.M. Walker. *Magnetohydrodynamic Waves in Geospace: The Theory of ULF Waves and their Interaction with Energetic Particles in the Solar-Terrestrial Environment*. Series in Plasma Physics. CRC Press, 2004. ISBN 9781420034004. URL `https://books.google.co.uk/books?id=tyc63onYuDwC`. 21

C. L. Waters, K. Takahashi, D.-H. Lee, and B. J. Anderson. Detection of ultralow-frequency cavity modes using spacecraft data. *Journal of Geophysical Research (Space Physics)*, 107:1284, October 2002. doi: 10.1029/2001JA000224. 73, 86

A. N. Wright. The interaction of Io's Alfven waves with the Jovian magnetosphere. *Journal of Geophysical Research*, 92:9963–9970, September 1987. doi: 10.1029/JA092iA09p09963. 62

A. N. Wright. Asymptotic and time-dependent solutions of magnetic pulsations in realistic magnetic field geometries. *Journal of Geophysical Research*, 97:6439–6450, May 1992. doi: 10.1029/91JA02666. 122, 157

A. N. Wright. Dispersion and wave coupling in inhomogeneous MHD waveguides. *Journal of Geophysical Research*, 99:159–167, January 1994. doi: 10.1029/93JA02206. 20, 21, 22, 27, 41, 60, 87

A. N. Wright and W. Allan. Structure, phase motion, and heating within Alfvén resonances. *Journal of Geophysical Research*, 101:17399–17408, August 1996. doi: 10.1029/96JA01141. 122

A. N. Wright and I. R. Mann. Global MHD Eigenmodes of the Outer Magnetosphere. In K. Takahashi, P. J. Chi, R. E. Denton, and R. L. Lysak, editors, *Magnetospheric ULF Waves: Synthesis and New Directions*, volume 169 of *Washington DC American Geophysical Union Geophysical Monograph Series*, page 51, 2006. 21, 44

A. N. Wright and G. J. Rickard. A numerical study of resonant absorption in a magnetohydrodynamic cavity driven by a broadband spectrum. *Astrophysical Journal*, 444: 458–470, May 1995a. doi: 10.1086/175620. 21, 22, 38, 60

A. N. Wright and G. J. Rickard. ULF pulsations driven by magnetopause motions: Azimuthal phase characteristics. *Journal of Geophysical Research*, 100:23703–23710, December 1995b. doi: 10.1029/95JA01765. 38, 40, 42, 43

A. N. Wright and M. J. Thompson. Analytical treatment of Alfvén resonances and singularities in nonuniform magnetoplasmas. *Physics of Plasmas*, 1:691–705, March 1994. doi: 10.1063/1.870815. 116, 124

S. T. Zalesak. Fully multidimensional flux-corrected transport algorithms for fluids. *Journal of Computational Physics*, 31:335–362, June 1979. doi: 10.1016/0021-9991(79)90051-2. 31

X. Zhu and M. G. Kivelson. Global mode ULF pulsations in a magnetosphere with a nonmonotonic Alfven velocity profile. *Journal of Geophysical Research*, 94:1479–1485, February 1989. doi: 10.1029/JA094iA02p01479. 22

C. W. S. Ziesolleck and D. R. McDiarmid. Auroral latitude Pc 5 field line resonances: Quantized frequencies, spatial characteristics, and diurnal variation. *Journal of Geophysical Research*, 99:5817–5830, April 1994. doi: 10.1029/93JA02903. 24